DISSERTATION

PART I: SYNTHESIS AND CHARACTERIZATION OF TITANIA AND MAGNESIUM NANOPARTICLES FOR HYDROGEN PRODUCTION AND STORAGE

PART II: CHARACTERIZATION AND GROWTH OF BRANCHED SILICON NANOWIRES GROWN VIA A SIMULTANEOUS VAPOR-LIQUID-SOLID AND VAPOR-SOLID-SOLID MECHANISM

Submitted by

Daniel Jay Shissler

Department of Chemistry

In partial fulfillment of the requirements

For the Degree of Doctor of Philosophy

Colorado State University

Fort Collins, Colorado

Spring 2015

Doctoral Committee:

Advisor: Amy Prieto

Matthew Shores
Anthony Rappé
Alan Van Orden
David Dandy

ABSTRACT

PART I: SYNTHESIS AND CHARACTERIZATION OF TITANIA AND MAGNESIUM NANOPARTICLES FOR HYDROGEN PRODUCTION AND STORAGE

PART II: CHARACTERIZATION AND GROWTH OF BRANCHED SILICON NANOWIRES GROWN VIA A SIMULTANEOUS VAPOR-LIQUID-SOLID AND VAPOR-SOLID-SOLID MECHANISM

Many things are taken for granted without the realization of the effect they have on our daily lives. Attention and time can be expended towards the more enjoyable things in life. Matters that once required attention are now automated and regulated without realization or effort. Ventures which may have taken days may now be accomplished in minutes. Treks that took years can now be traversed in days. Civilization today would not be as it is without the conveniences of technology.

Technology, however, requires energy. The majority of today's energy is derived from fossil fuels, an unsustainable resource. The dependence of modern technology and transport on these resources make them valued commodities. However, with dwindling reserves the modern way of life is threatened. In addition to the technological dependency, prolonged exploitations of these resources will cause irreversible ecological consequences. Climate change is a highly debated topic of discussion. Evidence shows a critical turning point may have already been passed, reversing the effects of climate change may no longer be practicable. Although change is inevitable, delaying the full onset is practicable. Transition towards a renewable energy economy is essential in order to reduce and eventually end fossil fuel consumption. To this end, development

of technologies to efficiently harness renewable resources is imperative. Furthermore, developing new methods of effectively storing energy is necessary because of the intermittency of renewable resources. All research in the Prieto Lab is oriented towards advancing these technologies.

Currently the research in the Prieto group is photovoltaic material-intensive in contrast to the days that it was once battery-oriented. Both topics are key elements for the transition to a renewable energy economy. Solar energy is available to all and could in theory power the planet. As stated though, solar power is intermittent and energy storage is required. The use of batteries to store excess energy is a reliable method. However, there are more promising approaches toward storing energy.

Hydrogen is an attractive fuel because of its high energy density (142 MJ/kg for H_2 versus 47 MJ/kg for liquid hydrocarbons) and clean burning nature. It is also the most abundant element on earth, although less than 1 % is composed of molecular hydrogen, H_2 (the vast majority exists as water). Efficient methods of producing hydrogen have become a key topic of interest because of the ever growing concern of the environmental impacts of the continued burning of fossil fuels for energy. The ideal method of producing hydrogen would be to split water by harnessing the power of the sun. This method would be most efficient by removing as many steps as possible and use the sun's energy to directly split the water using a photocatalyst. The oxide TiO_2 is cheap and abundant and is commonly used for photoconversion. However, this material has a wide band gap hence it only absorbs in the UV region of the spectrum. This means that dye-sensitization is necessary to achieve absorbance within the more intense, visible region of the solar spectrum. The most efficient dyes, however, are ruthenium based making them expensive. In addition to the requirement of an expensive photosensitizer, platinum is added as a catalyst in order for charge separation to occur and drive the splitting of water. Because of the expense of the required

materials, minimizing the amount necessary for effective water splitting is essential. For this purpose, a single pot synthesis has been developed in our lab to produce 5 nm dyed-platinized TiO_2 nanoparticles for hydrogen production. The particles produce hydrogen with Pt and Ru amounts as low as 0.15 wt%. and 0.02 wt%, respectively. Even with such low amounts the material exhibits significant increase in the catalysis of water splitting. The synthesis, characterization and hydrogen producing properties are described in Chapter 1.

Although hydrogen is a promising method of storing energy, its gaseous nature does pose some problems. Another hurdle hindering the use of hydrogen as a method to store energy is the ability is safely store and transport it. In its gaseous state, molecular hydrogen takes up a large volume and is extremely dangerous making it not practical for mobile storage. Mobile storage is necessary if hydrogen is to be used as a viable fuel for transportation. There are many potential candidates for storing hydrogen via both physical and chemical processes. Several active areas of research include storing molecular hydrogen in high porosity materials, adsorption of hydrogen on carbonaceous materials and chemisorption in metal hydride systems.

Light metal hydrides, in particular MgH_2, is a particularly attractive hydrogen storage material because of its high gravimetric (7.6 wt% H_2) and volumetric (110 kg H_2/m^3) capacities. However, bulk magnesium shows sluggish kinetics making it an impractical candidate at reasonable temperatures (below 600 K). Recent work has focused on two general approaches to improve sorption kinetics: nanostructuring the magnesium for greater surface area and incorporating dopants for enhanced kinetics. Both of these strategies are typically accomplished by ball milling to create small crystallites and incorporate various transition metal dopants. This technique, however, does not allow for control over crystallite size or shape, and impurity phases are common byproducts. Previous reports have demonstrated the use of a variety of transition

metal dopants including Ni, Ti, V, Fe, Cr, Nb and Pd. Some transition metal oxides have also been shown to enhance kinetic performance. [1-9]Nickel is a particularly intriguing candidate because it is known to be a catalyst for H-H bond dissociation and Mg-Ni alloys are known hydrogen storage materials (e.g. Mg_2Ni). It has been reported as a dopant previously, but only in samples that were prepared via a ball milling process. Ball milling does not allow for control over particle size so some enhanced kinetics may be due to small crystallites. Furthermore, in this synthesis method it is possible to obtain a mixture of pure magnesium, magnesium doped with small percentages of nickel, magnesium-nickel alloys and pure nickel metal. With all of these possible products, it is difficult, if not impossible, to isolate the effect of a nickel dopant on the sample because of the number of variables in this complicated system. Chapters 2 is adapted from a published book chapter and gives a broad overview of the use of Mg for hydrogen storage. It covers several methods of synthesizing Mg nanomaterials and the effects that various dopants have on its hydrogen storage properties. The chapter also specifies different techniques in which hydrogen storage properties can be analyzed. The Ni doped Mg nanoparticles mentioned in Chapter 2 was developed and studied in the Prieto lab and some of the work done thus far is detailed in Chapter 3. The Ni doped Mg nanoparticles are of particular interest because of the unexplained increase in hydrogen sorption kinetics. Sorption kinetics are expected to decrease after cycling due to particle agglomeration. However, Ni doped Mg particles exhibit an increase in performance after several cycles. For this reason, an in depth analysis of the material and it's kinetic behavior has been performed. Although hydrogen is a promising method of storing solar energy harnessed by the use of TiO_2 photocatalysts, other routes, such as batteries, need also be explored.

Silicon is a tried-and-true material for photovoltaics partially because it is the second most abundant material within the earth's crust. However, isolation of pure silicon is demanding since it must be extracted from SiO_2. Purification of Si for photovoltaic cells requires high temperatures and caustic gases. In spite of the incredible abundance of Si, the cost of processing diminishes its practicality. For this reason it is important to maximize its ability to collect solar energy while using a minimum amount of material. This can be achieved by producing a high surface area photoelectrode.

Production of Si nanowire arrays can be achieved by many methods.[10-12] Lithography can be used as a top-down process to build arrays. This is done by etching channels into silicon wafers. Although effective, this is an inefficient method because of the loss of material. A bottom up process would be most favorable. This can be achieved by using the Vapor-Liquid-Solid (VLS) growth mechanism.[13] Typically, Au catalyst seed particles are deposited on a Si substrate. Silane gas is passed over the particles. Silicon then dissolves into the Au particle, eventually reaching saturation. At that point, Si nucleates and begins to grow into a wire. Highly ordered wire arrays can be grown if the initial catalyst is properly deposited. A down side of this growth method is the incorporation of Au into the Si crystal.

Gold impurities pose a danger to efficient solar energy conversion. For example, Au impurities create trapped states that decrease carrier transport lifetimes. To this end, Cu is being used as a catalyst in place of the traditional Au catalyst. Silicon wires grown with Cu catalysts exhibit increased carrier transport compared to Au grown Si. For this reason Cu is becoming of greater interest as a catalyst for the VLS growth of Si nanowires. Cu has a greater diffusion rate and solubility in Si than Au at production temperatures. However, due to the inherent behavior of the copper silicide to form as precipitates and extrude to the surface, the contamination within the

Si tends to be lower. Because of the significance of this behavior towards the electronic performance of the material, it is important to understand this behavior at the temperatures and size scales at which the material will be produced. It is believed that the combination of the high diffusion rate of copper, silicide extrusion, and the orientation of the growing crystal is responsible for the observation branched silicon nanowires within our lab.

The initial synthesis of the branched silicon nanowires was a serendipitous event. The branched wires were originally observed whilst experimenting with the feasibility of growing Cu_2Sb nanowires via a Vapor-Liquid-Solid (VLS) mechanism. The compound Cu_2Sb is a Li-ion battery anode material that is of major interest in the Prieto group. The end goal was to produce high purity low defect crystals of Cu_2Sb nanowires that could be cycled and the lithiation and de-lithiation of the material could be well characterized without the effects of impurities or crystal defects. However, during the attempted synthesis of this compound, the growth of highly branched silicon nanowires was observed. The branched wires were characterized and the once serendipitously grown wires are now reproducible. Chapter 4 includes the characterization and initial proposed growth mechanism. My contribution to this project has been to improve upon the growth parameters and further understanding of the growth mechanism. Many assumptions had been made about the growth process and the roles of many growth parameters were misinterpreted, understating the importance of the parameters toward the wire growth. It was determined that the Au catalyst initially used to grow the branched wires was not necessary for wire growth and also detrimental to the yield of branched wires. Using only Cu as a catalyst increases the yield of the branched wires. However, the substrates must be properly treated prior to the reaction in order for Cu to deposit on the substrate to initiate wire growth during the reaction. Chapter 5 includes an in-depth study of substrate preparation and conditions necessary for branched Si nanowire growth. If

copper is to be used as catalysts for the growth of Si nanowire arrays, the interaction within the Cu-Si system need to be well characterized. Chapter 6 entails a description of the properties of the branched Si nanowires that expose interesting characteristics unique to the Cu-Si system. The unique interaction of Cu and Si allows for the growth of these novel nanostructures. The growth mechanism depends on the combination of the crystalline orientation of wire growth, defects within the crystal, and the fast diffusion of Cu into these defects, Although not fully confirmed, the proposed growth mechanism may aid in the development of clever ways to grow complex nanowire arrays for use as photovoltaics.

1. Oelerich, W.; Klassen, T.; Bormann, R., Metal Oxides as Catalysts for Improved Hydrogen Sorption in Nanocrystalline Mg-Based Materials. *Journal of Alloys and Compounds* **2001,** *315* (1-2), 237-242.
2. Oelerich, W.; Klassen, T.; Bormann, R., Hydrogen Sorption of Nanocrystalline Mg at Reduced Temperatures by Metal-Oxide Catalysts. *Advanced Engineering Materials* **2001,** *3* (7), 487-490.
3. da Conceicao, M. O. T.; Brum, M. C.; dos Santos, D. S.; Dias, M. L., Hydrogen Sorption Enhancement by Nb2o5 and Nb Catalysts Combined with Mgh2. *Journal of Alloys and Compounds* **2013,** *550*, 179-184.
4. Barkhordarian, G.; Klassen, T.; Bormann, R., Fast Hydrogen Sorption Kinetics of Nanocrystalline Mg Using Nb2o5 as Catalyst. *Scripta Materialia* **2003,** *49* (3), 213-217.
5. Sabitu, S. T.; Goudy, A. J., Dehydrogenation Kinetics and Modeling Studies of Mgh2 Enhanced by Transition Metal Oxide Catalysts Using Constant Pressure Thermodynamic Driving Forces. *Metals* **2012,** *2* (3), 219-228.
6. Shahi, R. R.; Yadav, T. P.; Shaz, M. A.; Srivastva, O. N., Studies on Dehydrogenation Characteristic of Mg(Nh2)2/Lih Mixture Admixed with Vanadium and Vanadium Based Catalysts (V, V2o5 and Vcl3). *International Journal of Hydrogen Energy* **2010,** *35* (1), 238-246.
7. Hanada, N.; Hirotoshi, E.; Ichikawa, T.; Akiba, E.; Fujii, H., Sem and Tem Characterization of Magnesium Hydride Catalyzed with Ni Nano-Particle or Nb2o5. *Journal of Alloys and Compounds* **2008,** *450* (1-2), 395-399.
8. Hanada, N.; Ichikawa, T.; Hino, S.; Fujii, H., Remarkable Improvement of Hydrogen Sorption Kinetics in Magnesium Catalyzed with Nb2o5. *Journal of Alloys and Compounds* **2006,** *420* (1-2), 46-49.
9. Friedrichs, O.; Sanchez-Lopez, J. C.; Lopez-Cartes, C.; Klassen, T.; Bormann, R.; Fernandez, A., Nb2o5 "Pathway Effect" on Hydrogen Sorption in Mg. *Journal of Physical Chemistry B* **2006,** *110* (15), 7845-7850.
10. Huang, R.; Zhu, J., Silicon Nanowire Array Films as Advanced Anode Materials for Lithium-Ion Batteries. *Materials Chemistry and Physics* **2010,** *121* (3), 519-522.
11. Putnam, M. C.; Boettcher, S. W.; Kelzenberg, M. D.; Turner-Evans, D. B.; Spurgeon, J. M.; Warren, E. L.; Briggs, R. M.; Lewis, N. S.; Atwater, H. A., Si Microwire-Array Solar Cells. *Energy & Environmental Science* **2010,** *3* (8), 1037-1041.
12. Warren, E. L.; Atwater, H. A.; Lewis, N. S., Silicon Microwire Arrays for Solar Energy-Conversion Applications. *J Phys Chem C* **2014,** *118* (2), 747-759.
13. Wang, N.; Cai, Y.; Zhang, R. Q., Growth of Nanowires. *Materials Science & Engineering R-Reports* **2008,** *60* (1-6), 1-51.

ACKNOWLEDGMENTS

I would like to thank my friends for getting me out of the lab when I needed it.

Many thanks to Ron Costello, Mike Olsen, and Tom Frederick for always being available and helpful even at the last minute.

It was a wonderful experience that was shared with my fellow lab mates, exclusively for those who shared the “dark times” within the lab.

I would also like to thank my parents and family for their love and support even though I rarely saw them during my years in grad school.

I would especially like to thank Amy for her patience and guidance over the many years (too many years), allowing me to take time off to hike the Appalachian Trail with my brother, and giving me the opportunity to accomplish something I never thought possible.
Nothing I write here could even begin to express the gratitude I have for her.

TABLE OF CONTENTS

LIST OF TABLES

LIST OF FIGURES

PART I: SYNTHESIS AND CHARACTERIZATION OF TITANIA AND MAGNESIUM NANOPARTICLES FOR OF HYDROGEN PRODUCTION AND STORAGE

Chapter 1

Direct Synthesis of Dyed Capped Platinized TiO_2 Nanoparticles for Subsequent Sensitization by Donor-Chromophore-Acceptors: Towards Hydrogen Generation from Water[i]

1.1 Introduction

With dwindling supplies of oil there is an ever-growing need to find another source of abundant energy. Solar energy is available to all and could in theory power the planet. Capture and conversion of this solar energy is a topic of great interest. The material TiO_2 is an inexpensive material available for such use.[1-3] However, TiO_2 only captures solar light higher in energy than the visible range, thus losing a significant portion of the solar spectrum.[4-5] To this end it is necessary to sensitize TiO_2 to absorb a broader spectrum (Figure 1.1).[2, 6]

In an attempt to convert solar energy into storable chemical energy, donor-chromophore (DC) and donor-chromophore-acceptors (DCA) are being used to sensitize the surface of platinized TiO_2 for hydrogen production. Numerous investigators have pursued various DC and DCA combinations with the most common non-porphyrin chromophores employing Ru, and to a lesser extent Pt, as the metal catalyst.[6-8] This effort is justified as the use of DC and DCA sensitizors on platinized TiO_2 allows for the photogeneration of hydrogen gas from aqueous solutions using visible light. In contrast, most transition metal oxides used for photocatalytic water splitting require wavelengths in the UV as the radiation source.[3-4, 9-10] The pursuit, however, to improve the platinized semiconductor nanoparticle has been conducted with a lot

[i] Daniel J.Shissler, Derek C. Johnson, & Amy L. Prieto.
Daniel Shissler and Derek Johnson equally contributed to the synthesis, XRD and TEM analysis of the TiO_2 nanoparticles. Derek Johnson performed XPS and electrochemical characterization of the TiO_2 nanoparticles. Daniel Shissler performed the UV-Vis spectral analysis and the hydrogen production experiments.This dissertation chapter is adapted from a manuscript being submitted to *ACS Nano*.

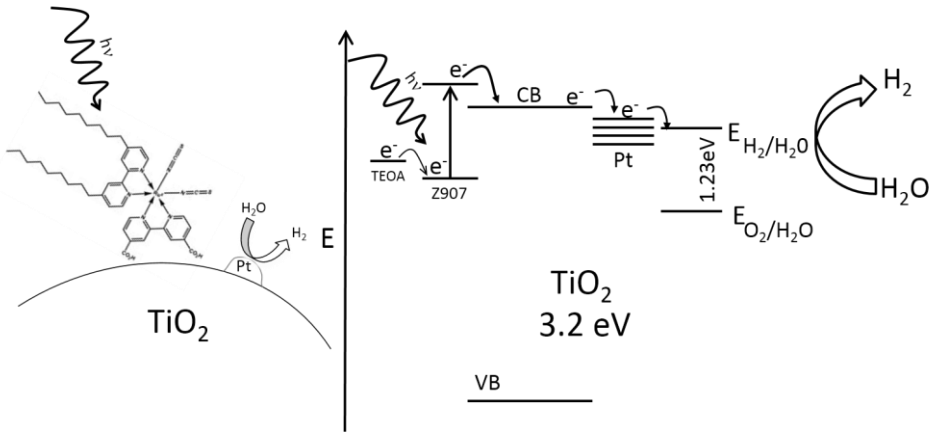

Figure 1.1: Schematic of dyed platininized TiO_2 nanoparticles and energy diagram of electron transfer through material.

less vigor. Although this aspect has been neglected to some extent, significant obstacles need to be overcome in order for this energy conversion option to be viable.

Titania is typically platinized post synthesis by a photoinduced reduction of a platinum-based acid or salt.[11-12] This method, however, has two repercussions when considering the viability of this process. First, because a surfactant is not used, the initial nanoparticle size is large, c.a. 100 nm; resulting in an undesirably low surface-to-volume ratio. However, if a surfactant were used to control particle growth, it would subsequently be destroyed during the photoinduced platinization reaction. Second, the nanoparticles agglomerate and do not suspend well in solution because a surfactant is not initially bound to the platinized TiO_2 surface. This makes binding the DC or DCA to the surface of the particle much more difficult and results in low yields. To overcome these obstacles, a new one-pot reaction that yields surfactant-capped 5 nm platinized TiO_2 nanoparticles has been developed and is described herein. Building upon the viability of this reaction a one pot reaction has been developed that not only platinizes the TiO_2 but also sensitizes the TiO_2 particles to visible light. Although the particles contain Pt and Ru, non-earth abundant elements, the particles contain as low as .15 wt% and .02 wt%, respectively, and still exhibit water splitting abilities.

1.2 Experimental

The synthesis of 80 nm titania nanoparticles is performed solvothermally by a similar procedure reported in the literature and is outlined as Scheme 1 in the Supporting Information of this chapter.[13-14] Titanium (IV) isopropoxide (TIP) (Aldrich, 97%) is added dropwise to anhydrous toluene (Sigma-Aldrich, anhydrous 99.8%) in a 23 mL Teflon® lined stainless steel acid digestion bomb. The total liquid volume in the stainless steel bomb is such that the pressure is approximately 125 atm when the reaction is at its maximum temperature. The reaction solution is heated at 4 °C/min to a temperature of 250 °C and held for 6 hrs. Once cooled, the solution is centrifuged and decanted leaving a fine white powder. The powder is resuspended in 2-propanol (Sigma Aldrich, 99.5% anhydrous) to remove the reaction byproducts. The solution is centrifuged and decanted. This procedure is referred to as the cleaning procedure in the reaction mechanism and is performed three times to ensure all reaction byproducts are removed. To modify the surface of the titania nanocrystals with platinum, a photo-initiated reduction reaction is performed by a similar procedure reported in the literature for titania.[12, 15-16] The nanocrystals are suspended in an aqueous methanol solution with chloroplatinic acid hexahydrate (Sigma-Aldrich, ACS grade). The solution is irradiated with UV light at 254 nm for 4 hrs. The resulting gray suspension is washed to remove the reaction byproducts by the same cleaning procedure described above. These nanoparticles are then compared to platinized TiO_2 nanoparticles that were synthesized using a single-pot procedure that we developed which has not been reported in the literature.

The synthesis routes of the 5 nm titania particles is similar to that in literature.[14] Reaction vessels are prepared similar to that of the 5 nm titania nanoparticles. However, oleic acid is added to the reaction vessel in addition to the toluene and TIP (Figure S1.1 Scheme 2). Platinized

5 nm particles are prepared with the addition of chloroplatinic acid (Figure S1.1 Scheme 3). Dyed-platinized 5 nm particles are prepared by the addition of *cis*-Bis (isothiocyanato)(2,2′-bipyridyl-4,4′-dicarboxylato)(4,4′-di-nonyl-2′-bipyridyl)ruthenium(II) (Z907) to the previous reaction solution (Figure S1.1 Scheme 4). Once cooled, the solution is centrifuged and decanted to separate larger non-capped particles. Acetone is then added to the remaining supernatant to precipitate 5 nm particles. This heterogeneous solution is then centrifuged and decanted. The resulting precipitate is resuspended in toluene and then once again precipitated with acetone and then centrifuged and decanted. The 5 nm particles are precipitated and separated a total of three times. The remaining precipitate is then once again suspended in toluene to form an indefinitely stable colloidal solution.

Particles prepared through reaction Schemes 1-3 were characterized through various methods. Powder X-Ray diffraction (XRD), transmission electron microscopy (TEM) imaging, and selected area electron diffraction (SAED) were also performed on the synthesized particles. XPS analysis was performed for elemental analysis, as well as to identify the oxidation states of the elements present. Elemental content was determined by the use of inductively coupled plasma optical emission spectroscopy (ICP-OES) performed by Robertson Microlit Laboratories. To analyze the catalytic behavior of the particles, electrochemical studies were performed on films prepared by depositing the various particles by either spin coating or dip casting.

Hydrogen production experiments were performed by illuminating a suspension of TiO_2 particles. Particles were first precipitated by addition of acetone and then centrifuged and decanted. An aqueous heterogenous suspension was then made by first suspending the particles in a minimal amount of MeOH, due to the hydrophobic capping ligands, and then diluted to 40 ml with 0.2 M triethanolamine (TEOA) solution with pH adjusted to 7. Then, the suspension was

transfered to a 50 ml round bottom flask. Triethanolamine was added as a sacrificial oxidant. This was required due to the slow kinetics of the oxidation side of the water splitting process. The head space of the flask was purged with Ar and a known amount of methane was injected as an internal standard. The light source was a Dolan Jenner Industries Fiber Lite DC950 Illuminator with a USHIO 3250K quartz halogen bulb purchased from Cole-Parmer filtered by a 400 nm longpass filter. The sample was illuminated at an average intensity of 230 mW/cm^3 measured with a Thor labs S302A Thermopile. The amount of hydrogen produced was tracked by performing GC-TCD on samples taken from the head space of the flask. GCs were performed using argon as a carrier gas flowing through a 6 ft-2 mm ID Restek column packed with 5A sieves. The molar amount of hydrogen produced was determined by comparing relative ratios of hydrogen and methane to that of an established calibration curve.

1.3 Results and Discussion

Different reaction routes were used to prepare TiO_2 and platinized TiO_2 nanoparticles of various sizes. This was done to compare morphologies and catalytic behavior of the particles prepared via separate routes. The particles with the larger surface area, 5 nm particles, are expected to exhibit greater catalytic activity. However, the platinization route of TiO_2 is via photoinduced reduction of platinum acid or salt. Because of the oleic acid surfactant of the 5 nm particles, this is not a viable option. The UV exposure necessary to reduce platinum would also degrade the oleic acid surfactant causing the particles to agglomerate. The UV exposure can be bypassed by platinizing in situ, during 5 nm particle formation. It was questioned whether this method would form good electronic adhesion between the Pt catalyst and the TiO_2 particles. But the analysis, as described herein, shows that this is not the case.

The final product of the 80 nm TiO_2 particle synthesis was a white powder. The XRD pattern of the powder can be indexed with the anatase TiO_2 crystalline structure (Figure S1.2a). Ex situ platinization results in a gray powder. The platinization process does not significantly alter the size or morphology of the TiO_2 particles. A peak for the Pt (111) plane can be identified in the XRD pattern of the platinized particles (Figure S1.2b). Also, Scherrer analysis of the (101) plane of TiO_2 suggests that a minor decrease in average particle size, 85 nm to 80 nm, occurs during platinization. TEM imaging of the particles before and after platinization confirm the XRD data (Figure S1.3-S1.4). TEM images reveal that the particles size is on the average of 80 nm. EDX confirms the presence of titanium and oxygen for both samples, as well as Pt for the platinized particles. Similarly the SAED confirms the TiO_2 crystalline phase. In high resolution TEM dark contrast islands can be observed on the TiO_2 particles, which would be expected of platinum deposited on the surface (Figure S1.4c-d).

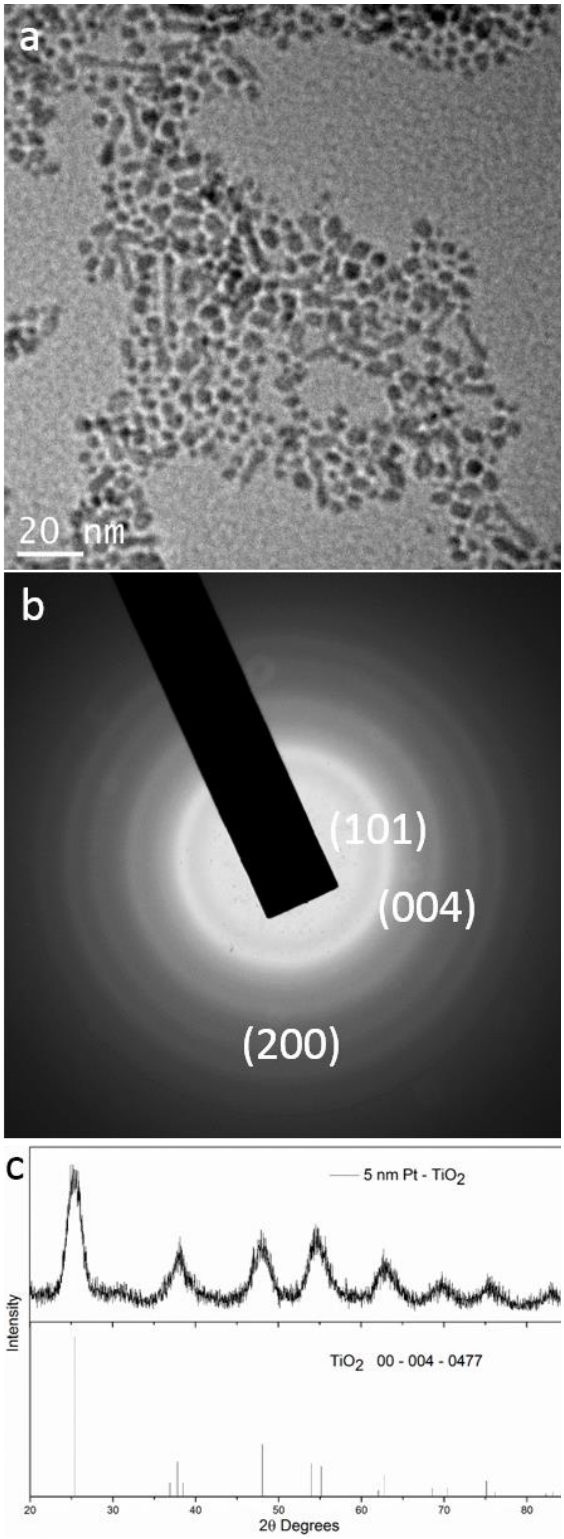

Figure 1.2: (a) A TEM image of 5 nm platinized TiO_2 nanoparticles. (b) A SAED pattern and (c) powder XRD pattern of 5 nm platinized that both index to anatase TiO_2.

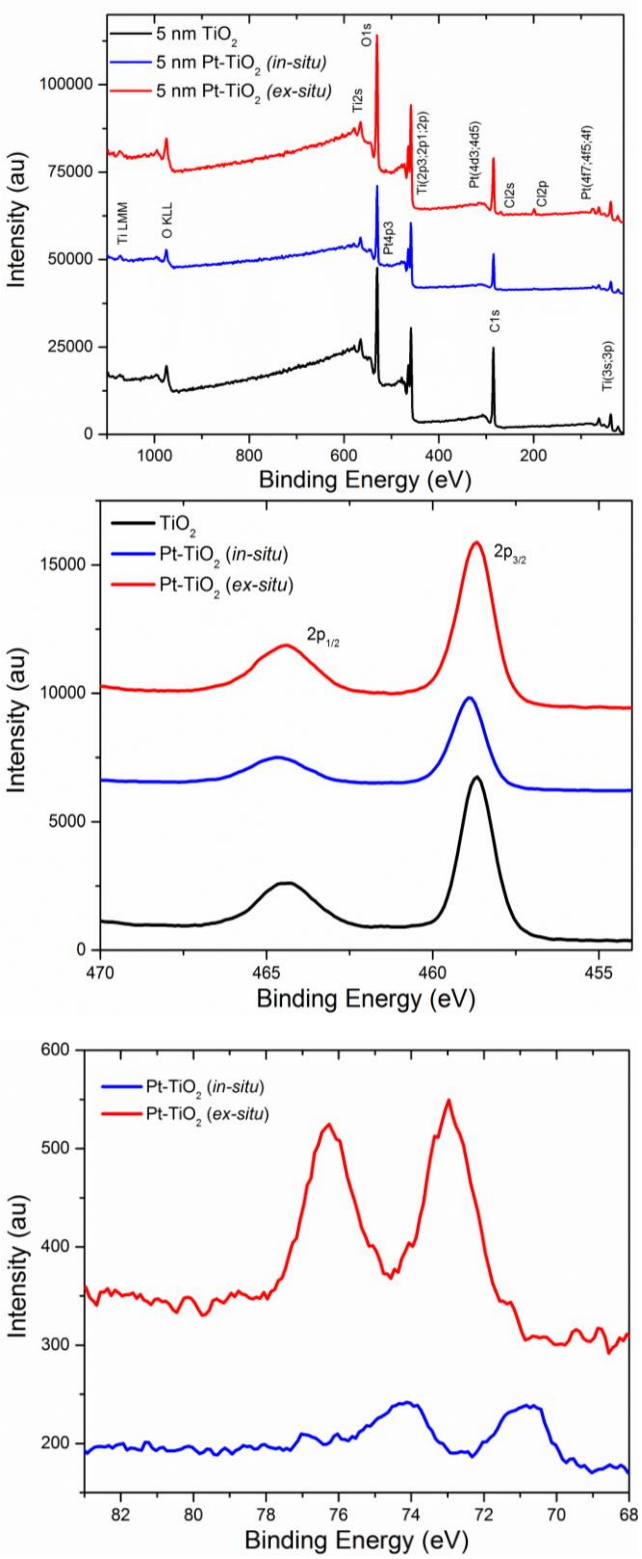

Figure 1.3: a) XPS of TiO_2 and platinized TiO_2 particles. b) Titanium high resolution XPS c) Platinum high resolution **XPS.**

Surfactant-capped 5 nm particles are characterized by the same route. Powder XRD patterns of the 5 nm particles can be indexed to anatase TiO_2. Significant broadening of the peaks can be observed. Scherrer analysis on the (101) plane indicates that the particles are approximately 5 nm in diamter. Scherrer analysis results are confirmed by TEM imaging. Also, SAED confirms the crystalline structure of the powder XRD as anatase TiO_2 (Figure. S1.5). Similar results are found for the platinized 5 nm particles (Figure 1.2). Platinum is not detected during XRD analysis of the platinized 5 nm particles. This is likely due to the low amount of Pt within the particles as well as the small size of the Pt islands.

The presence of Pt for the platinized 5 nm particles, however, is verified by high resolution XPS analysis (Figure 1.3). XPS analysis of 80 nm particles can be found in Figure S1.6 along with further high resolution scans of 5 nm particles in Figure

S1.7. For comparison, 5 nm particles were platinized by both the in situ (Figure S1.1 Scheme 3) and the photoinduced ex situ methods (Figure S1.1 Scheme 1). The platinum peaks of the in situ particles are shifted compared to those of the ex situ platinized 5 nm particles. High resolution analysis of the titanium peak does not exhibit a similar shift. Therefore, the shift is specific to the platinum peaks. The observed shift is a characteristic of Pt^{2+} instead of ground state Pt. This is due to the lack of an electron donating compound, MeOH, during the in situ platinization. It is likely that a reaction similar to the Meerwein-Ponndorf-Verley (MPV) reduction is occurring to reduce the Pt. TIP decomposes to produce isopropyl alcohol, which then could act as a reducing agent when catalyzed by the remaining TIP.[17-18] The different oxidation state of the Pt, however, does not affect the catalytic enhancements of the Pt observed during electrochemical characterization.

An electrochemical evaluation of these nanoparticles was conducted to determine hydrogen evolution efficiency. Figure 1.4 contains cyclic voltammograms of prepared films. Films of the 80 nm particles were prepared by spin casting, whereas films

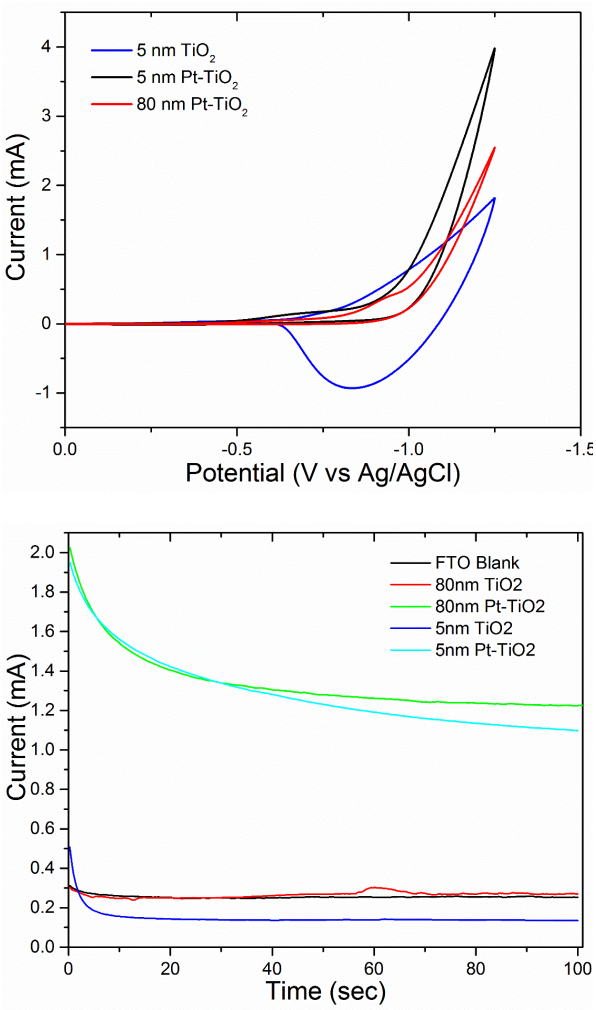

Figure 1.4: Comparison of the catalytic ability of prepared films. Cyclic Voltammetry (a) performed at 100 mV/s comparing the hydrogen evolution of platinized 5 nm TiO_2 with that nonplatinized 5 nm TiO_2 and 80 nm TiO_2 particles. Constant potentiometry at 1.2 V was performed to show the increased amount of hydrogen production of the prepared films and substrates.

composed of the 5 nm particles were prepared by dip casting. Dip casting of 80 nm particles results in patchy films due to the lack of surfactant on the particles. Film thicknesses are approximately 100 nm in thickness. For the non-platinized TiO_2, there is back oxidation during cyclic voltammetry that is a result of slow hydrogen adsorption-desorption kinetics at the surface of the electrode, i.e. TiO_2 (Figure 1.4a). This behavior is not observed for the platinized TiO_2, suggesting that the platinum is catalyzing the evolution of the gas from the surface of the electrode. Figure 1.4a shows that the increase in current is similar for particles platinized ex situ and in situ. The similar catalytic ability shows that the platinum forms good electronic contact for both methods of platinization despite the use of surfactant and the altered oxidation state of the platinum present on the 5 nm particles. Also, a reducing peak is observed prior to hydrogen formation during the first cycle of the 5 nm particles. This may be the reduction of the Pt^{2+} back to the ground state. By comparing the currents it is observed that the 5 nm particles produce a greater amount of hydrogen. This performance is further emphasized by the fact the weight percent of the 5 nm in situ platinized particles is a magnitude less wt% Pt than the 80 nm ex situ particles.

Figure 1.4b contains plots of current as a function of time for platinized and non-platinized TiO_2 and bare FTO (blank) electrodes at 1.2 V vs. Ag/AgCl. The current observed for the platinized TiO_2 is approximately five times higher when compared to non-platinized TiO_2 and FTO electrodes. It should also be noted that bubble formation is visible when using the platinized TiO_2 electrode, while bubble formation was not observed for the non-platinized TiO_2 or FTO electrodes.

Due to the success of the in situ platinization of TiO_2 in terms of the ability to generate hydrogen, the material was further studied for photocatalytic ability. A ruthenium based

chromophore was added to the reaction scheme (Figure S1.1 Scheme 4) to further expand on the applicability of preparing photocatalytic particles with a one pot synthesis. The chromophore Z907 was selected because of its greater stability compared to other commercial dyes.[19-21] UV-Visible absorption spectroscopy was performed on colloidal solutions of 5 nm particles (Figure 1-5a). As can be seen, particles without dye only absorb in the UV regime, whereas those that were dyed are now sensitized to absorb visible light. The absorption of visible light can be observed by the eye in Figure 1.5b. It is observed that platinized particles have a browner coloration to the solution. TiO_2 particles were also dyed ex situ by adding Z907 to an aqueous suspension of particles. This was done for comparison of color. The black solution contains heavily platinized TiO_2 particles. It should be noted that heavily platinized particles, >2 wt% Pt/TiO_2, destabilize and precipitated within a week of synthesis. Samples below this Pt conentration threshold remain stable and suspended essentially indefinetely.

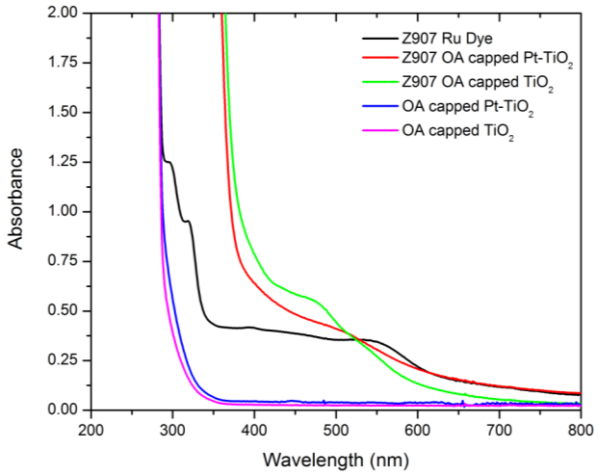

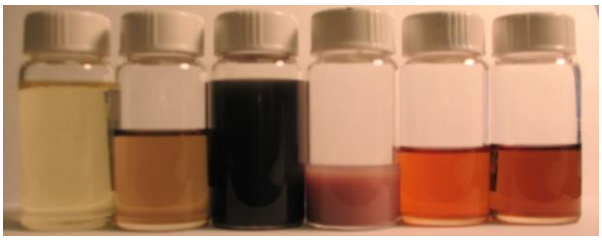

Figure 1.5: a) UV-Vis Absorption of TiO_2 particles and dye. b) Images, listed from left, of 5nm OA capped TiO_2 suspensions; untreated TiO_2, platinized 5 nm TiO_2, heavily platinized TiO_2, platinized TiO_2 dyed ex situ with Z907, nonplatinized TiO_2 dyed in situ with Z907, and platinized TiO_2 dyed in situ with Z907.

The photocatalytic abilities of the 5 nm particles were tested via the apparatus and conditions detailed in Figure S1.8. Only particles that were both dyed and catalyzed produced significant amounts of hydrogen (Figure 1.6). Hydrogen production is dependent upon the platinum content of the samples. The amount of hydrogen production increases with greater platinum percentage. There are two discrepancies to this trend, nevertheless, they can attributed to inconsistancies of the brightness of illumination. Because of the greater dependence of Pt, no correlation is seen between Ru content and hydrogen production (Figure S1.9). However, the amount of Ru required for hydrogen production is quite negligible. The Ru content of the sample producing the second greatest amount of hydrogen is below the detection limit of ICP-OES. This behavior is of note since the particles are producing hydrogen with weight percents of Pt and Ru as low as 0.15 wt% and 0.02 wt%, respectively.

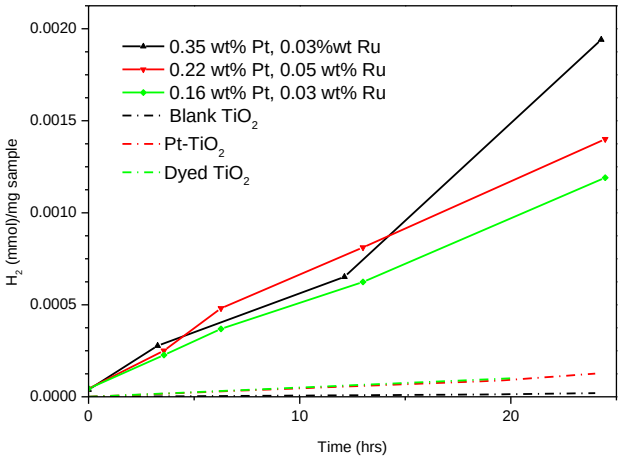

Figure 1.6: Hydrogen production vs time showing platinum dependence on hydrogen production. Complete hydrogen production comparison found in Figure S1.9.

1.4 Conclusion

A new synthesis method has been developed to produce a hydrogen producing photocatalyst with very low concentrations of precious metals. The catalyst material is produced via a single pot synthesis. The bulk of the material is composed of cheap and abundant TiO_2. Because of the nanoscale size of the material, the catalytic ability of the material is maximized

while minimizing the amount needed. In addition to the small amount of total material needed, the material is capable of producing hydrogen with Pt and Ru amounts as low as 0.15 wt%. Pt and 0.02 wt% Ru, expensive rare earth materials, because of the one pot nature of the synthesis method.

References

1. Fujishima, A.; Rao, T. N.; Tryk, D. A., Titanium dioxide photocatalysis. *Journal of Photochemistry and Photobiology C: Photochemistry Reviews* **2000,** *1* (1), 1-21.
2. Ni, M.; Leung, M. K. H.; Leung, D. Y. C.; Sumathy, K., A review and recent developments in photocatalytic water-splitting using TiO_2 for hydrogen production. *Renewable & Sustainable Energy Reviews* **2007,** *11* (3), 401-425.
3. Walter, M. G.; Warren, E. L.; McKone, J. R.; Boettcher, S. W.; Mi, Q.; Santori, E. A.; Lewis, N. S., Solar Water Splitting Cells. *Chemical Reviews* **2010,** *110* (11), 6446-6473.
4. Mills, A.; Le Hunte, S., An overview of semiconductor photocatalysis. *Journal of Photochemistry and Photobiology A: Chemistry* **1997,** *108* (1), 1-35.
5. Sato, S.; White, J. M., Photodecomposition of water over Pt/TiO_2 catalysts. *Chemical Physics Letters* **1980,** *72* (1), 83-86.
6. Jarosz, P.; Du, P.; Schneider, J.; Lee, S.-H.; McCamant, D.; Eisenberg, R., Platinum(II) Terpyridyl Acetylide Complexes on Platinized TiO_2: Toward the Photogeneration of H_2 in Aqueous Media. *Inorganic Chemistry* **2009,** *48* (20), 9653-9663.
7. Dhanalakshmi, K. B.; Latha, S.; Anandan, S.; Maruthamuthu, P., Dye sensitized hydrogen evolution from water. *International Journal of Hydrogen Energy* **2001,** *26* (7), 669-674.
8. Argazzi, R.; Iha, N. Y. M.; Zabri, H.; Odobel, F.; Bignozzi, C. A., Design of molecular dyes for application in photoelectrochemical and electrochromic devices based on nanocrystalline metal oxide semiconductors. *Coordination Chemistry Reviews* **2004,** *248* (13-14), 1299-1316.
9. Kudo, A.; Kato, H.; Tsuji, I., Strategies for the development of visible-light-driven photocatalysts for water splitting. *Chemistry Letters* **2004,** *33* (12), 1534-1539.
10. Gurunathan, K.; Maruthamuthu, P.; Sastri, M. V. C., Photocatalytic hydrogen production by dye-sensitized Pt/SnO_2 and $Pt/SnO_2/RuO_2$ in aqueous methyl viologen solution. *International Journal of Hydrogen Energy* **1997,** *22* (1), 57-62.
11. Li, Y.; Lu, G.; Li, S., Photocatalytic hydrogen generation and decomposition of oxalic acid over platinized TiO_2. *Applied Catalysis A: General* **2001,** *214* (2), 179-185.
12. Yang, J. C.; Kim, Y. C.; Shul, Y. G.; Shin, C. H.; Lee, T. K., Characterization of photoreduced Pt/TiO_2 and decomposition of dichloroacetic acid over photoreduced Pt/TiO_2 catalysts. *Appl. Surf. Sci.* **1997,** *121*, 525-529.
13. Christy, P. D.; Jothi, N. S. N.; Melikechi, N.; Sagayaraj, P., Synthesis, structural and optical properties of well dispersed anatase TiO_2 nanoparticles by non-hydrothermal method. *Cryst. Res. Technol.* **2009,** *44* (5), 484-488.
14. Kim, C. S.; Moon, B. K.; Park, J. H.; Choi, B. C.; Seo, H. J., Solvotherinal synthesis of nanocrystalline TiO_2 in toluene with surfactant. *J. Cryst. Growth* **2003,** *257* (3-4), 309-315.
15. Li, F. B.; Li, X. Z., The enhancement of photodegradation efficiency using $Pt\text{-}TiO_2$ catalyst. *Chemosphere* **2002,** *48* (10), 1103-1111.
16. Ravichandran, L.; Selvam, K.; Krishnakumar, B.; Swaminathan, M., Photovalorisation of pentafluorobenzoic acid with platinum doped TiO_2. *J. Hazard. Mater.* **2009,** *167* (1-3), 763-769.
17. Rahtu, A.; Ritala, M., Reaction mechanism studies on titanium isopropoxide-water atomic layer deposition process. *Chemical Vapor Deposition* **2002,** *8* (1), 21-28.

18. Degraauw, C. F.; Peters, J. A.; Vanbekkum, H.; Huskens, J., Meerwein-Ponndorf-Verley Reductions and Oppenauer Oxidations - An Integrated Approach. *Synthesis-Stuttgart* **1994,** (10), 1007-1017.
19. Zakeeruddin, S. M.; Nazeeruddin, M. K.; Humphry-Baker, R.; Pechy, P.; Quagliotto, P.; Barolo, C.; Viscardi, G.; Gratzel, M., Design, synthesis, and application of amphiphilic ruthenium polypyridyl photosensitizers in solar cells based on nanocrystalline TiO2 films. *Langmuir* **2002,** *18* (3), 952-954.
20. Chandrasekharam, M.; Rajkumar, G.; Rao, C. S.; Suresh, T.; Reddy, P. Y.; Soujanya, Y., Ruthenium(II)-bipyridyl with extended pi-system: Improved thermo-stable sensitizer for efficient and long-term durable dye sensitized solar cells. *J. Chem. Sci.* **2011,** *123* (5), 555-565.
21. Wang, P.; Zakeeruddin, S. M.; Moser, J. E.; Nazeeruddin, M. K.; Sekiguchi, T.; Gratzel, M., A stable quasi-solid-state dye-sensitized solar cell with an amphiphilic ruthenium sensitizer and polymer gel electrolyte. *Nature Materials* **2003,** *2* (6), 402-407.

Supporting Information for:

Direct Synthesis of Dyed Capped Platinized TiO_2 Nanoparticles for Subsequent Sensitization by Donor-Chromophore-Acceptors: Towards Hydrogen Generation from Water

Daniel J.Shissler, Derek C. Johnson, & Amy L. Prieto

Scheme 1: 80 nm TiO_2 particles

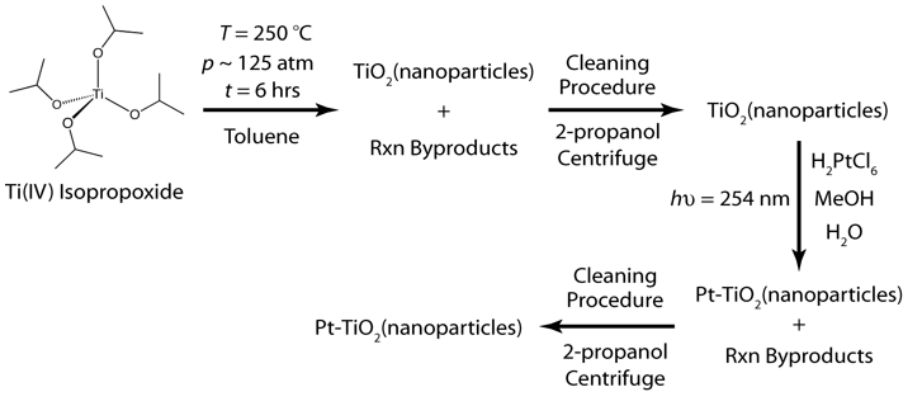

Schemes 2-4: Capped 5 nm particle synthesis

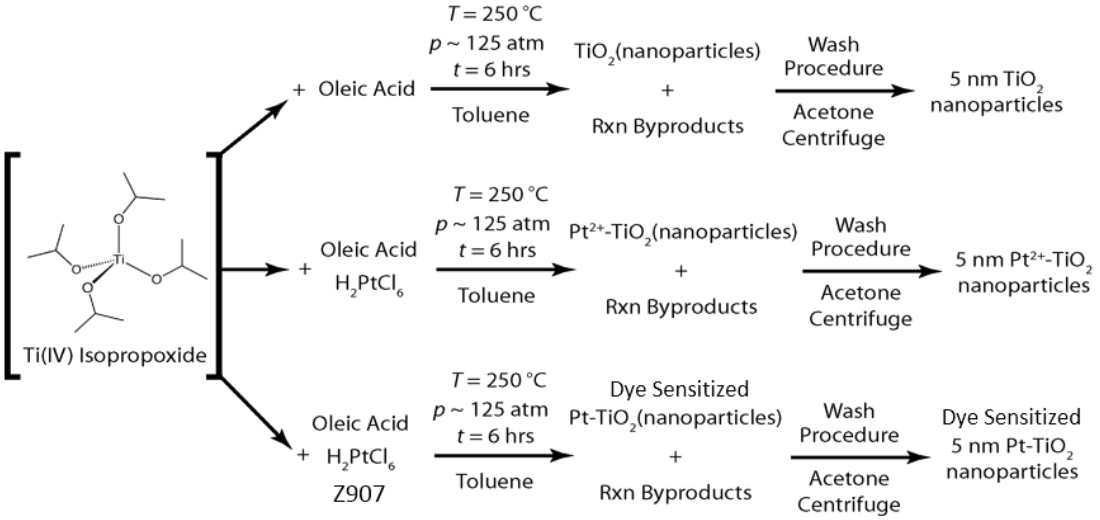

Figure S1.1: Solvothermal reaction schemes of TiO_2 nanoparticle synthesis. The synthesis of surfactant free 80 nm nanoparticles platinized via ex situ by photoindiced reduction of H_2PtCl_6 is illustrated in Scheme 1. Schemes 2-4 illustrate synthesis of oleic acid capped 5 nm TiO_2 particles as well as in situ platinization and sensitization.

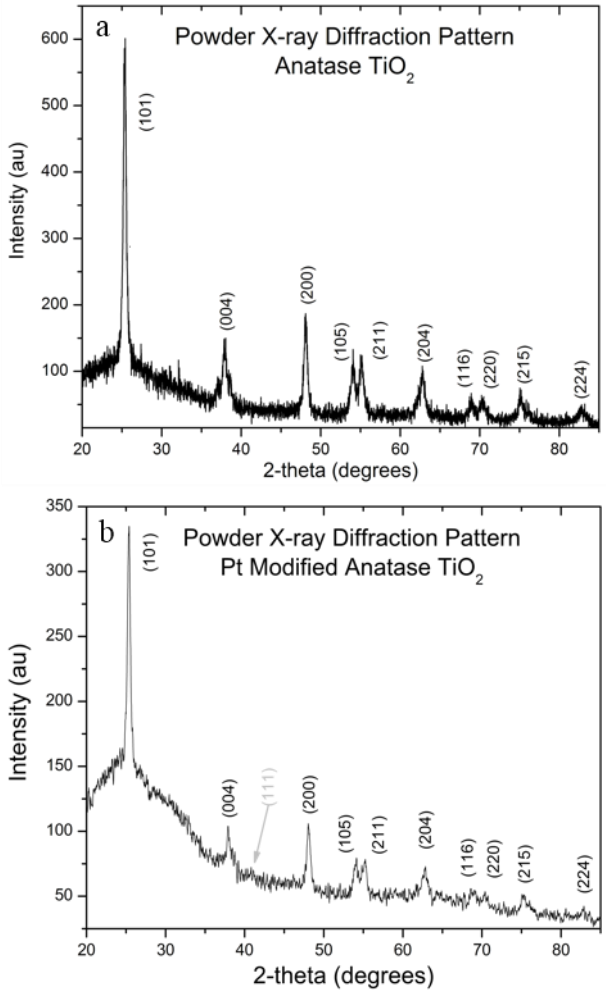

Figure S1.2: Powder patterns of ~80 nm nonplatinized (a) and platinized (b) particles indexed with Anatase TiO2. Platinization was performed ex situ by photoindiced reduction of H_2PtCl_6. Scherrer analysis on the (101) plane indicates nanoparticles with a diameter of 85 nm and 80 nm for the unplatinized (a) and platinized particles (b), respectively. A minor peak can be indexed with the (111) plane of platinium.

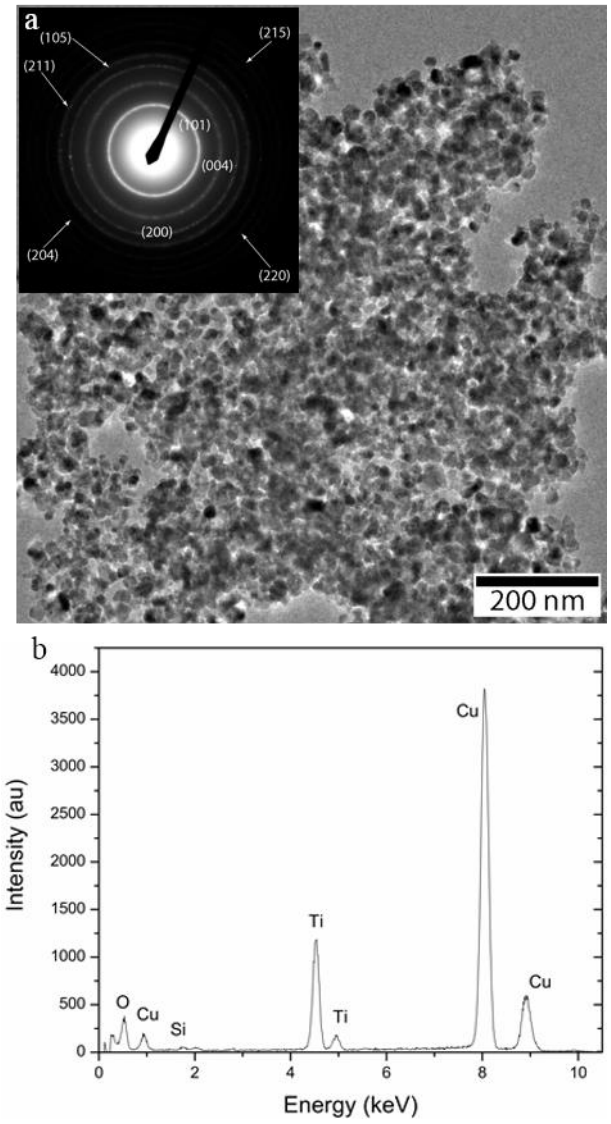

Figure S1.3: (a) A TEM image of 80 nm ex situ non platinized particles.with an inset image of a SAED pattern confirming anatase TiO_2. (b) EDX analysis confirms the presence of Ti and O. The Cu and Si signals are from the grid.

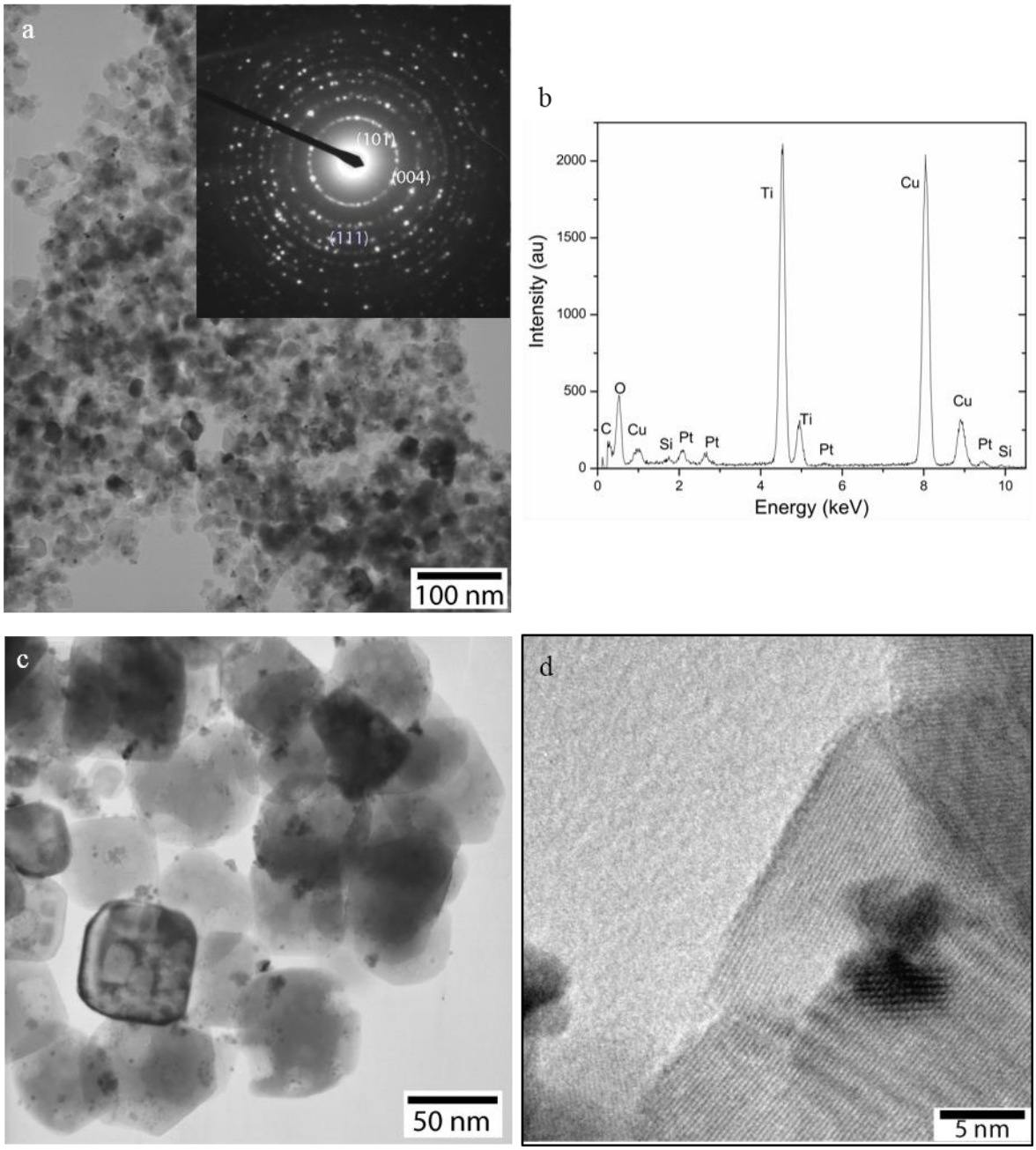

Figure S1.4: (a) A TEM image of 80 nm ex situ platinized particle with an inset image of SAED confirming anatase TiO_2. (b) EDX analysis confirms the presence of Ti, O, and Pt. Cu and Si are from the grid. (c-d) Islands of dark contrast are assumed to be Pt because of its greater contrast compared to that of the TiO_2 particles.

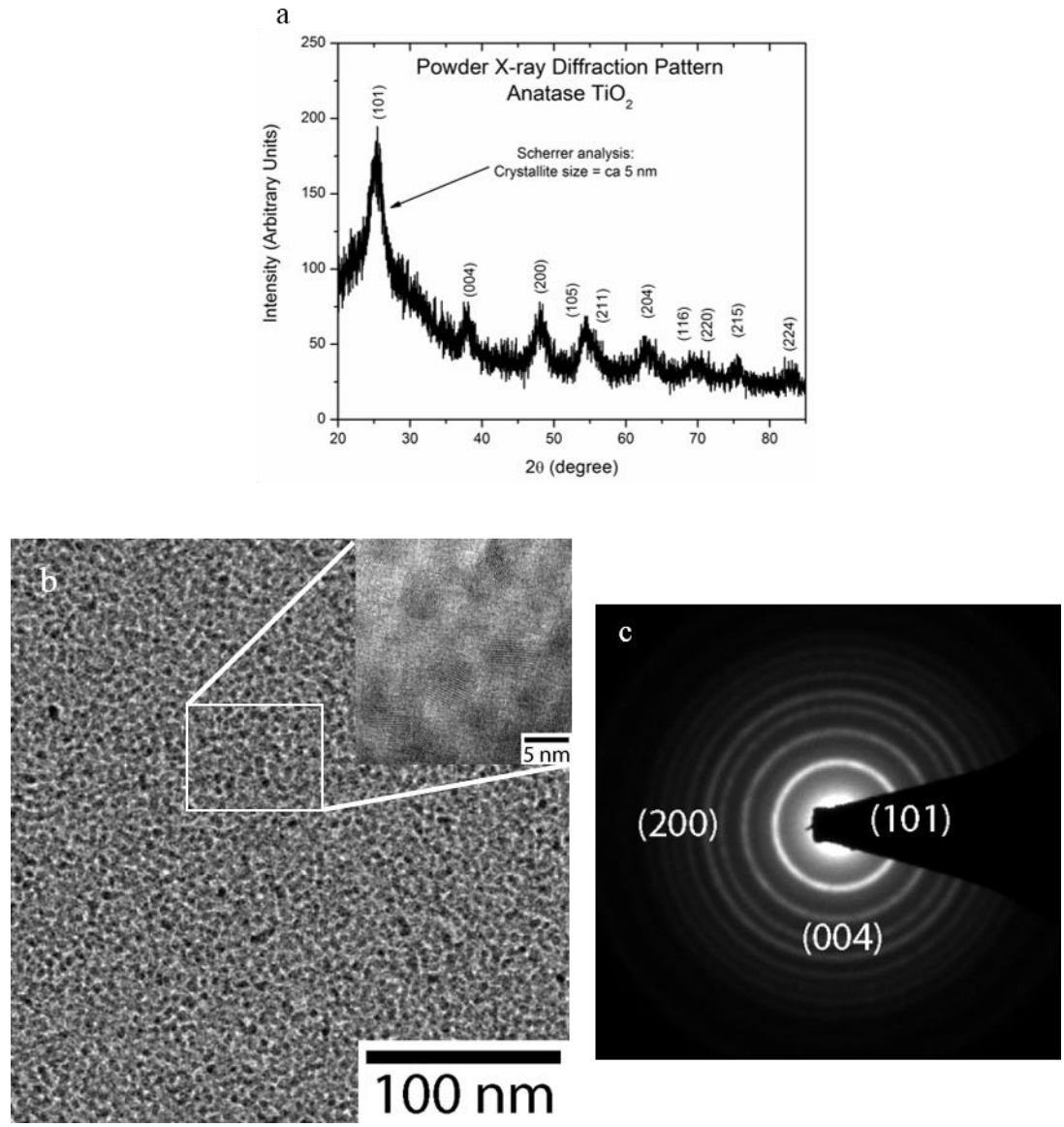

Figure S1.5: Powder XRD analysis of oleic capped 5 nm particles indexes as anatase TiO_2. Scherrer analysis of the (101) plane indicates and average particle size of 5 nm. TEM imaging (b) and SAED (c) confirm an average particle size of 5 nm in the crystalline state of anatase TiO_2.

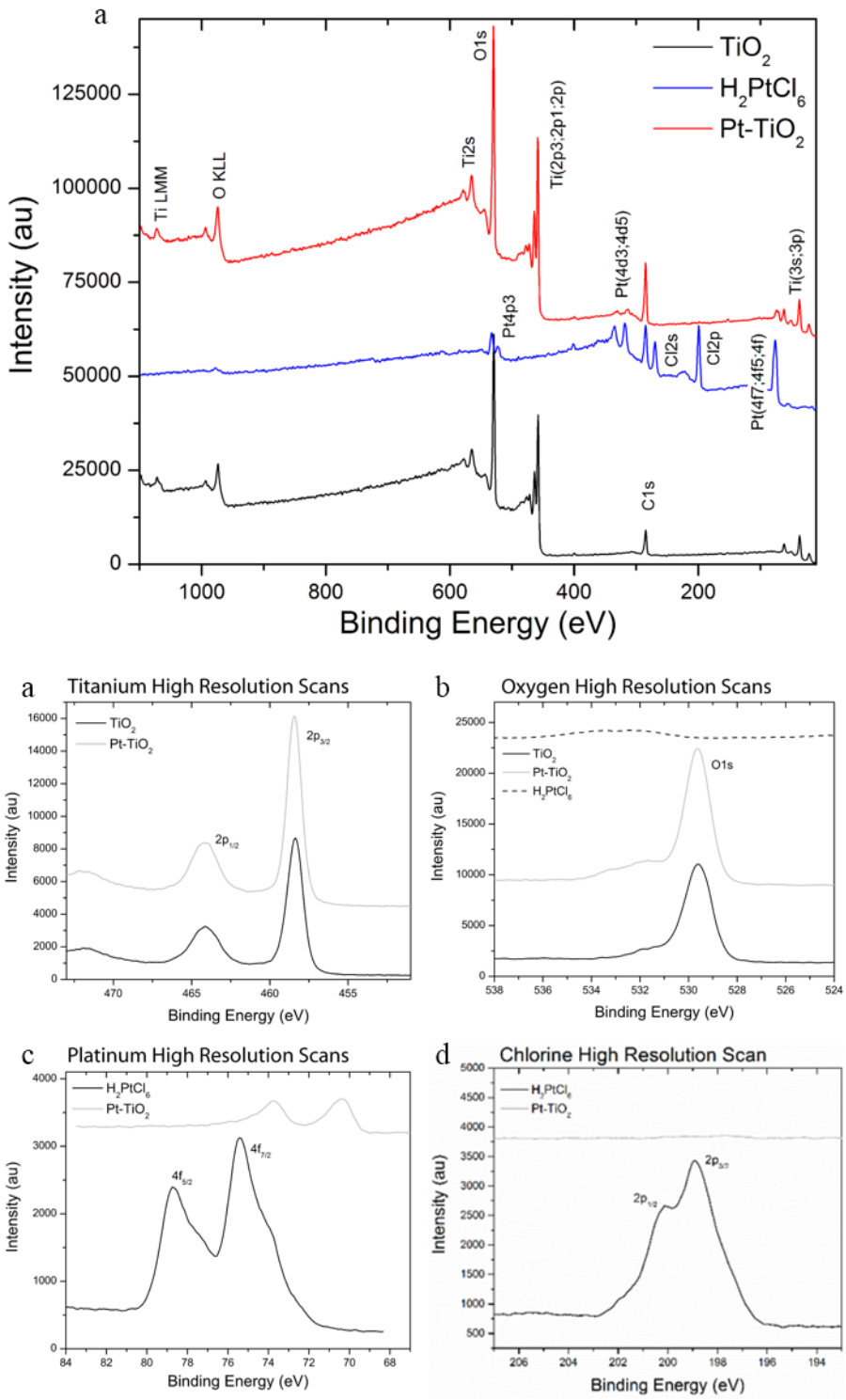

Figure S1.6: For comparison XPS analysis (a) was performed on of 80 nm TiO_2, platinum precursor H_2PtCl_6, and platinized TiO_2. High resolution scans of the titanium (b), oxygen (c), platinum (d), and chlorine (d) regions to identify differences of oxidation states. No shift in the titanium and oxygen peaks are observed after platenization. A shift in the platinum peak is observed between the precursor and the platinized TiO_2 due to the change from the 4+ state to the ground state of the platinum. No chlorine peaks observed in TiO_2 sample showing good washing procedure.

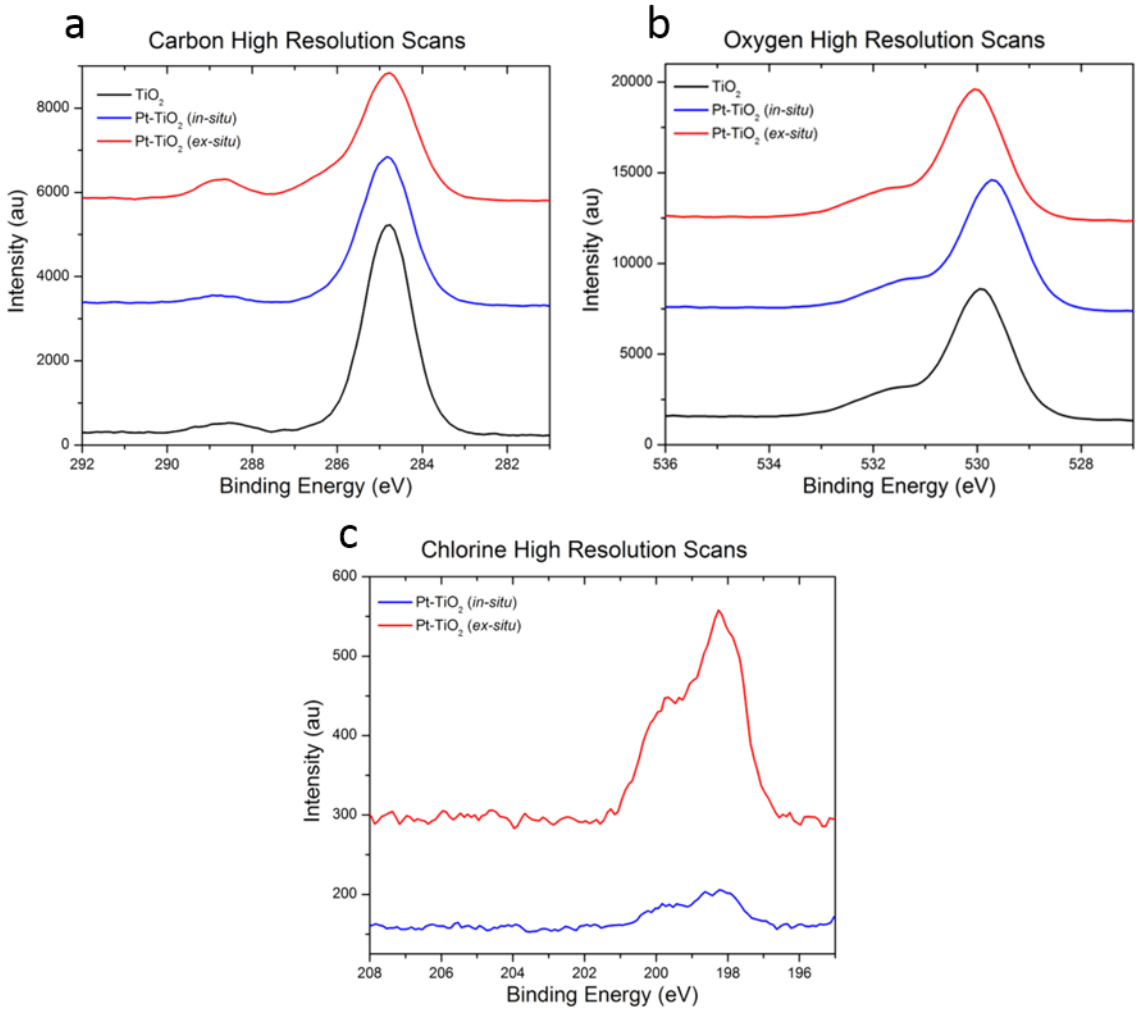

Figure S1.7: Comparisons of the carbon (a), oxygen (b), and chlorine (c) high resolution XPS scans of 5 nm TiO_2, in situ platinized 5nm particles, and ex situ platinized 80 nm TiO_2. No shifts in the Titanium and Oxygen peaks are observed after platenization.

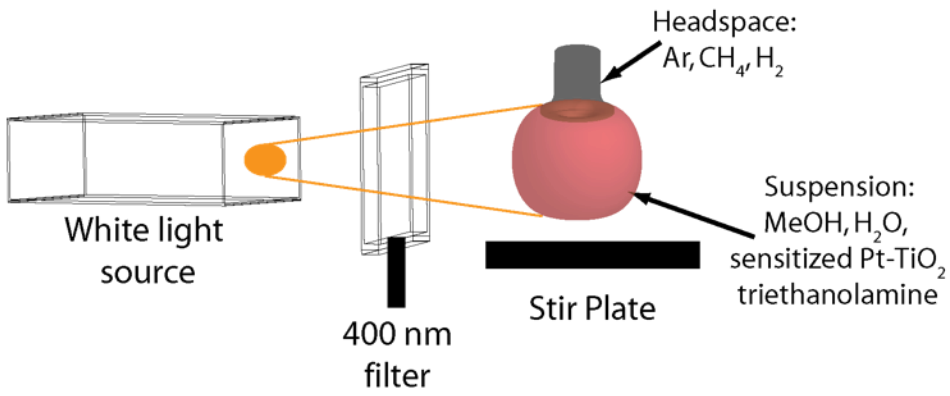

1. MeOH:H_20 is 1:1 by volume (total volume ~25 mL)
2. Approximately 0.5 mL triethanolamine
3. pH adjusted to 7 with 10% by volume HCL
4. Suspension purged with Ar
5. Methane added to the headspace as an internal standard
6. Approximately 50 mg TiO_2, ~1.0% by weight Pt, ~10% by weight Ru dye

Figure S1.8: Diagram and preparation of the experimental setup used for hydrogen production experiments.

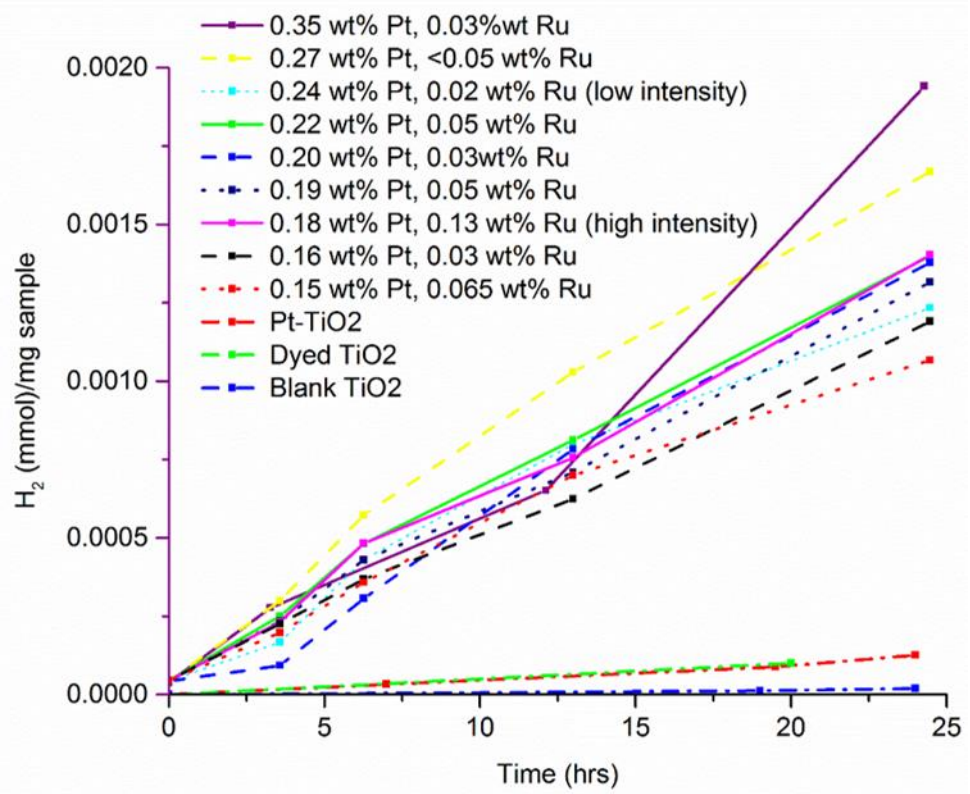

Figure S1.9: Comparison of the amount of hydrogen produced with varying weight percentages of platinum and ruthenium. Hydrogen production increases with Pt wt%. The 0.24 wt% Pt and 0.18 wt% Pt samples do not follow this trend due to variance in lamp intensity during the experiment.

Chapter 2

Magnesium and Doped Magnesium Nanostructured Materials for Hydrogen Storage[ii]

2.1 Introduction

Hydrogen is a very attractive fuel for many applications because it is the most abundant element on earth (although less than 1% is present as molecular hydrogen), the gravimetric energy density is three times higher than liquid hydrocarbons (142 MJ/kg versus 47 MJ/kg), and when burnt in oxygen the only exhaust is water. One significant hurdle to the widespread adoption of hydrogen-burning vehicles, however, is the development of new materials that can absorb and desorb large amounts of hydrogen safely at low pressures and ambient temperatures. The Department of Energy has set ambitious goals for the capacity, cycle life, and delivery pressures required to make hydrogen a viable fuel for mobile applications (Table 2.1). There are no current materials that can meet these goals to date.

Table 2.1: Targets set by the Department of Energy (released in 2009). Used with permission by Chen 2012.

Storage parameters	Units	2010	2015	Ultimate
System gravimetric capacity	kWh kg^{-1}	1.5	1.8	2.5
	kg H_2 kg^{-1} system	0.045	0.055	0.075
System volumetric capacity	kWh L^{-1}	0.9	1.3	2.3
	kg H_2 L^{-1} system	0.028	0.040	0.070
Min/max delivery temperature	°C	−40/85	−40/85	−40/95–1
Cycle life (1/4 tank to full)	Cycles	1000	1500	1500
Min/max delivery pressure for fuel cell	Bar (abs)	5/12	5/12	3/12
Min/max delivery pressure for internal combustion engine	Bar (abs)	35/100	35/100	35/100
Onboard reversible system efficiency	%	90	90	90
System fill rate	kg H_2 min^{-1}	1.2	1.5	2.0

[ii] Daniel J. Shissler, Sarah J. Fredrick, Max B. Braun, & Amy L. Prieto.
Sarah Frederick contributed to this dissertation chapter by writing the synthesis section. Daniel Shissler contributed by writing the kinetic evaluation portion. Max Braun contributed by writing the doping studies section.This dissertation chapter is adapted from a book chapter published in *Low-cost Nanomaterials:Toward Greener and More Efficient Energy Applications*

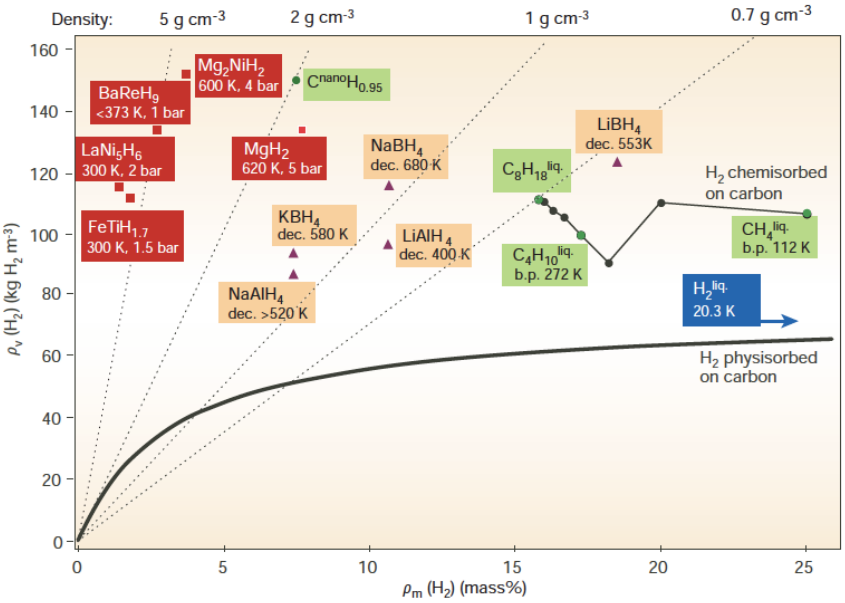

Figure 2.1: A comparison of a range of materials as a function of stored hydrogen per volume and per mass. Reproduced with permission from Schlapbach, 2001.

Current research in the storage of hydrogen is focused on several areas, including the synthesis of new materials with high porosity and controllable functionality,[1] the adsorption of H_2 in zeolites and carbonaceous materials including carbon nanotubes,[2] and the modification of existing metal hydride systems.[3] A comparison of a range of materials as a function of their volumetric and gravimetric hydrogen storage is shown in Fig. 2.1. Among these research areas, metal hydrides containing light elements such as MgH_2 offer high density storage at low cost.

The significant advantage to light metal hydrides such as MgH_2 is the potentially high hydrogen capacity in small volumes at ambient pressures and temperatures. However, essentially all of the target compounds are plagued by slow kinetics for the hydrogenation and dehydrogenation reactions, which means that they are currently cycled at elevated temperatures (typically near 300 ºC) and low/ high pressure for the dehydrogenation/hydrogenation reactions. The compounds that can cycle at or near room temperature are hindered by low mass density for hydrogen (such as Pd, which converts to $PdH_{0.6}$). [3] A fundamental understanding of the structure and properties of complex hydrides would be extremely helpful in decoupling the challenges in

terms of thermodynamic stability of the relevant phases as well as the kinetics. Without an understanding of the interplay between structure, bonding, and diffusion in these materials, optimization to improve the kinetics at lower temperatures and ambient pressures relies on trial and error. For that reason a portion of this chapter is dedicated to theoretical predictions that are guiding current research.

A reasonable argument can be made that *only* light hydrogen storage materials with high gravimetric capacities will be able to achieve the DOE targets. For that reason Mg, doped Mg, and Mg alloys are promising materials for hydrogen storage due to their high theoretical hydrogen storage capacities (e.g. 7.6 wt.% for MgH_2).[3,4] *Pure Mg particles can store 1 kg of H_2 in 6.9 L of solid metal hydride.* However, bulk Mg is less than ideal as a hydrogen storage material due to the slow kinetics and high temperatures required for hydrogen absorption/desorption.

One common approach to mitigating the sluggish kinetics for bulk magnesium is to increase the surface area to volume ratio of the material. The reaction of bulk Mg and molecular hydrogen first involves the adsorption of molecular hydrogen onto the surface of the magnesium, the breaking of the hydrogen-hydrogen bond, and the diffusion of the atomic hydrogen into the magnesium. Once a critical concentration is reached, MgH_2 nucleates and grows (shown in Fig 2.2). One can imagine that by reducing the physical dimensions of the material to the nanoscale, the diffusion length required for hydrogen to diffuse by solid-state diffusion from the surface of the material to the center is dramatically reduced, which can reduce the time necessary for hydrogenation (and the same effect should be true for the reverse reaction, removing hydrogen from the hydride).

Recent studies have shown that hydrogen storage properties can be greatly improved by preparing these materials with nanocrystalline grain sizes, often achieved by mechanical ball-

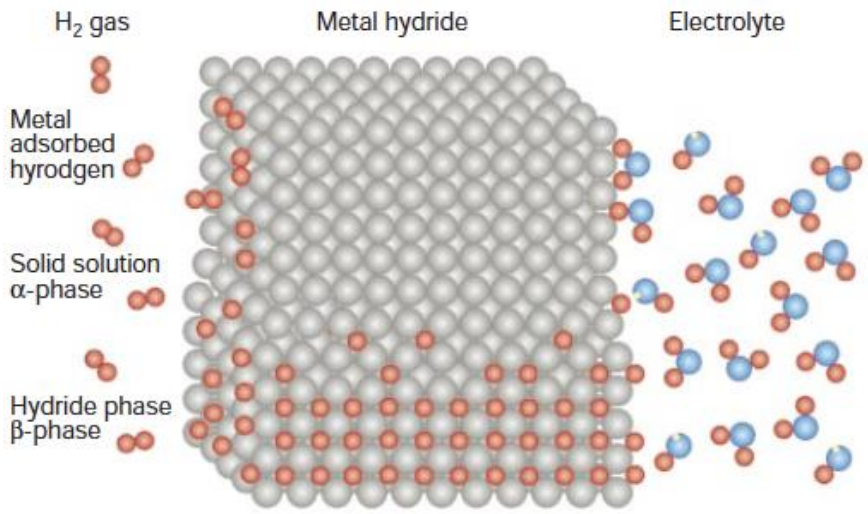

Figure 2.2: Schematic model of a metal structure with H atoms in the interstices between the metal atoms, and H_2 molecules at the surface. Hydrogen atoms are from physisorbed hydrogen molecules on the left-hand side and from the dissociation of water molecules on the right-hand side. Reproduced with permission from Schlapbach, 2001.

milling, and by alloying Mg with other metals.[3-5] Previous studies have shown that reducing the particle size of metal hydrides such as Mg_2Ni significantly increases the kinetics of hydrogen absorption.[4] The increase in the kinetics for hydrogen absorption may be a result of a decrease in the diffusion length for hydrogen due to the small sizes of the particles (as mentioned previously), but the lack of control over the size and homogeneity of the samples has made it difficult to determine this conclusively. The synthetic methods used (such as ball milling[4] and hydrogen plasma-metal reactions[6]) can produce samples that are inhomogeneous, poorly crystalline, and with ill-defined particle size. An important but unanswered question is still whether or not the increased kinetics observed for nanostructured materials are due purely to increased surface area, or if grain boundaries and trace impurities or catalysts are important for the hydridation reaction.

This chapter will provide an overview of the synthesis of nanostructured magnesium based materials, the resulting kinetics of these materials (and how these kinetics are currently modeled) as well as theoretical predictions of what can be obtained using different approaches toward magnesium. For the purposes of brevity we have focused on nanostructured magnesium, as well

as doped magnesium, but we have not included a discussion of composite materials where magnesium is not the major component. The references contained herein are meant to be as comprehensive as possible, to provide the reader with reasonable resources with which to read further about this fascinating material.

2.2 Synthesis Introduction

In order to optimize the performance of any material, a deep understanding of the effects of the synthesis of the material on the resulting properties is imperative. For hydrogen storage materials in particular, it is important to fully understand the sorption kinetics for these systems and how the kinetics depend on the quality of the material as made. The challenge with magnesium-based materials in particular is that elemental magnesium is very easily oxidized. Any synthetic method that is designed to produce zero valent magnesium will need to be carried out under inert conditions, and if the precursors are common magnesium salts, under fairly reducing conditions. For the purpose of studying the effects of parameters such as particle size and the incorporation of dopants (common variables that are tuned for magnesium as a hydrogen storage material), a synthesis that allows for fine control and manipulation of these variables is desired. The general goals of modern synthetic methods for magnesium are to control the size and morphology of the particles and/or to controllably incorporate dopants.

2.3 Undoped Magnesium Nanocrystal Syntheses:

There are two general strategies for synthesizing magnesium for hydrogen storage. The first is to start with bulk elemental magnesium, and then either ball mill the bulk material to reduce the grain size or to use vapor transport reactions to create nanostructures. For the purposes of clarity, a

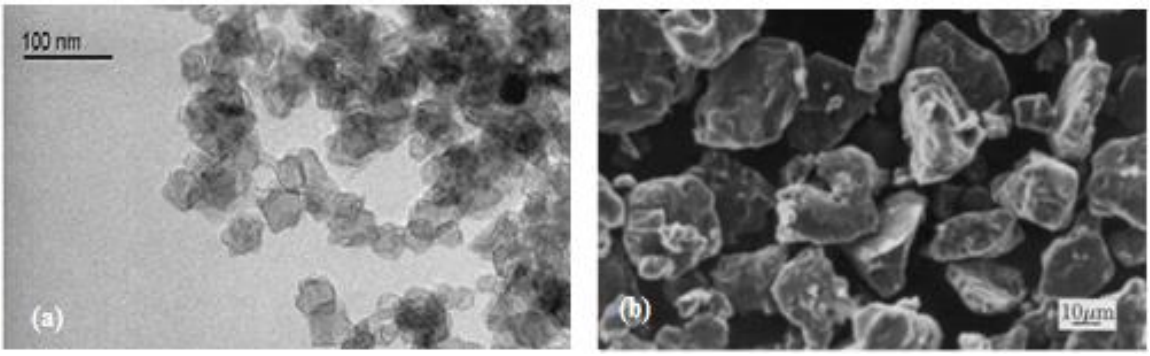

Figure 2.3: Comparison of (a) TEM micrograph of nanostructured magnesium synthesized by gas phase condensation reaction and (b) SEM micrograph of nanocrystalline magnesium microstructures. Reproduced with permission from Zaluska 1999 and Friedrichs 2007.

distinction must be made between nanostructured magnesium and nanocrystalline magnesium; while one can be both nanostructured (wherein the physical features of the particles are on the nanoscale) and nanocrystalline (where the grain sizes composing the particles are on the nanoscale), the other may be nanocrystalline but microstructured (Fig 2.3).[7-8] This is an important distinction because different synthetic methods are required to control the physical dimensions of the particles, versus the physical dimensions of the grains contained within a particle. The second general method for synthesizing magnesium for hydrogen storage is to start with magnesium precursors where magnesium is present in the +2 oxidation state, and then reduce the precursor in solution (either chemically or electrochemically, see Fig. 2.4) to form neutral magnesium.

The most prevalent synthesis in the current literature for reducing the grain sizes of bulk magnesium to micro or nanocrystalline grains is that of mechanical milling, or ball milling.[7, 9] In addition to standard ball milling, high energy mechanical milling (under either high pressure or high temperature) has been used by many for the synthesis of magnesium nanocrystals.[10] This technique can be utilized under hydrogen pressure to directly make MgH_2[11-13] rather than making the pure metal and hydriding it post-synthesis. Mechanochemical milling has also been used to produce magnesium nanocrystals in a similar fashion.[14] Another mechanical method for producing nanocrystalline magnesium is the method of cold rolling and cold forging to reduce grain sizes.[15]

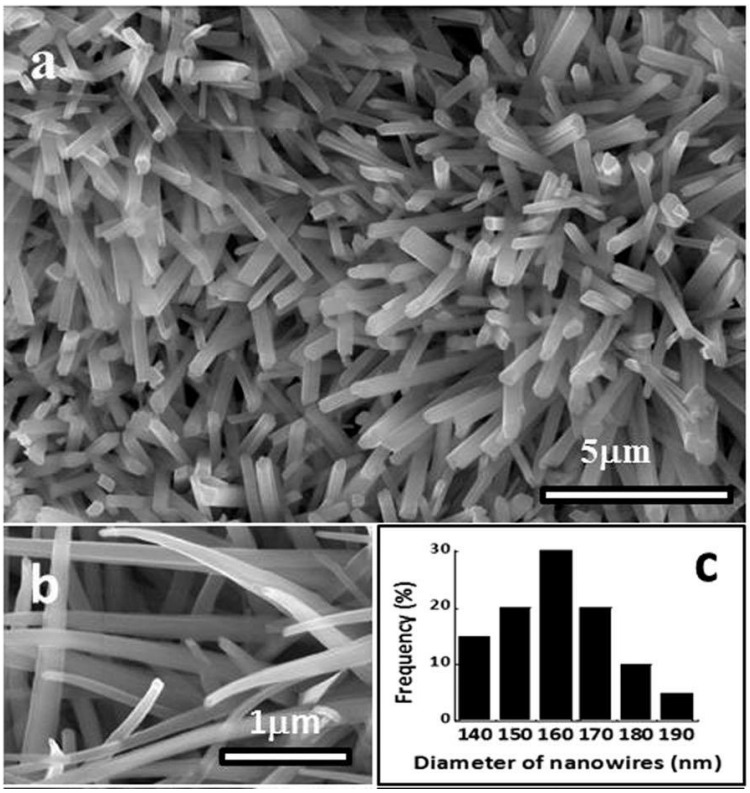

Figure 2.4: SEM image (a) of the nanowires obtained by electrochemical reduction of EtMgCl, (b) high resolution SEM and (c) size distribution of the diameters of the nanowires obtained by this method. Figure used with permission from Viyannalage, 2012.

Although these types of mechanical milling are effective in reducing grain size and incorporating dopant materials (to be discussed in section 2.4), they offer little control over nanocrystal size distribution, shape and impurity phases (Fig. 2.3b).

Plasma reactions[16-17] have been demonstrated to be effective in producing nanoscale magnesium, however impurity phases such as oxides can also be a problem in these systems. Gas phase condensation of metallic magnesium into nanocrystalline powders has been shown to be effective and have the advantage of in situ hydriding,[8, 18] but the high temperatures and/or pressures required for this synthesis make it less than ideal. Alternatively, vapor transport has been used to grow magnesium nanowires also used for hydrogen storage studies.[19] Direct decomposition of Grignard reagents in a presence of hydrogen was shown to give pure magnesium hydride that can

be used for dehydrogenation studies, however purity varied among samples.[20] A recent example of a solvated metal atom dispersion method followed by digestive ripening with organic surfactants produced small (2 – 4 nm in diameter), monodisperse nanocrystals.[21] This synthesis is arguably the most effective at making ultrasmall clusters of magnesium that are expected to show the fastest kinetics at lower temperatures as well as improved thermodynamics.

The solution-phase synthesis of nanoparticles has emerged as an elegant and rational method which can yield a high level of control over size[22], shape[23-24], surface properties[25], and connectivity.[26] Synthetic methods such as electrochemical reduction from solution result in small particles exhibiting improved kinetics, but are not amenable to the controllable addition of catalyst particles.[27] Mg nanoparticles synthesized from solution have been tested for hydrogen storage properties, but the early preparation methods were not designed to control particle size, and the average size and surface composition of these nanoparticles were not investigated, therefore not providing a good description of how much particle diameter can influence the material's properties.[28] Mg nanowires have been synthesized in high yield, and show enhanced kinetics for hydrogen sorption.[29] As mentioned previously, ball-milled Mg nanoparticles show even faster kinetics, although there is a large size distribution in these samples.[30] A solution-phase synthesis would provide a route toward narrow size-dispersion, high quality nanoparticles.

In a push towards lower energy methods for producing nanoscale magnesium, there have been several recent reports of solution synthesis methods. The low reduction potential of magnesium has allowed for electrochemical reduction to produce magnesium nanocrystals out of THF. [31] A similar synthesis has produced both nanoparticles and nanowires,[32] and there is no indication that impurities were a byproduct. Direct chemical reduction of magnesium salts to magnesium metal in glyme at near-room temperature has been shown.[33] This method has also

demonstrated control over particle size with corresponding enhanced kinetics. The powder X-ray diffraction characterization of this material showed pure, crystalline magnesium, with significant peak broadening indicative of the small size. (Fig. 2.5) One final example of a solution method not only reduces magnesium salts to magnesium metal at room temperature, but also encapsulates the nanoparticles in a polymer matrix, which keeps the highly pyrophoric magnesium air stable for weeks in air (Fig. 2.6).[34]

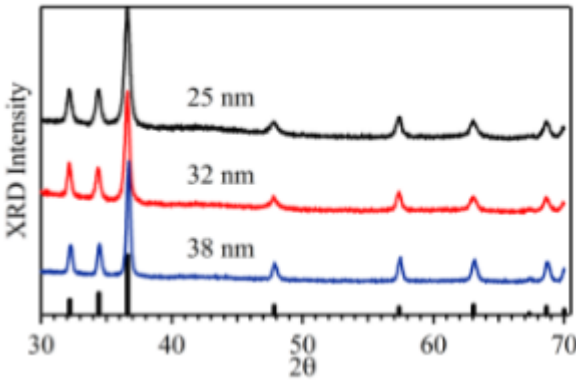

Figure 2.5: X-ray diffraction patterns of magnesium nanoparticles with varying sizes. Reproduced with permission from Norberg, 2011.

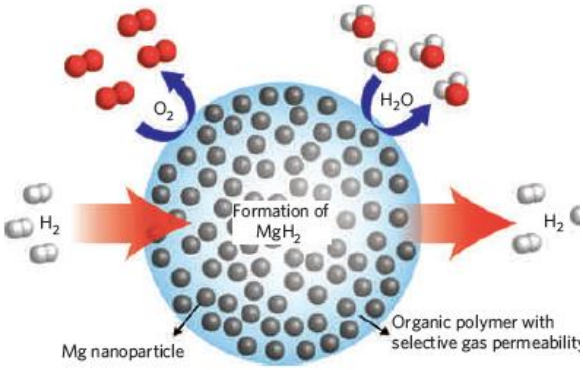

Figure 2.6: Mg/polymer composite hydrogen storage material. Here Mg nanoparticles are encapsulated in PMMA, a gas-permeable polymer. Reproduced with permission from Jeon, 2011.

2.4 Doped Magnesium Nanocrystal Synthesis

In addition to reducing particle size, dopants can be incorporated into the pure magnesium nanocrystals to enhance the poor sorption kinetics of magnesium. This chapter will not specifically address magnesium-based composites such as MgH_2-$LiAlH_4$, but rather will focus on dopants in small percentages (10 % or less). Information on composites can be found elsewhere.[35-38] A variety of dopants can be incorporated through many of the previously mentioned synthesis methods. Several papers have been written on a series or transition metals[5, 39-43] or transition metal oxides[44-46] while others have focused on specific elemental dopants, the most common being Al,[47-

[48] Si,[47, 49] Ti,[50-51] V and its corresponding oxides,[52-53] Cr,[54] Fe,[50, 55-57] Ni,[17, 50, 58-63] Ge,[64] Nb and corresponding oxides, [52, 54, 57, 60, 65-68] and Pd.[59] More discussion of these dopants and their effects on sorption kinetics will be discussed in later in this chapter.

2.5 Evaluating the Kinetics of Hydrogen Sorption and Desorption

There are several different methods by which the kinetics of hydrogenation and dehydrogenation can be determined. Non-isothermal methods, also known as Temperature Programmed Desorption (TPD), involve the use of either Thermogravimetric Analysis (TGA) or Differential Scanning Calorimetry (DSC). Isothermal approaches include the measurements of Gravimetric-Composition-Isotherms (GCI) and Pressure-Composition-Isotherms (PCI). GCI's measure the change in mass of a sample under constant temperature and pressure conditions. Conversely, a Sievert's apparatus is used with dynamic pressure and constant temperature to measure PCI's[69-70]. This is a volumetric method which determines the amount of hydrogen absorbed or desorbed by a sample through the ideal gas law, PV=nRT, by measuring the change in pressure in a system with known volume and temperature.[71]

A downside of TPD methods is that they can only be used to analyze desorption of hydrogen from a material, not the adsorption. However, since the measurements are done with a TGA or DSC instrument, common facility instruments, TPD methods are employable without an apparatus specifically built for hydrogenation/dehydrogenation purposes. Also, the data analysis is more flexible than that of the isothermal methods, i.e. PCI and GCI.

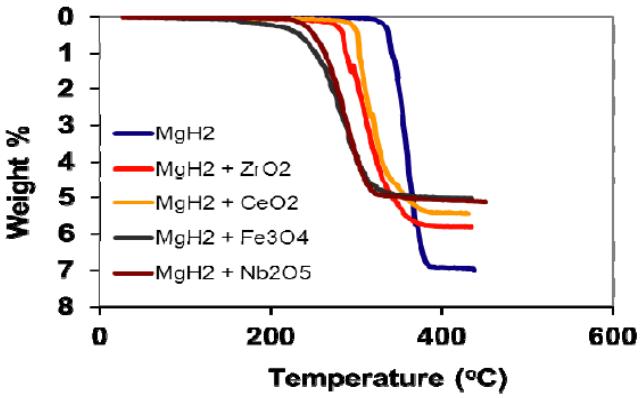

Figure 2.7: TGA measurements on magnesium hydride with and without different nanocomposites. Reproduced with permission from Sabitu 2012.

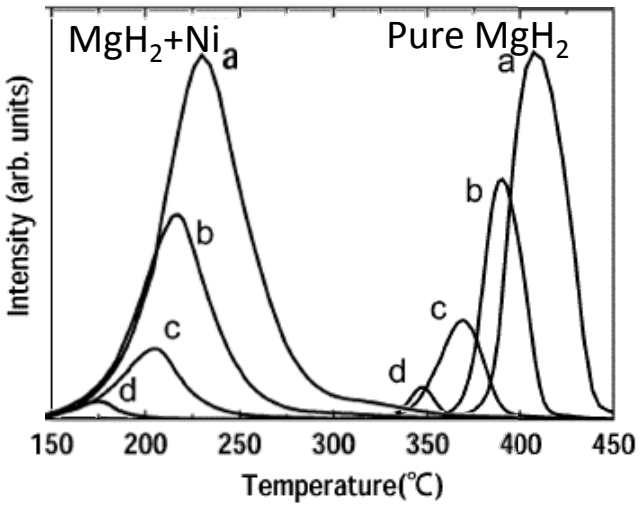

Figure 2.8: Thermal desorption mass spectra of hydrogen under various heating rates 1,5,10,20 °C/min (a),(b),(c), and (d) respectively for the pure MgH_2 milled for 15 min at 200 rpm and the 2 mol % Ni nano-catalyzed MgH_2 composite prepared by milling for 15 min at 200 rpm. The intensities of the longitudinal axes indicate the amount of hydrogen desorption per unit time. Adapted with permission from Hanada 2005.

2.6 Non-isothermal Methods

When using TGA or DSC, the hydrogen desorption kinetics of different materials can be qualitatively characterized by comparing the initial onset of transformation in the materials. For example, in TGA, a characteristic plot of weight percent vs. temperature (Fig. 2.7)[72] displays an onset of weight loss, corresponding to loss of hydrogen at different temperatures, for an assortment of materials. This onset can be observed at lower temperature for the various catalyzed materials than for that of the non-catalyzed MgH_2. Similarly in DSC, where a quantitative endotherm or exotherm signifies a phase change as different temperatures are scanned, it can be seen that hydrogen desorption for the nickel catalyzed sample occurs at a much lower temperature with respect to that of the non-catalyzed sample (Fig. 2.8)[40].

For the purposes of hydrogen storage, the better performing material will exhibit an onset of desorption at a lower temperature. However, due to the variation within experimental procedure

and instrument calibration, if the performance of a material is to be compared to that of other literature, an activation energy for desorption should be determined. The activation energy can be calculated by analyzing TGA and DSC data with one of the two following equations:

$$\ln \beta = -\frac{0.457E_a}{RT} - 2.315 - \log\left[\frac{R}{AE_a}\int_0^{\alpha}\frac{d\alpha}{f(\alpha)}\right] \quad (1)$$

$$\ln \frac{\beta}{T^2} = -\frac{E_a}{RT} - \ln\left[\frac{E_a}{RA}\int_0^{\alpha}\frac{d\alpha}{f(\alpha)}\right] \quad (2)$$

where β is the ramp rate, E_a is the activation energy, R is the gas constant, and A is the pre-exponential factor of the Arrhenius equation. The kinetic function, $f(\alpha)$, is dependent on the fraction of converted material at a given time over the maximum converted material.[73] These two variables will be discussed further in later sections. Determining the activation energy with equation (1) is known as the Ozawa-Flynn-Wall (OFW) method.[74-75] Alternatively, the Kissinger-Akahira-Sunose (KAS) method can be used to find the activation energy with equation (2).[76] By varying the ramp rates of several TGA or DSC scans, a linear relationship can be observed by plotting $ln(\beta)$ *vs* $1/T$ or $ln(\beta/T^2)$ *vs* $1/T$, depending on which method is used. The slope of the plot can then be used in correlation with equation (1) or (2) to calculate the activation energy. Different data sets are obtained in TGA than with DSC. As can be seen in the TGA data shown in Fig. 2.9,[74]

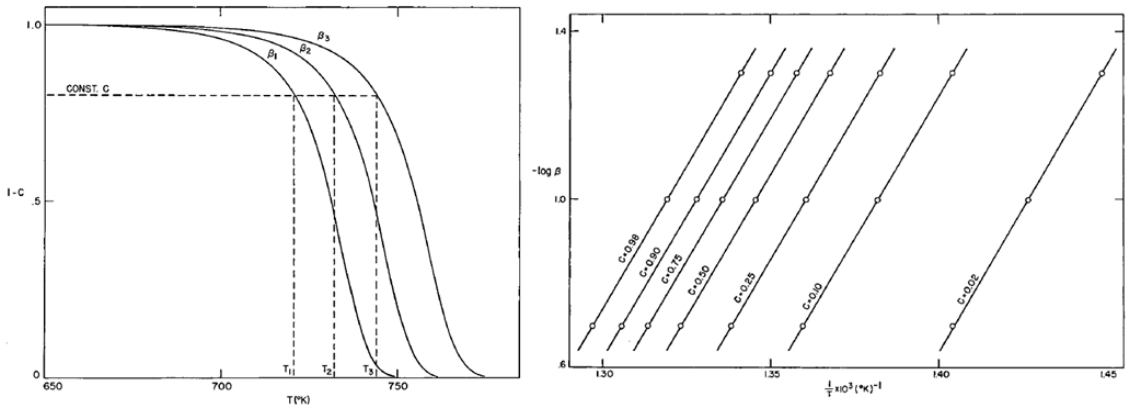

Figure 2.9: Residual fraction vs. temperature for three different rates of heating (left). Log (β) vs 1/T for different degrees of conversion, C. Adapted with permission from Flynn 1966.

different fractions of completion can be chosen prior to analysis. From here, the different values of ramp rates and corresponding temperatures can be used to form, for the purpose of repetition, several linear plots. Alternately with DSC, the various ramp rates are plotted with the temperature at which the reaction rate is greatest (Fig. 2.8).[40] There has been much debate about which method, OFW or KAS, should be utilized due to the accuracy of the calculated value. However, the discrepancies between the methods are small enough that a semi-quantitative comparison of activation energies can be done to compare the kinetics.[73, 77] The advantage of using these methods to study kinetics of desorption is that an activation energy may be calculated without the difficulty of fitting the desorption curve to an appropriate kinetic function, $f(\alpha)$. However, this is not the case for the PCI or GCI methods, which have the added advantage of being able to study both the hydrogen adsorption and desorption kinetics.

2.7 Isothermal Methods

Both GCI and PCI techniques require a reaction chamber that can be evacuated and highly pressurized, as well as a sample holder that can be thermally regulated. In order to calculate the activation energies using these methods, kinetics rate constants are used in association with the Arrhenius equation. However, to find the kinetic rate constant, the sorption curves must be fit to the modeled function, $f(\alpha)$, of the appropriate kinetic mechanism. As will be explained, the GCI and PCI methods differ by the manner in which the fraction of completion, α, is determined.

The method of determining PCIs, also known as Sievert's method, requires a chamber of known volume.[69] When a sample is exposed to hydrogen the change in pressure can be accounted for as absorption of hydrogen. Alternatively, when a hydrogenated sample is exposed to vacuum, or a pressure lower than the desorption equilibrium pressure, the pressure change can be attributed

to desorption of hydrogen.[78] The recorded change in pressure, *P*, with the known volume, *V*, and temperature, *T*, of the chamber, can be applied to the ideal gas law, *PV=nRT*, to determine the molar amounts, *n*, of absorption or desorption of hydrogen (*R* is the gas constant). From this calculation, a percent hydrogenation can be determined:

$$Percent\ Hydrogenation = \frac{mass\ H_2}{mass\ Mg + mass\ H_2} \quad (3)$$

which can then be used to to calculate α, where:

$$\alpha = \frac{H_2 weight\ \%}{Maximum\ H_2 weight\ \%} \quad (4)$$

which can then be used in kinetic fittings.

Using a similar apparatus to the one used in Sievert's method, with the addition of a microbalance, a GCI method measures the change in weight of the material that is a result of the absorption and desorption of hydrogen.[20, 79] Another main difference in the method lies in the fact that because the change of mass is measured and not the change of pressure, the pressure of the chamber can be held constant. This proves advantageous when a kinetic constant is calculated and applied, for reasons explained later. Despite this mentioned advantage, corrections must be made

Table 2.2: Kinetic equations used for fitting experimental sorption data. Adapted with permission from Barkhordarian 2006

Model Equation	Description
$\alpha = kt$	Surface controlled reaction with chemisorption being the RDS
$[-\ln(1-\alpha)]^{1/3} = kt$	JMA nucleation and growth: Three-dimensional growth of existing nuclei with constant interface velocity
$[-\ln(1-\alpha)]^{1/2} = kt$	JMA nucleation and growth: Two-dimensional growth of existing nuclei with constant interface velocity
$1-(1-\alpha)^{1/3} = kt$	CV: Three-dimensional growth with constant interface velocity
$1-(1-\alpha)^{1/2} = kt$	CV: Two-dimensional growth with constant interface velocity
$1-\left(\frac{2\alpha}{3}\right)-(1-\alpha)^{2/3} = kt$	CV: Three-dimensional growth with decreasing interface velocity

to the recorded mass to account for buoyancy effects from the differences in air density within the chamber and the surroundings[79].

As mentioned earlier, for PCI and GCI data the activation energy can be found by plotting *ln k vs. 1/T*. This plot is based on the Arrhenius equation:

$$\ln(k) = \frac{-E_a}{R}\frac{1}{T} + \ln(A) \qquad (5)$$

Before this can be done, however, the kinetic rate constant has to be deduced for various temperatures.

The kinetic rate constant is found by fitting the experimental data with different model equations, *f(α)* (Table 2.2).[80] Each function has a different rate-determining step, which is mentioned in the description in Table 2.2. The best function will produce a plot that is linear, with the slope that is equal to the rate constant, *k* (Fig. 2.10).[79-80] However, because of the high surface area-to-volume ratio of nanoscaled materials, fitting kinetic data to kinetic models based on bulk materials proves arduous, if not possible at all.[81-82] The two most common models used are the Johnson-Mehl-Avrami (JMA) model of Nucleation and Growth (NG)[83-86] and Contracting Volume (CV)[87] model (Fig. 2.11). Both models make assumptions that may not be valid during growth of differing phases of nanoparticles. For instance, the CV model makes the assumption that nucleation of the secondary phases are instantaneous (the nucleation of MgH_2, for example) and that the core/shell morphology is quickly reached. As a result of the model not accounting for the initial nucleation and growth, the fitting will likely have discrepancies for low

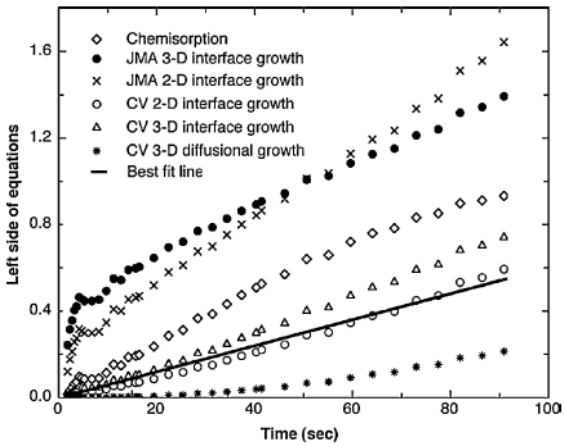

Figure 2.10: Different kinetic curves based on the equations in Table 2.2 for magnesium catalyzed with 1 mol% Nb_2O_5 and milled for 100 h (T=100°C). Reproduced with permission from Barkhordarian 2006.

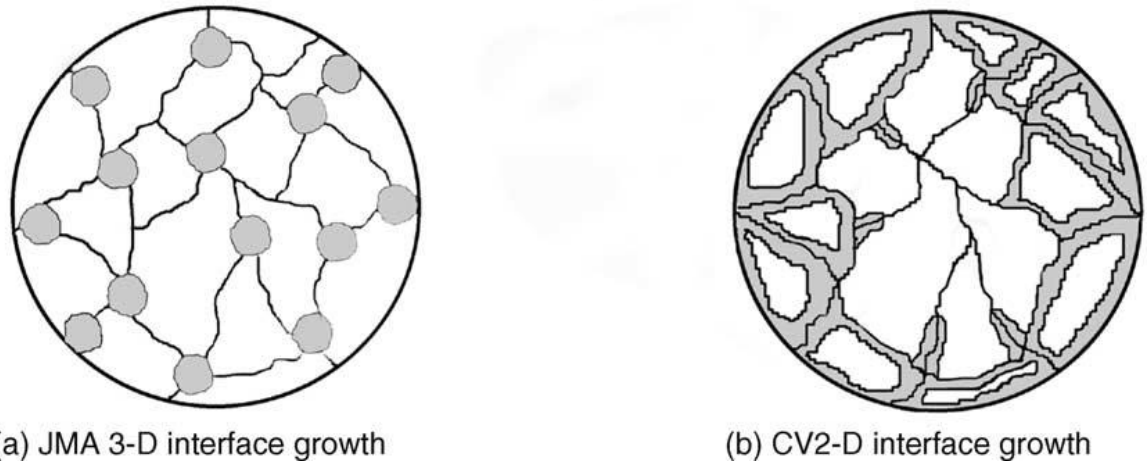

Figure 2.11: Schematic picture of phase growth according to (a) JMA and (b) CV models. The dark areas represent the transformed phase. Reproduced with permission from Barkhordarian 2006.

α values. In contrast, the fitting for JMA will likely have discrepancies for the high α values. This is because the JMA model does not account for the overlap of the growing phase that is likely to occur once most of the material is transformed to MgH_2.[70, 88] Due to the many assumptions made by these models, the experimental data rarely fit well for a whole data set.[70] However, even though an entirely acceptable fit may not be made, the nature of the mechanism can be inferred through characterization of a portion of the full data set.[70, 81]

As mentioned earlier, the GCI method can be performed at constant pressure, which is advantageous because pressure changes add even more complexity to isothermal measurements. In addition to the difficulty of fitting the data, the PCI method calls for data correction due to the kinetic behavior being dependent on both the temperature and pressure. It has been shown that as the change in pressure is measured, which is how the data is collected, the driving force for the exchange of hydrogen is altered.[89] This driving force is dependent on the equilibrium pressure, which is defined as the pressure the system must be above or below in order for hydrogenation or dehydrogenation to proceed, respectively. The change in driving force is not significant if the process is performed with a pressure considerably higher or lower than the equilibrium pressure,

depending on which process is monitored. However if this is not the case, the deviation of the driving force can be corrected for by plotting *F(α)/F(P) vs. t*, where *F(P)* is the pressure dependence function.[68, 89] Common *F(P)* functions can be found in Table 2.3.[89] Proper methods for determining the pressure dependence function can be found in the work of Sanchez et al.[90] *P* is the measured pressure at time *t*, P_{br} is the reaction bed pressure (described in detail in reference),[89] and P_{eq} is the equilibrium pressure of the $Mg + H_2 \rightarrow MgH_2$ reaction. P_{eq} values can be determined by performing the Pressure Sweep Method[91] or estimated by utilizing values reported in literature[68, 92] Again, the slope of the new plot, *F(α)/F(P) vs. t*, is the kinetic rate constant.

Table 2.3: Different pressure dependence functions, *F(P)*, used by investigators. Reproduced with permission from Ron 1999.

F(P)	***F(P)***
$\frac{\lvert P_{eq} - P \rvert}{P_0}; P_0 = 1\ atm$	$\left[\frac{P_{eq} - P}{P_0}\right]^n ; P_0 = 1\ atm$
$Ln\left(\frac{P_{eq}}{P}\right)$	$Ln\left(\frac{P}{P_{eq}}\right)$
P	$\sqrt{P}$
$\frac{\left(P_{eq} - P\right)}{P_{eq}}$	$\frac{\left(P_{eq} - P_b\right)}{P_{eq}}$
$P^{1/2} - {P_{eq}}^{1/2}\ for\ bulk$	${P_0}^{1/2} - {P_{eq}}^{1/2};\ P_0 = initial\ pressure$
$P_{eq} - P$	$P - P_{eq}$
$F\left(\frac{P_{eq}}{P}\right)^n, F\left(\frac{P}{P_{eq}}\right)^n$	$P_{eq} - P\ for\ surface\ control$
P=system pressure; P_b= reaction bed pressure; P_{eq}= desorption/absorption equilibrium pressure; Not all forms of *F(P)* that have been suggested are presented here.	

*

Quantitative characterization of the sorption kinetics of nano-scaled materials has proven difficult if not unattainable. However, with the methods that have been developed thus far, at least qualitative comparison of catalytic ability is possible. As will be evident in the next section, the

lack of activation energy values reported in the literature makes the comparison of hydrogenation and dehydrogenation kinetics elusive, and with respect to mechanism, arduous to fully understand.

2.8 Doping Studies

As mentioned earlier in section 2.4, in addition to reducing the grain size of magnesium-based hydrogen-storage materials, researchers have attempted alloying or "doping" Mg nanostructures with small amounts, less than ~10%, of various metals and metal oxides as catalysts to improve kinetic performance. Understanding the physical nature of the dopants in the magnesium requires an understanding of the structure, size, and shape of the nanoparticles. Using techniques such as x-ray diffraction (XRD), x-ray photoelectron spectroscopy (XPS), scanning electron microscopy (SEM), transmission electron microscopy (TEM) among others, researchers have attempted to understand the physical nature of these dopants. Having said that, the following sections will mainly concern themselves with understanding the kinetic and mechanistic abilities of the different dopants. Although direct comparison of the results is inherently difficult because of differences in the apparatuses, methods and calculations, and kinetic modeling (or lack thereof), the effects of additional chemical species on sorption kinetics are undoubtedly apparent. In light of the inability to directly compare the results of different doping papers with respect to each other, this section will attempt to highlight the findings in this area.

2.9 Dopant Effects on Hydrogen Sorption Kinetics

One of the earliest reports on the effects of alloying (~15-30% Cu) on the hydrogen storage properties of sub-bulk, micron-sized, magnesium was in 1979 when Karty et al. studied the hydrogen sorption kinetics of a Mg/Mg_2Cu microstructured eutectic alloy via a pressure sweep

method. Using the Johnson-Mehl-Avrami-Kolmogorov equation, an adapted version of the JMA equation discussed earlier, they were able to obtain suggestive evidence that the alloying of Mg with Cu reduced both the hydrogen desorption and adsorption activation energies with respect to measured activation for the pure Mg system. They propose that the Mg_2Cu's role in decreasing these activation energies is through offering an alternative pathway for diffusion of hydrogen into and out of the magnesium.[91] 20 years later, the next notable study, from Liang et al., compared the sorption kinetics of MgH_2 that was ball milled with different transition metals (MgH_2 5 %at. TM where TM = Ti, V, Mn, Fe, and Ni).[5] Using the CV model equation (Table 2.2) they were able to plot the desorption kinetics curves at different temperatures and obtain activation energies for the desorption (Fig. 2.12).[5] They were, 62.3, 67.6, 71.1, 88.1, and 104.6 kJ mol^{-1} for the MgH_2-vanadium, iron, titanium, nickel, and manganese nanocomposites, respectively. These values are much lower than the calculated pure balled milled MgH_2 desorption activation energy of 120 kJ mol^{-1}. They did not calculate the adsorption activation energies; however they report increased rate of absorption compared to pure ball milled MgH_2, for all nanocomposites at 10 MPa pressure and

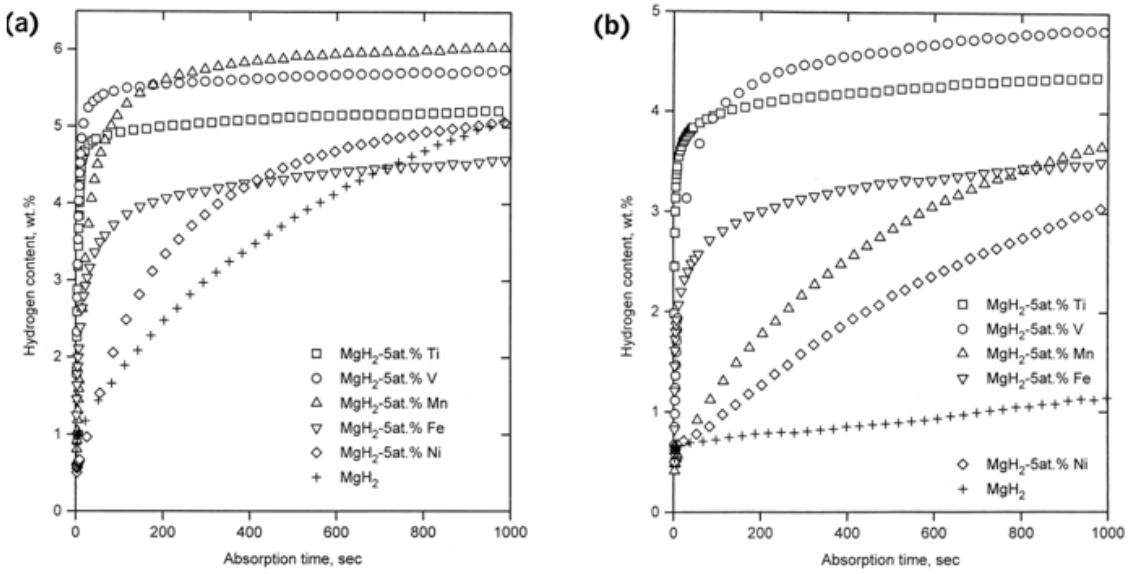

Figure 2.12: Hydrogen adsorption curves of Mg-TM composites at (a)273 K and (b) 373 K. Adapted with permission from Liang 1999.

temperatures of 473 K, 373 K, and 303 K. A mechanism of catalysis was not specified, but they ruled out changes in the Mg-H bond thermodynamics by measuring PCIs for all systems.[5, 68]

Oelerich and coworkers investigated a series of MgH_2/Me_xO_y nanocomposites that were synthesized through high energy ball milling (Me_xO_y= Sc_2O_3, TiO_2, V_2O_5, Cr_2O_3, Mn_2O_3, Fe_3O_4, CuO, Al_2O_3, and SiO_2). Only the transition metal oxides acted as catalysts in the hydrogen adsorption/desorption processes at ~573 K. As a result, the authors suggest that the ability of a metal to take on different oxidation states may play a part in the role of the catalyst. The best performing catalysts were Fe_3O_4 and Cr_2O_3 which allowed for rapid adsorption at room temperature and pressure of 8.4 bar, and desorption at ~473K and pressure of 0 bar.[45-46, 53] The team also compared the catalytic activity of V, V_2O_5, VC, and VN. They found that the vanadium already bonded with oxygen, nitrogen, or carbon resulted in the best performance, again supporting the theory that the oxidation state plays an important role. Additionally, they found that exposure of the MgH_2-V to small amounts of oxygen increased the catalytic activity of the vanadium. This further evidences that oxygen, or more specifically the oxidation state of vanadium is also playing a role in the catalytic mechanism.[53] Not long after, Barkhodarian et al. compared alloying NbO, NbO_2, and Nb_2O_5 with those researched by Oelerich et al (Fig. 2.13).[80] They found that 0.5 mole% Nb_2O_5 was a superior catalyst in both adsorption and desorption of hydrogen, with a tentative (based on JMA) lowered

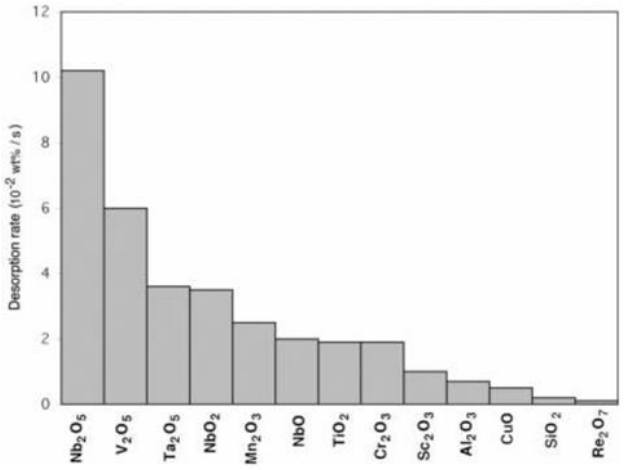

Figure 2.13: Catalytic effect of different transition metal oxides on the hydrogen desorption reaction rate of magnesium hydride at T=300°C. Reaction rates were calculated between 20% and 80% of the respective maximum capacity. Adapted with permission from Barkhordarian 2006.

desorption activation energy of 62 kJ mol^{-1}. In their numerous papers on the subject, Barkhordarian et al. present thorough discussion on the differences in the kinetic models that can be used. While using the different approaches discussed earlier in the chapter to analyze their kinetics, they ultimately conclude that the mechanism of the catalytic process is unclear, but they agree with Oelerich and coworkers[45-46, 53] that the ability of the transition metals to take on different electronic states must play a major role. It was proposed that the transition metal goes through electronic exchange reactions with the hydrogen molecule, which could accelerate the overall reaction. They claim there are five distinct steps in the reaction of metals with hydrogen: physisorption, chemisorption, surface penetration, diffusion, and hydride formation. The slowest of these steps will be the one that causes slow kinetics; they found that the rate limiting step changes with varying amounts of their catalyst, Nb_2O_5.[80] Tentatively, the different transition metal catalysts were concluded to influence both the chemisorption and diffusion steps.

Around the same time, Hanada et al. also performed kinetic studies on nanocomposites of MgH_2 with iron, cobalt, copper, nickel, and Nb_2O_5.[80, 93-95] They found that each of these catalysts improves kinetics, with nickel and Nb_2O_5 performing the best at 2 and 1 mol%, respectively. Using the JMA equation to model their kinetics and TDMS, they were able to effectively apply the Kissinger method[76] to estimate the activation energies to be 323 ± 40, 94 ± 3, and 71 ± 3 kJ $molH_2^{-1}$ for the non-catalyzed Mg-H_2, nickel catalyzed, and Nb_2O_5 catalyzed hydrogen desorption reaction, respectively. The difference in the activation energy of the pure MgH_2 desorption process compared to that found by Liang et al.[5] highlights the difficulty in comparing the capabilities of different catalysts to improve sorption kinetics. As with others, Hanada et al. conclude the absolute mechanism of catalysis is elusive; however, they propose the surface reaction is a first order process and that one must take into account certain surface conditions prior to modeling.[40, 66] In

their paper, Kalisvaart et al. describe a neutron reflectometry experiment that studies the effects of vanadium and chromium doping on Mg hydrogenation kinetics. It was found that with pure thin film Mg, the deuterium forms an MgD_2 blocking layer on the surface of the film, which slows the kinetics of hydrogenation. With the addition of catalysts, no such layer formed, and the deuterium was able to diffuse into the film without inhibition. Although this study was performed on thin films in the micrometer range, it further confirms the surface role of different catalysts is highly important.[54] The ability for the catalyst to remain on the surface may also come into play. Although discussion about the surface condition does not take place, Lillo-Rodenas et al. found that carbon supported nickel had superior kinetics to pure nickel. The role of the carbon is unclear, but based on their DSC measurements they surmise that the carbon support may stabilize the catalytic role of nickel over many cycles (i.e. no degradation in catalytic activity).[61] More recently, Callini et al. performed an in depth investigation on magnesium nanoparticles decorated with nickel by thermal evaporation. The nanoparticles were exposed to oxygen in order to form a protective MgO layer, which was suggested not to hinder diffusion of H_2. Using in situ powder XRD during different simultaneous annealing and hydrogen exposure experiments, they were able to confirm the presence of the nickel in the form of Mg_2Ni prior to hydrogenation and Mg_2NiH_4 after hydrogenation. The increased rate of the hydrogen sorption kinetics was clearly attributed to the formation of Mg_2Ni from Mg_2NiH_4. Nonetheless, a lowered hydrogen capacity of 4.4% was a definite downside of this doped material, attributed to the formation of the Mg_2NiH_4 (3.6 wt. percent hydrogen) and MgO (0 wt. percent hydrogen).[96]

With regards to MgO formation, Ares-Fernandez et al. investigated the possible catalytic effect of MgO addition prior to milling. They found that the MgO addition resulted in smaller Mg particle formation, referring to MgO as a lubricant for the sliding tribological interfaces. They rule

out the possibility that MgO, as have others,[97] is acting as a catalyst in the sorption processes, confirming it actually decreases sorption kinetics.[98] With this confirmation, they suggest that the main reason for increased sorption rates for the particles is a result of particle size; contrarily, a recent theoretical paper by Shevlin et al. has proposed that nanostructuring does not decrease dehydrogenation enthalpies unless the nanocluster contains less than 3 magnesium atoms, much smaller than those reported by Ares-Fernandez et al. This particular paper will be discussed more in the next section.[99] Another 2013 paper written by Ma et al. formulates a niobium gateway model to explain the superior catalytic ability of Nb_2O_5 in MgH_2 dehydrogenation. The gateway model begins by NbH_2 (confirmed by XRD of a 50 wt. % XRD) decomposing rapidly because of its thermodynamic instability. This is followed by formation of Nb, which then instigates diffusion of hydrogen to form an NbH_x solid solution. This solid solution allows for the flow of hydrogen from MgH_2 to the outside of the particle until MgH_2 is exhausted. They rule out the possibility of NbO acting as a catalyst by investigating Nb_2O_5, Nb, and NbO doped samples. They found that both Nb_2O_5 and Nb formed NbH_2 which allows for the Nb gateway to take place; however the NbO doped samples did not yield the same kinetic rates or NbH_2 species. This study is one of the more recent studies that straightforwardly attempts to characterize the mechanism of catalysis for doped Magnesium. However, as mentioned earlier, most of the niobium phases confirmed to be present in this study were confirmed by XRD of a 50 wt % dopant sample, much more than that used in most kinetic studies. Nonetheless, this paper gives insight into possible mechanisms for catalysis; further proposing the hypothesis that destabilization of the hydride phase occurs through bond formation between the catalyst and hydrogen itself.[96] Many other groups have worked with doping magnesium with nickel and Nb_2O_5 as well as their effects on the hydrogen sorption kinetics. For example, many of them have tried investigating the physical nature with high resolution

micrographs (Fig. 2.14),[60, 67] and the others can be sought out for more information than already mentioned.[13, 61-62, 65, 67] As with nickel and Nb_2O_5, more studies have since been conducted in order to further investigate the effects of adding various metals and metal composites to Mg, e.g. Ti, Fe, Ge, Si, Al, and Fe, however very little new insight has been given into the nature and mechanism these catalysts besides reconfirmation of their respective abilities to improve sorption kinetics.[17, 48, 50-51, 55, 57, 64, 100-104]

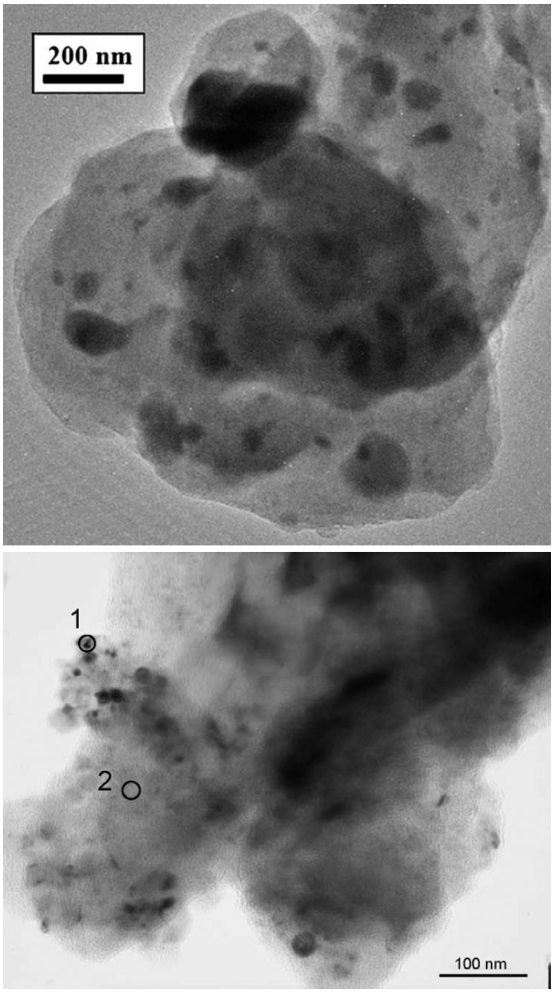

Figure 2.14: TOP: Bright field TEM micrograph suggesting that most of the Nb_2O_5 particles are embedded in the MgH_2 matrix (darker areas). BOTTOM: TEM micrograph of the MgH_2-Ni nanocomposite with (1) being 87.5% Ni and (2) being only 5.2 % Ni by EDX. Reproduced with permission from Porcu 2008 and Hanada 2008.

2.10 Theoretical Modeling Studies on Nature of Dopants

In attempt to investigate and characterize the kinetics and mechanism of the hydrogen sorption reactions, many groups have tried using different theoretical approaches to elucidate the nature of the reactions, both catalyzed and non-catalyzed. Song et al. carried out theoretical calculations to explore the effects of alloying Mg with Cu, Ni, Al, Nb, Fe, and Ti. Using the full-potential linearized augmented plane-wave method (based on density functional theory (DFT)) they found that alloying the magnesium should destabilize the MgH_2 by weakening the Mg-H bond, with increasing effect from Ti, Fe, Nb, Al, Ni, to Cu.[105] This is contrary to what Liang et al.

had previously reported[5], however the calculations were not necessarily taking into account particle size.[105] Similarly, Cleri and coworkers did extensive electronic structure and DFT calculations on the effects of doping with small amounts of Cu, Ni, Fe, Ti, Zr, Pd, Co, Al, Cr, and Nb. Comparing their results with experiment, they were able to establish a trend, with a few exceptions.[39] Additionally, Moser et al studied the stability of Mg-transition metal hydrides, where TM= Ti, Zr, Hf, V, Nb, and Ta. Their DFT calculations suggest the H is more strongly bonded to the transition metal, causing a stepwise dehydrogenation process[41]. Kelkar et al. also carried out a computational study on the effects of pure and aluminum and silicon doped alpha-, gamma-, and beta-MgH_2 hydrogen sorption kinetics. They did this using *ab initio* plane wave pseudopotential method based on DFT, similar to Song et al.[47, 105] More recently Zeng et al. used a similar method to characterize another group of 3d transition metals, with a few different considerations taken into account.[43]

As stated earlier, most of the above stated theoretical papers do not take into account the effects of nanostructuring. More recently, Shevlin et al. used DFT and many different exchange-correlation functionals, i.e. LDA, PBE, and PBESol, to investigate the thermodynamics of nanostructuring and transition metal doping. They found that unless the magnesium cluster contains less than 3 magnesium atoms, it will have a higher dehydrogenation enthalpy than the bulk. Thus, for all the experiments discussed thus far, all increased performance through nanostructuring is purely kinetic. However, they did find that nickel doping is highly effective in decreasing both dehydrogenation thermodynamics and kinetics.[99]

In summary, the effects of adding small amounts of dopants has been highlighted and briefly discussed. The mechanism and nature of these catalysts is still relatively unclear, however with the development of new kinetic models, and the incorporation of theoretical analysis, a deeper

understanding of these catalysts is on the horizon. Clearly, the catalysts play an important role in multiple steps of the hydrogen sorption process, and with more research, proper utilization of these catalysts may make the practicality of Mg nanostructures for hydrogen storage a potentially realizable goal.

2.11 Conclusions and Outlook

Bulk Mg itself is not likely to be a viable hydrogen storage material due to the slow kinetics at ambient temperatures and pressures. However, there are strong indications from experiments as well as theory that nanostructured magnesium particles doped with low percentages of other elements spanning the periodic table exhibit enhanced kinetics at lower temperature, but efficient hydrogenation and dehydrogenations at room temperature is a goal that has still not been achieved. Significant challenges in the field are structurally characterizing the doped materials effectively, so that an iterative loop between synthesis, structural characterization, evaluation of kinetics, and modeling can be achieved.

References:

1. Rosi, N. L.; Eckert, J.; Eddadoudi, M.; Vodak, D. T.; Kim, J.; O'Keeffe, M.; Yaghi, O., Hydrogen Storage in Microporous Metal-Organic Frameworks. *Science* **2003,** *300*, 1127-1129.
2. Hirscher, M.; Becher, M.; Haluska, M.; Dettlaff-Weglikowska, U.; Quintel, A.; Duesberg, G. S.; Choi, Y. M.; Downes, P.; Hulman, M.; Roth, S.; Stepanek, I.; Bernier, P., Hydrogen Storage in Sonicated Carbon Materials. *Appl. Phys. A* **2001,** *72* (2), 129-132.
3. Schlapbach, L.; Zuttel, A., Hydrogen-Storage Materials for Mobile Applications. *Nature* **2001,** *414*, 253-258.
4. Zaluska, A.; Zaluski, L.; Strom-Olsen, J. O., Structure, Catalysis and Atomic Reactions on the Nano-Scale: A Systematic Approach to Metal Hydrids for Hydrogen Storage. *Appl. Phys. A* **2001,** *72*, 157-165.
5. Liang, G.; Huot, J.; Boily, S.; Van Neste, A.; Schulz, R., Catalytic Effect of Transition Metals on Hydrogen Sorption in Nanocrystalline Ball Milled MgH_2-Tm (Tm=Ti, V, Mn, Fe and Ni) Systems. *Journal of Alloys and Compounds* **1999,** *292* (1-2), 247-252.
6. Shao, H.; Xu, H.; Wang, Y.; Li, X., Preparation and Hydrogen Storage Properties of Mg_2Ni Intermetallic Nanoparticles. *Nanotechnology* **2004,** *15*, 269-274.
7. Zaluska, A.; Zaluski, L.; Strom-Olsen, J. O., Nanocrystalline Magnesium for Hydrogen Storage. *Journal of Alloys and Compounds* **1999,** *288* (1-2), 217-225.
8. Friedrichs, O.; Kolodziejczyk, L.; Sanchez-Lopez, J. C.; Lopez-Cartes, C.; Fernandez, A., Synthesis of Nanocrystalline MgH_2 Powder by Gas-Phase Condensation and in Situ Hydridation: Tem, Xps and Xrd Study. *J. Alloys Compd.* **2007,** *434-435*, 721-724.
9. Huhn, P. A.; Dornheim, M.; Klassen, T.; Bormann, R., Thermal Stability of Nanocrystalline Magnesium for Hydrogen Storage. *J. Alloys Compd.* **2005,** *404-406*, 499-502.
10. Imamura, H.; Masanari, K.; Kusuhara, M.; Katsumoto, H.; Sumi, T.; Sakata, Y., High Hydrogen Storage Capacity of Nanosized Magnesium Synthesized by High Energy Ball-Milling. *J. Alloys Compd.* **2005,** *386* (1-2), 211-216.
11. Huot, J.; Tremblay, M. L.; Schulz, R., Synthesis of Nanocrystalline Hydrogen Storage Materials. *J. Alloys Compd.* **2003,** *356-357*, 603-607.
12. Doppiu, S.; Schultz, L.; Gutfleisch, O., In Situ Pressure and Temperature Monitoring During the Conversion of Mg into MgH_2 by High-Pressure Reactive Ball Milling. *J. Alloys Compd.* **2007,** *427*, 204-208.
13. Varin, R. A.; Czujko, T.; Chiu, C.; Wronski, Z., Particle Size Effects on the Desorption Properties of Nanostructured Magnesium Dihydride (MgH_2) Synthesized by Controlled Reactive Mechanical Milling (CRMM). *J. Alloys Compd.* **2006,** *424* (1-2), 356-364.
14. Paskevicius, M.; Sheppard, D. A.; Buckley, C. E., Thermodynamic Changes in Mechanochemically Synthesized Magnesium Hydride Nanoparticles. *J. Am. Chem. Soc.* **2010,** *132* (14), 5077-5083.
15. Leiva, D. R.; Floriano, R.; Huot, J.; Jorge, A. M.; Bolfarini, C.; Kiminami, C. S.; Ishikawa, T. T.; Botta, W. J., Nanostructured MgH_2 Prepared by Cold Rolling and Cold Forging. *J. Alloys Compd.* **2011,** *509* (Supplement 1), S444-S448.
16. Shao, H.; Liu, T.; Wang, Y.; Xu, H.; Li, X., Preparation of Mg-Based Hydrogen Storage Materials from Metal Nanoparticles. *J. Alloys Compd.* **2008,** *465* (1-2), 527-533.

17. Zou, J.; Sun, H.; Zeng, X.; Ji, G.; Ding, W., Preparation and Hydrogen Storage Properties of Mg-Rich Mg-Ni Ultrafine Particles. *J. Nanomater.* **2012**, 592147, 8 pp.
18. Zhu, C.; Akiyama, T., Zebra-Striped Fibers in Relation to the H_2 Sorption Properties for MgH_2 Nanofibers Produced by a Vapor-Solid Process. *Cryst. Growth Des.* **2012,** *12* (8), 4043-4052.
19. Li, W.; Li, C.; Ma, H.; Chen, J., Magnesium Nanowires: Enhanced Kinetics for Hydrogen Absorption and Desorption. *J. Am. Chem. Soc.* **2007,** *129* (21), 6710-6711.
20. Setijadi, E. J.; Boyer, C.; Aguey-Zinsou, K. F., Remarkable Hydrogen Storage Properties for Nanocrystalline MgH_2 Synthesised by the Hydrogenolysis of Grignard Reagents. *Physical Chemistry Chemical Physics* **2012,** *14* (32), 11386-11397.
21. Kalidindi, S. B.; Jagirdar, B. R., Highly Monodisperse Colloidal Magnesium Nanoparticles by Room Temperature Digestive Ripening. *Inorg. Chem.* **2009,** *48* (10), 4524-4529.
22. Redl, F. X.; Cho, K.-S.; Murray, C. B.; O'Brien, S., Three-Dimensional Binary Superlattices of Magnetic Nanocrystals and Semiconductor Quantum Dots. *Nature* **2003,** *423*, 968-971.
23. Peng, X.; Manna, L.; Yang, W.; Wickham, J.; Scher, E.; Kadavanich, A.; Alivisatos, A. P., Shape Control of CdSe Nanocrystals. *Nature* **2000,** *404*, 59-61.
24. Puntes, V. F.; Krishnan, K. M.; Alivisatos, A. P., Colloidal Nanocrystal Shape and Size Control: The Case of Cobalt. *Science* **2001,** *291*, 2115-2117.
25. Ouyang, M.; Awschalom, D. D., Coherent Spin Transfer between Molecularly Bridged Quantum Dots. *Science* **2003,** *301*, 1074-1078.
26. Milliron, D. J.; Hughes, S. M.; Cui, Y.; Manna, L.; Li, J.; Wang, L.-W.; Alivisatos, A. P., Colloidal Nanocrystal Hereostructures with Linear and Branched Topology. *Nature* **2004,** *430*, 190-195.
27. Aguey-Zinsou, K. F.; Ares-Fernandez, J.-R., Synthesis of Colloidal Magnesium: A near Room Temperature Store for Hydrogen. *Chem. Mater.* **2008,** *20*, 376-378.
28. Bogdanovic, B.; Spliethoff, B., *Int. J. Hydrogen Energy* **1987,** *12*, 863.
29. Li, W. Y.; Li, C. S.; Ma, H.; Chen, J., Magnesium Nanowires: Enhanced Kinetics for Hydrogen Absorption and Desorption. *Journal of the American Chemical Society* **2007,** *129* (21), 6710.
30. Huot, J.; Liang, G.; Schulz, R., Mechanically Alloyed Metal Hydride Systems. *Appl. Phys. A-Mater. Sci. Process.* **2001,** *72* (2), 187-195.
31. Aguey-Zinsou, K. F.; Ares-Fernandez, J. R., Synthesis of Colloidal Magnesium: A near Room Temperature Store for Hydrogen. *Chemistry of Materials* **2008,** *20* (2), 376-378.
32. Viyannalage, L.; Lee, V.; Dennis, R. V.; Kapoor, D.; Haines, C. D.; Banerjee, S., From Grignard's Reagents to Well-Defined Mg Nanostructures: Distinctive Electrochemical and Solution Reduction Routes. *Chemical Communications* **2012,** *48* (42), 5169-5171.
33. Norberg, N. S.; Arthur, T. S.; Fredrick, S. J.; Prieto, A. L., Size-Dependent Hydrogen Storage Properties of Mg Nanocrystals Prepared from Solution. *Journal of the American Chemical Society* **2011,** *133* (28), 10679-10681.
34. Jeon, K. J.; Moon, H. R.; Ruminski, A. M.; Jiang, B.; Kisielowski, C.; Bardhan, R.; Urban, J. J., Air-Stable Magnesium Nanocomposites Provide Rapid and High-Capacity Hydrogen Storage without Using Heavy-Metal Catalysts. *Nature Materials* **2011,** *10* (4), 286-290.
35. Aguey-Zinsou, K. F.; Ares-Fernandez, J. R., Hydrogen in Magnesium: New Perspectives toward Functional Stores. *Energy & Environmental Science* **2010,** *3* (5), 526-543.

36. Sakintuna, B.; Lamari-Darkrim, F.; Hirscher, M., Metal Hydride Materials for Solid Hydrogen Storage: A Review. *International Journal of Hydrogen Energy* **2007,** *32* (9), 1121-1140.
37. Wagner, L. K.; Majzoub, E. H.; Allendorf, M. D.; Grossman, J. C., Tuning Metal Hydride Thermodynamics Via Size and Composition: Li-H, Mg-H, Al-H, and Mg-Al-H Nanoclusters for Hydrogen Storage. *Physical Chemistry Chemical Physics* **2012,** *14* (18), 6611-6616.
38. Yang, J.; Sudik, A.; Wolverton, C.; Siegel, D. J., High Capacity Hydrogen Storage Materials: Attributes for Automotive Applications and Techniques for Materials Discovery. *Chemical Society Reviews* **2010,** *39* (2), 656-675.
39. Cleri, F.; Celino, M.; Montone, A.; Bonetti, E.; Pasquini, L., Experimental and Theoretical Characterization of the 3d-Dopants Bias on the H Desorption of Mg Hydrides. In *Research Trends in Contemporary Materials Science*, Uskokovic, D. P.; Milonjic, S. K.; Rakovic, D. I., Eds. 2007; Vol. 555, pp 349-354.
40. Hanada, N.; Ichikawa, T.; Fujii, H., Catalytic Effect of Nanoparticle 3d-Transition Metals on Hydrogen Storage Properties in Magnesium Hydride MgH_2 Prepared by Mechanical Milling. *Journal of Physical Chemistry B* **2005,** *109* (15), 7188-7194.
41. Moser, D.; Bull, D. J.; Sato, T.; Noreus, D.; Kyoi, D.; Sakai, T.; Kitamura, N.; Yusa, H.; Taniguchi, T.; Kalisvaart, W. P.; Notten, P., Structure and Stability of High Pressure Synthesized Mg-Tm Hydrides (Tm = Ti, Zr, Hf, V, Nb and Ta) as Possible New Hydrogen Rich Hydrides for Hydrogen Storage. *Journal of Materials Chemistry* **2009,** *19* (43), 8150-8161.
42. Shang, C. X.; Bououdina, M.; Song, Y.; Guo, Z. X., Mechanical Alloying and Electronic Simulations of (MgH_2 + M) Systems (M-Al, Ti, Fe, Ni, Cu and Nb) for Hydrogen Storage. *International Journal of Hydrogen Energy* **2004,** *29* (1), 73-80.
43. Zeng, X. Q.; Cheng, L. F.; Zou, J. X.; Ding, W. J.; Tian, H. Y.; Buckley, C., Influence of 3d Transition Metals on the Stability and Electronic Structure of MgH_2. *Journal of Applied Physics* **2012,** *111* (9).
44. Hanada, N.; Ichikawa, T.; Isobe, S.; Nakagawa, T.; Tokoyoda, K.; Honma, T.; Fujii, H.; Kojima, Y., X-Ray Absorption Spectroscopic Study on Valence State and Local Atomic Structure of Transition Metal Oxides Doped in MgH_2. *Journal of Physical Chemistry C* **2009,** *113* (30), 13450-13455.
45. Oelerich, W.; Klassen, T.; Bormann, R., Hydrogen Sorption of Nanocrystalline Mg at Reduced Temperatures by Metal-Oxide Catalysts. *Advanced Engineering Materials* **2001,** *3* (7), 487-490.
46. Oelerich, W.; Klassen, T.; Bormann, R., Metal Oxides as Catalysts for Improved Hydrogen Sorption in Nanocrystalline Mg-Based Materials. *Journal of Alloys and Compounds* **2001,** *315* (1-2), 237-242.
47. Kelkar, T.; Pal, S., A Computational Study of Electronic Structure, Thermodynamics and Kinetics of Hydrogen Desorption from Al- and Si-Doped Alpha-, Gamma-, and Beta-MgH_2. *Journal of Materials Chemistry* **2009,** *19* (25), 4348-4355.
48. Liu, T.; Qin, C.; Zhang, T.; Cao, Y.; Zhu, M.; Li, X., Synthesis of $Mg@Mg_{17}Al_{12}$ Ultrafine Particles with Superior Hydrogen Storage Properties by Hydrogen Plasma-Metal Reaction. *J. Mater. Chem.* **2012,** *22* (37), 19831-19838.
49. Vajo, J. J.; Mertens, F.; Ahn, C. C.; Bowman, R. C.; Fultz, B., Altering Hydrogen Storage Properties by Hydride Destabilization through Alloy Formation: Lih and MgH_2 Destabilized with Si. *Journal of Physical Chemistry B* **2004,** *108* (37), 13977-13983.

50. Shahi, R. R.; Tiwari, A. P.; Shaz, M. A.; Srivastava, O. N., Studies on De/Rehydrogenation Characteristics of Nanocrystalline MgH_2 Co-Catalyzed with Ti, Fe and Ni. *International Journal of Hydrogen Energy* **2013,** *38* (6), 2778-2784.
51. Lu, J.; Choi, Y. J.; Fang, Z. Z.; Sohn, H. Y.; Ronnebro, E., Hydrogenation of Nanocrystalline Mg at Room Temperature in the Presence of TiH_2. *J. Am. Chem. Soc.* **2010,** *132* (19), 6616-6617.
52. Schimmel, H. G.; Huot, J.; Chapon, L. C.; Tichelaar, F. D.; Mulder, F. M., Hydrogen Cycling of Niobium and Vanadium Catalyzed Nanostructured Magnesium. *Journal of the American Chemical Society* **2005,** *127* (41), 14348-14354.
53. Oelerich, W.; Klassen, T.; Bormann, R., Comparison of the Catalytic Effects of V,V_2O_5, Vn, and Vc on the Hydrogen Sorption of Nanocrystalline Mg. *Journal of Alloys and Compounds* **2001,** *322* (1-2), L5-L9.
54. Kalisvaart, P.; Luber, E.; Fritzsche, H.; Mitlin, D., Effect of Alloying Magnesium with Chromium and Vanadium on Hydrogenation Kinetics Studied with Neutron Reflectometry. *Chemical Communications* **2011,** *47* (14), 4294-4296.
55. Asselli, A. A. C.; Leiva, D. R.; Jorge, A. M.; Ishikawa, T. T.; Botta, W. J., Synthesis and Hydrogen Sorption Properties of Mg_2FeH_6-MgH_2 Nanocomposite Prepared by Reactive Milling. *Journal of Alloys and Compounds* **2012,** *536*, S250-S254.
56. Montone, A.; Aurora, A.; Gattia, D. M.; Antisari, M. V., Microstructural and Kinetic Evolution of Fe Doped MgH_2 During H_2 Cycling. *Catalysts* **2012,** *2* (3), 400-411.
57. Yavari, A. R.; Vaughan, G.; de Castro, F. R.; Georgarakis, K.; Jorge, A. M.; Nuta, I.; Botta, W. J., A Synchrotron X-Ray Diffraction Study of Hydrogen Storage and Enhanced Sorption Kinetics in a Mini-Tank of Mg with Crystalline and Amorphous Catalytic Particle Additions. *Journal of Alloys and Compounds* **2012,** *540*, 57-61.
58. Bogdanovic, B.; Hofmann, H.; Neuy, A.; Reiser, A.; Schlichte, K.; Spliethoff, B.; Wessel, S., Ni-Doped Versus Undoped Mg-MgH_2 Materials for High Temperature Heat or Hydrogen Storage. *Journal of Alloys and Compounds* **1999,** *292* (1-2), 57-71.
59. Gutfleisch, O.; Dal, T. S.; Herrich, M.; Handstein, A.; Pratt, A., Hydrogen Sorption Properties of Mg-1 Wt.% Ni-0.2 Wt.% Pd Prepared by Reactive Milling. *J. Alloys Compd.* **2005,** *404-406*, 413-416.
60. Hanada, N.; Hirotoshi, E.; Ichikawa, T.; Akiba, E.; Fujii, H., Sem and Tem Characterization of Magnesium Hydride Catalyzed with Ni Nano-Particle or Nb_2O_5. *Journal of Alloys and Compounds* **2008,** *450* (1-2), 395-399.
61. Lillo-Rodenas, M. A.; Aguey-Zinsou, K. F.; Cazorla-Amoros, D.; Linares-Solano, A.; Guo, Z. X., Effects of Carbon-Supported Nickel Catalysts on MgH_2 Decomposition. *J. Phys. Chem. C* **2008,** *112* (15), 5984-5992.
62. Varin, R. A.; Czujko, T.; Wasmund, E. B.; Wronski, Z. S., Catalytic Effects of Various Forms of Nickel on the Synthesis Rate and Hydrogen Desorption Properties of Nanocrystalline Magnesium Hydride (MgH_2) Synthesized by Controlled Reactive Mechanical Milling (CRMM). *J. Alloys Compd.* **2007,** *432* (1-2), 217-231.
63. Xie, L.; Liu, Y.; Zhang, X.; Qu, J.; Wang, Y.; Li, X., Catalytic Effect of Ni Nanoparticles on the Desorption Kinetics of MgH_2 Nanoparticles. *J. Alloys Compd.* **2009,** *482* (1-2), 388-392.
64. Walker, G. S.; Abbas, M.; Grant, D. M.; Udeh, C., Destabilisation of Magnesium Hydride by Germanium as a New Potential Multicomponent Hydrogen Storage System. *Chemical Communications* **2011,** *47* (28), 8001-8003.

65. da Conceicao, M. O. T.; Brum, M. C.; dos Santos, D. S.; Dias, M. L., Hydrogen Sorption Enhancement by Nb_2O_5 and Nb Catalysts Combined with MgH_2. *Journal of Alloys and Compounds* **2013,** *550*, 179-184.
66. Hanada, N.; Ichikawa, T.; Hino, S.; Fujii, H., Remarkable Improvement of Hydrogen Sorption Kinetics in Magnesium Catalyzed with Nb_2O_5. *Journal of Alloys and Compounds* **2006,** *420* (1-2), 46-49.
67. Porcu, M.; Petford-Long, A. K.; Sykes, J. M., Tem Studies of Nb_2O_5 Catalyst in Ball-Milled MgH_2 for Hydrogen Storage. *J. Alloys Compd.* **2008,** *453* (1-2), 341-346.
68. Liang, G.; Huot, J.; Boily, S.; Schulz, R., Hydrogen Desorption Kinetics of a Mechanically Milled MgH_2 5at.%V Nanocomposite. *Journal of Alloys and Compounds* **2000,** *305* (1-2), 239-245.
69. Blach, T. P.; Gray, E. M., Sieverts Apparatus and Methodology for Accurate Determination of Hydrogen Uptake by Light-Atom Hosts. *Journal of Alloys and Compounds* **2007,** *446–447*, 692-697.
70. Mintz, M. H.; Zeiri, Y., Hydriding Kinetics of Powders. *Journal of Alloys and Compounds* **1995,** *216* (2), 159-175.
71. Lee, Y.-W.; Clemens, B. M.; Gross, K. J., Novel Sieverts' Type Volumetric Measurements of Hydrogen Storage Properties for Very Small Sample Quantities. *J. Alloy. Compd.* **2008,** *452*, 410-413.
72. Sabitu, S. T.; Goudy, A. J., Dehydrogenation Kinetics and Modeling Studies of MgH_2 Enhanced by Transition Metal Oxide Catalysts Using Constant Pressure Thermodynamic Driving Forces. *Metals* **2012,** *2* (3), 219-228.
73. Markmaitree, T.; Ren, R.; Shaw, L. L., Enhancement of Lithium Amide to Lithium Imide Transition Via Mechanical Activation. *The Journal of Physical Chemistry B* **2006,** *110* (41), 20710-20718.
74. Flynn, J. H.; Wall, L. A., A Quick, Direct Method for the Determination of Activation Energy from Thermogravimetric Data. *Journal of Polymer Science Part B: Polymer Letters* **1966,** *4* (5), 323-328.
75. Ozawa, T., Kinetic Analysis of Derivative Curves in Thermal Analysis. *Journal of Thermal Analysis and Calorimetry* **1970,** *2* (3), 301-324.
76. Kissinger, H. E., Reaction Kinetics in Differential Thermal Analysis. *Anal. Chem.* **1957,** *29* (11), 1702-1706.
77. Li, C.-R.; Tang, T., Isoconversion Method for Kinetic Analysis of Solid-State Reactions from Dynamic Thermoanalytical Data. *Journal of Materials Science* **1999,** *34* (14), 3467-3470.
78. Karty, A.; Grunzweig-Genossar, J.; Rudman, P. S., Hydriding and Dehydriding Kinetics of Mg in a Mg/Mg_2Cu Eutectic Alloy: Pressure Sweep Method. *Journal of Applied Physics* **1979,** *50* (11), 7200-7209.
79. Stander, C. M., Kinetics of Decomposition of Magnesium Hydride. *Journal of Inorganic & Nuclear Chemistry* **1977,** *39* (2), 221-223.
80. Barkhordarian, G.; Klassen, T.; Bormann, R., Kinetic Investigation of the Effect of Milling Time on the Hydrogen Sorption Reaction of Magnesium Catalyzed with Different Nb_2O_5 Contents. *Journal of Alloys and Compounds* **2006,** *407* (1-2), 249-255.
81. Zhdanov, V. P., Avrami-Kolmogorov-Johnson-Mehl Kinetics for Nanoparticles. *Surface Review and Letters* **2008,** *15* (5), 605-612.

82. Berube, V.; Radtke, G.; Dresselhaus, M.; Chen, G., Size Effects on the Hydrogen Storage Properties of Nanostructured Metal Hydrides: A Review. *International Journal of Energy Research* **2007,** *31* (6-7), 637-663.
83. Avrami, M., Kinetics of Phase Change I - General Theory. *Journal of Chemical Physics* **1939,** *7* (12), 1103-1112.
84. Johnson, W. A.; Mehl, R. F., Reaction Kinetics in Processes of Nucleation and Growth. *Transactions of the American Institute of Mining and Metallurgical Engineers* **1939,** *135*, 416-442.
85. Avrami, M., Kinetics of Phase Change. II Transformation-Time Relations for Random Distribution of Nuclei. *The Journal of Chemical Physics* **1940,** *8* (2), 212-224.
86. Avrami, M., Granulation, Phase Change, and Microstructure Kinetics of Phase Change. III. *The Journal of Chemical Physics* **1941,** *9* (2), 177-184.
87. Tomkins, P. W. M. J. a. F. C., *Chemistry of the Solid State*. Butterworths: London, 1955.
88. Tran, N. E.; Lambrakos, S. G.; Imam, M. A., Analyses of Hydrogen Sorption Kinetics and Thermodynamics of Magnesium–Misch Metal Alloys. *Journal of Alloys and Compounds* **2006,** *407* (1–2), 240-248.
89. Ron, M., The Normalized Pressure Dependence Method for the Evaluation of Kinetic Rates of Metal Hydride Formation/Decomposition. *Journal of Alloys and Compounds* **1999,** *283* (1-2), 178-191.
90. Fernandez, J. F.; Sanchez, C. R., Rate Determining Step in the Absorption and Desorption of Hydrogen by Magnesium. *Journal of Alloys and Compounds* **2002,** *340* (1-2), 189-198.
91. Karty, A.; Grunzweiggenossar, J.; Rudman, P. S., Hydriding and Dehydriding Kinetics of Mg in a Mg-Mg_2Cu Eutectic Alloy - Pressure Sweep Method. *Journal of Applied Physics* **1979,** *50* (11), 7200-7209.
92. Reilly, J. J.; Wiswall, R. H., Reaction of Hydrogen with Alloys of Magnesium and Copper. *Inorganic Chemistry* **1967,** *6* (12), 2220-2223.
93. Barkhordarian, G.; Klassen, T.; Bormann, R., Catalytic Mechanism of Transition-Metal Compounds on Mg Hydrogen Sorption Reaction. *Journal of Physical Chemistry B* **2006,** *110* (22), 11020-11024.
94. Barkhordarian, G.; Klassen, T.; Bormann, R., Fast Hydrogen Sorption Kinetics of Nanocrystalline Mg Using Nb_2O_5 as Catalyst. *Scripta Materialia* **2003,** *49* (3), 213-217.
95. Barkhordarian, G.; Klassen, T.; Bormann, R., Effect of Nb_2O_5 Content on Hydrogen Reaction Kinetics of Mg. *Journal of Alloys and Compounds* **2004,** *364* (1-2), 242-246.
96. Callini, E.; Pasquini, L.; Jensen, T. R.; Bonetti, E., Hydrogen Storage Properties of Mg-Ni Nanoparticles. *International Journal of Hydrogen Energy* **2013,** *38* (27), 12207-12212.
97. Ma, T.; Ma, S.; Isobe, Y.; Wang, N.; Hashimoto, S.; Ohnuki, T.; Ma, Nb-Gateway for Hydrogen Desorption in Nb_2O_5catalyzed MgH_2 nanocomposite. *The journal of physical chemistry. C* **2013,** *117* (20), 10302-10307.
98. Ares Fernandez, J.-R.; Ares Fernández, K.-F.; Aguey Zinsou, J.-R.; Ares, F., Superior MgH_2 Kinetics with MgO Addition: A Tribological Effect. *Catalysts* **2012,** *2* (3), 330-343.
99. Shevlin, S. A.; Guo, Z. X., MgH_2 dehydrogenation Thermodynamics: Nanostructuring and Transition Metal Doping. *The journal of physical chemistry. C* **2013,** *117* (21), 10883-10891.
100. Fu, Y.; Groll, M.; Mertz, R.; Kulenovic, R., Effect of $LaNi_5$ and Additional Catalysts on Hydrogen Storage Properties of Mg. *J. Alloys Compd.* **2008,** *460* (1-2), 607-613.
101. Cermak, J.; Kral, L., Improvement of Hydrogen Storage Characteristics of Mg/Mg_2Ni by Alloying: Beneficial Effect of In. *Journal of Power Sources* **2012,** *214*, 208-215.

102. Liu, J.; Song, X. P.; Pei, P.; Chen, G. L., Hydrogen Storage Performance of Mg-Based Composites Prepared by Spark Plasma Sintering. *J. Alloys Compd.* **2009,** *486* (1-2), 338-342.
103. Niaz, N. A.; Hussain, S. T.; Nasir, S.; Ahmad, I., Improved Hydrogen Desorption Kinetics of MgH_2 Nanoparticles by Using Tic Nanocatalyst. *Key Eng. Mater.* **2012,** *510-511*, 371-377.
104. Shahi, R. R.; Yadav, T. P.; Shaz, M. A.; Srivastva, O. N., Studies on Dehydrogenation Characteristic of $Mg(NH_2)_2$/LiH Mixture Admixed with Vanadium and Vanadium Based Catalysts (V, V_2O_5 and VCl_3). *International Journal of Hydrogen Energy* **2010,** *35* (1), 238-246.
105. Song, Y.; Guo, Z. X.; Yang, R., Influence of Selected Alloying Elements on the Stability of Magnesium Dihydride for Hydrogen Storage Applications: A First-Principles Investigation. *Physical Review B* **2004,** *69* (9).

Chapter 3

Solution-synthesized Mg Nanocrystals Doped with Ni for Hydrogen Storage: Physical Characterization, Hydrogen Sorption Kinetics, and Deconstruction of Common Kinetic Characterization Methods[iii]

3.1 Introduction

Hydrogen is an attractive fuel source because of its high energy density (142 MJ/kg for H_2 versus 47 MJ/kg for liquid hydrocarbons) and clean burning nature. It is also the most abundant element on earth, although less than 1 % is composed of molecular hydrogen (the vast majority exists as water). [1] One hurdle hindering a true hydrogen-based economy is safe, portable, compact storage with readily accessible hydrogen. In its gaseous state, molecular hydrogen takes up a large volume and is not practical for mobile storage. There are many potential candidates for storing hydrogen via both physical and chemical processes.[2] Several active areas of research include storing molecular hydrogen in high porosity materials,[3] adsorption of hydrogen on carbonaceous materials[4] and chemisorption in metal hydride systems.[5]

Light metal hydrides, in particular MgH_2, are a particularly attractive hydrogen storage material because of its high gravimetric (7.6 wt% H_2) and volumetric (110 kg H_2/m^3) capacities.[1, 6] However, bulk magnesium shows sluggish kinetics, making it an impractical candidate at reasonable temperatures (below 600 K). Recent work has taken two general approaches to improve sorption kinetics: nanostructuring the magnesium for greater surface area[6-12] and incorporating

[iii] Daniel J. Shissler, Timothy S. Arthur, Sarah J. Frederick, Nick S. Norberg, & Amy L. Prieto Timothy Arthur and Sarah Frederick contributed to the synthesis and physical characterization of the Mg nanocrystals. Timothy Arthur and Daniel Shissler equally contributed to sorption data analysis. Nick Norberg developed the Ni doped Mg nanoparticle synthesis and built the initial Sieverts Apparatus. Daniel Shissler upgraded the initial Sieverts Apparatus which was utilized for collecting sorption data presented herein.This dissertation chapter is adapted from a manuscript being submitted to *Chemistry of Materials*.

dopants[7, 12-26] for enhanced kinetics. Both of these strategies are typically accomplished by ball milling to create small crystallites and incorporate various transition metal dopants. This technique, however, does not allow for control over crystallite size or shape, and impurity phases are common byproducts. Previous reports have demonstrated the use of a variety of transition metal dopants including Ni, Ti, V, Fe, Cr, Nb and Pd.[13-23] Some transition metal oxides have also been shown to enhance kinetic performance. [7, 24-31] Nickel is a particularly intriguing candidate because it is known to be a catalyst for H-H bond dissociation [32] and Mg-Ni alloys are known hydrogen storage materials (e.g. Mg_2Ni).[33-36] It has been reported as a dopant previously, [17-19, 29, 37-38] but only in samples that were prepared via a ball milling process. As previously stated, ball milling does not allow for control over particle size, so some enhanced kinetics may be due to small crystallites. Furthermore, in this synthetic method it is possible to obtain a mixture of pure magnesium, magnesium doped with small percentages of nickel, magnesium-nickel alloys and pure nickel metal. With all of these possible products, it is difficult, if not impossible, to isolate the effect of a nickel dopant on the sample because of the number of variables in this complicated system. This chapter seeks to isolate the variable of nickel doping and analyze its effect on the hydrogen sorption kinetics of monodisperse nanocrystals of pure magnesium.

We recently reported a solution synthesis of phase-pure magnesium nanocrystals (Mg NCs) made from a low temperature, solution process with tunable crystallite sizes.[39] In addition to the advantages of controllable size and phase purity, this solution synthesis allows for the facile incorporation of a variety of dopants. Herein we present a report of enhanced kinetic performance in Mg NCs doped with small amounts (1 - 5 wt%) of nickel. Although the exact nature of the Ni and its bonding to the Mg NCs is not fully understood, the enhanced kinetics are attributed to the small percentages of dopant in the material, and no other variable, such as size or impurity phases.

3.2 Experimental

Chemicals: Magnesocene [bis(cyclopentadienyl) magnesium] was synthesized using an established preparation from reference 40.[40] Its purity was confirmed via H-1 NMR. Glyme (1,2 dimethoxyethane, anhydrous, 99.5 %) was purchased from Aldrich. It was distilled over sodium and benzophenone (Aldrich) and degassed prior to use. Phenanthrene (98 %) and nickelocene [bis(cyclopentadienyl) nickel] were purchased from Aldrich and used as received.

Synthesis of doped Mg nanocrystals: All synthesis and purification steps were performed in a nitrogen glove box. *Caution: magnesium nanocrystals are extremely reactive and ignite when exposed to oxygen*. A previously reported method was used to synthesize phase-pure magnesium nanocrystals.[39] In order to isolate the effects of nickel doping and remove variations in nanocrystal size, only medium sized (32 nm diameter) nanocrystals were made. In a typical synthesis, 0.782 grams of phenanthrene (Phen) was dissolved in 7.6 g (8.8 mL) of glyme. To this an excess of potassium metal was added (~0.2 g) and the solution turned a dark green color. This was stirred for at least 30 minutes to ensure complete dissolution of the K. This solution was then centrifuged for 15 minutes to remove unreacted potassium metal. A solution of a desired amount of nickelocene (1, 5 or 20 wt%) was dissolved in 3.5 g (4 mL) of glyme and set aside until use. Then 0.301 g of magnesocene was dissolved in 34.66 g (40 mL) of glyme and heated to 70 °C. At this temperature the K/Phen solution was added rapidly to the magnesocene under vigorous stirring conditions. The reaction flask turned black immediately. The hot plate was turned off at this point to allow for slow cooling. The nickelocene solution was then added dropwise to the magnesium nanocrystals (rapid stirring continued). This was left to cool gradually. The nanocrystals were purified by centrifugation and rinsed with clean glyme several times until the supernatant was clear. The final product was dried under vacuum and stored under inert conditions.

Materials characterization: All sample preparation steps were performed in a nitrogen glove box due to the reactive nature of the magnesium samples. X-ray diffraction samples were prepared by coating dry MgNC powder with a 5:1 mixture of glyme and mineral oil to prevent oxidation in air. XRD data were obtained on a Scintag X-2 Advanced Diffraction system equipped with Cu Kα radiation (λ = 1.54Å). TEM samples were prepared by sonicating a small amount of dried sample in glyme. Carbon-coated copper TEM grids (200 mesh, Ted Pella Inc.) were dipped into this solution three times and dried. Low magnification TEM images used for particle size analysis were obtained on a JEOL TEM 1400 at a working voltage of 100 kV. High resolution TEM images were obtained on a Philips CM200 TEM at a working voltage of 200 kV. EDX analysis was performed on the same TEM using a Princeton Gamma-Tech Prism Energy Dispersive X-ray spectrometer. X-ray photoelectron spectroscopy samples were prepared by pressing a small amount of magnesium powder onto carbon tape. This was sealed in a nitrogen-filled container until transfer to the instrument, allowing for only several seconds of air exposure. XPS data were obtained on a PE-5800 with an Al ESCA source. Data were analyzed using MultiPak software version 9.3.0.3. All spectra were shifted to carbon at 284.8 eV. A lab-built Sievert's apparatus was utilized to monitor hydrogen absorption and desorption so the cycling rates could be determined. See reference 41 for details on Sievert's apparatus.[41]

3.3 Physical Characterization of Nanocrystals

Crystalline magnesium was synthesized via the reduction of magnesocene to magnesium metal via the mechanism in Scheme 3.1. It was

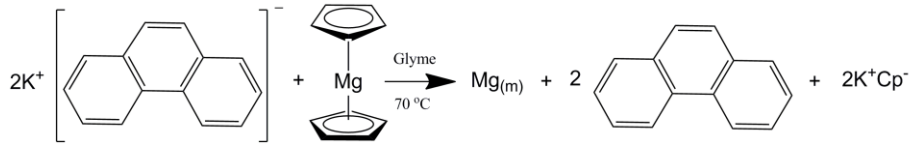

Scheme 3.1: The reaction scheme for the reduction of magnesocene to Mg(m).

presumed that the addition of nickelocene, which has an appropriate reduction potential to be reduced by the K-Phen solution, would undergo a similar reduction and produce small amounts of nickel metal on the surface of the magnesium nanocrystals. It could also form separate nickel metal (Ni(m)) nanocrystals that are not chemically bound to the Mg NCs. Although the possibility of the nickelocene being co-reduced with a small amount of unreacted magnesocene in the solution is unlikely (we presume the magnesocene is rapidly and completely reduced by the excess reducing solution), it may be possible. Mg_2Ni and $MgNi_2$ are both possible crystalline products if excess magnesocene is present when the nickelocene is added. The initial step in analyzing the reaction products for Ni-doped Mg nanocrystals was to perform powder x-ray diffraction to check for the formation of Ni(m) or Mg-Ni alloy phases. In both the doped and undoped magnesium samples, only crystalline magnesium is observed in the diffraction pattern. Figure 3.1 shows XRD patterns for both the 5 wt% and 20 wt% samples with corresponding PDFs indicating only crystalline Mg is present (nickel metal and $MgNi_2$ PDFs are plotted for reference). They have no additional peaks indicative of new crystalline phases. No Ni or Mg-Ni alloys are observed, even when the nanocrystals are doped with 20 wt% nickel. It is possible that the 1 and 5 wt% samples have insufficient Ni content and these peaks would be below the limit of detection for our diffractometer, but the 20 wt% samples would certainly give new peaks if new crystalline phases were formed. Although no

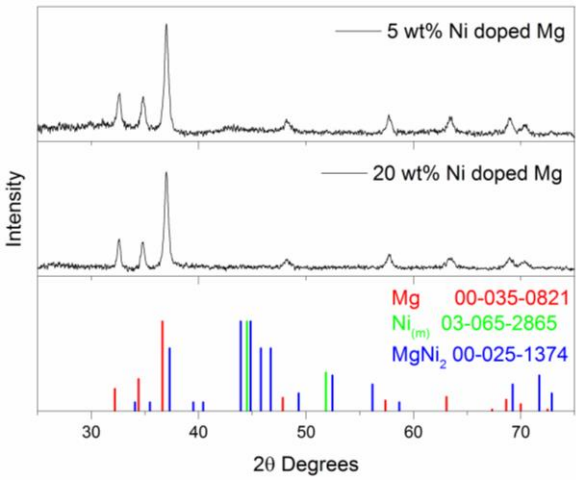

Figure 3.1: X-ray powder diffraction of 5 wt% (top) and 20 wt% (middle) Ni doping on Mg nanocrystals. Both patterns contain peaks for $Mg_{(m)}$ only, with no $Ni_{(m)}$ or Mg-Ni alloys (reference patterns in bottom panel for comparison).

crystalline nickel species are observed in the doped samples, the dramatic changes in kinetic performance (to be discussed later) suggest incorporation of nickel into the magnesium nanocrystals. If this nickel is inherently amorphous (i.e. there is no significant long-range order in the bonding), it will not be observed via XRD, but may still produce enhanced kinetics.

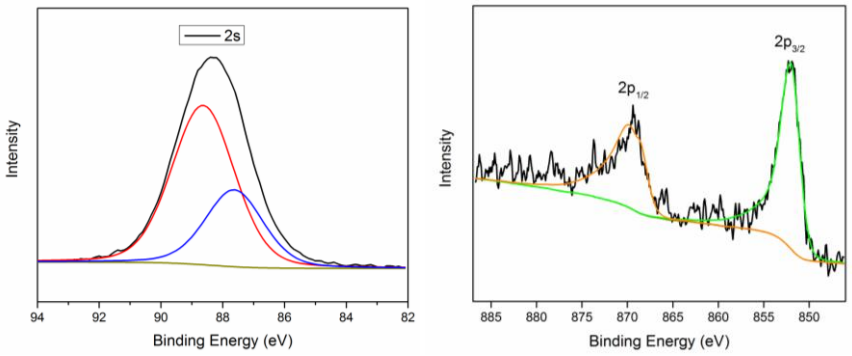

Figure 3.2: High resolution XPS spectra for a 20 wt% Ni doped Mg NC sample. The 2s Mg spectrum (left) contains both Mg (red) and MgO (blue) features as expected with air exposure. The Ni 2p region (right) has peaks for the $p_{3/2}$ and $p_{1/2}$ but they are lower than reported literature values.

To confirm the presence of Ni in the Mg NC samples, XPS was performed on pure and doped magnesium. In both the pure and doped magnesium samples, the Mg 2s spectra display two peaks; one characteristic of zero-valent magnesium at 88.64 eV[42] and the other at a slightly lower binding energy (87.6 eV) characteristic of magnesium oxide (Figure 3.2).[43] This oxidation is expected due to the fact that magnesium is highly reactive, and the sample was introduced to a small amount of oxygen for transfer to the XPS instrument (see experimental section for details). This oxide layer is not expected to affect the kinetics of hydrogenation since the hydrogenation samples were loaded in sample holders in a nitrogen atmosphere. Nickel was not observed with a reasonable signal-to-noise ratio in samples doped with 1 or 5 wt% nickel. These samples are ideal for kinetic studies, but do not allow for careful analysis of the binding environment of the nickel on the Mg NCs. Therefore, samples of a 20 wt% doping level were synthesized for the purpose of XPS analysis. We acknowledge that the 20 wt% samples may have different properties than those of the 1 – 5 wt% doping levels, but it is the closest approximation

to the samples used for hydrogenation that could be reasonably analyzed via XPS. Unlike the XRD data for the Ni-doped samples, there is an observable XPS signal for Ni that can be fit for peak positions. The $p_{3/2}$ and $p_{1/2}$ peaks at 852.0 and 868.9 eV, respectively, are near reported values for Ni metal and Mg-Ni alloys ($MgNi_2$ and Mg_2Ni). However, both peaks deviate significantly from the reported values. The Ni peaks in our samples are 0.5 – 1.0 eV lower than reported values.[44] This is a significant difference even when instrumental error is taken into account. Although we do not fully understand this discrepancy, we believe the bonding of the nickel on our magnesium samples is unlike currently known alloys. Further analysis via neutron and high energy x-ray scattering is underway to determine the bonding environment of the nickel dopants in these magnesium samples.

The size and morphology of the Mg NCs were analyzed via transmission electron microscopy in an attempt to visualize any Ni on the Mg NCs. Since Mg is an atomically light element, the contrast in TEM is very low, even for large nanocrystals (> 30 nm). Nickel, being a much heavier transition metal, should be observable if a sufficient amount of it is clustered on the Mg NCs. As can be seen in Figure 3.3, undoped and doped nanocrystals are identical via TEM.

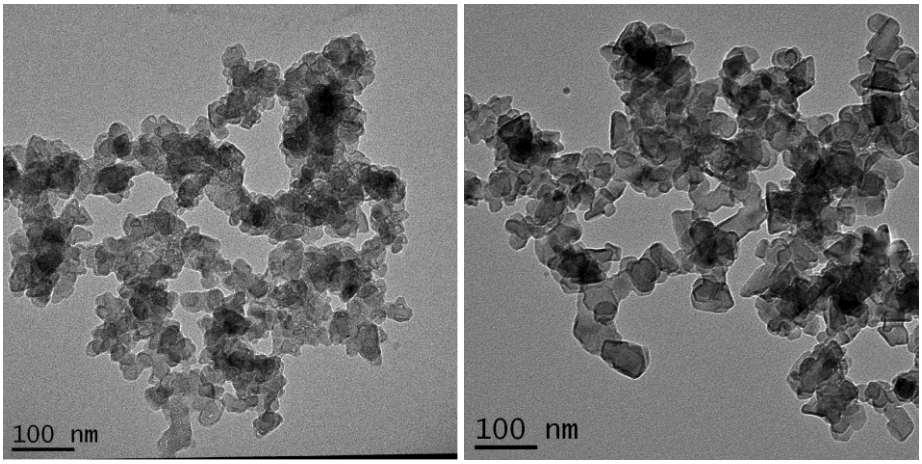

Figure 3.3: Undoped (left) and 5 wt% Ni doped (right) Mg NCs. The light contrast produced by Mg in addition to the agglomeration makes analysis of the images difficult when searching for changes due to Ni incorporation.

There are no areas of darker contrast among the particles that look significantly different. A difficulty in analyzing TEM for such information is that these particles clearly agglomerate and overlap with one another. This can cause differences in contrast, simply due to sample thickness. After analyzing many samples, it was determined that there are no significant morphological or contrast differences discernable through TEM imaging. Future studies utilizing EDS mapping may help elucidate differences between these samples.

3.4 Analysis of Sorption Kinetics

Hydrogenation and dehydrogenation kinetic studies were performed via a Sievert's apparatus on 5 wt% Ni, 1 wt% Ni, and pure Magnesium sample. Dopant levels were kept low to maximize the final H_2 wt% of the material. During the first hydrogenation cycle, the pure, undoped magnesium sample exhibits faster kinetics than that of the 1 wt% and 5 wt% samples. However, after multiple H/D cycles, the kinetic behavior of the doped and undoped materials change with opposing behavior.

After several H/D cycles, the kinetic performance of nanomaterials is expected to decrease due to the increased diffusion lengths of the hydrogen as the particles agglomerate.[22, 45-46] The pure magnesium samples behave in this fashion, however, both of the Ni doped samples exhibit an increase in H/D kinetics over multiple cycles (Figure 3.4). Both Ni doped samples exhibit faster hydrogenation than the 0 wt% Ni sample by the third cycle. The 5 wt% Ni sample exhibits the fastest H/D kinetics of the three samples after three cycles. The dehydrogenation of the 1 wt% Ni sample is still slower than the 0 wt% Ni after three cycles despite its increase in performance. The initial onset of the dehydrogenation is faster in comparison to the 0 wt% Ni sample but tapers off towards the end. The lack of Ni content may prevent the catalyst from fully incorporating into the

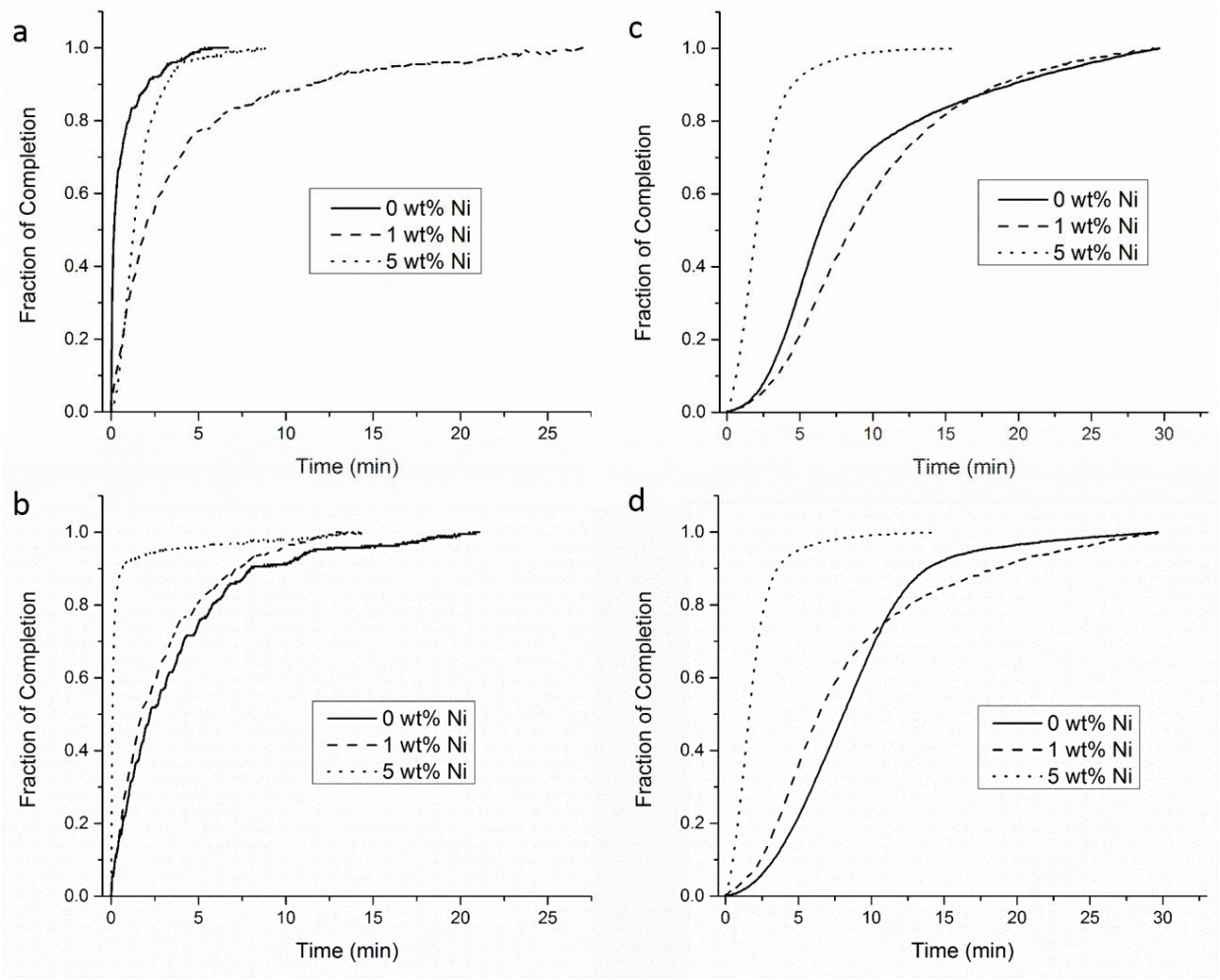

Figure 3.4: a-b) First and third hydrogenation cycles of Mg-Ni samples performed at 250°C and ~10 bar c-d) first and third dehydrogenation cycles of Mg-Ni samples performed at 325°C. Dehydrogenation graphs are a representation of dehydrogenations performed at 325°C and not the dehydrogenation of the samples hydrogenated in Figures 3.4a and 3.4b.

Mg particles. Figure 3.5 displays the same data represented in Figures 3.4c and 3.4d, but rather than the fraction of completion on the y-axis, the weight percent of hydrogen to MgH_2 is plotted. As observed the 0 wt% Ni and 1 wt% Ni samples only hydrogenated to about 4.5 wt%, as compared to the 7.6 wt% expected value. Commonly in literature, only the fractions of completion are reported since the addition of catalyst lowers the total hydrogen weight percentage of the material. However, only reporting the fraction of completion can also exaggerate the performance of the material.

It is important to include weight percentages for accurate sample comparison. In contrast to the 0 wt% Ni and the 5 wt% Ni samples, the 5 wt% sample nearly hydrogenates to the theoretical percentage of Mg. Although the weight percentages vary greatly, the data still accurately represents the differing kinetic behavior of the various materials (i.e. the faster kinetics of the 5 wt% material are apparent). Repeat samples all cycled to levels of similar weight percentages, and still shared the kinetic behavior seen here, the most important of which is the increased performance of the 5 wt% Ni sample after several cycles.

Cyclability studies have been performed on 5 wt% Ni samples (Figure S3.1). The kinetic performance stabilizes after three cycles, and no further enhancement of kinetics is seen. After five cycles, a decrease in performance is observed, which is likely due to agglomeration and oxidation of the particles. The reason for the increase in performance in the first three cycles is not yet understood. It is believed to be a unique behavior between the nickel and magnesium. It is possible that the nickel initially accumulates at concentrated sites on the magnesium nanoparticles due to the addition of the nickel after the magnesium particles have formed. Then, during the initial H/D cycles the nickel distributes evenly throughout the magnesium particles. As stated previously in XPS data, the oxidation state of the Ni is not metallic. Also, the peaks do not match that of what would be expected of any known Mg-Ni compounds. A more in depth study,

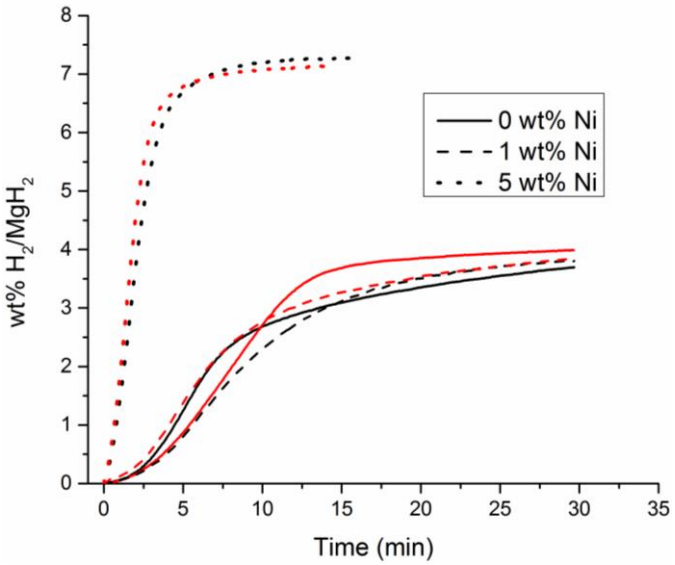

Figure 3.5: Weight percentages of the data represented in Figure 3.4c and 3.4d (dehydrogenation). The first cycle is black and third cycle is red.

including high energy X-ray and neutron scattering methods, is underway to identify the odd Mg-Ni speciation and what may be leading to the improved catalytic performance. The increased catalytic ability of the 5 wt% Ni sample over several cycles implies a different catalytic mechanism than the usual behavior of Ni. Ni is known to catalyze the dissociation of diatomic hydrogen to atomic hydrogen.[32] However, in the 5 wt% Ni samples, the rate of dehydrogenation increases more than that of the hydrogenation, implying that the nickel has a greater effect on the dehydrogenation step. If the mechanism of catalysis by the nichel was the dissociation of hydrogen, then the hydrogenation rate would be more greatly improved. Yet, this is not the case in this report. Preliminary analysis of X-ray and neutron scattering data suggests a high degree of disorder exists within the Mg matrix. The disarray may be a result of defects within the crystalline structure which may provide a pathway effect increasing the diffusion rate of hydrogen through the material.[12, 31] This coincides well with the greater increase of performance during the dehydrogenation because MgH_2 has a slower diffusion rate than that of Mg. The increased diffusion rate would have the greatest benefit to the cycle in which hydrogen diffusion is slowest.

3.5 Methods of Characterizing Sorption Kinetics

Since the catalytic nature of the Ni is not yet understood, further investigation is necessary. Understanding the behavior of the Mg and Ni system may reveal an approach not yet considered to increase the rate hydrogenation and dehydrogenation which can then be applied to other systems. To this end, calculation of activation energies for the different cycles may help improve our understanding. However, calculating the activation energies of the cycles has proven difficult due to the lack of a model that accurately represents the phase change kinetics of our Mg-Ni nanoparticles.

In order to calculate activation energies of the hydrogenation and dehydrogenation, the isothermal cycling must be fit to a model. However, kinetic models have been tailored to fit the phase changes of bulk materials and are based on several assumptions. This poses a problem for the isothermal data in this report because nanomaterials do not fit within the underlying assumptions, and the known models provide a very poor fit for our materials. The two models that are most commonly used to fit experimental data are the Contracting Volume (CV) and nucleation and growth models, better known as the Johnson-Mehl-Avrami (JMA) model[47-55]. These methods are commonly misused in literature to characterize the cycling kinetics of hydrogen storage materials. Several papers invoke the JMA model to describe the behavior of the material.[19, 22, 45, 55-60] Within their analysis, several transitional phases are identified as being essential to the improved performance of the material.[14, 19, 61] Whereas, the JMA equation is intended to model *only the transition of a single phase* to a final secondary phase. In our case, no other alternative phases are detected within the hydrogenated or dehydrogenated material. However, several other reasons can be attributed to why our data poorly fit the model.

The data collected in this study cannot be fitted with the JMA or the CV models. Martin et al states that the JMA model only fits the kinetic data from the initial point of nucleation, t_0, to the final stage of the phase change[62]. Fitting this model using a Sieverts apparatus may prove impossible because Sieverts apparatus tracks the reaction progress by measuring the pressure of hydrogen. The initial time of nucleation cannot be pinpointed since it blends with pressure drop caused by hydrogen adsorption on the surface of the nanocrystals. If the initial and final stage of the phase changes are ignored, as is done in most literature reports, one cannot claim that it fits a model of nucleation and growth.

These models are based on several assumptions and generalizations, such as, randomly distributed nucleation sites and the shape of the secondary phase growth.[47-49, 52-55] Many of the generalizations ignore surface energies and crystal defects because in bulk materials, their effects are insignificant compared to the behavior of the bulk of the material. However, on the nanoscale, due to the high surface area of the material compared to the bulk of the material, these effects can no longer be ignored and are, in fact, highly important.

The primary difference between the JMA and CV models is that they make assumptions about different phases within a reaction. The JMA model takes into consideration the behavior of the phase being formed during the reaction, whereas the CV model makes assumptions about the primary phase of the reaction.[47-49, 52-55]

The JMA model can be summarized as the nucleation of the secondary phase which then grows into a circular/spherical shape throughout the reaction. Two major assumptions made by this model are that the initial nucleation sites are randomly distributed on the surface of the primary phase and that the secondary phase grows into a spherical volume. The initial nucleation points are generalized as defect sites on the surface which would maintain a higher energy than the rest of the surface[47-49, 54]. On the bulk scale, the high-energy sites are likely randomly distributed across a polycrystalline surface. However on the nanoscale, the particles will behave as single crystalline particles with surface energies that are more dependent on the lattice of the primary phase.[63] Because of the different energies of the different crystal planes, nanoparticles may exhibit preferential nucleation on specific crystal planes or edges. Additionally, crystalline defects, step edges or twin boundaries, will possess higher energies as compared to the rest of the surface.[64] Because of these higher energies, nucleation on the nanoparticle surface is not likely to be randomly distributed, but rather will preferentially occur on higher energy surfaces. [8, 63] Since the

model assumes a highly ordered crystalline starting phase, and nanocrystals synthesizes at low temperatures are inherently disordered, the initial assumption of the JMA model no longer holds.

The JMA model also does not fully account for the overlap of the growing secondary phases. If initial nucleation sites are in close proximity, the growing spherical volumes will merge together. [54, 62] From the nature of the JMA model, the overlapping regions cause an overestimation of the growth of the secondary phase. For bulk samples, the nucleation points will be well distributed across the surface of the material. Again however, nucleation points of nanoscale particles will preferentially occur at defect sites and along lattice edges.[8, 63] This localization of the nucleation sites will cause greater overlapping of growing phases than what is predicted by the JMA model. Thus, the JMA model does not appropriately match the phase change reaction of nanoscale materials because the surface energies that are negligible for bulk materials become significant due to the reduced scale.

The poor fitting of the CV model to nanoscale materials can also be attributed to the greater surface area of the material. The CV model assumes that the entire surface of the particles will be quickly transformed to the secondary phase, forming a core-shell morphology.[52, 55] The remaining primary phase is then consumed as it is transformed into the secondary phase. In order for this to be true, there would need to be an even distribution of nucleation sites over the entire surface. However, as explained for the JMA model, the nucleation sites for nanoscale particles will be localized at crystalline defects and along lattice edges.[8, 63] This nucleation behavior does not fulfill the requirements for the transformation to fit that of the CV model. Furthermore, if the initial nucleation sites were to be evenly distributed across the surface, the model would not account for the time between the initial nucleation and the formation of the shell.[52, 55] If the time during the

formation of the shell is significant relative to the transformation process, the model does not fit well.

The CV model also assumes that the thickness of the shell is relatively thin compared to the diameter of the total volume[52, 55] and since a large percentage of the nanoparticle is composed of surface material, the initial shell is likely to be a significant portion of the particle, thus disregarding a key assumption that the CV model is based upon. The lack of models that appropriately fit the kinetic data of nanomaterials poses a problem for the field of hydrogen storage materials. Several other authors have expressed difficulty with fitting their kinetic data with a known model[57-59, 65-67] and others have attempted to find other approaches to rationalize the kinetic behavior.[8, 57, 62, 65-66, 68] A way in which materials could be more directly compared is to standardize the conditions in which the materials are studied.

3.6 Conclusion

A key goal in the research of hydrogen storage materials is not only reaching the target of 7.8 wt% H_2 but also increasing the rate at which the materials can be hydrogenated and dehydrogenated. To this end, the interest in shrinking the scale of the materials has grown. However, as previously stated, shrinking the materials to the nanoscale makes the known models inadequate for analyzing and comparing the data. In addition to this, the defined pressure restrictions covers a wide range of pressure, 5-100 bar, at which the material must be cycled. Since there is no set limit for these conditions, the materials are cycled at a variety of conditions throughout the research groups working on these materials.[14, 22, 36, 45, 59] This makes it difficult for the performance of the materials to be directly compared since the kinetic performance is dependent on what temperature and pressure at which they were cycled.[59, 67, 69] If there were models

that would appropriately fit the data, calculation of activation energies could be used to compare different kinetics performed at different conditions.

Mg nanoparticles have been successfully doped with a low percentage of Ni using a low-temperature, solution process. The kinetics show great improvement during both hydrogenation and dehydrogenation. Mysteriously the cycling rates increase after several cycles, but oddly, there is a greater increase during the dehydrogenation process. Both the improvement after cycling and the greater catalytic activity during the dehydrogenation cycle is not yet completely understood. The catalytic activity is believed to be a result of a unique Mg-Ni interaction. Characterization methods did not identify any known Mg-Ni compounds. Further work is being done to identify this unknown interaction. Calculations of activation energies could aid in characterizing the catalytic mechanism, however, due to the nanoscale nature of the material the data does not appropriately fit any known models of nucleation and growth of solid state phase transformation. Development of new models would greatly aid in the characterization and comparison of different materials in the hydrogen storage field.

References

1. Schlapbach, L.; Zuttel, A., Hydrogen-storage materials for mobile applications. *Nature* **2001,** *414* (6861), 353-358.
2. Jena, P., Materials for Hydrogen Storage: Past, Present, and Future. *Journal of Physical Chemistry Letters* **2011,** *2* (3), 206-211.
3. Rosi, N. L.; Eckert, J.; Eddaoudi, M.; Vodak, D. T.; Kim, J.; O'Keeffe, M.; Yaghi, O. M., Hydrogen Storage in Microporous Metal-Organic Frameworks. *Science* **2003,** *300* (5622), 1127-1129.
4. Hirscher, M.; Becher, M.; Haluska, M.; Dettlaff-Weglikowska, U.; Quintel, A.; Duesberg, G. S.; Choi, Y. M.; Downes, P.; Hulman, M.; Roth, S.; Stepanek, I.; Bernier, P., Hydrogen storage in sonicated carbon materials. *Appl Phys A* **2001,** *72* (2), 129-132.
5. Sakintuna, B.; Lamari-Darkrim, F.; Hirscher, M., Metal hydride materials for solid hydrogen storage: A review. *International Journal of Hydrogen Energy* **2007,** *32* (9), 1121-1140.
6. Zaluska, A.; Zaluski, L.; Strom-Olsen, J. O., Nanocrystalline magnesium for hydrogen storage. *Journal of Alloys and Compounds* **1999,** *288* (1-2), 217-225.
7. Oelerich, W.; Klassen, T.; Bormann, R., Hydrogen sorption of nanocrystalline Mg at reduced temperatures by metal-oxide catalysts. *Advanced Engineering Materials* **2001,** *3* (7), 487-490.
8. Mooij, L.; Dam, B., Hysteresis and the role of nucleation and growth in the hydrogenation of Mg nanolayers. *Physical Chemistry Chemical Physics* **2013,** *15* (8), 2782-2792.
9. Setijadi, E. J.; Boyer, C.; Aguey-Zinsou, K. F., Remarkable hydrogen storage properties for nanocrystalline MgH_2 synthesised by the hydrogenolysis of Grignard reagents. *Physical Chemistry Chemical Physics* **2012,** *14* (32), 11386-11397.
10. Zaluska, A.; Zaluski, L.; Strom-Olsen, J. O., Structure, catalysis and atomic reactions on the nano-scale: a systematic approach to metal hydrides for hydrogen storage. *Applied Physics a-Materials Science & Processing* **2001,** *72* (2), 157-165.
11. Shao, H.; Liu, T.; Wang, Y.; Xu, H.; Li, X., Preparation of Mg-based hydrogen storage materials from metal nanoparticles. *J. Alloys Compd.* **2008,** *465* (1-2), 527-533.
12. Berube, V.; Radtke, G.; Dresselhaus, M.; Chen, G., Size effects on the hydrogen storage properties of nanostructured metal hydrides: A review. *International Journal of Energy Research* **2007,** *31* (6-7), 637-663.
13. Hanada, N.; Ichikawa, T.; Fujii, H., Catalytic effect of nanoparticle 3d-transition metals on hydrogen storage properties in magnesium hydride MgH_2 prepared by mechanical milling. *Journal of Physical Chemistry B* **2005,** *109* (15), 7188-7194.
14. Liang, G.; Huot, J.; Boily, S.; Van Neste, A.; Schulz, R., Hydrogen storage properties of the mechanically milled MgH_2–V nanocomposite. *Journal of Alloys and Compounds* **1999,** *291* (1–2), 295-299.
15. Shahi, R. R.; Tiwari, A. P.; Shaz, M. A.; Srivastava, O. N., Studies on de/rehydrogenation characteristics of nanocrystalline MgH_2 co-catalyzed with Ti, Fe and Ni. *International Journal of Hydrogen Energy* **2013,** *38* (6), 2778-2784.
16. Moser, D.; Bull, D. J.; Sato, T.; Noreus, D.; Kyoi, D.; Sakai, T.; Kitamura, N.; Yusa, H.; Taniguchi, T.; Kalisvaart, W. P.; Notten, P., Structure and stability of high pressure synthesized

Mg-TM hydrides (TM = Ti, Zr, Hf, V, Nb and Ta) as possible new hydrogen rich hydrides for hydrogen storage. *Journal of Materials Chemistry* **2009,** *19* (43), 8150-8161.
17. Song, M. Y.; Kwon, S. N.; Park, H. R.; Bobet, J. L., Improvement of hydriding and dehydriding rates of Mg via addition of transition elements Ni, Fe, and Ti. *International Journal of Hydrogen Energy* **2011,** *36* (20), 12932-12938.
18. Shang, C. X.; Bououdina, M.; Song, Y.; Guo, Z. X., Mechanical alloying and electronic simulations of (MgH_2 + M) systems (M-Al, Ti, Fe, Ni, Cu and Nb) for hydrogen storage. *International Journal of Hydrogen Energy* **2004,** *29* (1), 73-80.
19. Liang, G.; Huot, J.; Boily, S.; Van Neste, A.; Schulz, R., Catalytic effect of transition metals on hydrogen sorption in nanocrystalline ball milled MgH_2-Tm (Tm=Ti, V, Mn, Fe and Ni) systems. *Journal of Alloys and Compounds* **1999,** *292* (1-2), 247-252.
20. Barkhordarian, G.; Klassen, T.; Bormann, R., Catalytic mechanism of transition-metal compounds on Mg hydrogen sorption reaction. *Journal of Physical Chemistry B* **2006,** *110* (22), 11020-11024.
21. Song, Y.; Guo, Z. X.; Yang, R., Influence of selected alloying elements on the stability of magnesium dihydride for hydrogen storage applications: A first-principles investigation. *Physical Review B* **2004,** *69* (9).
22. Lu, J.; Choi, Y. J.; Fang, Z. Z.; Sohn, H. Y.; Ronnebro, E., Hydrogenation of Nanocrystalline Mg at Room Temperature in the Presence of TiH_2. *J. Am. Chem. Soc.* **2010,** *132* (19), 6616-6617.
23. Lu, H. B.; Poh, C. K.; Zhang, L. C.; Guo, Z. P.; Yu, X. B.; Liu, H. K., Dehydrogenation characteristics of Ti- and Ni/Ti-catalyzed Mg hydrides. *Journal of Alloys and Compounds* **2009,** *481* (1–2), 152-155.
24. Sabitu, S. T.; Goudy, A. J., Dehydrogenation Kinetics and Modeling Studies of MgH_2 Enhanced by Transition Metal Oxide Catalysts Using Constant Pressure Thermodynamic Driving Forces. *Metals* **2012,** *2* (3), 219-228.
25. Oelerich, W.; Klassen, T.; Bormann, R., Metal oxides as catalysts for improved hydrogen sorption in nanocrystalline Mg-based materials. *Journal of Alloys and Compounds* **2001,** *315* (1-2), 237-242.
26. Shahi, R. R.; Yadav, T. P.; Shaz, M. A.; Srivastva, O. N., Studies on dehydrogenation characteristic of $Mg(NH_2)_2$/LiH mixture admixed with vanadium and vanadium based catalysts (V, V_2O_5 and VCl_3). *International Journal of Hydrogen Energy* **2010,** *35* (1), 238-246.
27. da Conceicao, M. O. T.; Brum, M. C.; dos Santos, D. S.; Dias, M. L., Hydrogen sorption enhancement by Nb_2O_5 and Nb catalysts combined with MgH_2. *Journal of Alloys and Compounds* **2013,** *550*, 179-184.
28. Barkhordarian, G.; Klassen, T.; Bormann, R., Fast hydrogen sorption kinetics of nanocrystalline Mg using Nb_2O_5 as catalyst. *Scripta Materialia* **2003,** *49* (3), 213-217.
29. Hanada, N.; Hirotoshi, E.; Ichikawa, T.; Akiba, E.; Fujii, H., SEM and TEM characterization of magnesium hydride catalyzed with Ni nano-particle or Nb_2O_5. *Journal of Alloys and Compounds* **2008,** *450* (1-2), 395-399.
30. Hanada, N.; Ichikawa, T.; Hino, S.; Fujii, H., Remarkable improvement of hydrogen sorption kinetics in magnesium catalyzed with Nb_2O_5. *Journal of Alloys and Compounds* **2006,** *420* (1-2), 46-49.
31. Friedrichs, O.; Sanchez-Lopez, J. C.; Lopez-Cartes, C.; Klassen, T.; Bormann, R.; Fernandez, A., Nb_2O_5 "pathway effect" on hydrogen sorption in Mg. *Journal of Physical Chemistry B* **2006,** *110* (15), 7845-7850.

32. Trasatti, S., Work function ,electronegativity, and electrochemical behavior of metals: 3. Electrolytic hydrogen evolution in acid solutions. *Journal of Electroanalytical Chemistry* **1972,** *39* (1), 163.
33. Zeng, K. J.; Klassen, T.; Oelerich, W.; Bormann, R., Thermodynamic analysis of the hydriding process of Mg-Ni alloys. *Journal of Alloys and Compounds* **1999,** *283* (1-2), 213-224.
34. Zou, J.; Sun, H.; Zeng, X.; Ji, G.; Ding, W., Preparation and hydrogen storage properties of Mg-rich Mg-Ni ultrafine particles. *J. Nanomater.* **2012**, 592147, 8.
35. Liang, G.; Boily, S.; Huot, J.; Van Neste, A.; Schulz, R., Mechanical alloying and hydrogen absorption properties of the Mg-Ni system. *Journal of Alloys and Compounds* **1998,** *267* (1-2), 302-306.
36. Cermak, J.; Kral, L., Improvement of hydrogen storage characteristics of Mg/Mg_2Ni by alloying: Beneficial effect of In. *Journal of Power Sources* **2012,** *214*, 208-215.
37. Xie, L.; Liu, Y.; Zhang, X.; Qu, J.; Wang, Y.; Li, X., Catalytic effect of Ni nanoparticles on the desorption kinetics of MgH_2 nanoparticles. *J. Alloys Compd.* **2009,** *482* (1-2), 388-392.
38. Varin, R. A.; Czujko, T.; Wasmund, E. B.; Wronski, Z. S., Catalytic effects of various forms of nickel on the synthesis rate and hydrogen desorption properties of nanocrystalline magnesium hydride (MgH_2) synthesized by controlled reactive mechanical milling (CRMM). *J. Alloys Compd.* **2007,** *432* (1-2), 217-231.
39. Norberg, N. S.; Arthur, T. S.; Fredrick, S. J.; Prieto, A. L., Size-Dependent Hydrogen Storage Properties of Mg Nanocrystals Prepared from Solution. *Journal of the American Chemical Society* **2011,** *133* (28), 10679-10681.
40. Wakefield, B. J., *Organomagnesium methods in organic synthesis*. Academic Press: London, 1995.
41. Blach, T. P.; Gray, E. M., Sieverts apparatus and methodology for accurate determination of hydrogen uptake by light-atom hosts. *Journal of Alloys and Compounds* **2007,** *446–447*, 692-697.
42. Jennison, D. R.; Weightman, P.; Hannah, P.; Davies, M., Calculations of Mg atom metal XPS and auger shifts using a Delts-SCF excited atom model. *Journal of Physics C-Solid State Physics* **1984,** *17* (20), 3701-3710.
43. Vasquez, R. P., MgO(100) by XPS. *Surf. Sci. Spectra* **1993,** *2* (1), 13-19.
44. Hillebrecht, F. U.; Fuggle, J. C.; Bennett, P. A.; Zolnierek, Z.; Freiburg, C., Electonic-structure of Ni and Pd alloys: 2. X-RAY photoelectron core-level spectra. *Physical Review B* **1983,** *27* (4), 2179-2193.
45. Montone, A.; Aurora, A.; Gattia, D. M.; Antisari, M. V., Microstructural and Kinetic Evolution of Fe Doped MgH_2 during H_2 Cycling. *Catalysts* **2012,** *2* (3), 400-411.
46. Friedrichs, O.; Aguey-Zinsou, F.; Fernandez, J. R. A.; Sanchez-Lopez, J. C.; Justo, A.; Klassen, T.; Bormann, R.; Fernandez, A., MgH_2 with Nb_2O_5 as additive, for hydrogen storage: Chemical, structural and kinetic behavior with heating. *Acta Materialia* **2006,** *54* (1), 105-110.
47. Avrami, M., Kinetics of Phase Change. I General Theory. *The Journal of Chemical Physics* **1939,** *7* (12), 1103-1112.
48. Avrami, M., Granulation, Phase Change, and Microstructure Kinetics of Phase Change. III. *The Journal of Chemical Physics* **1941,** *9* (2), 177-184.
49. Avrami, M., Kinetics of Phase Change. II Transformation-Time Relations for Random Distribution of Nuclei. *The Journal of Chemical Physics* **1940,** *8* (2), 212-224.

50. Johnson, W. A.; Mehl, R. F., Reaction kinetics in processes of nucleation and growth. *Transactions of the American Institute of Mining and Metallurgical Engineers* **1939,** *135*, 416-442.
51. Tomkins, P. W. M. J. a. F. C., *Chemistry of the Solid State*. Butterworths: London, 1955.
52. Mintz, M. H.; Zeiri, Y., Hydriding kinetics of powders. *Journal of Alloys and Compounds* **1995,** *216* (2), 159-175.
53. Mintz, M. H.; Bloch, J., Evaluation of the kinetics and mechanisms of hybriding reactions. *Progress in Solid State Chemistry* **1985,** *16* (3), 163-194.
54. Fanfoni, M.; Tomellini, M., The Johnson-Mehl-Avrami-Kolmogorov model: A brief review. *Nuovo Cimento Della Societa Italiana Di Fisica D-Condensed Matter Atomic Molecular and Chemical Physics Fluids Plasmas Biophysics* **1998,** *20* (7-8), 1171-1182.
55. Barkhordarian, G.; Klassen, T.; Bormann, R., Kinetic investigation of the effect of milling time on the hydrogen sorption reaction of magnesium catalyzed with different Nb_2O_5 contents. *Journal of Alloys and Compounds* **2006,** *407* (1-2), 249-255.
56. Karty, A.; Grunzweiggenossar, J.; Rudman, P. S., Hydriding and dehydriding kinetics of Mg in a Mg-Mg_2Cu eutectic alloyt – pressure sweep method. *Journal of Applied Physics* **1979,** *50* (11), 7200-7209.
57. Dill, E. D.; Josey, A. A.; Folmer, J. C. W.; Hou, F. E.; Martin, J. D., Experimental Determination of the Crystallization Phase-Boundary Velocity in the Halozeotype CZX-1. *Chemistry of Materials* **2013,** *25* (20), 3932-3940.
58. Stander, C. M., Kinetics of decomposition of magnesium hydride. *Journal of Inorganic & Nuclear Chemistry* **1977,** *39* (2), 221-223.
59. Fernandez, J. F.; Sanchez, C. R., Rate determining step in the absorption and desorption of hydrogen by magnesium. *Journal of Alloys and Compounds* **2002,** *340* (1-2), 189-198.
60. Liang, G.; Huot, J.; Boily, S.; Schulz, R., Hydrogen desorption kinetics of a mechanically milled MgH_2 +5at.%V nanocomposite. *Journal of Alloys and Compounds* **2000,** *305* (1-2), 239-245.
61. Liu, Y. N.; Zou, J. X.; Zeng, X. Q.; Wu, X. M.; Li, D. J.; Ding, W. J., Hydrogen Storage Properties of a Mg-Ni Nanocomposite Coprecipitated from Solution. *Journal of Physical Chemistry C* **2014,** *118* (32), 18401-18411.
62. Dill, E. D.; Folmer, J. C. W.; Martin, J. D., Crystal Growth Simulations To Establish Physically Relevant Kinetic Parameters from the Empirical Kolmogorov-Johnson-Mehl-Avrami Model. *Chemistry of Materials* **2013,** *25* (20), 3941-3951.
63. Zhdanov, V. P., Avrami-Kolmogorov-Johnson-Mehl Kinetics for Nanoparticles. *Surface Review and Letters* **2008,** *15* (5), 605-612.
64. Dick, K. A., A review of nanowire growth promoted by alloys and non-alloying elements with emphasis on Au-assisted III-V nanowires. *Progress in Crystal Growth and Characterization of Materials* **2008,** *54* (3-4), 138-173.
65. Martin, M.; Gommel, C.; Borkhart, C.; Fromm, E., Absorption and desorption kinetics of hydrogen storage alloys. *Journal of Alloys and Compounds* **1996,** *238* (1-2), 193-201.
66. Weinberg, M. C.; Birnie Iii, D. P.; Shneidman, V. A., Crystallization kinetics and the JMAK equation. *Journal of Non-Crystalline Solids* **1997,** *219*, 89-99.
67. Karty, A.; Grunzweig-Genossar, J.; Rudman, P. S., Hydriding and dehydriding kinetics of Mg in a Mg/Mg_2Cu eutectic alloy: Pressure sweep method. *Journal of Applied Physics* **1979,** *50* (11), 7200-7209.

68. Čermák, J.; Král, L., Hydrogen diffusion in Mg–H and Mg–Ni–H alloys. *Acta Materialia* **2008,** *56* (12), 2677-2686.
69. Ron, M., The normalized pressure dependence method for the evaluation of kinetic rates of metal hydride formation/decomposition. *Journal of Alloys and Compounds* **1999,** *283* (1-2), 178-191.

Supporting information for:

Solution-synthesized Mg Nanocrystals Doped with Ni for Hydrogen Storage: Physical Characterization, Hydrogen Sorption Kinetics, and Deconstruction of Common Kinetic Characterization Methods

Daniel J. Shissler, Timothy S. Arthur, Sarah J. Frederick, Nick S. Norberg, & Amy L. Prieto

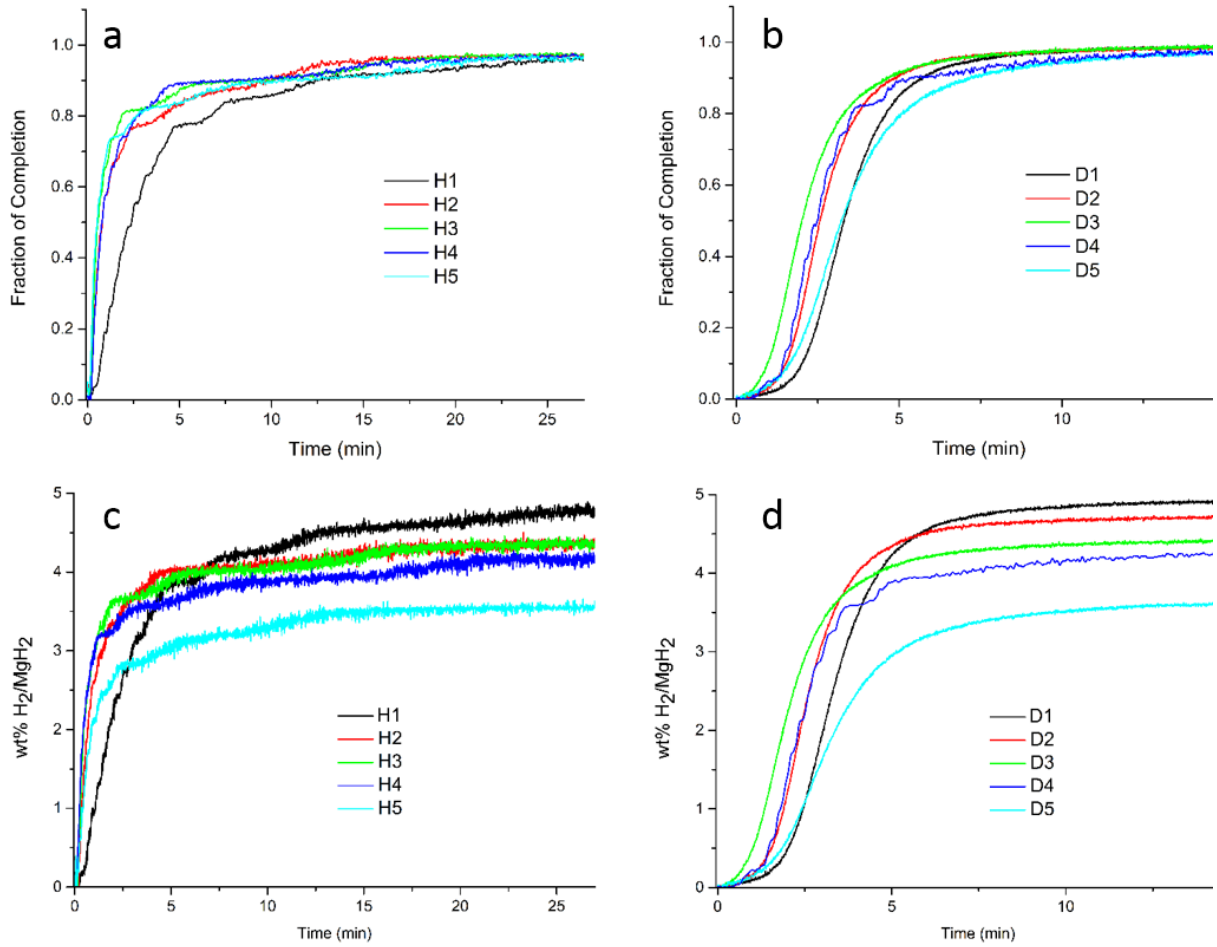

Figure S3.1: a-b) Fraction of completion graphs of H/D cycling studies,respectively, of 5%Ni Mg nanoparticles. c-d) Correlating H_2 wt% data of a-b. Low pressure gauge failed during 4th dehydrogenation so the high pressure gauge was used to record pressure. This run and fraction of completion hydrogenation cycles have been smoothed using FFT. Plots of wt% hydrogenation runs left unfiltered to show noise. Steps in readings are due to the sensitivity of the high pressure gauge.

PART II: CHARACTERIZATION AND GROWTH OF BRANCHED SILICON NANOWIRES GROWN VIA A SIMULTANEOUS VAPOR-LIQUID-SOLID AND VAPOR-SOLID-SOLID MECHANISM

Chapter 4

Nanowire Synthesis with Controllable Three-Dimensional Branching: Simultaneous Incorporation of Vapor-Liquid-Solid and Vapor-Solid-Solid Growth[iv]

4.1 Introduction

The study of nanoscale materials, such as nanoparticles,[1] carbon nanotubes,[2] and nanowires,[3] has led to an explosion of research due to the new properties that emerge as a function of reduced size[4] as well as ultra high surface area.[5] These studies have led to various ideas for technologies based on these size-dependent properties.[6-7] New technology is predicated, however, on the ability to rationally design synthetic methods with control over the size, morphology, and spatial location−1D, 2D, and 3D−of the desired product. A tool that has proven to be extremely useful for the synthesis of high-quality nanoscale materials is chemical vapor deposition (CVD) in conjunction with catalyst-assisted growth mechanisms. One way to exert partial control over the size and chemical composition of the final product is to use catalyst particles as a preferred deposition site resulting in the nucleation and growth of nanowires by the vapor-liquid-solid (VLS) and vapor-solid-solid (VSS) growth mechanisms.[8] Wagner and Ellis first proposed the VLS growth concept by utilizing a liquid gold droplet to dissolve a gaseous silicon precursor thereby initiating whisker growth.[9] Approximately three decades later, Morales and Lieber established the versatility of this synthesis route by demonstrating that catalyst materials and wire growth

---

[iv] Daniel J. Shissler, Derek C. Johnson, Beth S. Guiton, & Amy L. Prieto.
Derek Johnson and Daniel Shissler contributed equally to the synthesis of the branched silion nanowires. Beth Guiton and Derek Johnson contributed to the physical characterization of the branched silicon nanowires. Beth Guiton performed HI-Res TEM imaging, EELS, and EDX analysis.This section is an adaptation from a manuscript being submitted to the *Journal of Materials Chemistry A*.

conditions could be predicted from phase diagrams.[10] The use of phase diagrams to tune the solubility of gaseous precursors in catalyst particles has increased the level of rationality to CVD growth of nanowires by exerting finer control over the morphology and composition of the final products.

As the rationality has improved, the utilization of the VLS method has increased, resulting in numerous nanoscale materials and devices.[11-12] Using this method a plethora of examples including nanowire superlattices, [3] core-shell structures, [13-14] and doped materials [15-16] have been synthesized. The next critical step in the evolution of this synthetic method is the ability to add higher order functionality to 1D wires, i.e. adding branches. With respect to branched nanowires synthesized using a catalyst nanoparticle to initiate growth, examples have been reported in the literature using a single catalyst-assisted mechanism such as VLS [17-19] or solid-liquid-solid (SLS) growth.[20] These examples, however, all required multiple steps. The first reported example utilized a two-step process in which the Si trunk of the branched nanowire was synthesized using the VLS growth mechanism with Au as the catalyst and silane as the gas-phase precursor.[19] After the trunks were synthesized, Au nanoparticles of equal or smaller diameters were deposited from solution onto the trunks to serve as preferred deposition sites to initiate VLS growth of the branches, which were also silicon. A slight variation to this two-step approach was undertaken by Dick et al. where gallium phosphide trunks were grown using the VLS mechanism with Au serving as the catalyst.[17] Instead of using a solution-based process to subsequently seed the trunks for the second step, Au nanoparticles were aerosolized and deposited onto the trunks. The second VLS growth phase was then initiated resulting in branching. In addition, slight variations of the two aforementioned synthesis procedures have also be recently reported.[18, 20-23]

We, however, endeavor to develop a single-step process to synthesize branched nanowires; thereby eliminating post treatment and a second growth step. To the authors' knowledge, this is the first report of a single-step process for which a combination of catalyst-assisted growth mechanisms, VLS and VSS, have been employed simultaneously. The simultaneous implementation of both growth mechanisms allows one to exercise a level of control over the final branched nanowire by controlling independent reaction parameters such as gas phase precursor concentrations, VLS catalyst loading, and VLS catalyst diameter. Transmission electron microscopy (TEM), scanning electron microscopy (SEM), elemental analysis, computational fluid dynamics (CFD), and binary phase diagrams are used to explain the branched nanowire growth and thus validate the proposed mechanism.

4.2 Experimental

The synthesis of branched nanowires utilizing a 2.54 cm diameter horizontal CVD reactor is reported. Copper powder (Aldrich, 99.5% ≤ 425 μm) was pulverized with a mortar and pestle and used as the precursor solid. The growth substrate consisted of a n-type Si(100) substrate with 30 nm Au colloids (Ted Pella) weakly bound to the surface using poly-L-lysine (0.1% w/v aqueous, Ted Pella). After the Si substrate was cleaned thoroughly, poly-L-lysine was applied for 2 min and then thoroughly rinsed with Millipore® water and subsequently dried. The 30 nm Au colloid solution was then applied for 60 min to ensure a high density of Au particles on the surface of the substrate, which was also the source of Si for nanowire growth. To determine the growth substrate location, a CFD algorithm developed by Johnson et al. was utilized, for which the grid is contained in Figure S4.1.[24] Based on the CFD results contained in Figure S4.1, the growth substrates were placed between 100 mm and 175 mm downstream from the center of the furnace.

The carrier gas consisted of ultra high purity (UHP) Ar and UHP H_2 and was deoxygenated by passing the gas stream through columns containing BASF Puristar® Catalyst at flow rates of 70 sccm and 30 sccm, respectively. It is important to note that the H_2 partial pressure, while not accounted for in the mechanism, plays an important role in the branched reaction for this system (Au-Cu-Si). The H_2 helps promote the appropriate sublimation rates of both the Si and Cu. However, if the H_2 partial pressure is too high, the sublimation rate of Si overwhelms that of Cu thereby suppressing the formation of the branched nanowires. The base pressure of the reactor was held constant by an electronic control value at 50 torr.

4.3 Nanowire Characterization

Transmission electron microscopy (TEM) images were obtained using a JEOL JEM-2000 transmission electron microscope operating under an accelerating voltage of 160 kV. STEM images were obtained using a Hitachi HF-3300 FEG-TEM/STEM (ORNL SHaRE facility) operating at 300 kV, and a VG Microscopes HB501 UX STEM with Nion aberration corrector, operating at 100 kV. High spatial resolution energy-dispersive X-ray spectroscopy (EDS) data were collected on the Hitachi HF-3300 FEGTEM/STEM operated in bright field scanning mode, and electron energy loss spectroscopy (EELS) mapping was performed on the VG Microscopes HB501 UX STEM. The TEM samples were created by gently sonicating the nanowires from the growth substrate into 2-propanol (Sigma Aldrich, 99.5% anhydrous) and adding the solution, drop wise, to a copper or nickel TEM grid with a lacey carbon coating. Scanning electron microscopy images (SEM) and EDS spectra were collected using a JEOL JSM-6500F equipped with a Thermo Electron energy-dispersive spectroscopy detector with an applied voltage of 15 kV.

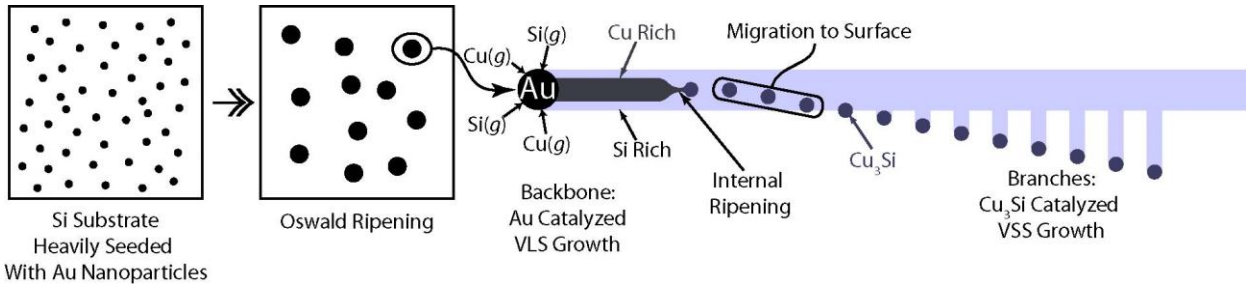

Figure 4.1: Proposed branched mechanism utilizing simultaneous VLS and VSS catalyst-assisted growth mechanisms with Au-Cu-Si as the model system. After the heavily Au (30 nm) seeded Si(100) substrate is heated to the desired growth temperature, the Au nanoparticles agglomerate through Oswald ripening to form larger preferred deposition sites for gas phase Si and Cu species. The Au catalyzes the VLS growth of the backbone nanowire while the Cu forms Cu_3Si, which catalyzes the VSS growth of the branched nanowires.

4.4 Results and Discussion

Our proposed mechanism, outlined in Figure 4.1, is a vapor transport process that allows branched nanowires to be synthesized with control over the trunk and branch compositions and diameter as well as branch spacing and length. First, a suitable vapor-liquid-solid (VLS) catalyst for the desired nanowire composition is chosen and subsequently deposited onto a growth substrate. To control the spatial location of the nanostructure, templates or traditional lithography techniques can be used. Next, an element that is soluble in the VLS catalyst and behaves as a type C catalyst, that is a catalyst material that can thermodynamically initiate VLS and VSS growth[8], is selected. Lastly, the binary phase diagrams of the elements of interest are examined to ascertain the appropriate temperature and growth position within the CVD reactor that promotes both catalyst-assisted growth mechanisms. To test the proposed mechanism, the Au-Cu-Si system was chosen where Au is the VLS catalyst, Si is the desired nanowire constituent, and Cu is the basis for the VSS catalyst because it meets the aforementioned requirements and has been heavily studied for semiconducting applications.

In addition to the aforementioned thermodynamic requirements, Cu demonstrates behaviors in Si which are distinct when compared to other 3d transition metals. These behaviors

are kinetically advantageous when considering the proposed mechanism and thus provide an additional rationale for choosing this ternary elemental system (Au-Cu-Si) to study the proposed branched nanowire growth mechanism. Because of its small ionic radius and weak interaction with the Si lattice, Cu has an unusually high diffusivity in Si; even at room temperature.[25] Additionally, the high solubility of Cu in Si results in a copper-rich silicide that is stable even though the silicide has a much larger cell volume than Si. [26-27] The cell volume mismatch is utilized in the proposed mechanism as the copper silicide impurity, while stable, has been shown to quickly diffuse out to the Si surface at temperatures greater than 400 °C.[28] It should be noted that this behavior and stability is primarily observed in n-type Si, hence the use of n-type Si as both the growth substrate and Si source. Since it has been shown that copper silicide is stable and is expelled from the Si lattice to the surface, it stands to reason that if Cu can be incorporated into a Si nanowire through the VLS catalyst, the silicide will form and diffuse to the nanowire surface. Once expelled to the Si surface, the silicide can initiate VSS growth.

The initial thermodynamic requirements for successful branched nanowire growth can be determined for a given system by examining the corresponding phase diagrams. Figure 4.2a and b

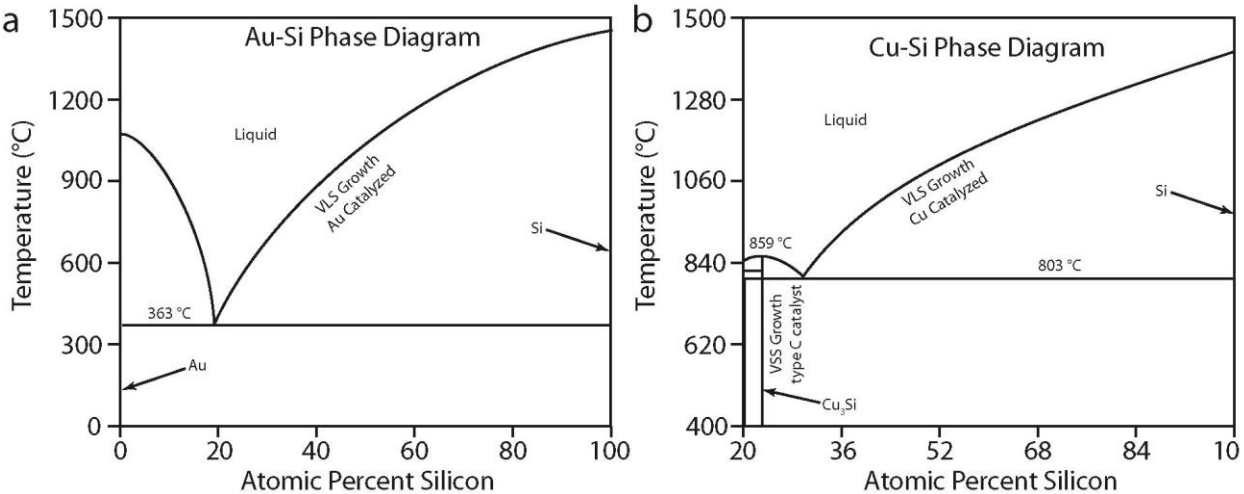

Figure 4.2: Phase diagrams adapted from reference 29 used to determine the growth position for the model Au-Cu-Si system. (a) Au-Si binary phase diagram for the entire composition range.1 (b) Cu-Si binary phase diagram from 20 to 100 atomic percent Si.

contains the binary phase diagrams for Au-Si and Cu-Si, respectively.[29] As illustrated by the Au-Si phase diagram in Figure 4.2a, the Au initiated VLS growth of Si temperature range spans from approximately 360 °C to over 1200 °C. Thus, a temperature that falls between 360 °C and 1200 °C which results in the formation of a copper silicide that thermodynamically can initiate VSS growth of Si branches, must be determined. Based on Figure 4.2b, these conditions are satisfied at approximately 800 °C. To determine the growth substrate location, the data contained in Figure S4.1[24] was used to determine the temperature as a function of location within our CVD reactor. Using the above described experimental conditions branched nanowires were synthesized and subsequently characterized to evaluate the proposed mechanism.

Figure 4.3 contains characteristic SEM images of the branched nanowire growth illustrating that the backbone can grow to lengths on the order of 100 μm. In addition to the length, the image contained in Figure 4.3a also shows the presence of a catalyst tip with a diameter larger than that of the nanowire; a characteristic feature of VLS growth. Figures 4.3b and c are higher magnification images that demonstrate the relatively uniform branch nanowire diameter, which is controlled by the VSS catalyst, and spacing between the branches. The images also clearly show the characteristic VSS catalyst tip at the end of the branches, as the catalyst diameter is identical to that of the wire. To highlight the uniformity of the branching structure, an ADF STEM image illustrating a consistent VSS catalyst particle diameter of approximately 60 nm and a particle spacing of approximately 150 nm is contained in Figure 4.4a. Once the Cu gas phase precursor is depleted however, the formation of the VSS catalysts ceases. This is demonstrated by the TEM image in Figure 4.4b which shows a gap of approximately 2 μm between the catalyst tip of the backbone nanowire and the closest VSS catalyst nanoparticle. Another feature to note from the image contained in Figure 4.3a is that the growth rate of the branches is much slower than that of

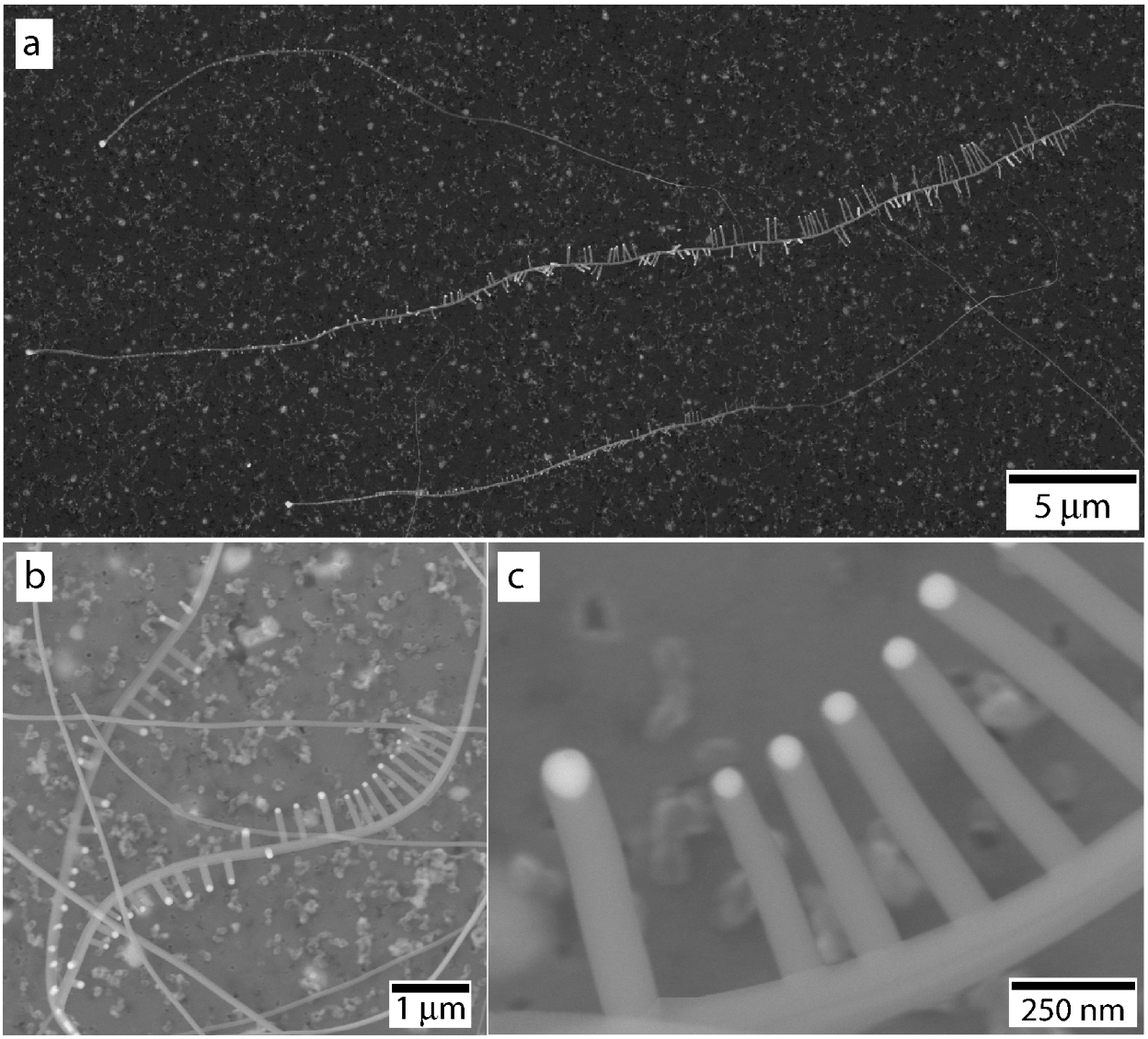

Figure 4.3: Characteristic low and high magnification SEM images of the branched nanowires. (a) Demonstrates the high aspect ratio of the backbone nanowire with lengths on the order of 100 µm and the low aspect ratio of the branched nanowires, suggesting different growth rates and thus different growth mechanisms. The characteristic catalyst tips for both the backbone and branches can clearly be seen. (b) Illustrates the finger-like morphology of the branches, the consistent VSS catalyst diameter, and relatively consistent spacing between the branches. (c) Shows the faceted nature of the backbone nanowire. The image also reveals that the branched wire diameters are exactly that of the catalyst tip, which is indicative of VSS growth.

the backbone nanowire; another indication that the backbone growth is VLS catalyzed while the branch growth is VSS catalyzed.[8] In addition to the low density growth region illustrated by Figure 4.3a, higher density growth regions were also observed as demonstrated by Figure S4.2. The nanowires shown in Figure S4.2 were synthesized at a slightly lower temperature than those

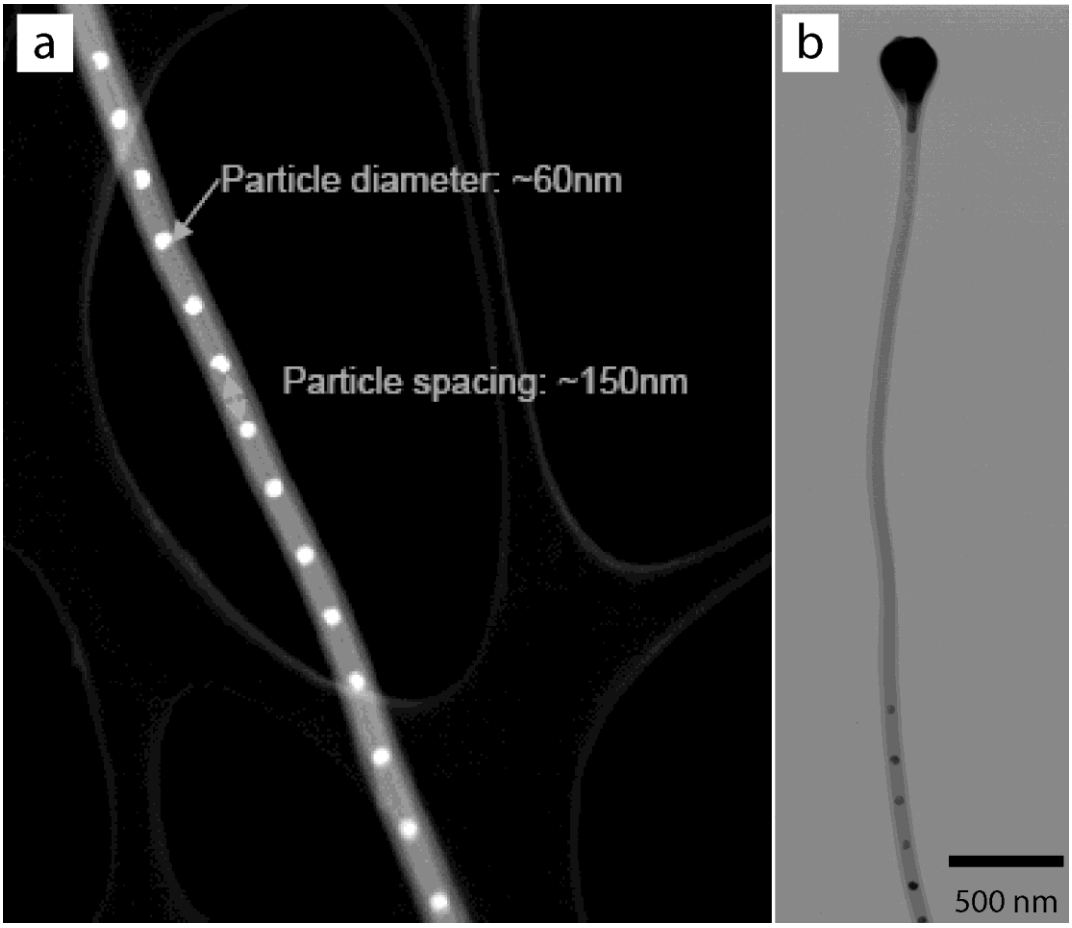

Figure 4.4: Characteristic STEM images that focus on the VSS catalyst particles. (a) Annular dark field image illustrates the consistent nature of the VSS catalyst particle diameter and spacing between particles with values of approximately 60 nm and 150 nm, respectively. (b) Bright field image demonstrates the effect on the formation of the VSS particles when sufficient gas phase Cu is not available, i.e. the backbone continues to grow without the formation of the catalyst particles.

contained in Figure 4.3. The lower growth temperature is more consistent with that predicted by the phase diagrams to promote branching. To confirm the proposed mechanism, an elemental analysis of the catalyst tips, backbone, and branches was performed.

A combination of EELS and EDS was used to determine the spatial location and relative atomic amounts of Au, Cu, and Si within the branch nanowire structure. Figure 4.5 contains EDS elemental mapping with the corresponding bright field STEM image of a branched nanowire. As illustrated in Figure 4.5, panels (a) through (e), the VLS catalyst tip at the end of the backbone contains a combination of Au and Cu with Si and O being confined to the perimeter.

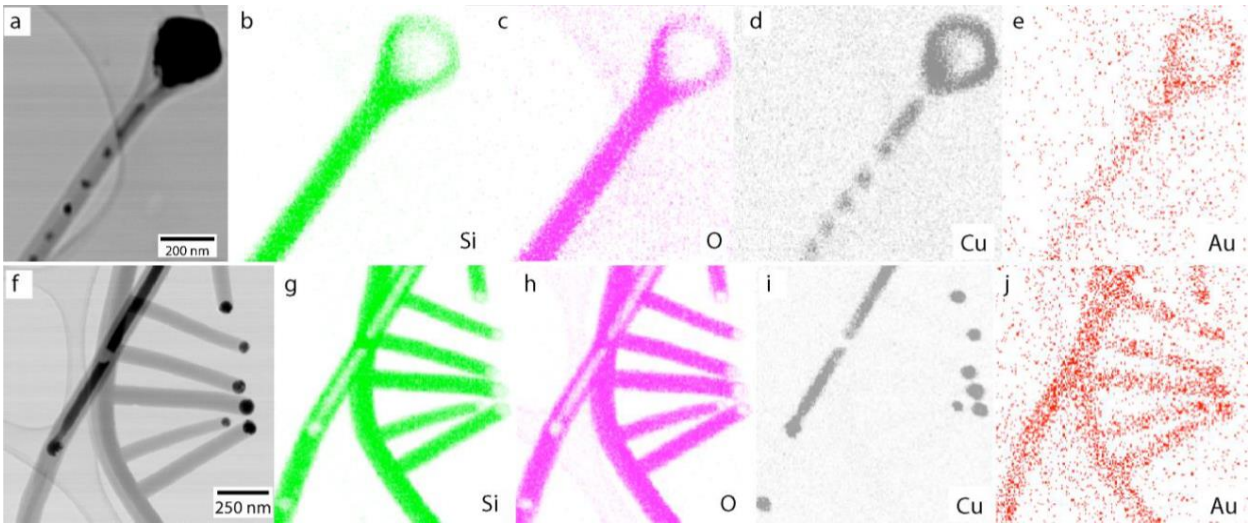

Figure 4.5: Bright field STEM images with corresponding EDS elemental maps. (a) STEM image of the backbone catalyst with VSS catalyst particles as well as the corresponding spatial maps of (b) silicon, (c) oxygen, (d) copper, and (e) gold. (f) STEM image of the backbone with a VSS catalyst particle being "pinched" off the internal feed stream as well as branches with VSS catalyst tips at the end of the nanowire. Corresponding spatial elemental maps are shown for (g) silicon, (h) oxygen, (i) copper, and (j) gold.

An EDS signal was not collected from the catalyst center most likely due to beam attenuation. However, it is expected that Au is concentrated in the center of the catalyst with a smaller amount of Cu and an equilibrium concentration of Si. This is consistent with the additional EDS and EELS analyses contained in Figure S4.3. Figure S4.3 contains a characteristic SEM image of the catalyst tip, Cu-Si rich EDS spatial phase map, and Au rich EDS spatial phase map in panels a through c, respectively. This data demonstrates the presence of all three elements and a concentration of Au in the center of the VLS catalyst. In addition, EELS spatial elemental maps contained in Figure S4.3, panels (d) through (g), provides high spatial resolution within the VLS tip for Cu, Si, and O. The enhanced spatial resolution illustrates the presence of high concentrations of Cu and Si along the periphery of the VLS catalyst and in the portion that protrudes into the backbone. However, regions of the VLS catalyst core cannot be accounted for with just Cu and Si and thus must be Au as suggested by the EDS data.

With respect to the nanowire backbone, EELS analysis suggests that Si is in the 4^+ oxidation state and that the relative atomic ratio of Si:O is 1:2. While the backbone is facetted,

which suggest structural order and thus a degree of crystallinity, further analysis has shown the backbone to be amorphous. This can be explained by the fact that Au, Cu, and Cu_3Si have been shown to catalyze the room temperature oxidation of Si to SiO_2 with thicknesses on the order of 1 μm. [30-33] As shown in Figures 4.5e and j, there is an observable presence of Au through the branched structure and dopant level equilibrium concentrations of Cu and Cu_3Si.[34] Thus, we postulate that the growth of the branched nanowires at high temperature results in crystalline Si, which is quickly oxidized once exposed to air at room temperature. Additionally, this mechanism can be used to explain the oxidation of the branches to SiO_2. Like the backbone nanowire, the oxidation of the branches is based on data from the characteristic Si4+ EELS edge in these regions. Even though the branches have undergone post-synthesis oxidation, the VSS catalyst particles are unaffected and remain crystalline. With respect to the VSS catalyst particles, Figure 4.5i shows that Cu is mostly confined to the internal VSS catalyst feed stream in the backbone and at the end of the branches. To confirm that the Cu species detected by EDS is Cu_3Si as suggested by the binary phase diagram contained in Figure 4.2, EELS elemental maps were used to provide high spatial resolution of the VSS catalyst particle for Cu, Si, and O. Figure S4.4a contains a STEM image of the VSS catalyst with corresponding spatial information for Cu, Si, and O contained in panels (b) through (d), respectively. It is clear that Cu is confined to the catalyst, O is not detected within the catalyst, and Si is observed throughout the branch. Additionally, unlike the Si4+ EELS edge observed in the backbone, the Si edge within the particle is characteristic of Si in the zeroth oxidation state, suggesting that the VSS catalyst is Cu_3Si. The ratio of Cu:Si has also been determined by EELS to be approximately 3:1; further confirming the presence of Cu_3Si and not metallic Cu. Now that compositional information regarding the major components of the branched wire has been ascertained, the mechanism is supported with the aid of Figure 4.6.

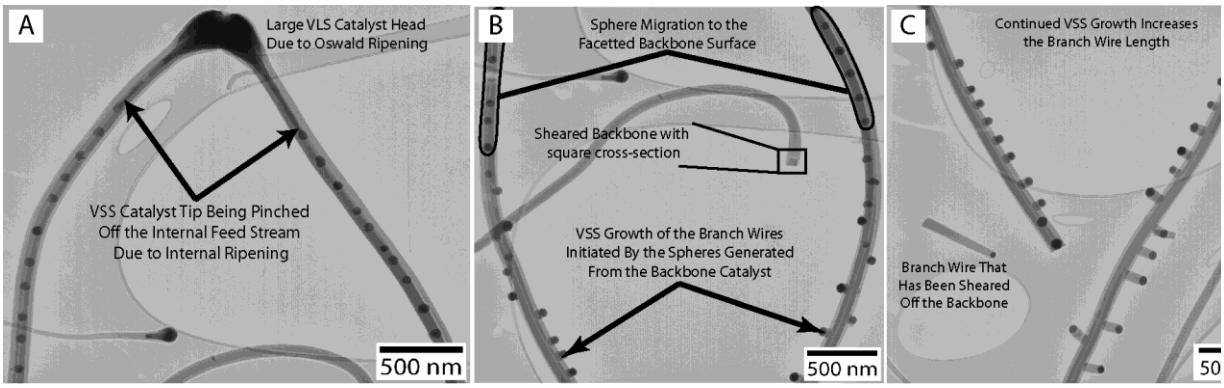

Figure 4.6: Characteristic TEM images of branch nanowire growth which visually supports the mechanism proposed in Figure 4.1. (a) Two backbone VLS catalyst tips that have merged. In addition to Si being extruded from the catalyst tip when supersaturated, a copper rich stream is also expelled resulting in the formation of spherical catalyst for VSS growth. (b) Illustrates sphere migration from the center of the backbone to the surface, thereby exposing the Cu_3Si to gas phase reactants. Initiation of VSS catalyzed branch nanowire growth is also shown. (c) Demonstrates the continued growth of the branched nanowire suggesting that both backbone length and branched length can be controlled by growth time and availability of gas phase precursors.

Figure 4.6 contains characteristic TEM images that provide a "snap-shot" in time of the branch nanowire growth process. These images highlight the important aspects of the mechanism proposed in Figure 4.1. Initially, the large VLS catalyst, which can be attributed to Ostwald ripening, can be observed in Figure 4.6a extruding both the material for the facetted backbone, which is Si during growth, and an internal feed stream of material for the VSS catalyst. Due to internal ripening, catalyst particles with a diameter of approximately 60 nm are "pinched" from the internal feed stream creating a peapod like structure. This is clearly illustrated in Figure 4.6a. When separated from the internal feed stream, diffusion of the catalyst spheres from the nanowire backbone core to the surface occurs readily because of the large relative molecular volume of Cu_3Si (46 Å3) when compared to Si (20 Å3).[35] This diffusion process from the core to the surface is depicted in Figure 4.6b. The Cu_3Si catalysts extrude preferentially to the crystal orientation of the backbone nanowire and rest on preferential crystalline facets on the surface. Once the Cu_3Si catalyst migrates to the facetted backbone surface and is exposed to a gas phase Si precursor, the VSS catalyzed growth of the branch nanowire commences as shown in Figure 4.6b. Proceeding

further down the facetted backbone away from the VLS catalyst (Figure 4.6c), the branches continue to grow but at a slower rate than the backbone nanowire. Evidence suggests that as long as gas phase Cu and Si precursors are available, growth time dictates the length of both the facetted backbone and branch nanowires. In addition, preliminary experiments qualitatively suggest that the distance between the branched nanowires is inversely proportional to the Cu gas phase partial pressure, enabling one to control the spacing of the particles with a single synthetic parameter. The effect of reducing the Cu gas phase precursor is demonstrated in Figure 4.4b as the production of the VSS catalyst particles ceases, while the backbone continues to grow.

4.5 Conclusion

The mechanism that has been proposed here provides a generalizable route toward increasingly complex structures, such as multi-level branched nanowires consisting of metallic, semiconducting, and insulating materials. These structures will help realize more complex three-dimensional morphologies and devices which exploit the unique properties of nanomaterials. The relative ease at which the defect-free branching is formed and the ability to introduce controlled heterogeneity may be the key to realizing high performance two- and three-dimensional interconnects for semiconducting applications. In addition, the proposed mechanism can be extended to other elemental combinations as long as the thermodynamics and kinetics are favorable for both catalyst-assisted growth processes. A preliminary screening suggests that this growth process can be extended beyond the tri-elemental system reported here by replacing the Cu with other transition metals. A systematic investigation of these systems is ongoing.

References

1. Murray, C. B.; Norris, D. J.; Bawendi, M. G., Synthesis and Characterization of Nearly Monodisperse Cde (E = S, Se, Te) Semiconductor Nanocrystallites. *J. Am. Chem. Soc.* **1993,** *115* (19), 8706-8715.
2. McEuen, P. L., Single-Wall Carbon Nanotubes. *Phys. World* **2000,** *13* (6), 31-36.
3. Gudiksen, M. S.; Lauhon, L. J.; Wang, J.; Smith, D. C.; Lieber, C. M., Growth of Nanowire Superlattice Structures for Nanoscale Photonics and Electronics. *Nature* **2002,** *415* (6872), 617-620.
4. Alivisatos, A. P., Semiconductor Clusters, Nanocrystals, and Quantum Dots. *Science* **1996,** *271* (5251), 933-937.
5. Oregan, B.; Gratzel, M., A Low-Cost, High-Efficiency Solar-Cell Based on Dye-Sensitized Colloidal Tio2 Films. *Nature* **1991,** *353* (6346), 737-740.
6. Bruchez, M.; Moronne, M.; Gin, P.; Weiss, S.; Alivisatos, A. P., Semiconductor Nanocrystals as Fluorescent Biological Labels. *Science* **1998,** *281* (5385), 2013-2016.
7. Cui, Y.; Wei, Q. Q.; Park, H. K.; Lieber, C. M., Nanowire Nanosensors for Highly Sensitive and Selective Detection of Biological and Chemical Species. *Science* **2001,** *293* (5533), 1289-1292.
8. Schmidt, V.; Wittemann, J. V.; Senz, S.; Gosele, U., Silicon Nanowires: A Review on Aspects of Their Growth and Their Electrical Properties. *Adv Mater* **2009,** *21* (25-26), 2681-2702.
9. Wagner, R. S.; Ellis, W. C., Vapor-Liquid-Solid Mechanism of Single Crystal Growth (New Method Growth Catalysis from Impurity Whisker Epitaxial + Large Crystals Si E). *Appl. Phys. Lett.* **1964,** *4* (5), 89-&.
10. Morales, A. M.; Lieber, C. M., A Laser Ablation Method for the Synthesis of Crystalline Semiconductor Nanowires. *Science* **1998,** *279* (5348), 208-211.
11. Kolasinski, K. W., Catalytic Growth of Nanowires: Vapor-Liquid-Solid, Vapor-Solid-Solid, Solution-Liquid-Solid and Solid-Liquid-Solid Growth. *Current Opinion in Solid State & Materials Science* **2006,** *10* (3-4), 182-191.
12. Kuchibhatla, S.; Karakoti, A. S.; Bera, D.; Seal, S., One Dimensional Nanostructured Materials. *Prog. Mater. Sci.* **2007,** *52* (5), 699-913.
13. Lauhon, L. J.; Gudiksen, M. S.; Wang, C. L.; Lieber, C. M., Epitaxial Core-Shell and Core-Multishell Nanowire Heterostructures. *Nature* **2002,** *420* (6911), 57-61.
14. Wu, Y. Y.; Yang, P. D., Germanium/Carbon Core-Sheath Nanostructures. *Appl. Phys. Lett.* **2000,** *77* (1), 43-45.
15. Radovanovic, P. V.; Barrelet, C. J.; Gradecak, S.; Qian, F.; Lieber, C. M., General Synthesis of Manganese-Doped Ii-Vi and Iii-V Semiconductor Nanowires. *Nano Lett.* **2005,** *5* (7), 1407-1411.
16. Yang, C.; Zhong, Z. H.; Lieber, C. M., Encoding Electronic Properties by Synthesis of Axial Modulation-Doped Silicon Nanowires. *Science* **2005,** *310* (5752), 1304-1307.
17. Dick, K. A.; Deppert, K.; Larsson, M. W.; Martensson, T.; Seifert, W.; Wallenberg, L. R.; Samuelson, L., Synthesis of Branched 'Nanotrees' by Controlled Seeding of Multiple Branching Events. *Nat Mater* **2004,** *3* (6), 380-384.
18. Doerk, G. S.; Ferralis, N.; Carraro, C.; Maboudian, R., Growth of Branching Si Nanowires Seeded by Au-Si Surface Migration. *J Mater Chem* **2008,** *18* (44), 5376-5381.

19. Wang, D.; Qian, F.; Yang, C.; Zhong, Z. H.; Lieber, C. M., Rational Growth of Branched and Hyperbranched Nanowire Structures. *Nano Lett* **2004,** *4* (5), 871-874.
20. Dong, A.; Tang, R.; Buhro, W. E., Solution-Based Growth and Structural Characterization of Homo- and Heterobranched Semiconductor Nanowires. *J Am Chem Soc* **2007,** *129* (40), 12254-12262.
21. Bierman, M. J.; Lau, Y. K. A.; Kvit, A. V.; Schmitt, A. L.; Jin, S., Dislocation-Driven Nanowire Growth and Eshelby Twist. *Science* **2008,** *320* (5879), 1060-1063.
22. Doerk, G. S.; Radmilovic, V.; Maboudian, R., Branching Induced Faceting of Si Nanotrees. *Appl Phys Lett* **2010,** *96* (12).
23. Oehler, F.; Gentile, P.; Baron, T.; Den Hertog, M.; Rouviere, J.; Ferret, P., The Morphology of Silicon Nanowires Grown in the Presence of Trimethylaluminium. *Nanotechnology* **2009,** *20* (24).
24. Johnson, D. C.; Morris, W. D.; Prieto, A. L., Effects of Transport Gradients in a Chemical Vapor Deposition Reactor Employing Vapor-Liquid-Solid Growth of Ternary Chalcogenide Phase-Change Materials. *Nanotechnology* **2010,** *21* (16), 9.
25. Anderson, O. L.; Stuart, D. A., Statistical Theories as Applied to the Glassy State. *Industrial and Engineering Chemistry* **1954,** *46* (1), 154-160.
26. Istratov, A. A.; Weber, E. R., Physics of Copper in Silicon. *J Electrochem Soc* **2002,** *149* (1), G21-G30.
27. Mesli, A.; Heiser, T., Defect Reactions in Copper-Diffused and Quenched P-Type Silicon. *Phys. Rev. B* **1992,** *45* (20), 11632-11641.
28. Shabani, M. B.; Yoshimi, T.; Abe, H., Low-Temperature out-Diffusion of Cu from Silicon Wafers. *J. Electrochem. Soc.* **1996,** *143* (6), 2025-2029.
29. Hansen, M. A., Kurt, *Constitution of Binary Alloys*. 2nd ed.; McGraw-Hill: New York, 1958; p 1305.
30. Harper, J. M. E.; Charai, A.; Stolt, L.; Dheurle, F. M.; Fryer, P. M., Room-Temperature Oxidation of Silicon Catalyzed by Cu3si. *Appl. Phys. Lett.* **1990,** *56* (25), 2519-2521.
31. Hinode, K.; Takeda, K.; Kondo, S., Abnormal Room-Temperature Oxidation of Silicon in the Presence of Copper. *J. Vac. Sci. Technol. A-Vac. Surf. Films* **2002,** *20* (5), 1653-1658.
32. Liu, C. S.; Chen, L. J., Room-Temperature Oxidation of Silicon in the Presence of Cu3si. *Thin Solid Films* **1995,** *262* (1-2), 187-198.
33. Xie, T.; Schmidt, V.; Pippel, E.; Senz, S.; Gosele, U., Gold-Enhanced Low-Temperature Oxidation of Silicon Nanowires. *Small* **2008,** *4* (1), 64-68.
34. Johnson, D. C.; Mosby, J. M.; Riha, S. C.; Prieto, A. L., Synthesis of Copper Silicide Nanocrystallites Embedded in Silicon Nanowires for Enhanced Transport Properties. *J Mater Chem* **2010,** *20* (10), 1993-1998.
35. Ronay, M.; Schad, R. G., New Insight into Silicide Formation - the Creation of Silicon Self-Interstitials. *Phys. Rev. Lett.* **1990,** *64* (17), 2042-2045.

Supporting information for:

Nanowire Synthesis with Controllable Three-Dimensional Branching: Simultaneous Incorporation of Vapor-Liquid-Solid and Vapor-Solid-Solid Growth

Daniel J. Shissler, Derek C. Johnson, Beth S. Guiton, & Amy L. Prieto

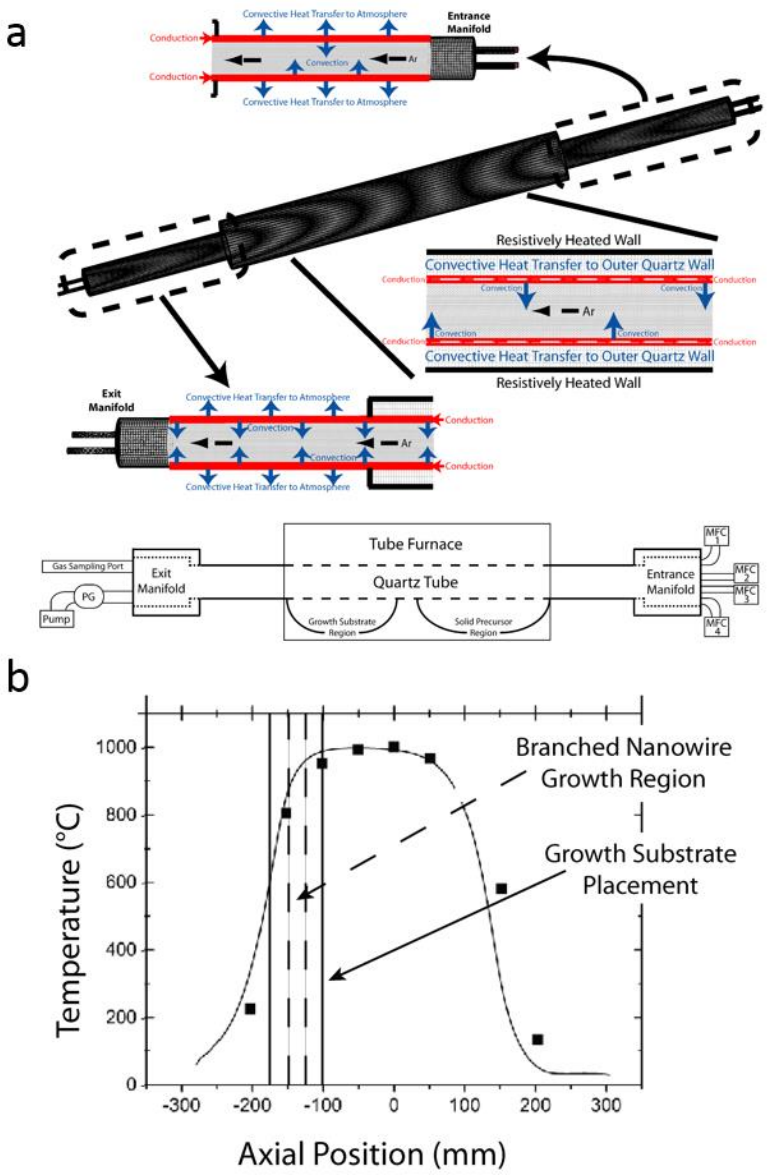

Figure S4.**1**:(a) Computational fluid dynamics grid and corresponding heat transfer processes used to model the thermal profiles as a function of furnace temperature and axial position. Figure adapted from reference 3. Illustration of the horizontal tube CVD reactor used in the experiments and modelled by the CFD simulations is also included. (b) Predicted thermal profile (solid curve) and measured temperature as a function of position, figure adapted from reference 3. Growth substrate placement based on the Cu-Si binary phase diagram and branched nanowire growth region are also indicated.

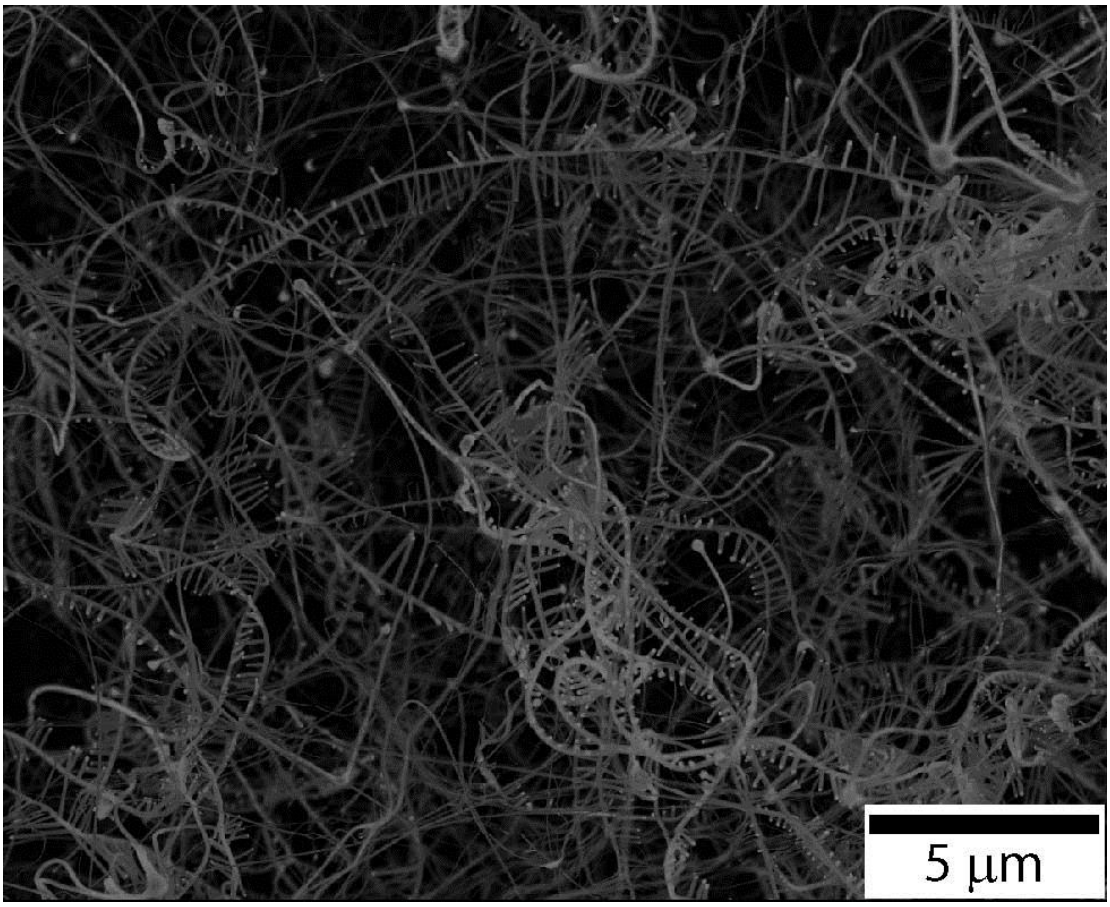

Figure S4.2. Characteristic SEM image of a region of the growth substrate where branch nanowires are the majority product with a high growth density. Note that branches with lengths on the order of a micrometer can be achieved.

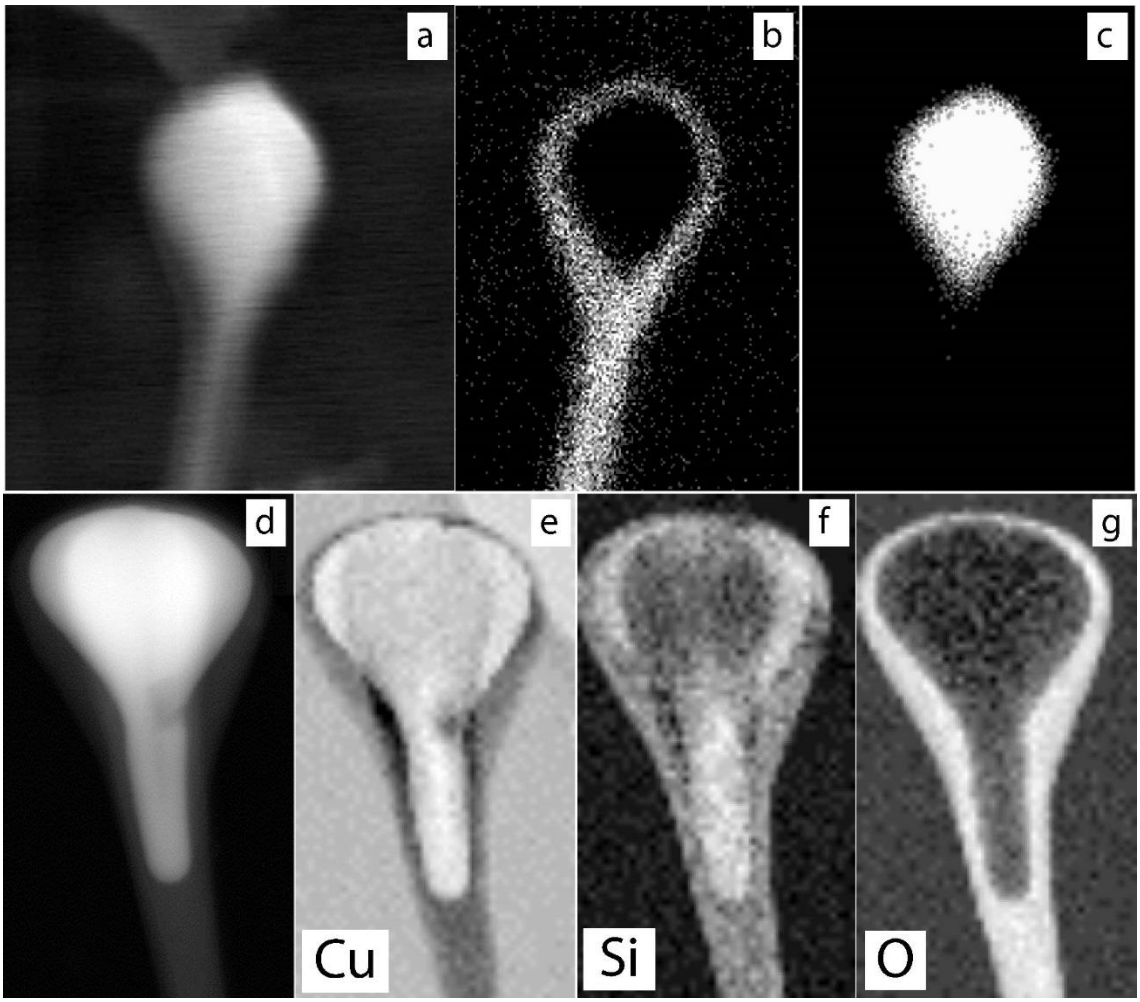

Figure S4.3: SEM-EDS mapping images for (a) the time averaged electron micrograph representing the duration of the EDS collection time, (b) the copper-silicon rich phase, and (c) the gold rich phase. (d) Characteristic ADF STEM image of the VLS backbone catalyst with corresponding EELS elemental edge maps for (e) copper, (f) silicon, and (g) oxygen.

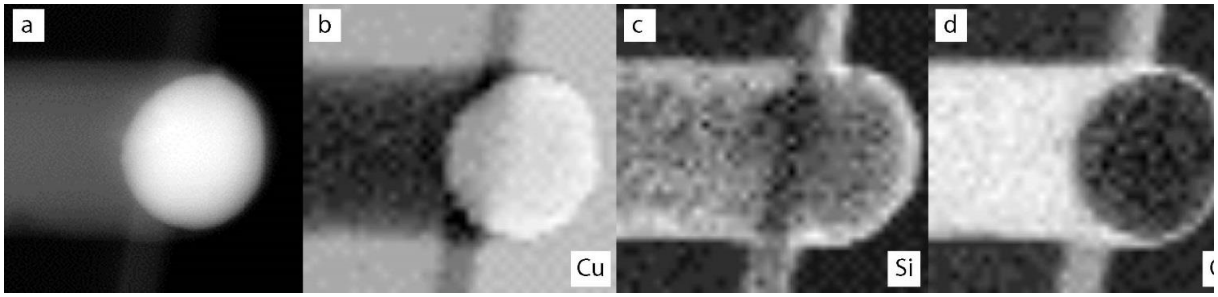

Figure S4.4: (a) Characteristic STEM image of the branching VSS catalyst particle with corresponding EELS elemental edge maps for (b) copper, (c) silicon, and (d) oxygen.

Chapter 5

Detailed Study of Substrate Preparation and Reaction Parameters Towards the Reproducibilty of Branched Silicon Nanowires[v]

5.1 Introduction

Further discoveries have been made towards the nature of the reaction, with the overall goal of understanding the origin of branched wire growth in more detail, and increasing of the yield of branched wires during the reaction. The reaction parameters have been significantly changed from that reported in the Chapter 4.

Originally the wires were grown on a Si substrate with 30 nm colloidal Au deposited on the surface. Prior to Au deposition substrates were cleaned by sonication in soapy water and then thoroughly rinsed by multiple sonications in Milli-pore (MP) water. The precursors used were ground copper powder and the Si growth substrate itself acted as a Si precursor. The wires were grown in a Lindbergh Blue Mini-mite tube furnace at 1050 ^{o}C for 10 hours with a ramp time of 35 minutes. The interior of the quartz tube was coated with glassy carbon via thermal oxidation of house gas, CH_4. The tube coating prevents the outgassing of O_2 and H_2O absorbed in the quartz matrix. Carrier gases during the reaction were UHP argon and UHP hydrogen flowing at rates of 70 and 30 sccm, respectively.

These reaction conditions were originally designed to grow Cu_2Sb nanowires, a battery anode material. The conditions were optimized to sublimate Cu and counteract any impurities. Unexpectedly, the mix of conditions unintentionally led to the branched wires. The high

[v] Daniel J Shissler, Josh Page, & Amy L. Prieto.
Daniel J Shissler performed the majority of reactions and analysis presented within this chapter. Josh Page assisted by performing optical profilometry analysis on variously treated substrates as well as performing reactions for the Cu deposition study.

temperature, fashioned to vaporize the Cu powder, also caused the unexpected vaporization of the Si substrate. Vaporization of the Si substrate was aided by the H_2 flow originally intended to produce a reducing atmosphere to negate any oxidizing species that may be present (O_2 and H_2O). Because of the unique interaction between Cu and Si, the cocktail of vaporous Cu and Si resulted in branched Si nanowires. Since the initial conditions were not intended for branched wire growth there were serious ramifications such as substrate degradation and excess non-branched wire growth.

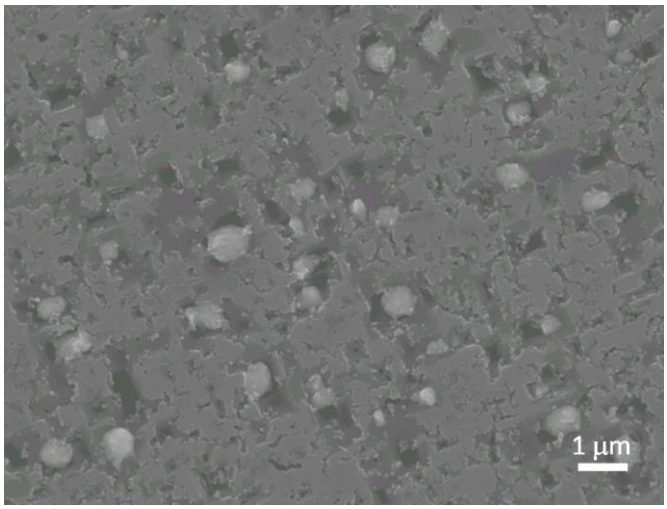

Figure 5.1: An SEM image of the degradation of the silicon substrate after a reaction.

Substrate preparation methods, precursor materials, and carrier gas flow conditions have been significantly revamped to optimize the conditions for branched wire growth. The original conditions utilized for branched wire growth had two issues of concern. The first was the degradation of the silicon substrate. SEM imaging of pristine Si shows a nearly featureless surface. As can be observed in Figure 5.1, there are large droplets accompanied by pitting of the surface. This degradation would leave these areas of the substrate barren to wire growth. The other issue was the excess growth of non-branched silicon nanowires (Figure 5.2). The excess of non-branched wires made it difficult to isolate branched wires for characterization. The problems of excess wire growth and substrate degradation both can resolved by alteration in reaction conditions and substrate preparation.

Current reaction conditions are as follows. Reactions are still ramped in 35 minutes and performed at 1050 ^{o}C. The reaction time has been cut to only 3 hours and 20 minutes. This

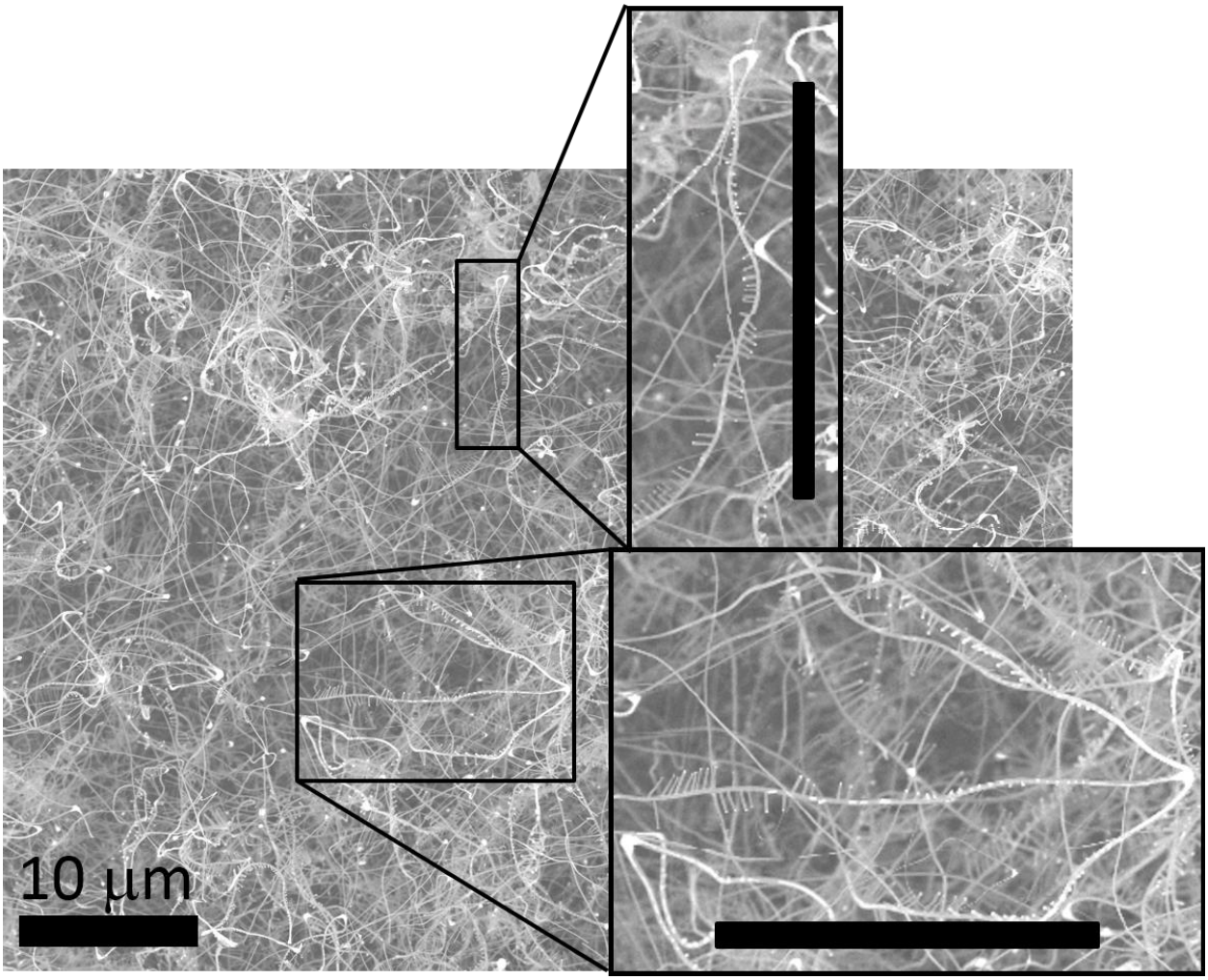

Figure 5.2: SEM image of dense wire growth. Scale bars of insets are 10 μm. The difficulty of finding branched wires in wire mass can be observed. Image taken in a region of substrate where branched wire density is highest.

shorter growth time helps reduce the excess growth of wires. The 3 hours and 20 minutes consists of a 3 hour growth segment preceded by a 20 minute Cu deposition time. During the ramp process and the first 20 minutes only Ar is used as a carrier gas at a rate of 100 sccm. During the ramp and initial 20 minutes because of the chosen precursors and lack of H_2 only Cu transport occurs. After this time the original 70:30 sccm of Ar:H_2 is flown and Si transport commences. The addition of a Cu deposition time and change in flow rate condition is possible because of the changes to precursor materials.

Altering precursor materials and the method in which the substrate is prepared has proven the most affective for increasing the yield of branched wires. The silicon is now supplemented by the use of ground silicon powder. The Cu source is now a 1:1 weight ratio powder of CuO and powdered graphite. Detailed rationalization of the changes to precursors can be found in section 5.3. As for the substrate prep, the deposition of Au is no longer performed. This is due to the discovery that the growth of wires can actually be initiated by Cu particles. Cu particles are deposited during the ramp time and the first 20 minutes of the reaction. It is believed that the deposition of Cu is highly dependent upon the method of treatment prior to the reaction.

Substrates are now prepared by sonication in 200 proof ethanol and then rinsed by sonication in MP water. The substrates are then given a 2 minute HF bath and then immediately given a brief 10 second dip in a KOH solution. Several other substrate treatments were attempted before this method was determined. Changes made to the substrate preparation resolved the problems of substrate degradation and excess wire growth but developed other complications of their own. The process and reasoning for determining proper substrate preparation, as well as, the observations made to utilize different precursor materials are described throughout the remainder of this chapter.

5.2 Au Deposition and Substrate Degradation

The wires are grown through the VLS growth mechanism. The mechanism is initiated by depositing Au nanoparticles onto the surface of the substrate prior to the reaction. This is done by a two-step process. After the substrates are washed and rinsed, a poly-lysine solution is applied to the surface of the substrate and then thoroughly rinsed. Once dry, a solution of colloidal 30 nm Au nanoparticles is then applied to the surface. The poly-lysine binds with the

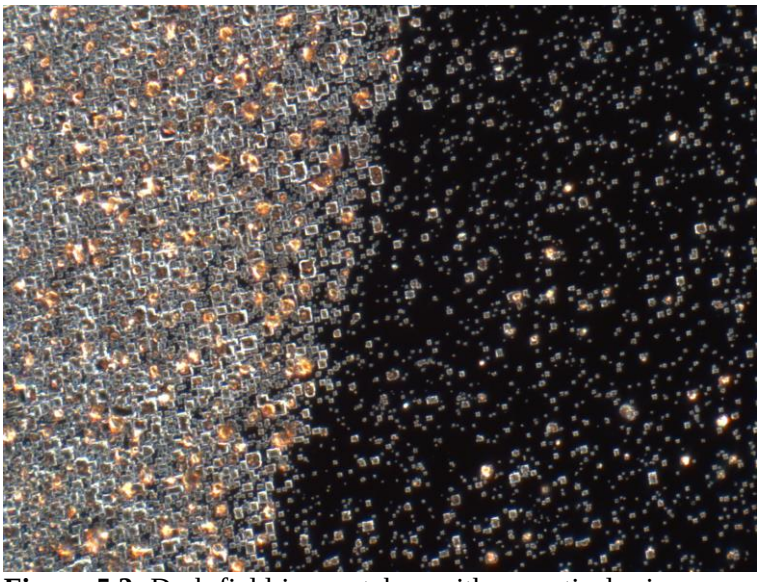

Figure 5.3: Dark field image taken with an optical microscope at X100. The left of the image shows etching where Au was deposited due to proper solution wetting. The right side of the image there is minimal etching where Au was not deposited. A defined line separates the different regions where the deposition solution did and did not wet well to the surface.

native SiO_2 layer on the silicon substrate. The positively charged amine then binds with the negatively charged citrate capping of the Au nanoparticles.[1] The electrostatic binding between the poly-lysine and the citrate ligands essentially glues the nanoparticles to the surface of the Si substrate. This section will demonstrate that minor details in the preparation of the substrates led to the observed degradation of the substrates.

The native oxide layer on the silicon surface is hydrophobic. Because of this, the poly-lysine does not wet well to the edges and corners of the substrate. For some reactions, it was observed that the degradation was not present around the edges and corners of the substrate (Figure 5.3). The pattern of the post reaction etching matches the surface that gets properly treated during the poly-lysine step. The hypothesis is that the etching is a result of the poly-lysine treatment or the Au treatment. It may be a result of either treatment since Au only binds to where poly-lysine is applied. So, if the Au is the cause of the etching, the etching pattern will match the area that is properly treated by poly-lysine. To distinguish which treatment, poly-lysine or Au, is causing the etching, different treatment procedures were attempted.

The two steps of the reaction preparation procedure were performed separately in order to determine which step of the Au deposition was leading to the degradation of the substrate.

Reactions that were run only with the poly-lysine treatment did not exhibit degradation. So, the degradation must be a result of the Au solution. To confirm this, Au was evaporated onto Si substrates and similar degradation was observed after reactions were performed. Degradation of the Si after these preparation methods is peculiar since they are common preparation methods reported in literature.[2-5]

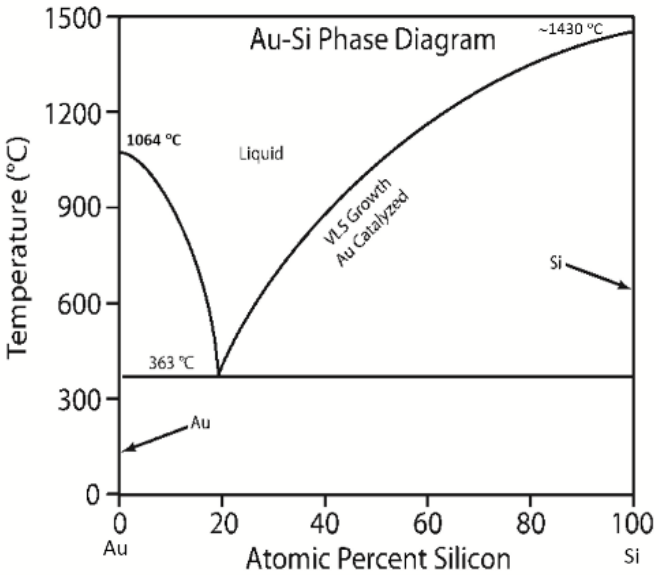

Figure 5.4: Au-Si binary phase diagram adapted from Ref. 7 to show low temperature of eutectic alloy formation.

The degradation of the Si substrate is not mentioned in literature for typical silicon wire growth.[2-5] The colloidal Au deposition and evaporation of Au onto Si are the common preparation methods. The degradation may occur in other labs but is not reported since the substrates still produce wires. Another reason for it not being reported may also be that CVD reactions performed by other labs are typically several hundred degrees cooler.[2-3, 6] This is because they are performing the reactions near the Au-Si eutectic point (Figure 5.4)[7], 363 ^{o}C, and are also using silane, a gaseous Si compound, as a precursor which also allows for much cooler temperatures.[7] The high temperatures utilized in our lab are anomalous compared to other Si nanowire work because of the temperatures necessary for our choice of precursors.

The reaction temperature was originally chosen to vaporize the copper precursor. Because of this elevated temperature, the Au readily forms a eutectic alloy with the substrate surface, which is then molten under the conditions. Because of the molten surface, no growth

could occur in that region. So if Au is the cause of the degradation, the only way to minimize the degradation is to reduce the amount of Au deposited on the surface. However, reducing the amount of Au on the surface would also reduce the amount of branched wires grown.

Depositing Au via colloidal solution allows versatility in Au particle density as well the particle size. The density can be controlled by varying the length of time that the substrate is treated with the poly-lysine and colloidal solutions. However, reducing deposition times to a minimum still deposited too much Au to negate the degradation. Another method was attempted to reduce the adhesion of Au to the Si. Pyranha Etch, 3:1 H_2SO_4: H_2O_2, was used in place of poly-lysine. Treating surfaces with Pyranha Etch is known to cap treated surfaces with –OH groups[8], forming Si-OH in the case described here, making the surface highly hydrophilic. The thought was that the electrostatic attraction of the citrate to the –OH groups would be less than the attraction to the poly-lysine but still enough for Au adhesion. At first the experiment appeared to be successful. There was minimal substrate degradation with intermittent patches of densely packed branched wires, as seen in Figure 5.5a. Also, Figure 5.5b is a dark field optical microscope image of similar patchy growth taken with an optical microscope. Due to the nature of the dark field imaging the substrate appears black and any growth, deposition, or etching has a bright contrast compared to the substrate. This form of imaging is the primary method used throughout the remainder of this chapter to identify the effectiveness of different substrate preparation techniques toward the even distribution of wire growth. In Figure 5.5b the bundles are the bright patches intermittently dispersed with no growth occurring between them. At the bottom and right sides larger patches of growth can be seen as a result of scratches on the substrate. This matter will be discussed later. Reactions were performed by treating the surface with piranha etch and colloidal Au for a time until the true nature of the growth was realized.

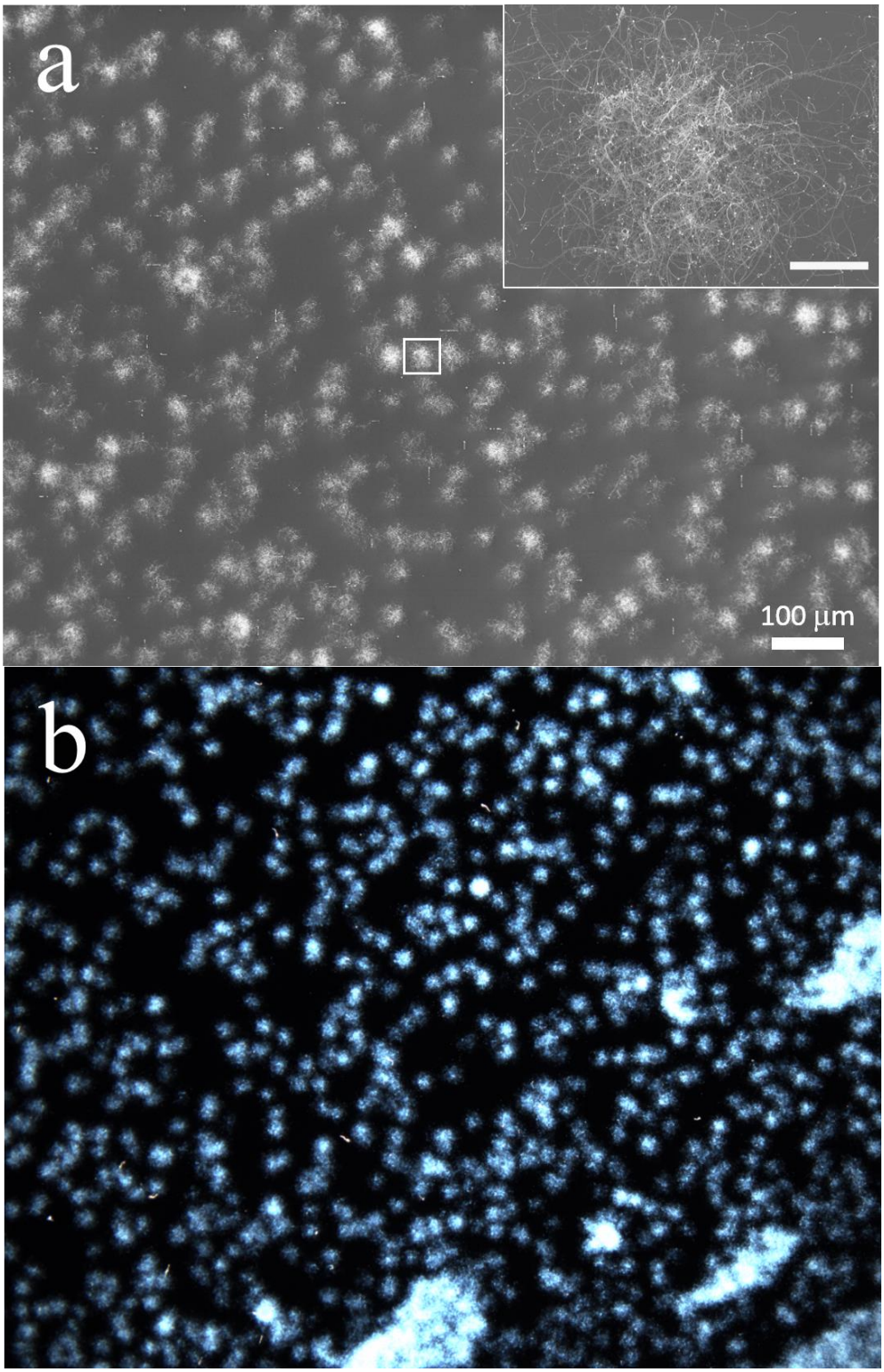

Figure 5.5: (a) An SEM image of patchy wire growth. The inset image is a zoomed in image of the bundle defined by the white square within the center of the image. The inset scale bar is 10 μm. (b) A dark field image taken with optical microscope at X100 of similar wire growth distribution.

5.3 Copper Transport and Deposition

At this time deeper insight was being made into the behavior of the materials used as precursors. The better understanding of precursor behavior proved critical to the progression of this project. Up to this point, it was believed the sources of Cu and Si vapor were due to the sublimation of copper powder and the Si substrate. However, by close observation it was discovered that this was not the case. After reactions, the Cu powder would exhibit a brighter metallic sheen. The increase in reflection was due to the removal of an oxide layer on the copper precursor. To test whether the presence of this oxide layer was important to the reaction, subsequent reactions were performed with copper oxide in place of pure Cu. After the reaction, what remained in the precursor boat was not copper oxide but metallic Cu. Not only was the clear reduction of the copper oxide evident but the substrate had large deposits of Cu. The reduction of copper could only be explained by the hydrogen gas that is used as a carrier gas to produce a reducing atmosphere. To confirm this, reactions were performed similarly but with the absence of hydrogen. Without hydrogen, no Cu transport occurs and the copper oxide powder does not become metallic. So, the previous use of copper during the reactions was quite restrictive. The quantity of active precursor was actually only that of the oxide layer present on the Cu powder. The use of copper oxide as a precursor provides a greater supply of volatile Cu and eventually led to a further evolution of the reaction.

Throughout the project, control of the distance between the branches has been an interest. This goal will likely require control of the amount of the individual precursors being transported. Typical methods of controlling the vaporous species is the use of volatile compounds containing the elements which decompose upon heating. Silane and organometallic copper compounds are commonly used as precursors to supply silicon and copper for CVD reactions. However, silane is

highly hazardous and demands specific seals and precaution during its use. Also, copper carbonyl complexes used as Cu precursors require the additional use of a bubbler system. Because of the additional hazards and requirements of using these precursors it is preferable that they are avoided. However, control over the vapor phase components is required for control of the reaction.

Since the volatilization of the Si and Cu precursors, SiO_2 and CuO, depend upon the flow of hydrogen, minor control of the vaporous species is possible by altering the flow rate of the hydrogen. However, lowering the content of one would also lower the other, because of the dual dependence. Being able to decouple this interaction would be greatly advantageous. By adding graphite to the copper oxide, this can be done.[9-10] At higher temperatures the graphite oxidizes and reduces the copper oxide to Cu. This method of reducing copper does not require the flow of hydrogen. So, once the reactor reaches high enough temperatures, with only argon flow, the Cu gets reduced and becomes vaporous and transports to the substrate. Granted, this means a constant supply of copper, but it allows for the Si content to be controlled by varying the flow of hydrogen. Control of inter-branching distances has not yet been achieved, but this precursor decoupling allows for a deposition step to occur during the reaction.

During the ramp step, only argon is used as a carrier gas. Once the reactor reaches a higher temperature the reduction and transport of the copper occurs via its reaction with carbon. Once the reactor reaches reaction temperature, the argon is held for a period of time now called the deposition period. During this time copper transports and deposits on the substrate. This way the amount of copper catalyst deposited on the substrate can be controlled before the transport of Si. Further benefits of this step will be discussed in Chapter 6 pertaining to the growth mechanism and a plot of reaction conditions can be found in Appendix I. The use of the

graphite/CuO precursor was not developed until later in the development of the substrate preparation. However, the use of the copper oxide precursor and hydrogen flow increased the copper content enough to make further realizations about the active catalyst.

Reactions prepared with the piranha etch/colloidal Au treatment were not proceeding as intended. The intention of the treatment was to deposit less Au nanoparticles on the surface. The piranha etch treatment was to replicate the poly-lysine treatment by capping the Si surface with –OH groups. The citrate ligands of the Au nanoparticles would then bind to the –OH capped surface by hydrogen bonding. Because of the lowered affinity of the citrate to the –OH capped surface compared to the amine of the poly-lysine. The difference in attraction worked, however, greater than expected.

The density of Au particles was significantly lowered. The substrate was no longer heavily etched and wire growth was primarily branched wires. However, from EDS analysis of branched wires it was found that the ratio of Au to Cu in the primary catalysts was minimal. The lowered Au deposition showed that the Au content within the catalyst may not be contributing to branched wire growth. So, the increased branched wire growth did not occur because of lack of Au but because of the increased relative percentage of Cu within the catalysts. To prove this was the case reactions were performed without Au deposition. Astonishingly, dense patches of branched silicon wires, similar to those mentioned previously (Figure 5.5), grew intermittently within a region of the substrate. The wires had the characteristic catalyst tip of VLS growth. EDS confirms the composition to be entirely Cu and Si. This growth is surprising, given the temperature at which the wires are grown.

The Cu-Si phase diagram can be observed in Figure 5.6. It can be inferred that the melting points indicated by the diagram are higher than what are necessary during the reaction

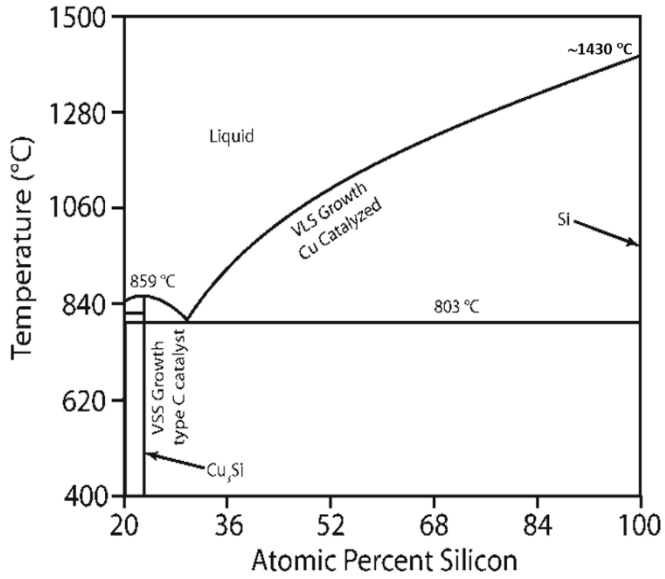

Figure 5.6: A simplified Cu-Si phase diagram adapted from Ref. 7.

because of the behavior of nanomaterials to exhibit melting point suppression. Only the general shape of the liquidus line and relative temperatures are to be taken into consideration.[11-16] Therefore, with the consideration of both VLS and VSS occurring at the same time growth aspects of the wire growth can be inferred.

Because of the solid state of the secondary VSS catalysts (Cu_3Si) and the phase diagram it must be assumed that the wires grow at temperature lower than 859°C. Further yet, for the Cu_3Si catalyst to grow Si via VSS, the temperature would need to be lower than 803°C because of the eutectic point at 30 at% Si. Originally the liquid primary catalyst tip could be attributed to formation of a eutectic allow with Au. However, based on the composition, VLS growth from a Cu catalyst should not be possible below 800°C. In this temperature zone, a Cu-Si alloy should exist in the solid state.

From this determination of the growth temperature and the phase diagram, a Cu-Si alloy of any composition should not be able to form the liquid primary catalyst. Melting point suppression of the nano-scale alloy could explain its liquid state. However, the presence of the solid Cu_3Si secondary catalyst, approximately a third to half the size of the primary catalyst, this explanation is negated. As studies show, nano-scaled materials do not behave like that of their bulk counterparts. Unlike the bulk, nano-scaled material exhibit melting point suppression. But,

perhaps nanoscaled materials share the characteristic of bulk materials to exhibit supercooling during freezing.

Literature shows that Au nanoparticles exhibit a significant hysteresis between the melting and freezing points. [15, 17] Melting point suppression implies that when solid Au nanoparticles are heated they melt at a lower temperature than that predicted by the bulk phase diagram. Looking at the opposite process, bulk materials can undergo supercooling when lowering their temperatures. While cooling a liquid can pass below the melting point of the material before freezing actually occurs. Once solidification begins the temperature rises back up to the melting point and the material continues to freeze. If the same occurs with nanomaterials the melting temperature is lower due to melting point suppression. So the freezing point would be even lower if it were to undergo supercooling. Thus, not only do nanomaterials possibly exhibit melting point suppression, but also a greater freezing point suppression. It is likely that Cu exhibits a similar behavior.

The VLS growth of the wires via a Cu catalyst can be explained by the nature of how the Cu is deposited. Copper first deposits as small liquid droplet. These particles remain as a liquid because of the melting point suppression influenced by their small size. These liquid droplets then act as the primary catalysts and grow larger as they absorb both Si and Cu from the vapor state. Eventually, a saturation point is reached and growth of Si nanowires occurs. During the swelling prior to growth the melting point of the catalysts also rise. Eventually a critical diameter is reached in which the particles should solidify. However, the particles remain a liquid because of the supercooling that is necessary for solidification. Contrary to this process, the secondary catalysts are extruded from the primary wire already in the solid state. The diameters of the secondary catalysts, being larger than the critical diameter, remain solid. The secondary catalysts

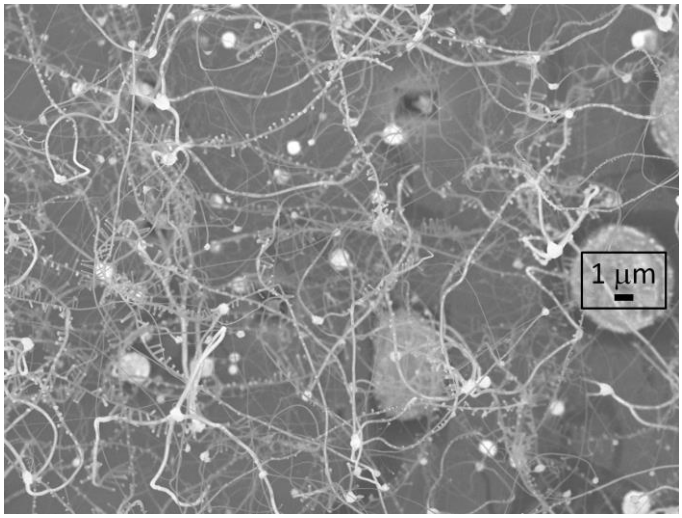

Figure 5.7: An SEM image of a region with primarily branched nanowires.

then begin to grow a secondary wire due to the continuous flow and absorption of Si. Even though this entire process occurs below the suppressed melting point of the material, as indicated by the solid Cu_3Si particles, it is yet above the suppressed freezing point motivated by supercooling. So because of the nanoscale effects and the hysteresis between melting and freezing points, simultaneous VLS and VSS growth is possible from the same elemental binary system.

Growing wires purely from this Cu-Si binary system also helped improve branched wire yields (Figure 5.7). The percentage of branched wires was increased with the absence of Au from reactions. This is likely due to the increased solubility of Si in Au, which would then require a greater amount of Si to reach supersaturation within the Au catalysts. Without Au, catalysts require less Si to reach a supersaturated state and branched wire growth is promoted. Rationalization of this thought can be found in Chapter 6. The removal of Au may have increased the percent of branched wires, but overall, reduced the total wires produced. As mentioned, wires grown without predeposited catalyst grow in dense entangled bundles grown intermittently across the surface similar to Figure 5.5. Preparation of TEM samples proved troublesome because of the low quantity of wires, Due to the bundled nature the wires also proved difficult to remove from the substrate and deposit on a TEM grid. Producing an even distribution of wires across the substrate would prove useful for the characterization of wires, as well as better understanding of the growth process.

5.4 Wire Distribution

Interesting growth patterning was observed during SEM imaging of growth substrates (Figure 5.8a). The patterning appears to be in the shape of scratches. It is likely that the surface of the Si substrate was scratched during reaction preparation, altering the surface of the substrate. To try and replicate this effect the surface was purposefully abraded using sand paper. The results gave an interesting insight into what may be occurring to promote wire growth (Figure 5.8b). A line of growth can be observed where the substrate was scratched in the image. However, it can also be observed that in some regions wires did not grow. It was observed with higher magnification that within these regions the substrate appears scored, whereas, where the wires did grow the substrate does not appear to be scratched. From this observation it is thought that growth may occur only when the native oxide is affected. Perhaps, the native oxide layer needs to be altered but if the deeper silicon is affected no wires will grow. Because of this behavior it was determined that mechanically altering the surface was not feasible.

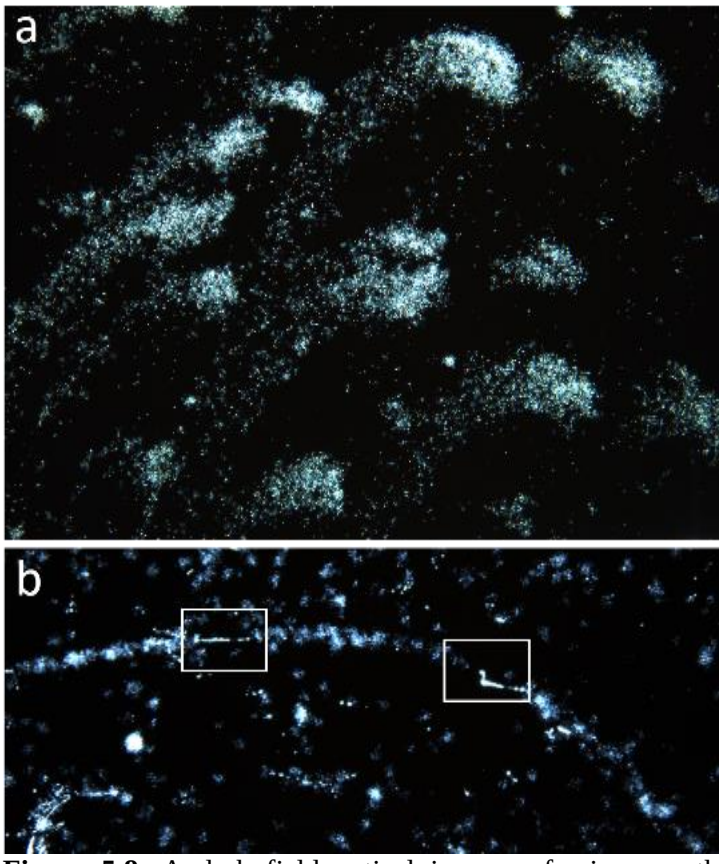

Figure 5.8: A dark field optical images of wire growth within scratches. (a) Scratches accidentally made during substrate preparation. (b) A scratch made with sand paper. Regions defined by squares have no wire growth but looks as though the substrate is scored.

Thankfully, a fortuitous accident occurred which led to an avalanche of progress towards developing a reliable method to grow an even distribution of wires across the surface and determining what promotes wire growth. Substrates are prepared for reactions by sonicating the substrate for 5 minutes in 200 proof ethanol. Then, the substrate is sonicated again in MP water. After sonication the substrate is then heavily rinsed with MP water and then dried with nitrogen. The drying must be done in a way so that the water that is wetting the surface sheets off uniformly or else patterning can be observed after the reaction. Also, care must be taken to blow out the water that has wicked up between the tweezer prongs. During reaction prep, this certain care was not taken. After drying the substrate, water dripped from between the tweezers and ran the length of the substrate. Instead of rinsing and redrying, the substrate was placed in the tube and the reaction was performed. After the reaction, the region of the substrate that was left wet had interesting features (Figure 5.9).

The upstream end of the substrate was etched with square pitting. But what was most interesting was the region of the substrate where branched wires typically grow. In this area, there was a high density of evenly distributed branched wires. This observation made it clear that there was a method of growing well-distributed wires. However, the difficult part would be reproducing it

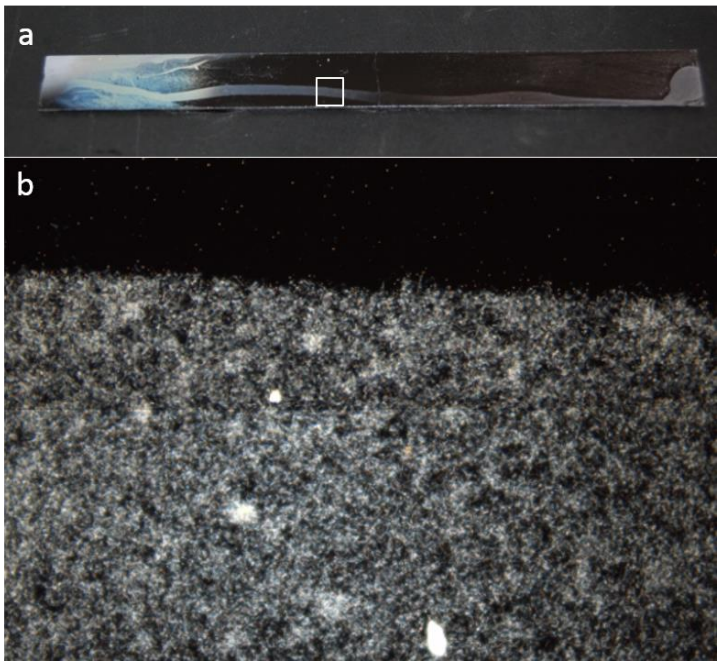

Figure 5.9: (a) A photo of the substrate that a line of water was left on and used for a reaction. (b)A dark field image taken with the optical microscope of the region defined by the white square.

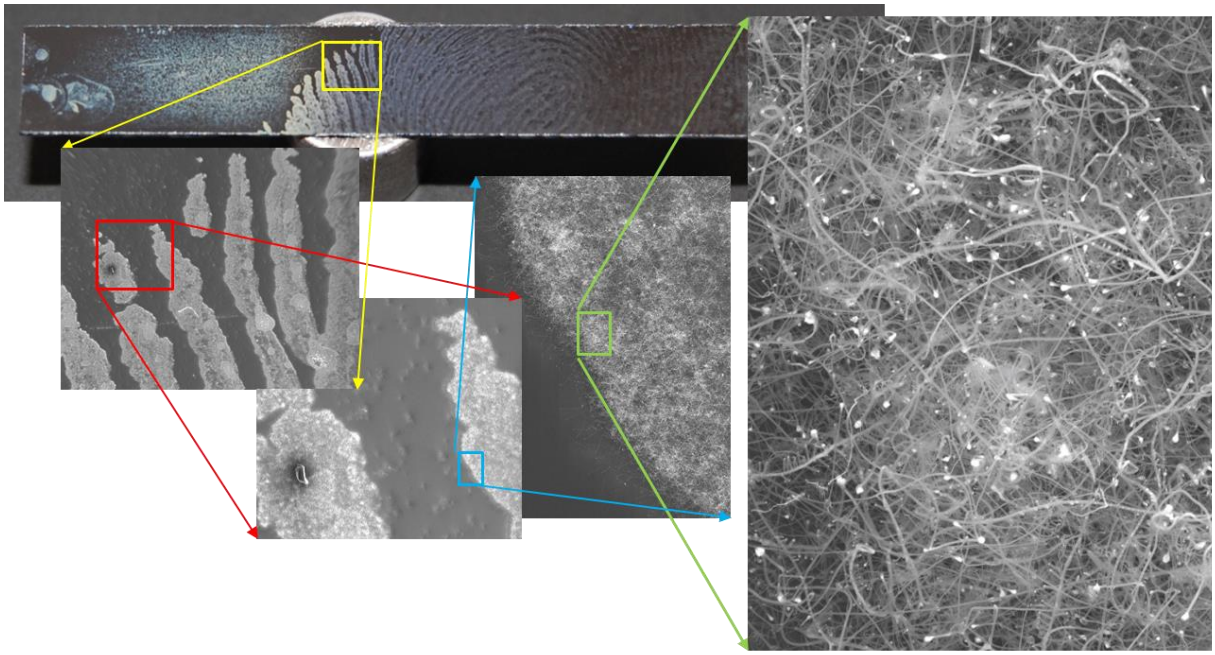

Figure 5.10: Picture of substrate with finger print and SEM images zooming in showing that wire growth occurs only in the finger print

in a controllable fashion.

Thinking that the growth may be a result of the etching caused by impurities left by the water a very crude experiment was performed. After washing a substrate, a finger print was purposely placed on the substrate. The consideration was that the salts and oils from the skin would replicate the impurities left by the water. As a result, there was significant wire deposition in the shape of a fingerprint (Figure 5.10). EDS analysis revealed salt contaminants that would be expected in a finger print. This experiment was only done to demonstrate that it may be the salt residue that caused the etching. Although effective, the results may not be controllably reproduced.

Several methods were attempted to try and reproduce the effect of the water residue. The simplest method would of course be to purposely leave water on the substrate. However simple as this may seem, it turned out to be difficult. Because of the hydrophobicity of the Si, typically the water would bead up and not remain distributed over the surface. Also, because of the high

contact angle between the water and surface a significant meniscus forms (Figure 5.11) requiring a large quantity of water to fully cover the substrate surface. The excessive amount of water would leave a large quantity of residue which would then over etch the substrate, destroying the surface. The beading was an effect of two causes. The first of these causes cannot be changed (the surface tension of the water). The second was the hydrophobicity of the Si surface. As mentioned previously, the application of piranha etch to a Si surface caps it with hydroxyl groups, turning it highly hydrophilic. By treating the surface with piranha etch first, a thin film of water could be formed on the surface.

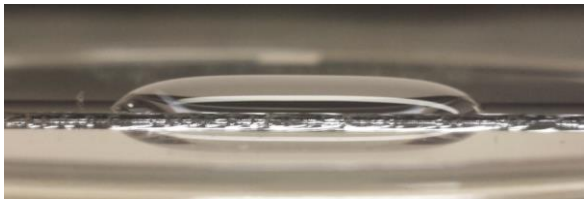

Figure 5.11: Picture of large meniscus formed on the hydrophobic surface.

Several reactions were performed in this manner. Well-distributed wire growth occurred where residue remained on the substrate (Figure 5.12a). However, as the layer evaporated the water receded towards the center of the substrate carrying all the impurities with it. There was significantly greater wire growth in the substrate since the impurities were of a higher final concentration

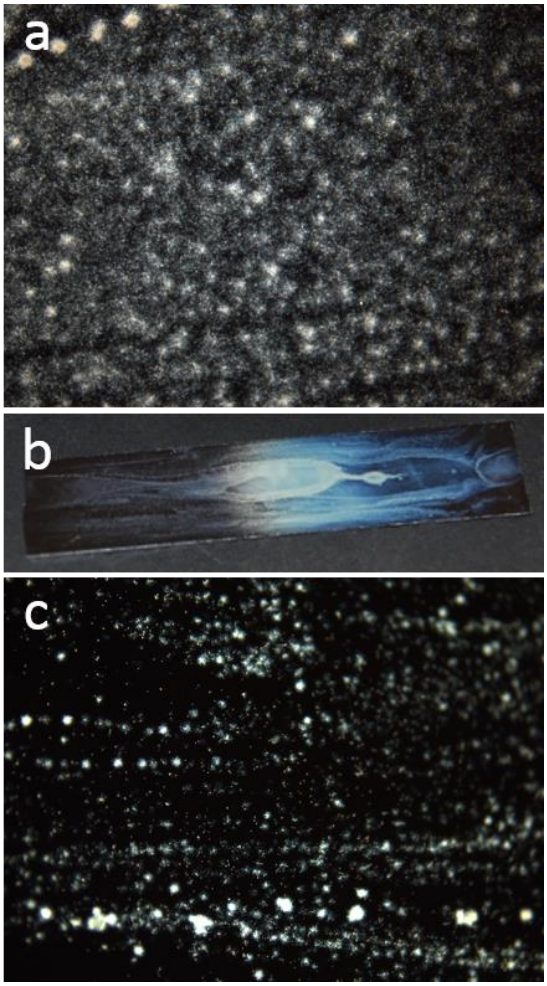

Figure 5.12: (a) A dark Field optical image of growth on a piranha etch/MP water treated substrate. (b) A picture of substrate with patterning formed by water pulling into the center. (c) A dark field optical image of substrate prepared with piranha etch/MP water after MP filters changed.

(Figure 5.12bb). Although the process worked well where the final impurities were deposited growth was not uniform across the width of the substrate. Also, at this time the Millipore filters were replaced. The new filters effectively removed, as they should, all impurities from the water. Further reactions no longer grew an even growth of wires due to the lack of impurities (Figure 5.12c). The wicking of the water towards the center and the variability of the contaminants make this method vary unreliable. A method to controllably distribute impurities would be much more preferable.

Devising a method to uniformly contaminate a sample in a controllable manner was interesting. A procedure was adapted from a method previously discussed. The original Au catalyst was deposited by initially applying poly-lysine to the surface followed by a colloidal Au solution. This treatment proves very affective because the citrate capping ligands on the Au particles electrostatically bind to the amine of the poly-lysine. By adapting this process it should be possible to bind salt to the surface by replacing the colloidal Au solution with a sodium citrate solution. The citrate would similarly bind to the poly-lysine as it did during the colloidal Au solution. However, instead of binding Au particles to the surface it would be binding sodium ions. Sodium is thought to be a cause of the etching of the Si substrates. Sodium was detected within the finger print experiment via EDS and was also found in the Millipore water due to old filters. The reduction of growth after the

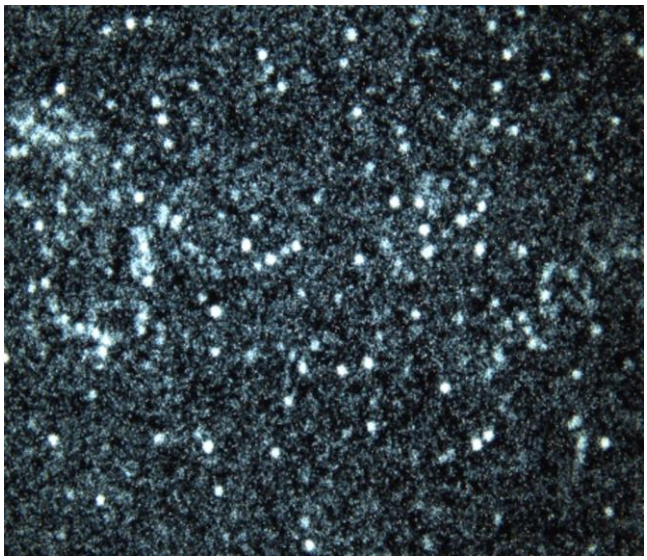

Figure 5.13: A dark field optical image of a substrate prepared with Poly-Lysine and then sodium citrate solution.

Millipore filters were replaced reinforces this theory. The poly-lysine/Citrate treatment proved effective. Substrates prepared in this manner still grew wires in dense bundles but also grew wires evenly distributed across the surface between the bundles (Figure5.13). Many reactions were done to prove the reproducibility of the procedure.

The poly-lysine and citrate treatment improved the growth of branched silicon nanowires. However, reliable reproducibility proved to be elusive. It was found that the method in which the citrate solution was rinsed has crucial impact on the performance of the treatment. The substrate had to be rinsed precisely in order for the treatment to perform to its maximum. If the substrate was rinsed too thoroughly, etching and wires growth was a minimum. But if the substrate was not rinsed enough a residue film would be left on the surface which would inhibit the wire growth. Since it is difficult to rinse substrates the same every time, the growth with this substrate preparation is not consistent.

Improving the substrate preparation procedure was important for the study of controlling the architecture of the branched wires. Architecture control was being done by tampering with various reaction conditions; pressure, flow rates, and temperature. The unreliability posed a significant problem during these trials. If a reaction performed poorly it would be unknown whether it was due to the alteration in the reaction conditions or a badly prepared substrate. It was necessary to discover a method of substrate preparation that would reliably produce the same results. It can be observed that etching occurs on the hotter end of the substrate due to the presence of Na. From this, a new approach was taken towards preparing the substrates. Instead of controllably contaminating the surface, replicating the effects of the contamination was attempted.

Si substrates have a layer of amorphous SiO_2. It could be believed that the etching lead to wire growth because of the removal of this amorphous layer. However, from previous studies it was already known that removal of the native oxide with HF negates the growth of wires. For this reason, it was considered that the etching increases surface roughness of the Si. Because of the Si industry several Si etchants are known. Because of the single crystalline nature of the Si, it can be etched either isotropically or anisotropically. However, anisotropic etching would not increase the roughness of the surface, so an isotropic etchant is necessary.

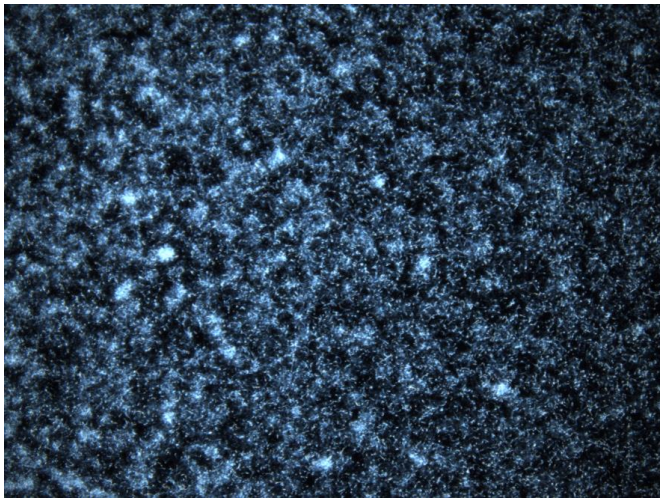

Figure 5.14: Dark Field optical image of substrate prepared by etching with KOH solution.

An isotropic etchant that was found in literature was a simple KOH solution.[18] The solution also contained isopropanol (IPA) because of the hydrophobic nature of the Si. Without the isopropanol there is minor etching due to the poor wetting of the solution to the surface. This solution proved effective in properly treating the substrate to grow wires (Figure 5.14). Wire growth was evenly distributed where the substrate was significantly etched. Typically the wires would grow more densely in some regions compared to others due to poor wetting of the solution to the Si (Figure 5.15a). Also, due to the formation of gaseous bubbles, vigorous stirring was necessary to dislodge the bubbles. If bubbles remained attached to the surface they would prevent the KOH solution from etching the substrate. In Figure 5.15b it can be observed where a bubble formed on the surface and no etching occurred in that area, and thus no wire growth. Whereas to the left of the bubble, dense wire growth can be observed.

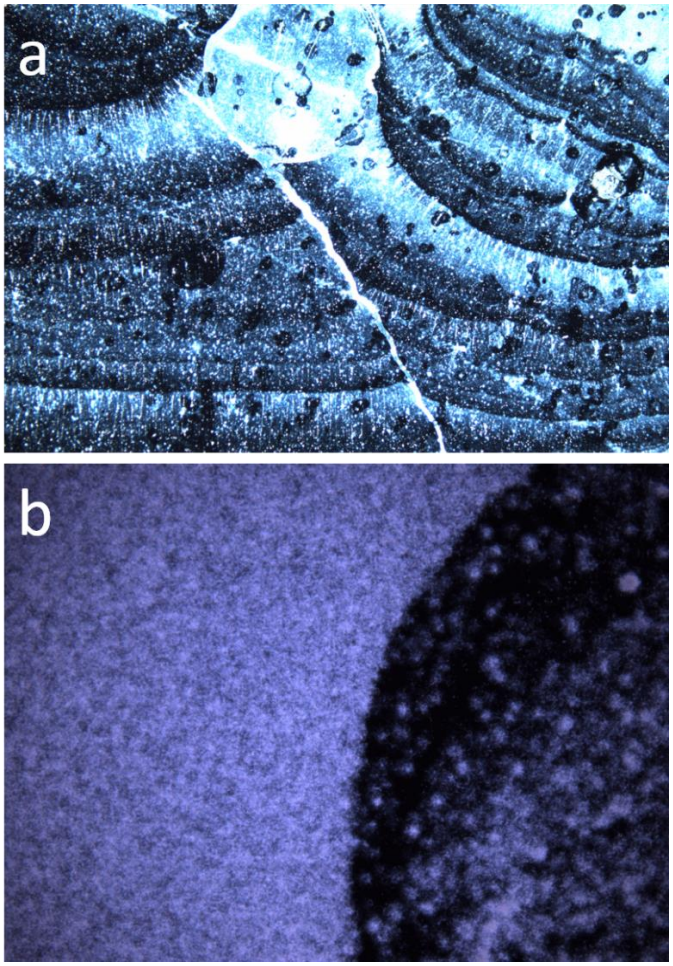

Figure 5.15: A dark Field image of substrates. (a) Uneven etching from poor wetting during KOH bath. (b) The edge of where a bubble formed on the substrate during KOH bath.

The uneven wetting was not the only problem that was experienced. The optimized KOH solution consisted of KOH, IPA, and H_2O at a gravimetric ratio of 12.5:10:40, respectively. Increasing the amount of isopropanol of the solution increased wetting of the solution to the substrate. However, a solution of high alcohol content makes other steps of the procedure less reproducible. The vapor pressure of the solution increases as the alcohol content increased. Also, the temperature of the solution greatly affects the strength of the etching action. The combination of temperature dependence and volatility made the timing of the treatment procedure rather specific. If the temperature of the solution was not hot enough the substrate would not be etched well. However, if heated for too long the isopropanol would evaporate and the solution would not wet well to the substrate. An appropriate length of time for the KOH bath was never specifically determined. Etching was determined to be sufficient by visual observation with the optical microscope.

The microscope was not used in a traditional manner. Imaging substrates with the optical microscope requires the use of the dark field illumination. While using the dark field

illumination only objects with a large side profiles are visible. Since the Si substrate is highly polished it does not scatter any light and thus appears black through the eyepiece while under dark field illumination. Features on the surface, however, can be observed because of the scatter from their side profile. Because of this the degree of etching can be observed. As the Si surface is etched more heavily more light scatters. So, as the Si surface is etched, the contrast of the surface increases. However, the proper etching was not determined by direct imaging of the surface.

When the microscope light is shown on a pristine Si surface the light cannot be seen by the eye when looking at it from the side because it reflects at too high of an angle to be seen and reflects at too low of an angle to be seen through the eyepiece. However, if the surface is effectively etched, the rough surface scatters the light at wider angles and can be observed from the sides. Figure 5.16 portrays this behavior.

The pictures on the left show the substrate from the side, whereas, the right images show how the substrate with the same degree of etching appears through the microscope. Figure 5.16a is a cleaned non-etched substrate. From the side no light can be seen on the surface and the substrate appears black through the eyepiece. After 2 minutes of etching (Figure 5.16b), from the side, the substrate appears the same but in the microscope minor pitting can be observed. This degree of etching was not sufficient enough to produce an even distribution of wires across the surface. However, the substrate etched to the extent of the one in the next images (Figure 5.16c) would produce a nice even distribution of wires. As observed the substrate as seen through the eyepiece does not differ much from that of Figure 5.16b. However, if the substrate is observed from the side a ring of light can be seen. Further etching then produces results seen in Figure 5.16d. Substrates etched to this extent would result in evenly distributed growth in some regions but not others. The etching time between the images in Figure 5.16c and d is a fraction of the

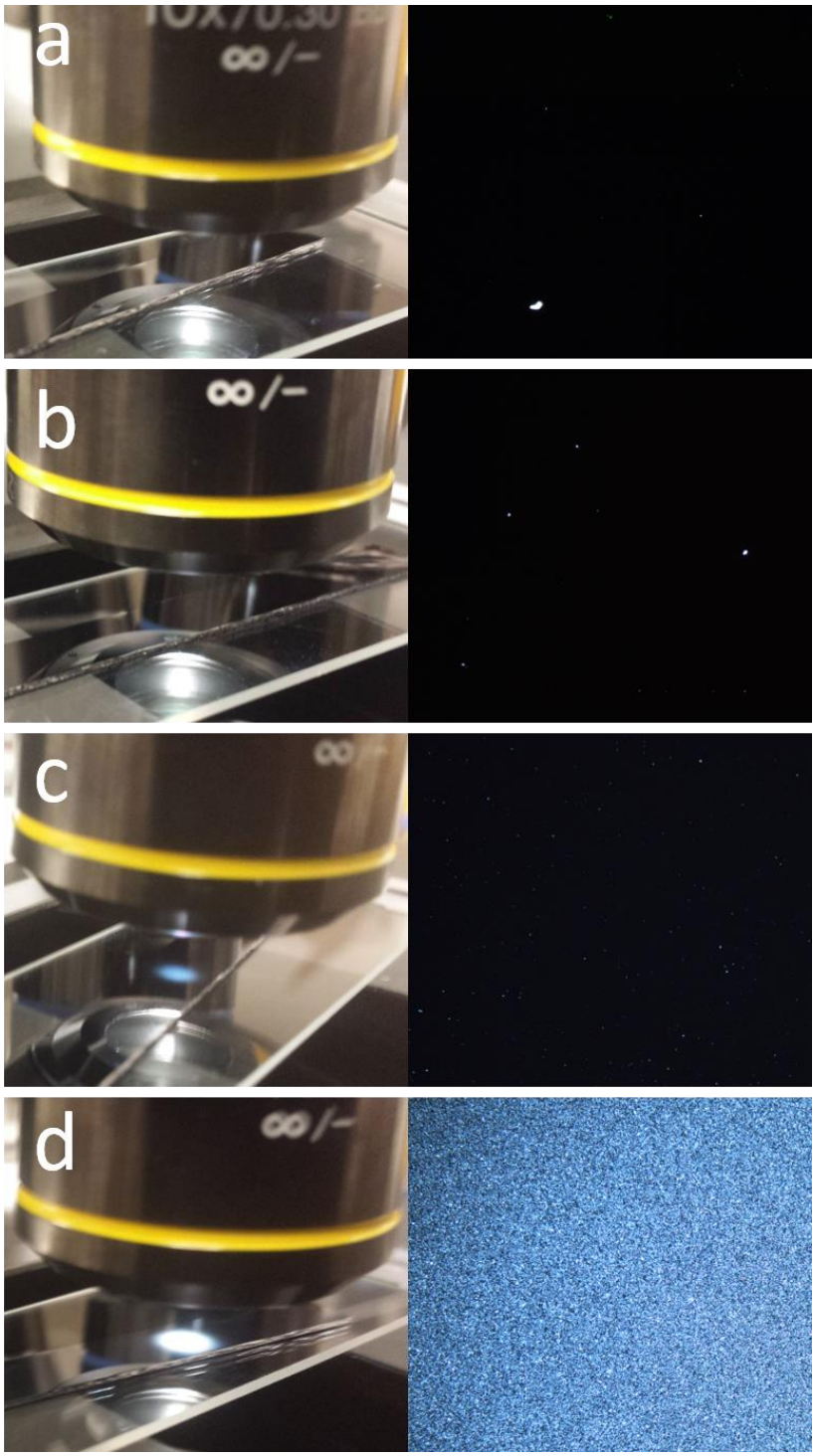

Figure 5.16: On the left are photos of the microscope shining on the substrate. On the right are images of the same substrate seen through the eyepiece of the microscope. (a) Cleaned non-etched substrate. (b) Substrate after 2 minutes in KOH bath. (c) Substrate further etched. Ring of light can be seen on substrate but no major change of appearance through eye peace. (d) A heavily etched substrate. An intense circle can be seen from the side. Heavy etching can be seen from through the eyepiece.

total etch time and typically not the same amount of time. Producing the same degree of etching within the appropriate window is difficult and would likely produce different results from reaction to reaction. Because of the erratic results produced from the same preparation procedure, even with thorough scrutiny of the procedure, a substrate preparation procedure with consistency would be preferred. So, once again, a different approach was attempted.

Additional hypotheses were developed to explain what may actually be happening to promote wire growth on some surfaces and not on others. Clearly, some areas of the substrate were being etched more than others. The wire growth should occur proportionally with the amount of etching if it were only the roughness of the substrate. However, wire growth typically was either there or not. The only explanation for this could be that in some regions the etching had fully removed the SiO_2 layer and in other regions had not. But, if it were only the removal of the native oxide layer then a substrate treated with an HF bath should produce similar results, yet, it does not. The HF dissolves SiO_2 and leaves the Si surface capped with Si-H. So treating Si with HF removes the SiO_2 native oxide layer and leaves the surface with a smooth Si-H capped surface. After rinsing, the surface is highly hydrophobic because of the Si-H species on the surface. It is likely that the Si-H species on the etched surface is what prevents branched wire growth averse to substrates etched by the KOH treatment. From this analysis, yet another method of substrate preparation was tried.

The native SiO_2 layer is stripped off with HF, and the substrate is very briefly (to minimize etching) dipped in a KOH solution for 10 seconds, and then rinsed with Millipore water. With this treatment, substrates reliably grow an even distribution of branched silicon wires (Figure 5.17). The KOH rinse “neutralizes” the Si-H surface and caps it with Si-OH. The KOH etching, similarly, would have left the same speciation on the roughened surface. Although

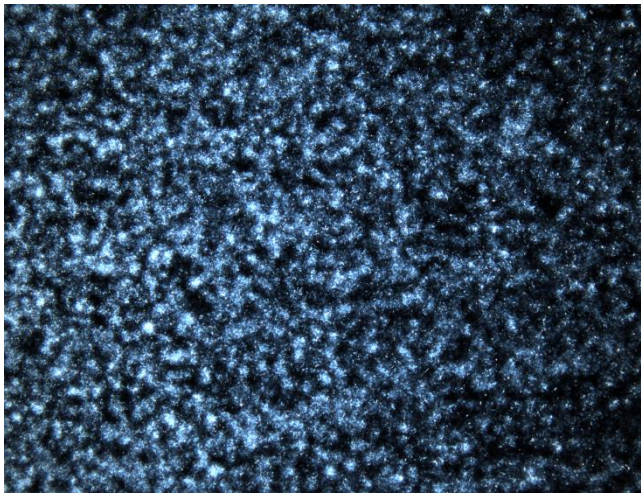

Figure 5.17: A dark Field optical image of the reaction results with HF- KOH treated substrate.

this gives us a reliable method of preparing the substrate, why this method works is not fully understood. To this end, reactions were performed using all the previous methods of substrate preparation to build a table and directly compare the results. During this screening a reaction was attempted by preparing a substrate with only the 10 second KOH bath. Unexpectedly, it worked well and resulted in growing evenly distributed wires. Again, there were regions of good and bad growth due to wetting issues. However, this disproved the hypothesis of why the HF-KOH treatment worked.

Different methods of surface analysis were then attempted to characterize the properties bestowed upon the substrate by the various preparation methods. Originally it was believed to be a combination of surface roughness and chemical speciation on the surface. However, the latter is now believed to be the primary attribute that improves the branched wire growth. Optical profilometry was performed on substrates prepared by the variety of treatments discussed. It was discovered that the roughness of the substrates are relatively the same. Single-bounce IR reflectometry was attempted to characterize the speciation of the surface. However, there was not a strong enough signal since there is only a monolayer of material with which the beam was to interact. Multi-bounce IR reflectometry or Grazing Angle Reflectometry may resolve this issue. Unable to quickly identify the surface speciation in the lab, a thorough literature search was made to identify the speciation of the different preparation methods. Due to the importance of Si

in the semiconductor industry, certainly there has been some work on the characterization of the surface after different washing methods.

A lot of literature was found on the topic. Most of it just confirmed what was already inferred. Hydrophilic substrates are capped with an Si-OH layer and hydrophobic substrate are Si-H capped. However, the literature states that once the surface is capped with Si-OH, formation of SiO_2 is nearly immediate.[19] This is likely the case by comparison of our results, but further specifics found in literature cannot be directly applied to our study. In the literature, RCA cleaning[20] is the method used to hydroxylate the surface and form a hydrophilic layer. This method includes an HF bath to strip the native layer off which is then followed by a rinse in ammonium hydroxide and hydrogen peroxide, the basic equivalent of piranha etch. Any reactions performed using piranha etch as a method of substrate treatment never succeeded in the even distribution of branched nanowires. Therefore the in depth study of the surface speciation provided on literature cannot be applied to our reasoning.

Even though the chemical hydroxylation methods in literature may not fit our uses, another paper was found that may be informative.[21] In this source a method used for surface hydroxylation is simply heating the Si in near boiling water. In their work the Si was then oxidized by heating to 1000 °C under O_2. The resulting oxide layer was compared to that formed on a substrate that was oxidized on an HF cleaned Si. It was found that the oxide layer formed on the hydroxylated substrate contained OH groups within the Si/SiO_2 interface. Also within the interface, there was a greater mix of Si oxidation states. It was also observed that the hydroxylated surface formed a thinner oxide layer than that of the HF washed Si. Whether these findings can be used to address our observations is not clear. But, the paper did bring to light another method of hydroxylating the surface.

Si substrates were prepared similarly to that prepared by Grunthaner et al.[21] They were cleaned via sonicating and placed in a boiling water bath for an hour. When the substrate was removed from the bath it was hydrophilic and had a clean sheet of water with no contact angle, characteristic of a Si-OH capping. Substrates prepared in this fashion grew evenly distributed wires across the surface. Since the boiling process should not affect the native oxide layer one may presume that the surface is a native oxide layer capped with Si-OH. To give deeper insight into these results another reaction was prepared in similar fashion. A substrate with a 100 nm thermal oxide layer was cleaned and boiled. When removed from the boiling water bath the substrate was not uniformly hydrophilic as the Si substrates were. This substrate was then used for a reaction and resulted with mixed growth (Figure 5.18b). It is thought that the surface did not become completely hydroxylated. This may be due to the greater stability of the crystalline SiO_2 surface. Patterns can be observed in the wire growth due to the poor wetting. From analyzing all of the reaction results by the various methods of substrate treatment (Table 5.1), a new hypothesis can be made as to what is necessary for uniform wire distribution.

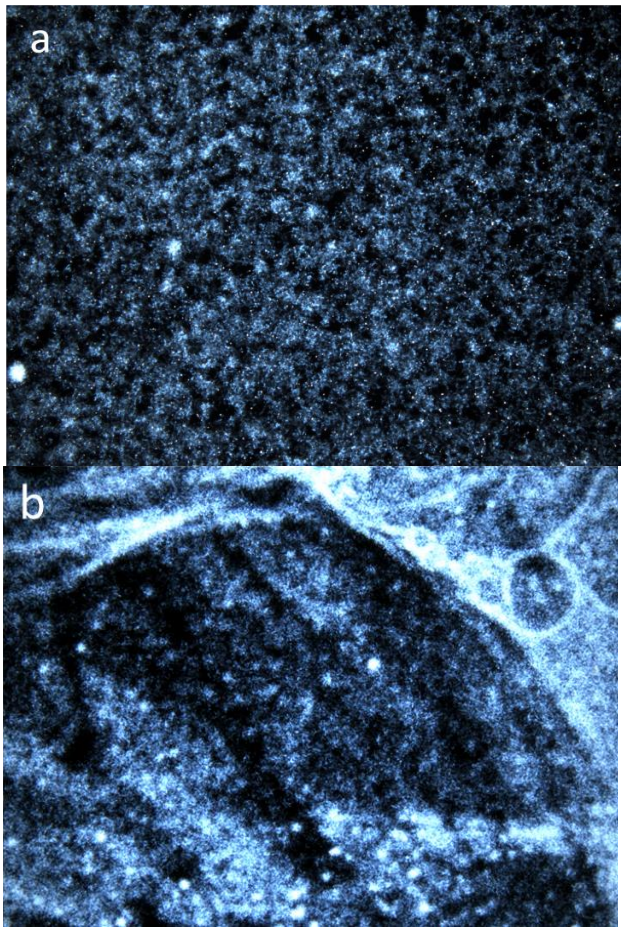

Figure 5.18: Dark field optical images of reaction results after preparing substrate by submersing Si (a) and thermally oxidized Si (b) in boiling water for one hour.

Table 5.1: Comparisons of substrate treatment, likely surface chemistry, and growth results.

Substrate treatment	Surface characteristics	Growth results
Wash only	Clean native oxide layer, literature states should be a mixed capped surface of Si-O-Si and Si-OH. Due to hydrophobicity can be inferred low level of Si-OH	Dense patches of wires intermittent across the surface growth
Piranha etch (H_20_2/H_2SO_4)	Si-OH capped native oxide	Patchy intermittent growth
Base piranha (H_2O_2/NH_4OH)	Si-OH capped native oxide	Patchy intermittent growth
HF bath	Si-H capped Si	No growth
Finger print	Heavy salt contamination Organic contamination	Dense wire growth in regions with finger print
Piranha etch/Water residue	Salt contamination, heavily adsorbed H_2O on native oxide layer	Dense patches of wires with light wire growth between them. Patterning occurring where heavy impurity resulted
Poly-lysine/Sodium Citrate	Native oxide lay capped with poly-Lysine and sodium impurity	Dense patches of wires with light wire growth between them. Over rinsing results in poor growth.
KOH etching	Etched surface, possibly removing the entire native oxide layer. If so, literature suggests new oxide would form and be capped with KOH	Evenly distributed wire growth. Could be intermittent due to uneven etching.
HF bath KOH rinse	Clean Si surface capped with Si-OH. Literature suggests it is likely freshly formed oxide layer capped with Si-OH	Evenly distributed wire growth.
10s KOH bath	Mildly etched native oxide capped with Si-OH	Evenly distributed wire growth. Possible intermittency due to poor wetting
Boiled Si substrate	Amorphous native oxide capped with Si-OH	Evenly distributed wire growth
Boiled thermally oxidized Si	~100 nm crystalline oxide layer capped with Si-OH capping	Evenly distributed wire growth

5.5 Si-OH Capping

Some reasoning can be now be applied to the observations now seen as a whole. Substrates that can be said to have an SiO_2 layer capped with Si-OH produce evenly distributed branched nanowires. However, the ineffectiveness of the piranha etched substrate to produce wires is baffling. The only thought is that perhaps the mechanism of hydroxylation differs somehow. Possibly it may be that there is also Si-OOH capping, due to the presence of the peroxide, which inhibits the growth. As for the controlled impurity treatments, different allegations could be made that the impurities present help cap the surface with Si-OH.

Because of the massive amount of impurities from the finger print many assertions could be made. Perhaps the salts act as a trap for moisture within the finger print residue, which upon heating decompose and leave an Si-OH later. The same could be said about the piranha etch/water residue treatment. The piranha etch alone has proven ineffective for growing wires. So it is likely the water film and its impurities aid in the wire growth. The remaining impurities can be said to be a key role because of the lack of activation by the more pure water (Figure 5.12). The impurities could increase the affinity of the water towards the Si, preventing it from being fully desorbed during the pump purge process. Likewise could be said of the poly-lysine and the sodium for the poly-lysine/sodium citrate treatment. All of the treatments that could potentially produce an even distribution of wires could be said to have a SiO_2 layer capped with Si-OH once the precursor materials start transporting. But why might this lead to an even distribution of wires?

Typically VLS wire growth is initiated by depositing the VLS catalyst prior to the reaction, as was originally done with the Au colloid solution. However, in our case the VLS catalyst for the branched nanowires is the Cu that deposits on the substrate during the reaction. The importance

of the Si-OH capped SiO_2 layer may be that it promotes this deposition of Cu. To test this, substrates were treated by the various means discussed and the amount of copper deposited on them was analyzed. This was done by running reactions that only included the deposition segment (mentioned in Section 5.3 of this chapter) and no growth segment. The substrate and precursors were loaded into the tube which was then ramped to reaction temperature and then held for 20 minutes. The reactor was then cooled and the substrates were imaged with SEM. As can be seen in Figure 5.19 the substrates treated with methods that produce patchy wire growth (Figures 5.19 a-b) have large copper droplets scattered across the surface. Whereas, substrates

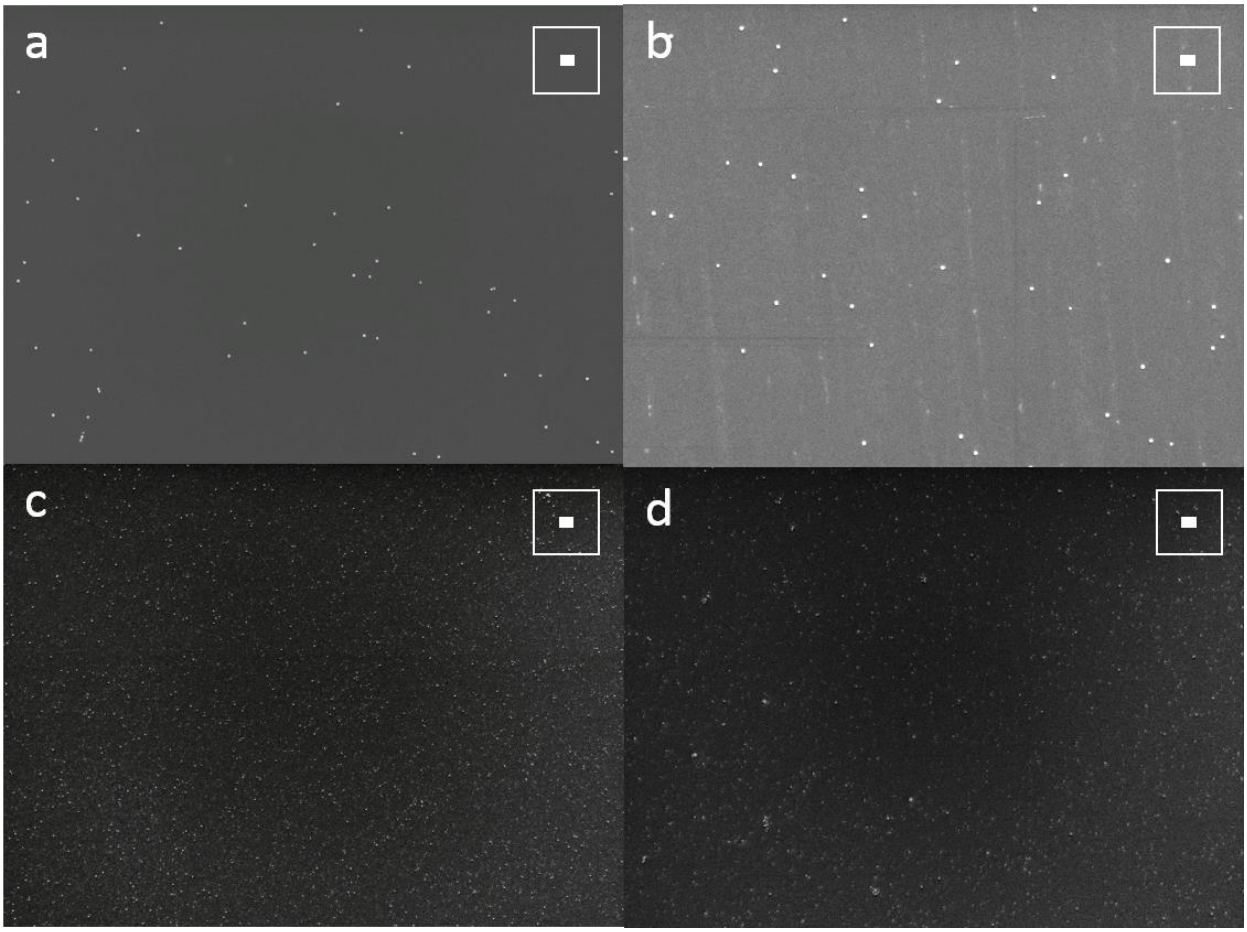

Figure 5.19: SEM images of copper deposited on substrates prepared by different methods, (a) Washing only (b) 2 min HF bath (c) 2 min HF bath followed by 10 sec KOH dip, and (d) 10 sec KOH dip. Image c exhibits lines which are likely minor scratches produced during preparation. Images c + d are dark due to contrast adjustments to resolve copper droplets from image graininess. All scale bars are 10 μm.

prepped via methods producing evenly distributed wires (Figures 5.19 c-d) have a greater number of smaller Cu droplets well-distributed across the surface. The increased Cu deposition could be a result of a more favorable interaction between the surface and Cu.

Just as hydrophobic and hydrophilic surfaces are a result of higher and lower surface energies between the surface and water the same could be said of the increased Cu deposition. The Si-OH capping may have a lower energy surface interaction with the copper; lowering the activation energy necessary for the Cu to deposit on the surface. Once initial deposition of Cu occurs the vaporous Cu then deposits on the existing copper droplets which then become VLS catalysts once Si transport begins. This hypothesis can further be rationalized by the dense clusters of wires formed on substrates without the Si-OH capping. It is possible that defects or impurities exist on the surface that act as Cu deposition sites which accumulate an abundance of copper. Being the only favorable site for which the Si vapor can interact with, an excessive amount of wires grow at these locations forming the dense pack of wires. This may also rationalize why the controlled impurity treatments have a positive effect. The salts that are left on the surface again act as preferential deposition sites for the Cu and evenly distribute across the surface. This is a feasible hypothesis as to why the Si-OH layer improves the growth of branched wires, yet, another possibility is the chemical interaction of the Si-OH layer and the vaporous Cu species.

During CVD reactions the vaporous content is not usually atomic species. For carbon layer depositions, the active species is described as C_2 and for silicon reactions SiH_2.[22-28] It is not likely that during our reactions the vaporous state of copper is atomic copper. A possibility for the promoted Cu deposition is the interaction of the Si-OH layer with the vaporous species. Atomic layer depositions take advantage of such interaction to limit the deposition to a single

atomic layer.[29-30] In some situations the surface is capped with –OH groups, similar to ours, which then react with the vaporous species and deposit on the surface.[30] Since the reaction is limited by the amount of –OH on the surface only a single layer can be deposited. It is possible that during our reactions a similar situation is occurring. Maybe our Si-OH reacts with the vaporous form of Cu which then deposits on the surface. However, perhaps our reactions then occur similar to standard VLS growth. The deposited Cu then acts as a catalyst for the decomposition of the vaporous species similar to the way that the Au catalysts act as preferential decompositions sites for silane.[31-32] This way our reactions are not limited by the Si-OH for continuous deposition. This hypothesis also agrees with observation. Reactions with Si-OH layers produce an even distribution of wires. The wires without Si-OH may have impurities scattered across the surface that trigger the initial deposition of copper which then catalyzes further deposition and creates the dense clusters. Several different methods of analysis may be done to try and differentiate the two hypotheses.

5.6 Conclusion

Although the promotion of wire growth is not fully understood, it has been deduced that a Si-OH capped SiO_2 layer is likely what is necessary for an even distribution of branched wires. Most importantly a reliable method has been developed to consecutively produce the same results. With this improvement it is now possible to alter reaction conditions with intent to tailor the wire growth and know that the resulting changes to the growth is due to the condition change and not the failure of the substrate. Also, the ability to observe the wires in a well-distributed environment has allowed the observation of the entire length of the branched wire, from nucleation point to catalyst tip. This broad observation of the wire length has allowed

for an in depth characterization of the growth process of the wire which is described in detail in the next chapter.

Determining the actual cause of the improved wire growth is not essential for the progression of the branched wire project but may prove fruitful to the CVD discipline. As mentioned before, multibounce IR or grazing angle IR could be used to verify the surface speciation. Current literature has only characterized the speciation of surfaces treated with Base Piranha. Due to the drastic difference of the results obtained in our work this study may prove enlightening to the field. Once the surface speciation is identified, the interaction between the different Si surfaces and Cu should be characterized. Studies should be performed using nanoscale Cu on Si because of the higher surface energies of nanomaterials. This could possibly entail measuring the contact angle between molten Cu nanoparticles on Si. In addition to these studies, sampling of the reaction vapor should be performed to identify the actual speciation of the vapor content. Methods seen in literature include either modeling reaction conditions [26-28] or use of Optical Emission Spectrometry or Mass Spectrometry which is capable of analyzing the vapor in situ.[23, 25] However, all of these methods would either require an extensive overhaul on the reactor system or would likely require collaboration since to the writer's knowledge, the appropriate methods are not readily available.

References

1. Jiang, M.; Popa, I.; Maroni, P.; Borkovec, M., Adsorption of poly(L-lysine) on silica probed by optical reflectometry. *Colloid Surface A* **2010,** *360* (1-3), 20-25.
2. Wu, Y.; Cui, Y.; Huynh, L.; Barrelet, C. J.; Bell, D. C.; Lieber, C. M., Controlled growth and structures of molecular-scale silicon nanowires. *Nano Lett* **2004,** *4* (3), 433-436.
3. Cui, Y.; Lauhon, L. J.; Gudiksen, M. S.; Wang, J. F.; Lieber, C. M., Diameter-controlled synthesis of single-crystal silicon nanowires. *Appl Phys Lett* **2001,** *78* (15), 2214-2216.
4. Tian, B. Z.; Zheng, X. L.; Kempa, T. J.; Fang, Y.; Yu, N. F.; Yu, G. H.; Huang, J. L.; Lieber, C. M., Coaxial silicon nanowires as solar cells and nanoelectronic power sources. *Nature* **2007,** *449* (7164), 885-U8.
5. Ozaki, N.; Ohno, Y.; Takeda, S., Silicon nanowhiskers grown on a hydrogen-terminated silicon {111} surface. *Appl Phys Lett* **1998,** *73* (25), 3700-3702.
6. Kim, B. J.; Tersoff, J.; Wen, C. Y.; Reuter, M. C.; Stach, E. A.; Ross, F. M., Determination of Size Effects during the Phase Transition of a Nanoscale Au-Si Eutectic. *Phys Rev Lett* **2009,** *103* (15).
7. Hansen, M. A., Kurt, *Constitution of Binary Alloys*. 2nd ed.; McGraw-Hill: New York, 1958; p 1305.
8. Hull, M. C.; Cambrea, L. R.; Hovis, J. S., Infrared spectroscopy of fluid lipid bilayers. *Analytical Chemistry* **2005,** *77* (18), 6096-6099.
9. Wang, H. T.; Zhang, Z.; Wong, L. M.; Wang, S. J.; Wei, Z. P.; Li, G. P.; Xing, G. Z.; Guo, D. L.; Wang, D. D.; Wu, T., Shape-Controlled Fabrication of Micro/Nanoscale Triangle, Square, Wire-like, and Hexagon Pits on Silicon Substrates Induced by Anisotropic Diffusion and Silicide Sublimation. *Acs Nano* **2010,** *4* (5), 2901-2909.
10. Zhang, Z.; Wong, L. M.; Ong, H. G.; Wang, X. J.; Wang, J. L.; Wang, S. J.; Chen, H. Y.; Wu, T., Self-Assembled Shape- and Orientation-Controlled Synthesis of Nanoscale Cu3Si Triangles, Squares, and Wires. *Nano Lett* **2008,** *8* (10), 3205-3210.
11. Hock, C.; Strassburg, S.; Haberland, H.; Issendorff, B. V.; Aguado, A.; Schmidt, M., Melting-point depression by insoluble impurities: A finite size effect. *Phys Rev Lett* **2008,** *101* (2).
12. Sutter, E. A.; Sutter, P. W., Size-Dependent Phase Diagram of Nanoscale Alloy Drops Used in Vapor-Liquid-Solid Growth of Semiconductor Nanowires. *Acs Nano* **2010,** *4* (8), 4943-4947.
13. Letellier, P.; Mayaffre, A.; Turmine, M., Melting point depression of nanosolids: Nonextensive thermodynamics approach. *Phys Rev B* **2007,** *76* (4).
14. Matsuda, Y.; Matsukage, M.; Sakamoto, N.; Suzuki, H.; Tasaka, S., Depression of melting point of eutectic metal alloy by the interaction with polyacrylates in metal-polymer composites. *Mater Lett* **2009,** *63* (21), 1886-1888.
15. Xu, Q.; Sharp, I. D.; Yuan, C. W.; Yi, D. O.; Liao, C. Y.; Glaeser, A. M.; Minor, A. M.; Beeman, J. W.; Ridgway, M. C.; Kluth, P.; Ager, J. W.; Chrzan, D. C.; Haller, E. E., Superheating and supercooling of Ge nanocrystals embedded in SiO(2). *J Phys Conf Ser* **2007,** *61*, 1042-1046.
16. Sutter, E.; Sutter, P., Phase diagram of nanoscale alloy particles used for vapor-liquid-solid growth of semiconductor nanowires. *Nano Lett* **2008,** *8* (2), 411-414.

17. Sharp, I. D.; Xu, Q.; Yuan, C. W.; Yi, D. O.; Liao, C. Y.; Glaeser, A. M.; Minor, A. M.; Beeman, J. W.; Ridgway, M. C.; Kluth, P.; Ager, J. W.; Chrzan, D. C.; Haller, E. E., Melting kinetics of confined systems at the nanoscale: Superheating and supercooling. *Aip Conf Proc* **2007,** *893*, 191-192.
18. Darling, R. B. EE-527: MicroFabrication - Wet Etching. https://www.ee.washington.edu/research/microtech/cam/PROCESSES/PDF%20FILES/WetEtching.pdf (accessed 04/07/2012).
19. Grundner, M.; Jacob, H., Ivestigation on Hydrophilic and Hydrophobic Silicon (100) Wafer Surfaces by X-Ray Photoelectron and High-Resolution Electron-Energy-Loss-Spectroscopy. *Appl Phys a-Mater* **1986,** *39* (2), 73-82.
20. Kern, W.; Puotinen, D. A., Cleanig Solutions Based on Hydrogen Peroxide for Use in Silicon Semiconductor Technology. *Rca Review* **1970,** *31* (2), 187-&.
21. Grunthaner, F. J.; Maserjian, J., Experimental -Observations of Chemsitry of SiO2-Si Interface. *Ieee Transactions on Nuclear Science* **1977,** *24* (6), 2108-2112.
22. Shu, H.; Tao, X.-M.; Ding, F., What are the active carbon species during graphene chemical vapor deposition growth? *Nanoscale* **2015**.
23. Robertson, R.; Gallagher, A., Monosilicon and Disilicon Radicals in Silane and Silane - Argon DC Discharges. *J Appl Phys* **1986,** *59* (10), 3402-3411.
24. Bruno, G.; Capezzuto, P.; Cicala, G.; Cramarossa, F., Deposition of Silicon Films from SiCl4 Glow -Discharges - A Kinetic -Model of the Surface Process. *J Appl Phys* **1987,** *62* (5), 2050-2056.
25. McCauley, T. G.; Gruen, D. M.; Krauss, A. R., Temperature dependence of the growth rate for nanocrystalline diamond films deposited from an Ar/CH4 microwave plasma. *Appl Phys Lett* **1998,** *73* (12), 1646-1648.
26. Riccardi, C.; Barni, R.; Fontanesi, M.; Tosi, P., Gaseous precursors of diamond-like carbon films in CH4/Ar plasmas. *Chem Phys Lett* **2000,** *329* (1-2), 66-70.
27. Redfern, P. C.; Horner, D. A.; Curtiss, L. A.; Gruen, D. M., Theoretical studies of growth of diamond (110) from dicarbon. *Journal of Physical Chemistry* **1996,** *100* (28), 11654-11663.
28. Riccardi, C.; Barni, R.; Sindoni, E.; Fontanesi, M.; Tosi, P., Gaseous precursors of diamond-like carbon films: chemical composition of CH4/Ar plasmas. *Vacuum* **2001,** *61* (2-4), 211-215.
29. Johnson, R. W.; Hultqvist, A.; Bent, S. F., A brief review of atomic layer deposition: from fundamentals to applications. *Materials Today* **2014,** *17* (5), 236-246.
30. Knisley, T. J.; Kalutarage, L. C.; Winter, C. H., Precursors and chemistry for the atomic layer deposition of metallic first row transition metal films. *Coordination Chemistry Reviews* **2013,** *257* (23-24), 3222-3231.
31. Lauhon, L. J.; Gudiksen, M. S.; Wang, C. L.; Lieber, C. M., Epitaxial core-shell and core-multishell nanowire heterostructures. *Nature* **2002,** *420* (6911), 57-61.
32. Schmidt, V.; Wittemann, J. V.; Senz, S.; Gosele, U., Silicon Nanowires: A Review on Aspects of their Growth and their Electrical Properties. *Adv Mater* **2009,** *21* (25-26), 2681-2702.

Chapter 6

Growth Mechanism Hypothesis of Branched Si Nanowires: Observations Made, Supporting References, and Attempts Made to Preserve Crystallinity[vi]

6.1 Introduction

The mechanism proposed in Chapter 4 is accurate, but, the work is primarily the characterization of the wire architecture and the explanation of how the secondary catalysts are formed by the extrusion of the Cu_3Si core which then go on to grow the complex branched structure. However, the initial formation of the Cu rich core is left unexplained. This can be attributed to the inability, at the time, to examine the entire length of wire from nucleation point to catalyst tip. This was due to the excess growth of non- branched wires which tangled with the branched wires. Reaction preparation and conditions have now been altered so that wire growth is composed primarily of branched wires. Table 6.1 lists previous and current reaction conditions as well as the significance of the change. Observations made to justify these changes can be found in Chapter 5. The alteration of substrate treatment, choice of copper precursor, and carrier gas flow conditions played essential roles allowing the necessary observations to be made in order to develop the following hypothesis.

Changing the substrate treatment played a crucial role into characterizing the growth mechanism for multiple reasons. Gold deposition was thought necessary to grow wires, however, it was learned to be detrimental to wire growth and not necessary. The presence of the Au on the substrate was causing extensive substrate degradation rendering large regions of the substrate barren for wire growth. The absence of gold from the substrate also prevents the excessive growth of non-branched wires. Restricting the growth of non-branched wires clarified the

[vi] Daniel J. Shissler & Amy L. Prieto.
Daniel Shissler solely contributed to synthesis and analysis presented in this dissertation chapter.

Table 6.1: A list of changed reaction conditions and how the changes have affected the growth of branched Si nanowires.

Reaction parameter	**Original**	**Current**	**Importance of change**
Substrate treatment	Poly-Lysine/ Colloidal Au treatment of Si substrate	-OH capped substrate 2 min HF/ 10 sec KOH	Au would cause substrate degradation and excess non branching wire growth. –OH capping promotes Cu deposition producing evenly distributed wire growth.
Silicon precursor	Silicon substrate	Si Powder	Si source is the SiO_2 native oxide layer on the silicon. H_2 reduces this layer allowing it to transport. If the native oxide layer is stripped off the silicon substrate prior to reaction there is no SiO_2 to transport. Using SI powder provides greater surface area of SiO_2.
Copper precursor	Cu powder	CuO/graphite powder	Original Cu source was oxide layer on Cu powder reduced by H_2 flow during reaction. Cu content restricted by the only active material being the surface oxide. CuO powder increases active source of Cu. The graphite powder reduces CuO allowing it to transport without H_2 flow.
Carrier gas flow	70:30 sccm Ar:H2 flow during furnace ramp\hold\cool down	100 sccm Ar during ramp and 20 minutes of hold. 70:30 sccm Ar:H_2 for remainder of hold. Ar purge till reactor cools to 700 °C. 400 sccm Ar during remainder of cool down.	Original conditions transported precursors during warm up and cool down causing excess growth and deposition. Ar flow during ramp and deposition time (first 20 min of hold) allows for control of Cu deposition prior to Si transport. Purge and high Ar flow flushes active species from reactor, minimizing growth and deposition during cool down

substrate so that the growth was not a dense mat of wires and branched wires could be traced to their origin. This however still proved difficult because of the resulting growth.

A substrate that is left untreated prior to reaction results in patchy growth of dense wire bundles. The density of the bundles made tracing a single wire difficult unless they were on the outer edge of the bundles. Also, transferring wires to TEM grids proved difficult because the wires were so intertwined removing them from the substrate was problematic. Thorough sonication was required to separate wires from the bundles. Typically only wire fragments could be transferred to grids for TEM analysis. As described in Chapter 5, it was discovered that evenly distributed wire growth can be achieved by capping the Si substrate with –OH groups. Evenly distributed wires can then be observed from nucleation point to catalyst tip via SEM. The density of wires could also be controlled with the addition of a deposition step.

Metal catalyst must first be deposited prior to wire growth. Originally this was the purpose of the colloidal gold. However, it was discovered to be detrimental as well as not necessary. During the time this was realized, the copper precursor was copper oxide powder. Copper oxide requires the flow of H_2 in order to transport Cu. But H_2 is also necessary for the transport of silicon. Because both precursors are dependent on the flow of H_2, copper catalyst could not be deposited prior to silicon transport. Due to this coupled transport, the catalyst size was small during the initial nucleation of the wire. Wire diameter is dependent upon the catalyst size.[1-3] Therefore, initial wire diameters were small causing there to be long lengths of non-branched wire prior to branching. However, the use of a CuO/graphite powder as a precursor negated this problem.

Alterations of carrier gas flow rates were changed to address the precursor transport problems as well as others. The use of the CuO/graphite powder enabled the ability to transport Cu without the flow of H_2. This behavior decouples the transport of Cu and Si during the reaction. Copper transport occurs once the temperature rises high enough with only Ar present. This way Cu can be transported and deposit catalyst particles prior to the transport of Si. This is done by only flowing argon during the ramp stage. Argon flow is still held once reaction temperature is reached to allow for Cu deposition. The duration of this segment can be varied to control the amount of copper deposited and therefore the initial catalyst size can be adjusted. Once the allotted deposition time is over, hydrogen flow starts and prompts the transport of Si. Because of the larger initial Cu catalysts, wire diameters are increased. The significance of this will be brought to light later in this chapter. Another alteration to the flow conditions is a purge step that occurs after the growth process. Hydrogen flow is terminated and the Ar and vacuum valves are completely opened. These conditions are held until the temperature drops to below

700 °C. At this point, the argon flow is dropped to 400 sccm until cooling is complete. This process flushes any vaporous content from the system quenching any further growth and prevents the remaining vaporous content from depositing on the substrate during the cooling process (plot of reaction can be found in the appendix). This limits any deposition or growth to the intended segments. All these changes to reaction preparation and conditions were necessary to make the proper observation so that the following hypothesis could be formulated.

6.2 Silicide Formation

The proposed hypothesis does not discredit the former growth mechanism but expands upon it and reveals that the growth process is much more complex than what was previously understood. The original proposed mechanism stresses the importance of the formation of a silicide phase which forms in the core of the silicon nanowire. If the branched wire growth is solely dependent upon the formation of a silicide phase, the growth of branched wires should be possible using other elemental combinations. Instead of Cu, it should be possible to grow branched nanowires by forming the silicides of Fe, Ni, and Mn, based on phase diagram data.[4] Several attempts were made to synthesize branched wires with the use of various Fe, Ni, and Mn precursors to no avail. The growth of non-branched Si nanowires was accomplished, but was not the intended goal. Some reactions did produce branched wires, however, it was discovered that the branches were the result of Cu contamination within the reaction system. After consistent failure to produce branched wires with various metal precursors, a more thorough examination of the Cu/Si interaction was performed. From the literature, it was discovered that the interaction of Cu and Si is rather unique compared to other elemental combinations. The diffusion of Cu into Si is remarkably higher than that of other metals.[5-6] This higher rate of diffusion explains why

the other elemental combinations did not produce wires. The formation of the silicide core is not solely dependent on the metals ability to form a silicide phase, but also requires the ability to quickly diffuse into the silicon wire.

However, the literature reports that Cu and Si have an exclusive nature that does not easily explain the growth behavior of the grown branched nanowires. The literature primarily contains information about the effects of copper contamination in Si, because of the use of Si in the semiconductor industry. Most literature reports that a solid solution is highly disfavored and the Cu agglomerates and silicide formation occurs. The silicide is observed to form in voids of the material, crystalline defects, or is extruded to the surface of the material. [6-11] This studied behavior could answer a lot of standing questions about the formation of the silicide core and its extrusion during the initial stages of branched wire growth.

With most elemental mixtures, the expected behavior would be to diffuse into the wire homogenously across the diameter. However, it was observed that the Cu forms a silicide core within the wire. Combined with what is found in literature this behavior would imply either a void or defect along the length of the wire. Interestingly enough, TEM images show that this is likely a possibility. With TEM

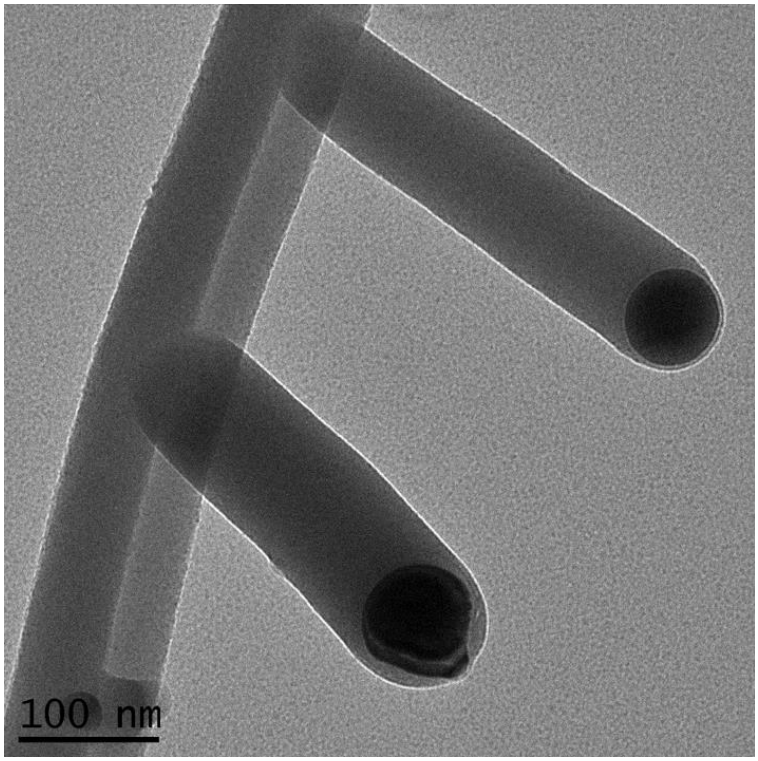

Figure 6.1: A TEM images of primary and secondary wires. A contrast line can be observed in primary wire.

imaging along the length of the branched section of wire there is a line of brighter contrast (Figure 6.1). In literature this line is an indication that there is a twinning defect along the wire.[12-15] However, this observation cannot be directly attributed to the presence of a twinning defect since the branched wires are not crystalline at the time of imaging. The wires with the contrast line in literature are still in a crystalline state. Since the branched wires instantly oxidize upon exposure to atmosphere, the crystalline nature of the wires during growth remains unknown. Without crystalline data the growth mechanism cannot be directly identified, nevertheless, a mechanism may be speculated from Si growth nature reported in literature and observations of the branched silicon nanowires.

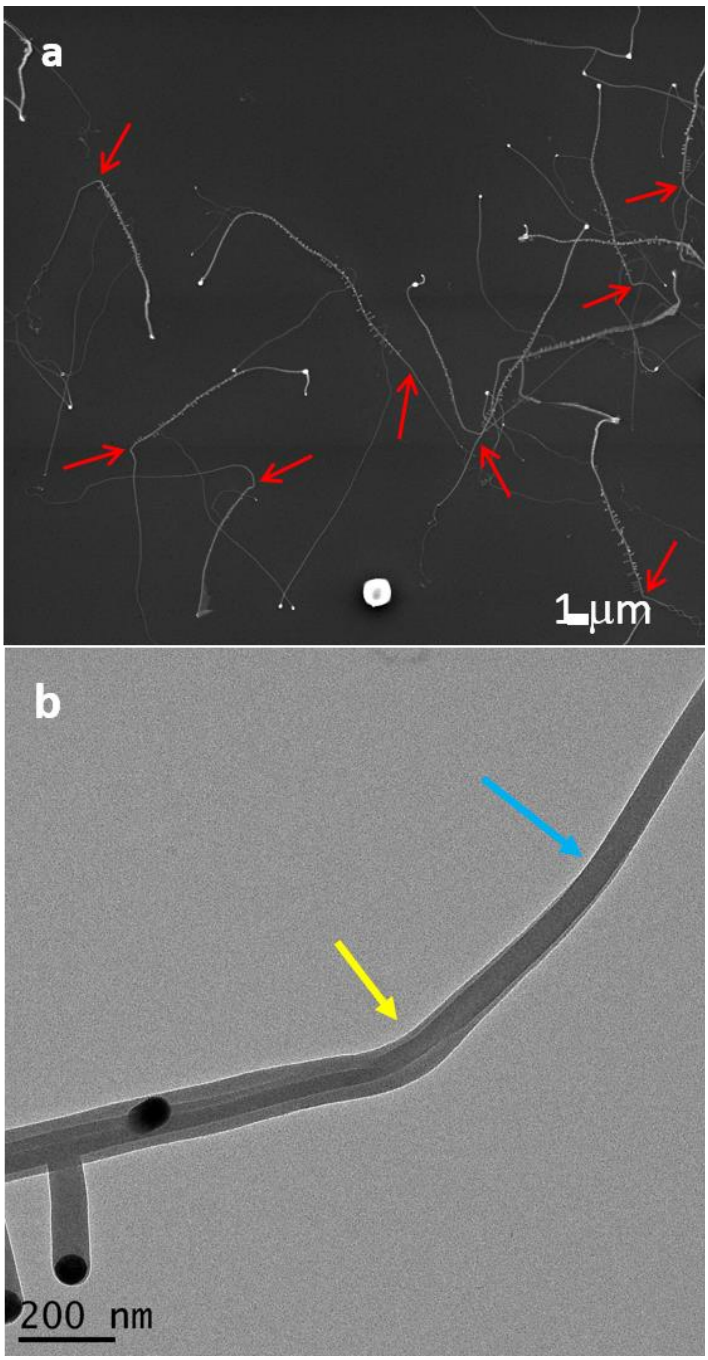

Figure 6.2: (a) An SEM image of multiple wire with minor to abrupt kinks (red arrows) just prior to branched wire growth. (b) TEM image of duel kinks in wire.

6.3 Si Wire Growth Direction

The growth of crystalline Si nanowires is something that has been

thoroughly characterized and discussed in literature.[1-3, 13-32] Comparing the collected knowledge of typical Si nanowire growth with observations of branched wire morphologies and wire diameter has led to the development of an in depth growth mechanism hypothesis. The most foretelling discovery was the observation of multiple wires kinking just prior to the growth of branching wires (Figure 6.2a). SEM images reveal that the entire length of the wire is not branched. When the wires initially grow, the wire diameter is smaller and no branching is observed. At some point during this initial growth the wires form a kink and then branching occurs. Upon closer observation with TEM (Figure 6.2b), it was discovered that the wires contain two distinct kinks and a change in structure. In the top right of the image in Figure 6.2b the wire is composed of a single contrast. After the first kink, indicated by the blue arrow, two contrasts can be observed forming a core shell structure. Along this length of wire approaching the second kink, indicated by the yellow arrow, and an increase in diameter is noticeable. Then, after the second kink a core shell structure can still be observed but now with the addition of a contrast line. Shortly after the second kink branches begin to form. As previously mentioned, the line may indicate that there is a twinning defect within the wire during growth. It is not known whether this line would still appear after oxidation, however, there is a visible line with no other explanation. In silicon nanowire growth, a stacking fault can occur and form a twinning defect which changes the direction of growth, kinking the wire.[12] So, the kinks that occur prior to branching may be caused by a change in the direction of wire growth. Also coinciding with the kinks in the wire, a significant change in wire diameter can be observed.

Si nanowires typically grows in one of three different crystalline directions. Several sources have reported that the growth direction is dependent upon wire diameter.[1-3] This dependence is due to the differing interface energies between the solid Si wire and the liquid Au

catalyst. The three growth directions; ⟨110⟩, ⟨112⟩, and ⟨111⟩; grow over a range of wire diameters. Reported by Lieber et al, the three size regions are 1-10, 10-20 and 20+ nm for the ⟨110⟩, ⟨112⟩, and ⟨111⟩ growth directions, respectively.[2] The paper states that the growth direction correlates with differing ranges of wire diameter. However, the ranges specified will differ with alternate reaction parameters. At different temperatures the energies between the catalyst and wire will change and the ranges at which growth direction changes will shift. In addition to temperature differences, if the catalyst is composed of an alternative alloy the interaction between the catalyst and the wire will also be different. Since our reactions are performed several hundreds of degrees higher and utilize a Cu-Si alloy averse to the Au-Si used in literature, discrepancies are expected.

Typically during silicon nanowire growth, the catalyst material is deposited prior to the actual reaction, via evaporation or colloidal solution. During an early stage before wire growth, swelling of the catalyst occurs, due to the absorption of Si, until the catalyst reaches saturation point. Once this point is reached, Si nucleates and nanowire growth initiates. During wire growth a steady state is reached and the wire grows at the rate at which Si is absorbed. Because of this steady state, the wire grows at a uniform diameter along the length of the wire. In contrast, the catalyst in our work is deposited from the vaporous state in the early stages and throughout the reaction. Then, during wire growth, catalyst material is continuously being transported which increases the catalyst size. As mentioned previously, wire diameter is dependent upon catalyst size, therefore the diameter of the wire also increases along with the catalyst. Once the diameter reaches a size at which the catalyst/wire interface becomes unstable the growth direction changes, creating a kink. As the wire diameter grows further the growth direction again changes creating the second kink. Wire diameters of the three sections of wires have been analyzed with

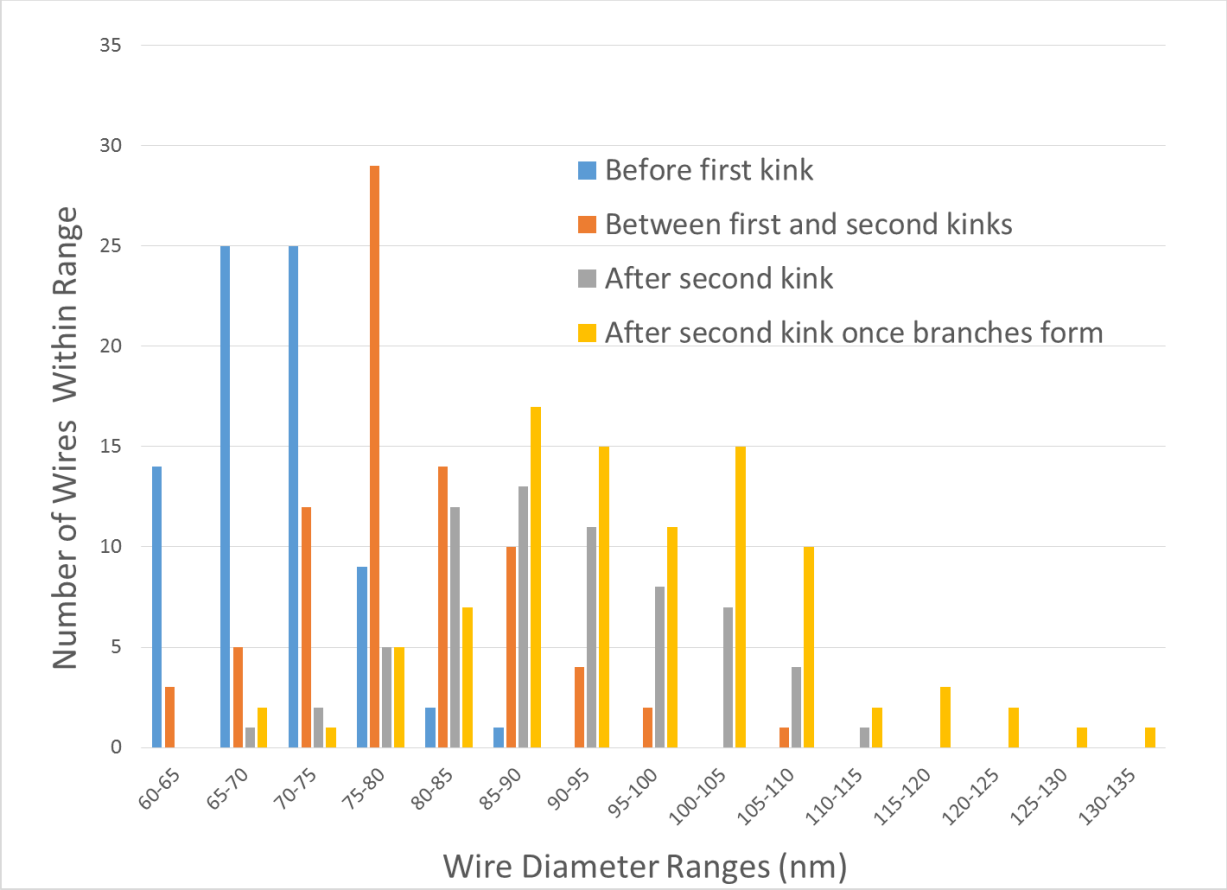

Figure 6.3: Hysteresis plots representing wire diameter distribution between kinks in wire.

TEM imaging (Figure 6.3). As can be seen the second and third measurements form well shaped histogram peeks. The first measurement, before the first kink, is shifted to the left. This is because the measurements were taken just prior to the kink. So it represents the maximum diameter which growth is stable in that direction. As for the fourth measurement, it was taken at the point at which the first branch forms after the second kink. The larger diameters of these measurements can be attributed towards the extra catalyst swelling that occurs prior to its incorporation into the wire. These results greatly support the hypothesis that the kinks are caused by a change in growth direction due to the increase in wire diameter. It is believed that along with the second change in growth direction a twinning defect occurs allowing for the incorporation of catalyst material into the core of the wire.

From the work of Lauhon et al it is known that during nanowire growth, catalyst material can be incorporated into crystalline defects within the wire, specifically twinning defects.[30] They explain the incorporation of Au catalyst are a few Au atoms along the wire length. However, they suggest wires grown with catalyst of smaller atomic radii would likely have an increased amount of catalyst material incorporated. This analysis, along with the known high diffusivity behavior of Cu and Si, supports the hypothesis that Cu catalyst is quickly incorporating into the Si twinning defect. Once there, Cu_3Si forms and is then extruded to the surface to reduce interfacial energy within the crystal. The formation and extrusion of Cu_3Si within a Si matrix is common and even observed on the bulk scale.[6-11] However, there is a caveat to findings of Lauhon et al that does not fully support the hypothesis.

6.4 Twinning Defect Formation

Growth direction of Si nanowires typically goes from ⟨110⟩ to ⟨112⟩ to ⟨111⟩ as the wire diameter increases. This would indicate that the first kink in our nanowires is the change from ⟨110⟩ to a ⟨112⟩ direction and then the second kink is a change to the ⟨111⟩ direction. However, Lauhon's findings show that twinning defects only occur in the ⟨110⟩ and the ⟨112⟩ directions of which only the ⟨112⟩ direction incorporates catalyst. This would indicate that our final growth direction does not in fact possess a twinning defect.

However, the work of Picraux et al implies that growth direction is not solely dependent upon wire diameter.[12] Picraux et al demonstrate that during fast growth conditions, driven by a high Si partial pressure, a wire forms a stacking fault which leads to a twinning defect, forcing the wire from a ⟨111⟩ growth direction to ⟨112⟩.[12] Several other sources also observe that kinks accompany twinning defects initiated by a high Si partial pressure.[13-14, 19, 33] One even implies

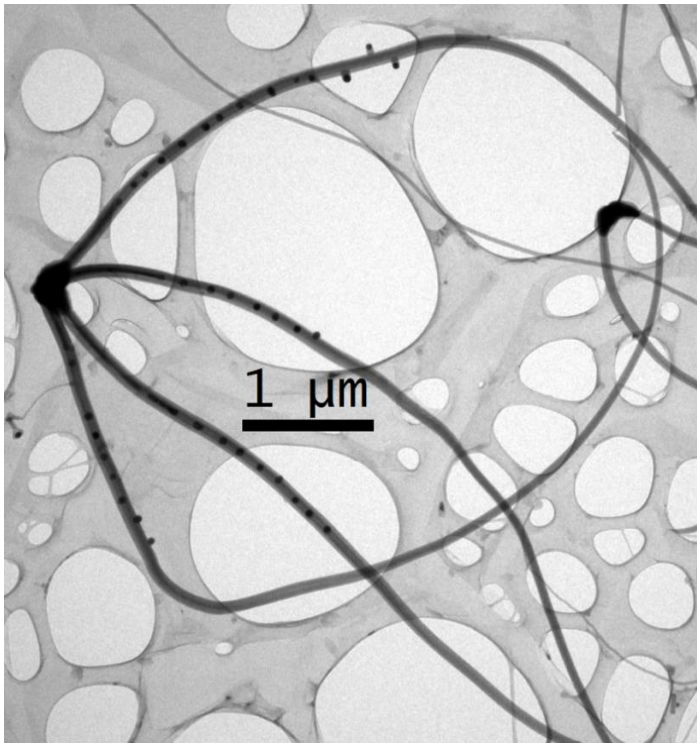

Figure 6.4: A TEM image of a single catalyst forming multiple branched wires

that the formation of the twinning defect may be dependent upon the diameter of the wire.[14] It could be said that because of the fast growth an error occurs in the crystalline structure and this defect then propagates as the crystal grows. During our growth it is common to see several wires growing from a single catalyst (Figure 6.4). This indicates that Si levels are high enough within the catalyst to promote multiple nucleation points to try and dissipate the silicon content. With such high levels of Si in the catalyst it is likely that the wires are growing under “fast growth conditions" and have high Si supersaturation. It is thought that this is also a possible benefit of removing Au from the reaction. A combined Au-Cu catalyst would increase the solubility of Si within the catalyst requiring higher levels of Si to reach supersaturation levels. So, removing the Au would allow high supersaturation levels to be reached more easily and increase branched wire growth. Perhaps in our wires the ⟨112⟩ growth direction is initially skipped. The first kink is perhaps a direction change from the ⟨110⟩ direction to the ⟨111⟩ growth direction. Then, high supersaturation levels are reached forcing a ⟨112⟩ growth direction with a twinning defect. With these finding of Picraux et al the standing hypothesis is still feasible.

So to recap on the entire branched wire process, Cu catalyst is transported and deposited during the initial deposition segment of the reaction. Silicon transport is then initiated by starting

the flow of hydrogen. The vaporous Si dissolves into the Cu catalyst increasing catalyst size and Si content. Once the point of Si supersaturation is reached, Si nucleates and a wire begins to grow. As both Cu and Si are transported the catalyst swells and the wire diameter increases. Once the initial growth direction becomes unfavorable due to the increased wire diameter, the growth direction changes forming the first kink. Then as the wire diameter increases more the growth direction changes again either due to the unfavorable wire diameter or high supersaturation levels. Within this final segment of wire, a twinning defect forms which the Cu then diffuses into forming the Cu_3Si core. This core then segments into spheres to reduce surface interaction with the Si shell. These Cu_3Si spheres extrude to the surface of the wire to further reduce the surface contact with the Si shell. Once reaching the surface, the Si diffuses into the Cu_3Si particles which then become saturated and begin to grow as a branch on the primary wire. By observation and literature findings this is a feasible growth mechanism. Crystalline data would be pivotal in confirming the growth mechanism. Be that as it may, crystalline data has not been collected due to the immediate oxidation of the wires upon exposing to atmosphere.

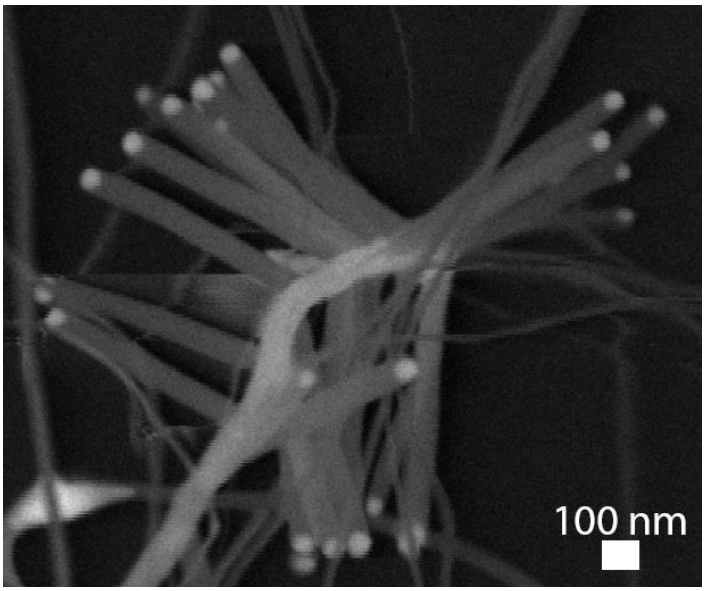

Figure 6.5: An SEM image looking down the primary wire axis. It can be observed that secondary wires grow with three fold symmetry.

Because of the amorphous nature of the wires the proposed mechanism has not been varified due to the lack of crystalline data. It has been asked how it is known that there is not oxygen contamination and the wires are not grown as amorphous SiO_2. The nature of

the growth as well as several observations suggest they are grown as crystalline Si. VLS growth by nature produces crystalline wires. Also, non-branched wires grown during the reaction diffract and index as Si. It is likely that if there was oxygen contamination all wires grown during the reaction would be SiO_2. The most revealing evidence that the wires grow as crystalline Si is a fortunate observation made during SEM imaging (Figure 6.5). The image is looking down the length of a primary wire. As can be seen, the secondary wires grow out of the primary with three fold symmetry. The only explanation for this would be if the wires grow preferentially on specific crystalline faces. This could only mean that the wires are crystalline during growth. Identifying the crystalline orientation of the wires would be most fruitful.

6.5 Prevention of Si Oxidation

Several different attempts to maintain crystallinity of the wires have been employed. Prior to my involvement several attempts were made to minimize the exposure of the wires to atmosphere by transferring the substrate to a glove box while under inert conditions. TEM grids were then prepared in the glove box. TEM grids were transported to the TEM under inert atmosphere. Although great scrutiny was taken to minimize atmospheric exposure prior to TEM, the transfer to the actual TEM chamber requires a moment in which the sample must be exposed. From these attempts no crystalline data was ever achieved. Other attempts made towards maintaining crystallinity involve the removal of oxidizing catalyst rather than negating exposure to atmosphere.

Exposing the wires to atmosphere cannot be avoided while transferring the wires to the TEM chamber, so different methods to remove the oxidative catalyst prior to atmospheric exposure was attempted. One of these methods was a quick and simple procedure. An HF bath

should completely remove any metals, including Cu, and silicon oxides from the substrate. Attempts were made to transfer the substrate, while under inert conditions, from the reaction chamber to a bath of degassed HF. This way the Cu would be removed and the oxidation of the wires halted. Although the removal of Cu was successful, there was no evidence of branched wires remaining. Only non-branched wires remained on the substrate. A brief exposure to atmosphere was necessary while transferring the substrate to the HF bath. Because oxidation occurs so quickly, a method was developed to try and remove the Cu prior to opening the reactor to atmosphere.

As previously mentioned Cu contamination was present during reactions attempted with Fe, Ni, and Mn. This contamination was eventually determined to originate from the inlet lines of the reactor. The contamination was likely deposited there during another reaction performed in the furnace. Along with the Cu contamination there was also mild traces of sulfur. It was assumed that during the annealing, sulfur vaporized and transported Cu into the lines. The observed transport of Cu via sulfur, a bane at the time, was then later taken advantage.

Because of the easy transport of Cu by S, it was proposed that it may be possible to remove the Cu from the branched wires by flowing H_2S over the wires after they had been grown. Literature suggested that this should be possible without affecting the wires themselves.[34] Cu transport should occur at much lower temperatures than that of Si. Attempts were made to grow branched Si wires and then during the reactor cool down H_2S would be flown over the substrate to transport the Cu away and leave the Si wires unharmed. Although this seemed plausible, it proved otherwise in practice. It was observed that Si transport was significant at lower temperatures than proposed by literature.

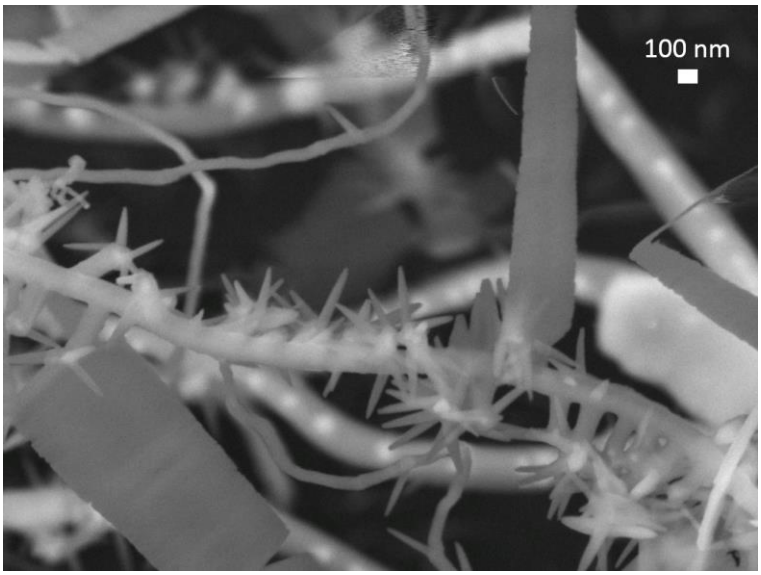

Figure 6.6: An SEM image of Si spikes and ribbons growing from secondary catalysts as a result of H_2S treatment.

Sulfur-treated substrates showed interesting forms of growth while imaging with SEM. Spikes and ribbons were observed growing from the copper catalysts (Figure 6.6). By EDS mapping these were determined to be composed of Si. It is likely that the H_2S is transporting the Si further and then the catalysts absorb the Si producing more growth. The high surface area of the wires likely provide more reactive silicon than compared to the work done in literature making it more reactive. In addition to the unexpected Si transport, the transport of Cu appeared to be minimal. Cu droplets usually can be found in pits of the Si substrate. After the H_2S treatment similar pits could be found. However, the Cu droplet are no longer present and the edges of the pit is lined with copper and sulfur. It is likely that the H_2S successfully etches the Cu but only transports it a minimal amount. Addition of hydrogen to the H_2S treatment aids in Cu transport. However, it increases the growth of Si ribbons indicating a greater transport of Si. Further adjustments of conditions during the H_2S treatment may provide better results, but instead another treatment method was conceived.

Instead of removing the Cu from the wires it may be possible to coat the wires to prevent the exposure to oxygen. Reactions are performed in quartz tubes coated with carbon so that oxygen and water do not diffuse out of the quartz during the reaction. The carbon coating is deposited by thermally decomposing methane gas. If the carbon coating can prevent the diffusion

of oxygen and water at elevated temperature certainly it should do the same at room temperature.

As was done with the H_2S treatment, the wires were treated with methane during the cool down process. Preliminary experiments show that the wires were successfully coated. However, the coatings are not likely fully reduced carbon. During SEM analysis, large amounts of charging occurs during imaging. The wires also exhibit large amounts of contrast change during the imaging. This is a sign that the coating is likely hydrocarbons burning off because of the electron beam. TEM analysis is necessary in order to collect crystal data on the wires. However, the hydrocarbon coating would likely contaminate the column. Resolving the issue of the hydrocarbon coating would be preferable before TEM imaging of the coated wires.

6.6 Conclusion

A sound hypothesis of the growth mechanism of branched silicon nanowires has been devised. The primary catalyst swells as it absorbs Si and Cu during wire growth. The enlarged catalyst causes the wire diameter to increase as it grows. A critical wire diameter is reached which destabilizes the catalyst/wire interface. The wire growth reorients to a different growth direction to accommodate the instability. Then as the wire continues to grow the growth direction again changes. The second direction change may be a result of the continued increase in diameter size or the formation of a twinning defect brought on by fast growth conditions. In this final growth direction there is a twinning defect. Copper from the primary catalyst then diffuses into the twinning defect because of its inherent behavior to form Cu_3Si in Si defects. The silicide core then segregates and extrudes to the surface to minimize surface interaction with the Si shell. The ejected silicide then acts as secondary catalysts, absorb Si, and then begin to grow wires themselves. Observations made to formulate this growth mechanism is supported by

knowledge found in literature. Proving the hypothesis is completely dependent upon the determination of the crystalline growth direction of the wires. The amorphous state of the wires proves most disadvantageous since it inhibits our ability to characterize growth direction. Many attempts to retain crystallinity have been made without success. The H_2S and carbon coating methods may yet prove fruitful with further manipulation of reactor conditions. If crystallinity cannot be maintained, an in depth study of the wire morphology may expose further details of the growth mechanism. TEM tomography may prove most effective towards this end. A three dimensional construction of the wire may unmask the nature of the contrast line observed during TEM imaging. Several structural oddities, including wire fracturing and veining, have been observed during TEM imaging which may also prove essential to the growth process. With limited resources these observations have gone unexplained. The new Jeol 2100F TEM is an incredible addition to the Chemistry Department and may prove invaluable to the advancement of the branched Si nanowire project.

References

1. Cui, Y.; Lauhon, L. J.; Gudiksen, M. S.; Wang, J. F.; Lieber, C. M., Diameter-Controlled Synthesis of Single-Crystal Silicon Nanowires. *Appl Phys Lett* **2001,** *78* (15), 2214-2216.
2. Wu, Y.; Cui, Y.; Huynh, L.; Barrelet, C. J.; Bell, D. C.; Lieber, C. M., Controlled Growth and Structures of Molecular-Scale Silicon Nanowires. *Nano Lett* **2004,** *4* (3), 433-436.
3. Schmidt, V.; Senz, S.; Gosele, U., Diameter-Dependent Growth Direction of Epitaxial Silicon Nanowires. *Nano Lett* **2005,** *5* (5), 931-935.
4. Hansen, M. A., Kurt, *Constitution of Binary Alloys*. 2nd ed.; McGraw-Hill: New York, 1958; p 1305.
5. Holmberg, V. C.; Collier, K. A.; Korgel, B. A., Real-Time Observation of Impurity Diffusion in Silicon Nanowires. *Nano Lett* **2011,** *11* (9), 3803-3808.
6. Istratov, A. A.; Weber, E. R., Physics of Copper in Silicon. *J Electrochem Soc* **2002,** *149* (1), G21-G30.
7. Li, X. Q.; Yang, D. R.; Yu, X. G.; Que, D. L., Phosphorus Gettering of Precipitated Cu in Single Crystalline Silicon Based on Rapid Thermal Process. *J Cryst Growth* **2010,** *312* (21), 3069-3074.
8. Li, X. Q.; Yang, D. R.; Yu, X. G.; Que, D. L., Precipitation and Gettering Behaviors of Copper in Multicrystalline Silicon Used for Solar Cells. *T Nonferr Metal Soc* **2011,** *21* (3), 691-696.
9. Solberg, J. K., Crystal-Structure of Eta-Cu3si Precipitates in Silicon. *Acta Crystallogr A* **1978,** *34* (Sep), 684-698.
10. Wen, C. Y.; Spaepen, F., Filling the Voids in Silicon Single Crystals by Precipitation of Cu3si. *Philos Mag* **2007,** *87* (35), 5565-5579.
11. Das, G., Precipitation of Copper in Silicon. *J Appl Phys* **1973,** *44* (10), 4459-4467.
12. Dayeh, S. A.; Wang, J.; Li, N.; Huang, J. Y.; Gin, A. V.; Picraux, S. T., Growth, Defect Formation, and Morphology Control of Germanium-Silicon Semiconductor Nanowire Heterostructures. *Nano Lett* **2011,** *11* (10), 4200-4206.
13. Boukhicha, R.; Vincent, L.; Renard, C.; Gardes, C.; Yam, V.; Fossard, F.; Patriarche, G.; Jabeen, F.; Bouchier, D., Gold Nanocluster Distribution on Faceted and Kinked Si Nanowires. *Thin Solid Films* **2012,** *520* (8), 3304-3308.
14. Akhtar, S.; Usami, K.; Tsuchiya, Y.; Mizuta, H.; Oda, S., Size-Dependent Structural Characterization of Silicon Nanowires. *Japanese Journal of Applied Physics* **2008,** *47* (6), 5053-5056.
15. Carim, A. H.; Lew, K. K.; Redwing, J. M., Bicrystalline Silicon Nanowires. *Adv Mater* **2001,** *13* (19), 1489-+.
16. Schmidt, V.; Wittemann, J. V.; Senz, S.; Gosele, U., Silicon Nanowires: A Review on Aspects of Their Growth and Their Electrical Properties. *Adv Mater* **2009,** *21* (25-26), 2681-2702.
17. Schwarz, K. W.; Tersoff, J., Elementary Processes in Nanowire Growth. *Nano Lett* **2011,** *11* (2), 316-320.
18. Tan, T. Y.; Lee, S. T.; Gosele, U., A Model for Growth Directional Features in Silicon Nanowires. *Appl Phys a-Mater* **2002,** *74* (3), 423-432.
19. Cayron, C.; Den Hertog, M.; Latu-Romain, L.; Mouchet, C.; Secouard, C.; Rouviere, J. L.; Rouviere, E.; Simonato, J. P., Odd Electron Diffraction Patterns in Silicon Nanowires and

Silicon Thin Films Explained by Microtwins and Nanotwins. *Journal of Applied Crystallography* **2009,** *42*, 242-252.
20. den Hertog, M. I.; Cayron, C.; Gentile, P.; Dhalluin, F.; Oehler, F.; Baron, T.; Rouviere, J. L., Hidden Defects in Silicon Nanowires. *Nanotechnology* **2012,** *23* (2).
21. Wang, D.; Qian, F.; Yang, C.; Zhong, Z. H.; Lieber, C. M., Rational Growth of Branched and Hyperbranched Nanowire Structures. *Nano Lett* **2004,** *4* (5), 871-874.
22. Tian, B. Z.; Xie, P.; Kempa, T. J.; Bell, D. C.; Lieber, C. M., Single-Crystalline Kinked Semiconductor Nanowire Superstructures. *Nat Nanotechnol* **2009,** *4* (12), 824-829.
23. Kim, B. J.; Tersoff, J.; Wen, C. Y.; Reuter, M. C.; Stach, E. A.; Ross, F. M., Determination of Size Effects During the Phase Transition of a Nanoscale Au-Si Eutectic. *Phys Rev Lett* **2009,** *103* (15).
24. Wen, C. Y.; Reuter, M. C.; Tersoff, J.; Stach, E. A.; Ross, F. M., Structure, Growth Kinetics, and Ledge Flow During Vapor-Solid-Solid Growth of Copper-Catalyzed Silicon Nanowires. *Nano Lett* **2010,** *10* (2), 514-519.
25. Ross, F. M.; Wen, C. Y.; Kodambaka, S.; Wacaser, B. A.; Reuter, M. C.; Stach, E. A., The Growth and Characterization of Si and Ge Nanowires Grown from Reactive Metal Catalysts. *Philos Mag* **2010,** *90* (35-36), 4769-4778.
26. Allen, J. E.; Hemesath, E. R.; Perea, D. E.; Lensch-Falk, J. L.; Li, Z. Y.; Yin, F.; Gass, M. H.; Wang, P.; Bleloch, A. L.; Palmer, R. E.; Lauhon, L. J., High-Resolution Detection of Au Catalyst Atoms in Si Nanowires. *Nat Nanotechnol* **2008,** *3* (3), 168-173.
27. Perea, D. E.; Wijaya, E.; Lensch-Falk, J. L.; Hemesath, E. R.; Lauhon, L. J., Tomographic Analysis of Dilute Impurities in Semiconductor Nanostructures. *J Solid State Chem* **2008,** *181* (7), 1642-1649.
28. Perea, D. E.; Hemesath, E. R.; Schwalbach, E. J.; Lensch-Falk, J. L.; Voorhees, P. W.; Lauhon, L. J., Direct Measurement of Dopant Distribution in an Individual Vapour-Liquid-Solid Nanowire. *Nat Nanotechnol* **2009,** *4* (5), 315-319.
29. Lensch-Falk, J. L.; Hemesath, E. R.; Perea, D. E.; Lauhon, L. J., Alternative Catalysts for Vss Growth of Silicon and Germanium Nanowires. *J Mater Chem* **2009,** *19* (7), 849-857.
30. Hemesath, E. R.; Schreiber, D. K.; Gulsoy, E. B.; Kisielowski, C. F.; Petford-Long, A. K.; Voorhees, P. W.; Lauhon, L. J., Catalyst Incorporation at Defects During Nanowire Growth. *Nano Lett* **2012,** *12* (1), 167-171.
31. Vincent, L.; Boukhicha, R.; Gardes, C.; Renard, C.; Yam, V.; Fossard, F.; Patriarche, G.; Bouchier, D., Faceting Mechanisms of Si Nanowires and Gold Spreading. *J Mater Sci* **2012,** *47* (4), 1609-1613.
32. Hyun, Y. J.; Lugstein, A.; Steinmair, M.; Bertagnolli, E.; Pongratz, P., Orientation Specific Synthesis of Kinked Silicon Nanowires Grown by the Vapour-Liquid-Solid Mechanism. *Nanotechnology* **2009,** *20* (12).
33. Madras, P.; Dailey, E.; Drucker, J., Kinetically Induced Kinking of Vapor-Liquid-Solid Grown Epitaxial Si Nanowires. *Nano Lett* **2009,** *9* (11), 3826-3830.
34. Raichoud.P; Noreika, A. J., Hydrogen Sulfide as an Etchant for Silicon. *J Electrochem Soc* **1969,** *116* (4), 539-&.

Appendix I

Reactor Automation and Renovation

A difficulty with CVD reactions is reproducibility. To minimize this issue, it is required to have precise control over temperature, flow rates, and pressure. Currently these parameters are regulated by a collection of devices which are united within a single LabVIEW interface. Reactions are performed in Lindberg Blue Single-Zone Tube Furnace (Figure I.1L) controlled by a Tokigawa UP 1500 temperature controller. Flow rates of gases are controlled by Sierra Instruments Smart-Trak Mass Flow Controllers (Figure I.1A-D). Pressure is measured by a convection gauge tube and a thermal conductivity tube (Figure I.1P) and displayed on gauges (Figure I.1J) which is then recorded by the LabVIEW interface via connection through a National instruments DAQ card (Figure I.1K). The pressure is then regulated by a solenoid valve (Figure I.1P) driven by valve drivers (not displayed in Figure I.1) controlled by the same LabVIEW interface. The LabVIEW program utilizes a Proportional-Integral-Differential (PID) function to optimize the signal to maintain a stable pressure. To minimize human error during reactions, the system is fully automated by programming the reaction parameters prior to the reaction. This allows precise timing of the different reaction parameters. By these means it is possible to arrive to the lab in the morning to a freshly produced sample by setting up the reaction and programming it the night before. This could be said to be an ideal way of performing CVD reactions, however, the reactor has been considerably grown since its initial inception.

Upon my joining the Prieto group the CVD reactor consisted of only the tube furnace, four MFC's, a needle valve to regulate output to a vacuum pump, and pressure gauges. The tube furnace is controlled by a programmable temperature controller. The controller can be programmed to

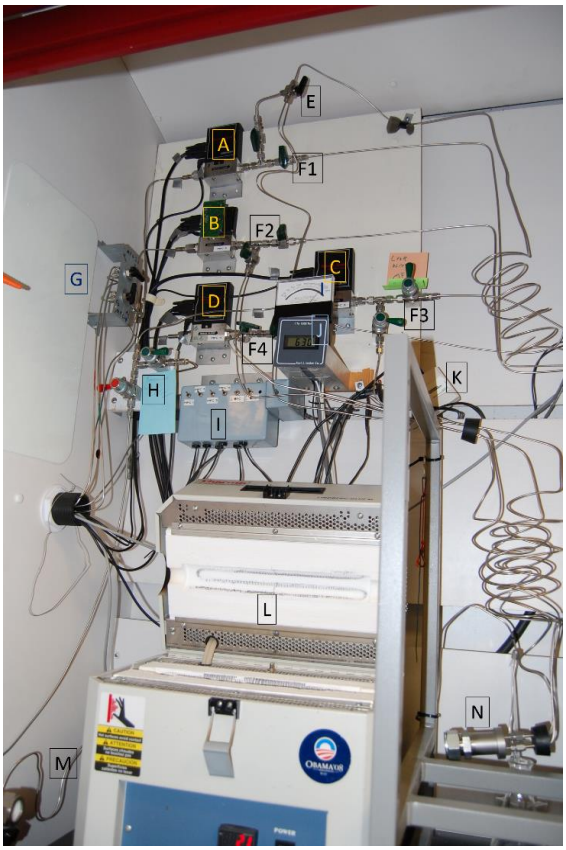

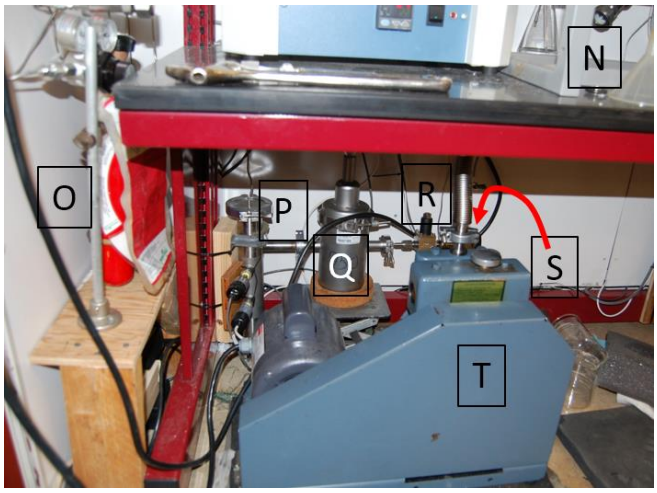

Figure I.1: Pictures of the CVD reactor and its parts labeled. A-D) Mass flow controllers (MFC) for carrier gases. MFC C is equipped with Kalrez seals as well as diaphragm valves (F3) for caustic gases E)Three way ball valve to switch between inlet manifolds F)Valves to control carrier gas flow between the single zone or three zone furnace G) Three way ball valves to switch carrier gases of MFCs 2 and 4 H) Stainless steel diaphragm valves to switch carrier gases of MFC C. Also used to purge lines of caustic gasses I) Power switches to MFCs and solenoid valve drivers J) Pressure gauge displays K) National Instruments DAQ card L) Lindeberg-Blue single zone furnace M) Outlet Manifold N) Inlet Manifold O) Caustic Gas cylinder holder P) Stainless steel tube equipped with pressure sensors Q) Liquid nitrogen trap R) Solenoid valve for pressure control S) Three way ball valve for venting trap T) DuoSeal belt driven vacuum pump.

ramp the reactor to set temperature within a set amount of time and then hold that temperature for a desired time span. At the time the MFC's were operated by four individual computer interfaces and required the manual entry of flow rates at the appropriate times. Excruciatingly, the pressure was controlled by manually adjusting the needle valve so that the desired pressure was reached. Then, the needle valve needed to be correctly positioning so that the outlet flow was balanced with the inlet flow, stabilizing the pressure. This procedure was troublesome enough for running a reaction. However, prior to running each reaction pump/purge cycling is performed. So, reaction preparation required at least 30 minutes of supervision. Also, adjustments during reactions were very irreproducible since flow rates and pressures had to be entered and adjusted manually. Reactions currently being performed would not be possible with a manually controlled reactor. With the current incarnation of the reactor, one can now preprogram the pump purge process, furnace conditions, and reaction pressures and flow rates push a button and walk away with no further supervision. Appendix A will explain the growth and changes to the reactor during my time here.

The first improvement upon the reactor was the creation of a single interface by use of National Instruments LabVIEW. LabVIEW visualizes typical programming code by a flowchart representation. It took several nights to become familiar with the different options and commands. Thankfully, I am familiar with programming logic due to courses taken during primary education.

Within the LabVIEW interface, the first devices integrated were the MFCs. Sierra Instruments had provided a LabVIEW interface to operate a single MFC. Using the original interface provided by sierra, I was able to integrate the four MFCs into a single interface. This enabled the ability to enter flow rates for different gasses simultaneously. This was only a minor improvement. The purchase of a DAQ card, a solenoid valve, and valve driver provided a greater

benefit. The DAQ card is used to record pressure and control the solenoid valve. The solenoid valve was attached between the reactor and the vacuum pump.

Solenoid valves operate by opening when an electric current is applied to the solenoid. This current is provided by the solenoid driver. The driver is controlled by a 0-5 DCV signal applied by the NI DAQ card. The position of the valve is proportional to the voltage applied to the driver. The signal voltage is entered via LabVIEW interface. From the interface a value can be entered to position the valve. So if vacuum is desired a value of 5 is entered, the valve opens and vacuum is pulled. However if a particular pressure needs to be achieved, one would need to enter a value and pull vacuum to that pressure and then shut it off. Now if that pressure needed to be maintained while flowing a carrier gas, one would need to adjust that value till the pressure stabilized as desired. Pointedly, this is the same procedure that had been performed prior with the needle valve. However, now that the solenoid valve is integrated into a LabVIEW interface a PID function can be utilized to optimize the signal to achieve and maintain the desired pressure.

A PID function operates by taking the difference of two input values and altering the output value to minimize the difference. The two input values are the desired value, Set Point (SP) value, and the actual reading, Process Variable (PV). If the difference between the SP and the PV is large, the output signal will be high so that the difference is quickly reduced. Contrary, if the difference is small, the output signal will be low so the actual value does not over shoot the SP value. The PID function can be tuned by altering the three variables of the function; Proportional, Integral, and Derivative variables. Poor tuning typically results in two errors, either the SP is never reached or the PV never stabilizes. With a finely tuned PID function, a desired pressure can be quickly reached and well maintained.

The integration of the solenoid valve with the LabVIEW interface, via PID function, enables a variety of benefits whilst running CVD reactions. The first of which, as just mentioned, is the ability to automatically achieve a pressure and maintain it. This ability makes several parts of the reaction more manageable. Prior to the reaction, the pressure has to be adjusted to the pressure at which the reaction was to be run. Previously, this was done while flowing gases at the rates at which they were to be flown during the reaction. The needle valve had to be adjusted so that the outlet flow equaled the inlet flow. This was a laborious task due to the sensitivity of the needle valve. Also, since this was done at room temperature, during the reactions the pressure would rise from that initially set. Another major concern, during some reactions the precursor material would quickly vaporize causing a rapid rise in pressure. This results in two problems. First, the reaction would not run at a constant pressure. Since the reaction pressure was not recorded at this time, the pressure spike would likely go unnoticed, causing reaction inconsistency. Also, in some cases the pressure would spike to the extent that the tube manifolds would blow off. As can be imagined, if a reaction was being run with either flammable or toxic gases this could prove very unsafe. Thankfully though, the addition of the solenoid valve would prevent this by regulating the pressure if a spike were to occur. In addition to setting and maintaining a pressure, the integration of pressure control into a single interface with gas flow control allows for precise timing of pressure with flow rates.

Having control over both pressures and flow rates enables the ability to automate both the pump purge cycling and the reaction itself. The system could be set up to pull vacuum, then pressurize, and then once again pull vacuum. This process can be performed a specified number of times prior to the reaction. At this time, the temperature controller of the furnace had not yet been integrated with the LabVIEW interface. So once the pump purge process was complete, it

was still required that the reaction flow rates and pressure regulation be initiated manually along with the furnace. The manual initiation of the furnace was required so that the reaction conditions would be synced with the timing of the furnace. Although the reaction still needed to be initiated manually the flow conditions were fully automated through the interface. Several reaction segments with various flow rates and pressures could be programmed to be initiated at precise times. It was the addition of the solenoid valve that enabled the ability to run complex reactions such as those currently performed. More importantly, since the reaction parameters are all integrated and automated, the reaction parameters are more reliably reproduced, as well as recorded. Integration of the reactor components insures the precision of reaction pressure, temperature, and gas flow rates. Eventually, the temperature controller of the furnace was finally interfaced with LabVIEW.

Furnace control was achieved by reverse engineering a simple LabVIEW program provided by National Instruments. The interface allows for complete control of the furnace temperature controller. Single temperatures can be used to manually control the furnace as well as entering advanced programs. With the advanced programs, ramp rates and hold times can be entered for reactions. More importantly, the interface can now initiate the reaction process along with gas flow condition. So, the reactor can be assembled and then with a single push of a button the LabVIEW program will perform the pump purge process and then once complete bring the reactor to reaction parameters and then initiate the oven program. This turns what was once an hour long process of babysitting the reactor into a five minute process. With the automation of the reactor more complex reactions can be run along with minimal time consumption. Figure I.2 is a recording of a common reaction. As can be observed, reaction conditions have become quite

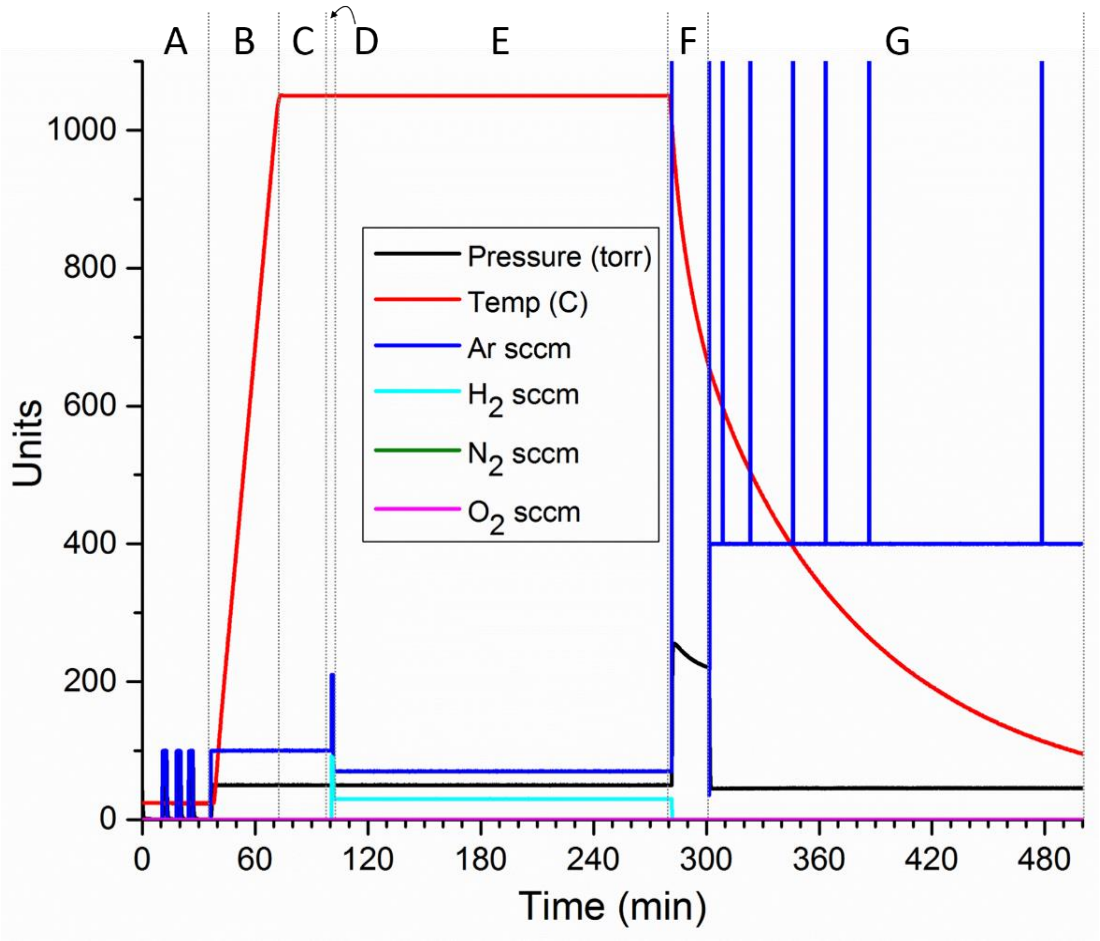

Figure I.2: Plot of the conditions recorded during a reaction. Different reaction segments are labeled at top. A) Pump and purge B) Ramp segment C) Deposition time D) Flush segment E) Growth time F) Purge G) Remainder of cool down. Spikes of Ar flow is only and error in the reading.

complex with automation. Similar reaction parameters could not likely be done manually. In addition to the integration of the furnace, the time at which the reaction starts can be delayed.

During some reactions supervision is needed at the end of the reaction. This could entail filling the liquid nitrogen trap (Figure I.1Q) or being present during flowing of toxic gasses. So, either the reaction must be set up early in the day in order to be present at the end or start the reaction in the middle of the night and arrive at the end. Because of the delay function reactions could be started at 2 AM by the LabVIEW interface. This way the reaction would be coming to a finish in the morning ready for supervision. Several additional alterations have been made to the reactor.

As with all reactions, reduction of contamination is an important issue. If a foreign substance is unknowingly introduced during a reaction, the results are not likely to be reproducible. Several precautions are taken to reduce the likelihood of contamination. For starters, the interior of tubes are prepared with a glassy carbon film by thermal decomposition of methane. The carbon coating prevents desorption of O_2 and H_20 at the high temperature at which reactions are run. Also, tubes are only reused for reactions which require the presence of similar elements. So for instance, a tube used for growing Cu catalyzed wires will not be reused for a reaction that does not require Cu. With this precaution, elemental cross contamination has been kept to a minimum. However, this precaution only proves effective if gas is flowing through the tube.

The reaction tube is the only easily interchangeable part of the reactor. Although the inlet and outlet manifolds are reused, the nature of CVD reactions prevents contamination of the reaction chamber. Any elements introduced during the reaction are introduced in the tube, downstream of the inlet manifold (figure I.1N). Therefore, the inlet manifold is never exposed to elements from different reactions. On the contrary, the outlet manifold (Figure I.1M) is downstream of the reaction and is exposed to several different contaminates. However, this contamination does not matter to the reaction, since it is downstream of where the reaction takes place. Therefore, during a reaction with flow, the inlet is never contaminated and any contamination on the outlet does not matter. However this does not hold true during a static reaction.

Other members of the lab have used the CVD system to anneal conditions under inert atmosphere. The annealing is performed under static conditions. So, while annealing any volatile material vaporizes and then deposits at the cooler ends of the tube. Thus, not only is the outlet manifold contaminated during the use of the reactor, but the inlet manifold is contaminated as well. With the inlet manifold contaminated, the foreign material can transport and interact with

following reactions. This once happened and led to the Cu contamination while trying to grow branched wires with Fe Mn, and Ni referred to in Chapter 6. To prevent similar contamination from again happening, a secondary inlet manifold and a valve (Figure I.1E) to switch between manifolds was added to the reactor. The additional manifold is employed during static anneals, whereas, the original manifold can be used for dynamic anneals. Thus preventing contamination of both types of reactions. Regular maintenance of both manifolds is necessary to ensure no leaks develop. Leaks not only can expose the reaction to atmosphere but also may leak hazardous gases into the atmosphere.

CVD systems use a variety of gasses, many of which, are not the safest to use. Silane gas is typically used for silicon nanowire growth. Silane is both highly toxic as well as pyrophoric. So, special precautions must be made so that silane is not uncontrollably released into the atmosphere. Silane has not yet been used but preparation for the use has been taken into consideration. As explained in Chapter 6, H_2S gas was used as a post reaction etchant. Clearly precaution must be made so the reactor itself is not etched. Not only is H_2S caustic, but it is also highly toxic and pyrophoric. A significantly dangerous aspect of H_2S is its scent. H_2S smells of rotten eggs and can be smelled at concentrations below toxic limits. However, olfactory receptors become saturated at toxic concentration. So, at toxic limits H_2S cannot not be smelled. This fact must be taken into consideration if one were to smell rotten eggs. If the smell goes away, it either means the gas has dissipated and it is safe or it has reached toxic levels and evacuation should be considered. To prevent exposure, precautions must be made.

Both silane and H_2S are highly toxic, as well as, caustic and pyrophoric. It is important to make specific considerations while purchasing parts for the use of these gasses. Seals that will be exposed to these gases need to be highly resistant to degradation. Seals need to be composed of

either 316 stainless steel, Teflon, or Kalrez. Viton is not acceptable. It is also important to reduce the length of time that the seals are exposed to the mentioned gasses. For this reason it is important to purge the lines after use. Purging is also important to reduce possibility of exposing the user to the toxic gas.

The use of dangerous gasses, H_2S and silane, was taken into consideration while designing the reactor. Valves (Figure I.1H) were added up stream of the MFCs so they can be used for a variety of gases (not simultaneously). In particular, adding the valves prior to MFC C allows the purging of the entire line used for the caustic gases. This way, the lines are only exposed to the gasses while in actual use. Also, to prevent the exposure of the vacuum pump to the caustic conditions a nitrogen trap is placed just prior to the vacuum pump. Exposing the pump to H_2S would degrade the pump oil, as well as, corrode the steel within the pump. In contrast, when silane is exposed to pump oil it forms SiO_2 (sand) which then mechanically grinds away the insides of the pump. Although the pump is protected during the reaction the trapped gas must then be controllably vented. For this purpose, a three way valve (Figure I.1S) was positioned between the trap and the vacuum pump. After a reaction is run and cooled, an overpressure is formed by filling the system with inert gas. At this point the three way valve is adjusted so that the venting gas flows through a flask of water. This way any excess of the trapped gasses is quenched by the water before being released into the hood. Many reactions using H_2S have been performed without complication. However, it is important to change the pump oil more periodically. Not all H_2S is trapped during the reaction due to excessively high flow rates. This extra precaution will prolong the lifetime of the pump without maintenance.

The mentioned improvements to the CVD system allows for broad variety of reactions. Many further additions are yet possible. Currently only two of the MFCs are capable of higher

flow rates. The addition of more MFCs may be necessary in the future. Also, the addition of Bubbler would be greatly beneficial. A Bubbler would expand the variety of reactions that could be performed. With a Bubbler liquid precursors can be utilized during reactions. Many elements can only be introduced by vaporizing a liquid precursor. Typically Cu is introduced to CVD reactions via a Bubbler. The addition of a Bubbler would allow better control of Cu concentration for branched nanowires since the flow rate through the bubbler can be tuned. Control of Cu concentration may be necessary to control wire architecture.

Appendix II

Maintenance and Leak Testing

Reliable inert conditions are vital to the reproducibility of CVD reactions. Because of this, it is important to regularly test the system for leaks. In addition to reproducibility, the use of toxic gases also raises the concern for possible leaks. Most sensitive points are areas that experience wear and tear during reactions. These points are typically the Swagelok ferrules within the manifolds that seal the tube. If over tightened the Teflon becomes compressed and no longer seals well. Also, the ferrules can degrade and pitted due to chipping of the tube and Alumina dust from the furnace. Another delicate seal is the VCR seals that connect the reactor lines to the manifolds. If VCR fitting are overly torqued the VCR faces can be separated from the gasket causing a minor leak. A dependable procedure has been developed to ensure that there are no leaks.

Finding a leak can be difficult due to the numerous possibilities where a leak can form. Thankfully, the reactor can be incrementally sealed. Since this can be done the location of the leak can be isolated. Leaks are detected by pulling full vacuum on the system and seeing how fast the pressure rises once the valve is closed. If the leak is slower than 1 mtorr/min, the reactor is considered to be sound. It is best to start by isolating the system from the bottom up. By placing an acrylic plug within the outlet manifold, the lower portion of the reactor can be isolated from the rest of the system. If no leak is detected, a tube is place between the inlet and outlet manifolds with the gas inlet valves closed (Figure I.1F). It is important to perform this step with fresh ferrules within the inlet and outlet manifolds. It is likely that the pressure will rise greater than a mtorr/min due to constriction of the tubing and desorption from the reactor walls. If the leak is a few mtorr/min move on to the next step which is to open the inlet valves of the carrier gasses that are to be used and the same procedure be repeated. At this point it is best to pull vacuum on the system

overnight and look for a rise in pressure in the morning. Pulling vacuum all night removes the remaining gasses from the lines and helps desorb gasses from the inner walls. If there is no increase in pressure after pulling vacuum overnight the system is sound. If there is still significant leakage the fittings should be checked to make sure that they are all snug. If the leak still persists, at times leakage can occur across the MFC's. The leak is typically is too low for the MFCs to detect it but is enough to show a rise in pressure. To test if it is leakage across the MFCs, the high pressure lines upstream of the MFC's should be vented by closing the valves on the catalyst tubes or the upstream ball valves (Figure I.1G-H) and fully opening the MFC. Once this is done pull vacuum again and redo the leak test. If it is determined that the leak is across the MFC it can either be ignored (knowing that it's a carrier gas leaking into the chamber) or the MFC can be disassembled and cleaned.

Appendix III

Carbon Coating

The quartz tubes and boats used for reactions are coated with glassy carbon. O_2 and H_20 desorb from the amorphous matrix when quartz is heated. At lower temperatures the amount desorbed is not significant to interfere with the reaction. However, the amount desorbed at higher temperatures becomes quite significant. Blocking of O_2 and H_2O desorption is essential to keep the products from oxidizing during the reaction.

Tubes are coated by thermal decomposition of methane. Initially the source of methane was the house gas, but now, research grade methane is used. No major increase in performance was observed at this change. An advantage of using methane from a cylinder though is the ability to control the gas flow by using a MFC. The tank can be attached by using the auxiliary line that was prepared for use of toxic gases.

The procedure described herein is for coating tubes in the three zone furnace. Coating in the single zone furnace has a few difference that will be pointed out. Carbon coating in the three zone furnace produces better films. For this reason it is better to coat the tubes while still 4 feet in length and then bisected. The three zone furnace has a max temp of 1200 °C compared to the 1100 °C of the single zone furnace. The higher temp produces glassier looking coatings and adhere to the tube better. Care must be taken to properly scrub out the tube prior to loading it into the furnace. It has been learned that any residue in the tube will prevent good adhesion of the carbon coating to the interior surface of the tube. The inside and the outside of the tube should be scrubbed well and rinsed with Millipore water. Gloves need to be worn during this or else residue from skin will etch the exterior of the tube at elevated temperatures.

The coating procedure can take 5-6 hours. However, the procedure must be carried out twice so that both ends of the tube get coated. The three zone and single zone furnaces coat different ends of the tube. The three zone furnace coats the upstream end of the tube, whereas, the single zone coats the downstream end. If large substrate boats are in need of coating they should be positioned inside the tube accordingly so that it gets coated. It is best to lay them in the tube top down to reduce the contact surface area between the boat and the interior of the tube. Once the tube is loaded into the furnace the manifolds should be attached using old ferrules. The inlet manifold should be placed flush against the ceramic of the furnace. Doing so will melt the ferrules used but will maximize the length of the tube that will be coated. The manifold with a small hole between the VCR fittings will be used for the outlet manifold. The hole should be plugged with a quarts rod rapped well with Teflon tape. This does not form the greatest seal but proves effective for purposes stated later. Caution must be taken while connecting the inlet and outlet manifolds. At 1200 °C quartz becomes malleable. If there is torque on the tube, it will bow a substantial amount during the coating process. If the tube is too bowed it makes loading into the furnace difficult. If a tube is bowed during the first coating, it is possible to reduce the bow by applying opposite torque during the application of the second coat.

Once the tube is sealed ramping can begin. The furnace should be ramped to 900 °C at a rate of 10 °C/min. To further insure a clean surface in the tube while ramping Ar and O2 are flown through the tube. This way any carbon residue in the tube will burn out. This can only be done prior to the first coating. Doing so before the second will burn out the first coating. When 900 °C is reached, vacuum should be pulled and a pump purge process done to expel all oxygen. From here the ramping is continued to 1200 °C at 30 °C/min. Once 1200 °C is reached the system is

pressurized to 1000 torr with Ar. Once an overpressure is reached the quartz/Teflon plug can be removed from the hole with 400 sccm of Ar flowing.

At this point the flow of methane can be started and the Ar flow can be cut to 100 sccm. The methane flow rate may vary. Start at 10sccm and then make proper adjustments. The vapor coming out of the outlet hole should not be black but lite brown and have an organic chemical smell similar to naphthalene. Methane should flow for about two minutes. Once that time is up, the Ar should be set to purge and the methane flow stopped. Purge for two minutes, then set Ar flow to 400sccm. Max temp should be held for at least ten minutes at this state. This is so any residual hydrocarbons that may have formed are vaporized from the carbon coating. Longer anneal times, up to 30 min, produce better coats, however, prolonged exposure of the tube to 1200 °C will cause excess bowing. Once the anneal step is complete, the furnace is turned off and left to cool.

Care must be taken while removing the tube from the furnace. Carbon soot will have deposited in the tube. Once the manifolds are removed the tube should not be turned vertical unless over a trash can. Excess powder can then be rinsed out in the sink. Once the carbon powder is removed the tube will need to be scrubbed clean. Where the manifold was attached there will be a buildup of organic residue. Acetone works best to remove this residue. Soaking may be necessary to fully remove the residue. Once properly cleaned and rinsed with Millipore water, the tube is then reloaded into the furnace as done for the first coating but with the ends inverted.

Before ramping a pump/purge cycling is carried out. If the atmosphere inside the tube is not kept inert the carbon already applied will burn off. After pump/purge cycling the ramping may proceed. Again, ramp to 900 °C at 10 °C/min. This initial slow ramp is so any adsorption of water to the walls will sufficiently be removed, also, so unnecessary shock to the furnace does not occur. Once 900 °C is reached the faster rate of 30 °C/min may be used to ramp at 1200 °C.

At 1200 °C the same procedure is followed; pressurization, plug removal, and methane flow. However, it is best to reduce the length of time of methane exposure. If too thick of a coating is formed, it will peel during cooling. Since the middle of the tube has partially been coated, a second full application may cause too thick of a carbon film. After the film has been applied and annealed, the furnace is again turned off and let cool while flowing Ar. When the furnace is cool the tube may be removed and cleaned in a similar fashion as that of the first coating. The tube can be easily bisected by Mike Olsen, the glassblower, in the basement. Also, flame polishing the ends of the tube makes for easier insertion into manifolds. An Oxy-Acetylene flame will be necessary for this to be easily done. If one is not available in the lab, once again, it can be done by Mike Olsen.

The coatings are surprisingly robust if properly applied. Flaking of the coating may be observed during the initial uses of a freshly coated tube. Flaking is minimized by keeping the thickness to an effective minimum. Yet, the coating still should not be translucent. In addition to flaking, the coating may form minor scratches as a result of scrubbing. These have not shown to affect the performance of the coating. Prolonged use of the tube may lead to excess scratching.

If the coating becomes too degraded it can be fully removed and recoated. Removal of the carbon coating can be done by baking the tube in the single zone furnace at 900 °C while exposed to atmosphere (no manifolds). Positioning of the tube should be considered. It is best to try and position the tube so that the area burned off is the similar to the area that will be coated in a single coating process. Once the original coating is removed and cooled, the tube should be thoroughly cleaned and then rinsed with Millipore water. Recoating of the tube in the single zone furnace should be carried out similarly to the procedure specified for the second coat applied in the three zone furnace.

The degradation of the carbon coating with oxygen at high temperatures has several benefits other than removing the coating. Because of the carbons reactivity with oxygen, during a high temperature reaction the coating will act as a getter and react with free oxygen within the system. For this same reason, it can be clear that a leak has formed. If there is a significant leak the carbon coating will be stripped off during a reaction that can easily be seen. As long as there are no significant leaks the carbon coating should last the lifetime of the tube.